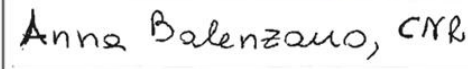# D3: Final Report

SARSimHT-NG – Simulation of Hydroterra SAR System Performance in the Mediterranean and the Alps Based on Experimental Airborne SAR Data

(ESA Contract No. 4000134680/21/NL/FF/an)

Reference: DLR-HR-TR-SARSimHT-NG-03

	Name	Signature
Prepared by	Horn, Ralf	*Ralf Horn* (Digitally signed by Ralf Horn, DN: O=Deutsches Zentrum fuer Luft- und Raumfahrt e.V. (DLR), CN=Ralf Horn, E=ralf.horn@dlr.de, Reason: I attest to the accuracy and integrity of this document, Location:, Date: 2024.09.13 20:09:00+02'00', Foxit PDF Editor Version: 13.1.3)
	Nagler, Thomas	*Thomas Nagler* (enveo, Environmental Earth Observation Information Technology GmbH)
	Balenzano, Anna	*Anna Balenzano, CNR*
Released by	Reigber, Andreas	*A. Reigber* (Digital signiert von Dr. Andreas Reigber, DN: C=DE, S=Nordrhein-Westfalen, L=Koeln, O=Deutsches Zentrum fuer Luft- und Raumfahrt e.V. (DLR), DN=Reigber, G=Andreas, CN=Dr. Andreas Reigber, Grund: Ich genehmige dieses Dokument, Ort:, Datum: 2024.09.16 17:04:43+02'00', Foxit PDF Editor Version: 13.1.2)

Approval and release information:
This document has been approved either by manual signatures or via electronic workflow.

Document Preparation

The document on hand was prepared with contributions from the personnel listed below:

Name	Organization
Horn, Ralf	DLR-HR
Scheiber, Rolf	DLR-HR
Fischer, Jens	DLR-HR
Basargin, Nikita	DLR-HR
Nagler, Thomas	ENVEO IT
Rott, Helmut	ENVEO IT
Scheiblauer, Stefan	ENVEO IT
Balenzano, Anna	CNR-IREA
Francesco, Mattia	CNR-IREA
Palmisano, Davide	CNR-IREA
Satalino, Giuseppe	CNR-IREA

Distribution List

Name	Organization	Type
Moreira, Alberto	DLR-HR	PDF
Reigber, Andreas	DLR-HR	PDF
Nagler, Thomas	ENVEO IT	DOCX, PDF
Balenzano, Anna	CNR-IREA	DOCX, PDF
Julia Kubanek	ESA	DOCX, PDF

Document Change Details

Latest changes to the document are listed first.

Issue	Date	Modified Pages/Sections	Changes
0.1	12.02.2024	all	Initial issue
0.2	28.03.2024	all	Chapter 4 on SWE (WP320) added
0.3	08.04.2024	all	Chapter 6 on SSM (WP430) added
0.4	22.05.2024	all	Chapter 3 (WP 240) added & updated
0.5	17.06.2024	all	Chapter 5 on SSM (WP420) added
1.0	12.07.2024	all	Draft issue
1.1	12.09.2024	all	Final issue

Table of Contents

List of Acronyms and Abbreviations

AoI	Area of Interest
CNR-IREA	National Research Council of Italy - Institute for Electromagnetic Sensing of the Environment
CPD	Co-polarized Phase Difference
CR	Corner Reflector
CREA-CI	Consiglio per la Ricerca in agricoltura e l'analisi dell'Economia Agraria – Centro di ricerca per le Colture Industriali
DAR	Data Acquisition Report
DLR	Deutsches Zentrum für Luft- und Raumfahrt e.V., German Aerospace Center
DLR-HR	German Aerospace Center, Microwaves and Radar Institute
ENVEO IT	Environmental Earth Observation Information Technology GmbH
ESA	European Space Agency
HT01x01	Simulated Hydroterra product, 01 x 01 pixels (azimuth x range)
HT04x01	Simulated Hydroterra product, 04 x 01 pixels (azimuth x range)
InSAR	Interferometric SAR
MB	Mittlerer Boden (Wörgetal)
NESZ	Noise Equivalent Sigma Zero
OB	Oberer Boden (Wörgetal)
PRF	Pulse Repetition Frequency
RMSE	Root Mean Square Error
RoI	Region of Interest (sites with in-situ measurements)
ROSE-L	L-Band Radar Observation System for Europe
RP-InSAR	Repeat-Pass Interferometric SAR
SAR	Synthetic Aperture Radar
SE	Snowfall Event
SD	Snow Depth
Sentinel-1 NG	Sentinel-1 Next Generation
SLC	Single-Look Complex
SNR	Signal-to-Noise Ratio
SSM	Surface Soil Moisture
SWE	Snow Water Equivalent
UB	Unterer Boden (Wörgetal)
w.e.	water equivalent
WCA	Wind Correction Angle
WP	Work Package

Documents

Applicable Documents

[A1]   Statement of Work. SARSimHT-NG – Simulation of Hydroterra SAR System Performance in the Mediterranean and the Alps Based on Experimental Airborne SAR Data. ESA-EOPSM-CAMP-SOW-3812, Issue 1, Revision 6, 04/02/2021.

[A2]   D1: Data Acquisition Report of SWE Experiment. DLR-HR-TR-SARSimHT-NG-01, Issue 2, 25-11-2021.

[A3]   D2: Data Acquisition Report of SSM Experiment. DLR-HR-TR-SARSimHT-NG-02, Issue 1.7, 06-09-2023.

Reference Documents

[1]   SARSimHT 2019: "Final Report", Technical Report: DLR-HR-TR-SARSimHT-2019-003, Oct. 2020.

[2]   Ralf Horn, Marc Jaeger, Martin Keller, Markus Limbach, Anton Nottensteiner, Matteo Pardini, Andreas Reigber, Rolf Scheiber (2017), "F-SAR – Recent Upgrades and Campaign Activities". In: 13th International Radar Symposium (IRS), 2017-06-28 - 2017-06-30, Prague, Czechia. CUVILLIER VERLAG. ISBN 978-3-7369-9542-0.)

[3]   Fierz, C., Armstrong, R.L., Durand, Y., Etchevers, P., Greene, E., McClung, D.M., Nishimura, K., Satyawali, P.K. and Sokratov, S.A. 2009. The International Classification for Seasonal Snow on the Ground. IHP-VII Technical Documents in Hydrology No. 83, UNESCO-IHP, Paris. 90 pp.

[4]   R. Scheiber, S.-K. Lee, K. P. Papathanassiou, N. Floury, "Extrapolation of Airborne Polarimetry and Interferometric SAR Data for Validation of Bio-Geo-Retrieval Algorithms for Future Spaceborne SAR Missions", Proc. IGARSS, Cape Town, 2009.

[5]   Description of Simulated Amplitude Results for Hydroterra (Technical Report: DLR-HR-TR-SARSimHT-2019-002).

[6]   Curlander, J. C., and R. N. McDonough, "Synthetic Aperture Radar: Systems and Signal Processing", pp. 647, John Wiley, New York, 1991.

[7]   Hydroterra Earth Explorer 10 Mission Candidate Mission Assumptions and Preliminary Technical Requirements (MATER). Ref: EOP-ΦMP/2018-12-2114, issued 14-05-2020.

[8]   DLR's Airborne SAR System F-SAR PRODUCT DESCRIPTION, Version: 3.2.

[9]   Valeria Gracheva, Pau Prats, Rolf Scheiber, Ralf Horn, Martin Keller, Jens Fischer, Andreas Reigber, Alberto Moreira, "Simulation of Geosynchronous Hydroterra Image Products with Airborne SAR Data", Proceedings of the European Conference on Synthetic Aperture Radar (EUSAR), March 2021, pp.581 586.

[10]   Valeria Gracheva, Rolf Scheiber, Pau Prats, Ralf Horn, Martin Keller, Jens Fischer, Alberto Moreira, Julia Kubanek, Roger Haagmans, "Airborne SAR Experiment to Simulate Geosynchronous Hydroterra Data and Investigate the Detection of Diurnal Changes", Proceedings of the IEEE International Geoscience and Remote Sensing Symposium (IGARSS), July 2021, pp. 3285-3288.

[11]   S. Leinss, G. Parrella, I. and I. Hajnsek, "Snow height determination by polarimetric phase differences in X-Band SAR data ", IEEE J. Select. Top. Appl. Earth Obs. Rem. Sens., vol. 7, pp.3794–3810, 2014.

[12]   S. Leinss, H. Löwe, M. Proksch, J. Lemmetyinen, A. Wiesmann, and I. Hajnsek, "Anisotropy of seasonal snow measured by polarimetric phase differences in radar time series ", The Cryosphere, vol. 10, pp. 1771–1797, https://doi.org/10.5194/tc-10-1771-2016, 2016.

[13]   T. Guneriussen, K. A. Hogda, H. Johnson and I. Lauknes, "InSAR for estimating changes in snow water equivalent of dry snow", IEEE Trans. Geosci. Rem. Sens., vol. 39, no. 10, pp. 2101-2108, 2001.

[14]   H. Rott, T. Nagler and R. Scheiber "Snow mass retrieval by means of SAR interferometry", Proc. of ESA Fringe 2003 Workshop, Frascati, Italy, ESA SP-550, 2004.

[15] C. Mätzler, "Microwave permittivity of dry snow", IEEE Trans. Geosci. Rem. Sens., vol. 39, no. 2, pp. 573-581, 1987.

[16] R. Bamler and P. Hartl, "Synthetic aperture radar interferometry", Inverse Problems, 14: R1-R54, 1998.

[17] C. Fierz, R.L. Armstrong, Y. Durand, P. Etchevers, E. Greene et al. The International Classification for Seasonal Snow on the Ground, IHP-VII Techn. Documents in Hydrology No. 83, IACS Contribution No. 1, UNESCO-IHP, Paris, 2009.

[18] A. Balenzano, F. Mattia, G. Satalino, and M. W. J. Davidson, "Dense temporal series of C- and L-band SAR data for soil moisture retrieval over agricultural crops", IEEE Journal of Selected Topics in Applied Earth Observations and Remote Sensing, vol. 4, no. 2, pp. 439–450, 2011. DOI: 10.1109/JSTARS.2010.2052916.

[19] I. Hajnsek, E. Pottier, and S. R. Cloude, "Inversion of surface parameters from polarimetric SAR," IEEE Transactions on Geoscience and Remote Sensing, vol. 41, no. 4, pp. 727–744, 2003.

[20] T. Jagdhuber, I. Hajnsek, and K. P. Papathanassiou, "An iterative generalized hybrid decomposition for soil moisture retrieval under vegetation cover using fully polarimetric SAR", IEEE Journal of Selected Topics in Applied Earth Observations and Remote Sensing, vol. 8, no. 8, pp. 3911–3922, 2014.

[21] F. De Zan, A. Parizzi, P. Prats-Iraola, and P. López-Dekker, "A SAR interferometric model for soil moisture", IEEE Transactions on Geoscience and Remote Sensing, vol. 52, no. 1, pp. 418–425, 2013.

[22] S. Zwieback, S. Hensley, and I. Hajnsek, "Soil moisture estimation using differential radar interferometry: Toward separating soil moisture and displacements", IEEE Transactions on Geoscience and Remote Sensing, vol. 55, no. 9, pp. 5069–5083, 2017.

[23] M. T. Hallikainen, F. T. Ulaby, M. C. Dobson, M. A. El-Rayes, and L.-K. Wu, "Microwave dielectric behavior of wet soil-part 1: Empirical models and experimental observations," IEEE Transactions on Geoscience and Remote Sensing, no. 1, pp. 25–34, 1985.

[24] Berizzi, Fabrizio, et al., "Autofocus of wide azimuth angle SAR images by contrast optimisation", IGARSS'96. 1996 International Geoscience and Remote Sensing Symposium. Vol. 2. IEEE, 1996.

[25] Touzi, R., Lopes, A., Bruniquel, J., Vachon, P. W., "Coherence estimation for SAR imagery", IEEE Trans. Geoscience and Remote Sens. 1999, 37, 135–149.

[26] Gracheva, V., Horn, R., Scheiber, R., Fischer, J., Keller, M., Prats, P., Reigber, A., Moreira, A.: "Hydroterra's Geosynchronous Image Product Simulation using Polarimetric Airborne SAR Data", ESA Advanced RF Sensors and Remote Sensing Instruments (ARSI), 11-13 November 2019, Noordwijk, The Netherlands.

[27] A. K. Fung, Microwave Scattering and Emission Models and Their Applications. Norwood, MA: Artech House, 1994.

[28] S. C. Brown, S. Quegan, K. Morrison, J. C. Bennett, and G. Cookmartin, "High-resolution measurements of scattering in wheat canopies - Implications for crop parameter retrieval", IEEE Trans. Geosci. Remote Sens., vol. 41, no. 7, pp. 1602-1610, 2003.

[29] G. Picard, T. Le Toan, and F. Mattia, "Understanding C-band radar backscatter from wheat canopy using a multiple-scattering coherent model", IEEE Trans. Geosci. Remote Sens., vol. 41, no. 7, pp. 1583-1591, 2003.

[30] F. Mattia, T. Le Toan, G. Picard, F. I. Posa, A. D'Alessio, C. Notarnicola, A. M. Gatti, et al., "Multitemporal C-band radar measurements on wheat fields", IEEE Trans. Geosci. Remote Sens., vol. 41, no. 7, pp. 1551-1560, 2003.

[31] Palmisano, D., F. Mattia, A. Balenzano, G. Satalino, N. Pierdicca, A. Monti Guarnieri, "Sentinel-1 Sensitivity to Soil Moisture at High Incidence Angle and the Impact on Retrieval Over Seasonal Crops", IEEE Trans. on Geoscience and Remote Sensing, Vol. 59, Issue 9, pp. 7308-7321, Sept. 2021, Print ISSN: 0196-2892, DOI: 10.1109/TGRS.2020.3033887.

[32] A. A. Swartz, H. A. Yueh, J. A. Kong, L. M. Novak, R. T. Shin, "Optimal polarizations for achieving maximum contrast in radar images", Journal of Geophysical Research: Solid Earth. Vol. 93, Issue B12, pp. 15252-15260, 1988, https://doi.org/10.1029/JB093iB12p15252.

[33]   A. Balenzano, F. Mattia, G. Satalino, F. P. Lovergine, D. Palmisano, J. Peng, P. Marzah, U. Wegmüller, O. Cartus, K. Dąbrowska-Zielinska, J. P. Musial, M. W. J. Davidson, V. R. Pauwels, M. H. Cosh, H. McNairn, J. T. Johnson, J. P. Walker, S. H. Yueh, D. Entekhabi, Y. H. Kerr, T. J. Jackson, 2021, "Sentinel-1 soil moisture at 1 km resolution: a validation study", Remote Sensing of Environment, 263, 112554, DOI: https://doi.org/10.1016/j.rse.2021.112554.

[34]   G. Satalino, A. Balenzano, F. Mattia, and M. W. J. Davidson, "C-band SAR Data from Mapping Crops Dominated by Surface or Volume Scattering", IEEE Geosci. Remote Sens. Lett., vol. 11, no. 2, pp. 384-388, 2014.

[35]   A. Balenzano, Satalino, G., Lovergine, F., Rinaldi, M., Iacobellis, V., Mastronardi, N., Mattia, F., "On the use of temporal series of L- and X-band SAR data for soil moisture retrieval. Capitanata plain case study", Eur. J. Remote Sens. 46, 2013. https://doi.org/10.5721/EuJRS20134643.

[36]   J. D. Ouellette, J. T. Johnson, A. Balenzano, F. Mattia, G. Satalino, S. B. Kim, et al., "A time-series approach to estimating soil moisture from vegetated surfaces using L-band radar backscatter", IEEE Trans. Geosci. Remote Sens., vol. 55, no. 6, pp. 3186-3193, 2017. https://doi.org/10.1109/TGRS.2017.2663768.

1 Introduction and Purpose of the Document

The main objective of the SARSimHT-NG study, as requested by ESA, is to assess the potential to obtain snow water equivalent (SWE) and surface soil moisture (SSM) measurements from future SAR systems in geosynchronous orbit [A1]. This assessment is based on data sets specifically collected in winter 2021 (SWE) and spring 2022 (SSM) with DLR's scientific airborne F-SAR radar system. In parallel to the radar measurements, extensive field work was carried out in both years, with the field data complementing the radar data. The data collection has been summarised in two data acquisition reports D1: DAR for SWE [A2] and D2: DAR for SSM [A3].

The data collection campaigns have taken place:

1. **21HTERRA**: On SWE at the Austrian test site 'Woergetal' in winter 2021, more precisely from 2nd to 19th March 2021. The field work was carried out by ENVEO IT in Innsbruck, Austria.

2. **22HTERRA**: On SSM at the Italian test site 'Apulian Tavoliere' in spring 2022. Two missions were carried out, the first from 28 to 29 April and the second from 15 to 16 June. The field work was led by CNR-IREA in Bari, Italy.

This report concludes the SARSimHT-NG study. It presents the results obtained by the project partners from the analyses of the two thematically distinct data sets and concludes with a summary of considerations for the design of future spaceborne SAR missions.

2   SARSimHT-NG Study –Objectives and Work Structure

The SARSimHT-NG study investigates capabilities of spaceborne SAR instruments of deriving measured values on two important environmental parameters, which are snow-water-equivalent (SWE) and surface-soil-moisture (SSM). For this purpose, two airborne SAR measurement campaigns have been carried out over dedicated test sites employing DLR's F-SAR radar system. The measurements were carried out in C- and L-bands in regard to Sentinel-1 and upcoming Hydroterra, ROSE-L and Sentinel-1 Next Generation (NG) space systems. The present study, however, focuses on a future Hydroterra space system concept, which envisages a C-band SAR on geostationary platform. To simulate any image data product of such a space system the airborne SAR data are post-processed to match Hydroterra EE10 mission scenario 4, which is a scenario adopted for glacier flow among others [7]. Post-processing parameters are listed in Table 2-1.

Table 2-1: Relevant parameters of scenario 4 of the interferometric type used for Hydroterra product simulation. For comparison, the nominal values of an individual F-SAR data take (right column).

Parameters	Hydroterra	F-SAR
Single-look azimuth resolution	5 m	0.5 m
Multi-look azimuth resolution	50 m	5 m
Number of looks in azimuth	10	10
Range bandwidth	6 MHz	384 MHz
Single-look slant range resolution	22.2 m	0.5 m
Multi-look slant range resolution	22.2 m	0.5 m
Number of looks in range	1	1
Noise Equivalent Sigma Zero	-21.1 dB	< -30 dB

2.1   Study objectives recalled

In agreement with SoW [A1], the main objectives for the retrieval of SWE were:
- Proof of the geostationary measurement concept for InSAR SWE retrieval in mountainous regions.
- Assessment of image quality in snow covered mountain areas due to different disturbances during long image acquisitions.
- Investigation of InSAR coherence over snow covered mountain areas due to different disturbances during long image integration times.
- Investigation of InSAR coherence over snow with spatial-temporal changes.
- Assessment of InSAR phase related to snow mass changes (e.g., by snow fall or drift).

The main objectives for the retrieval of SSM were:
- Simulation of Hydroterra amplitude and interferometric phase products from acquired SAR image stacks.
- Analysis of simulated Hydroterra products quality and comparison to conventional SAR products.
- Evaluation of the temporal decorrelation impact on Hydroterra products.

2.2 Work package breakdown structure recalled
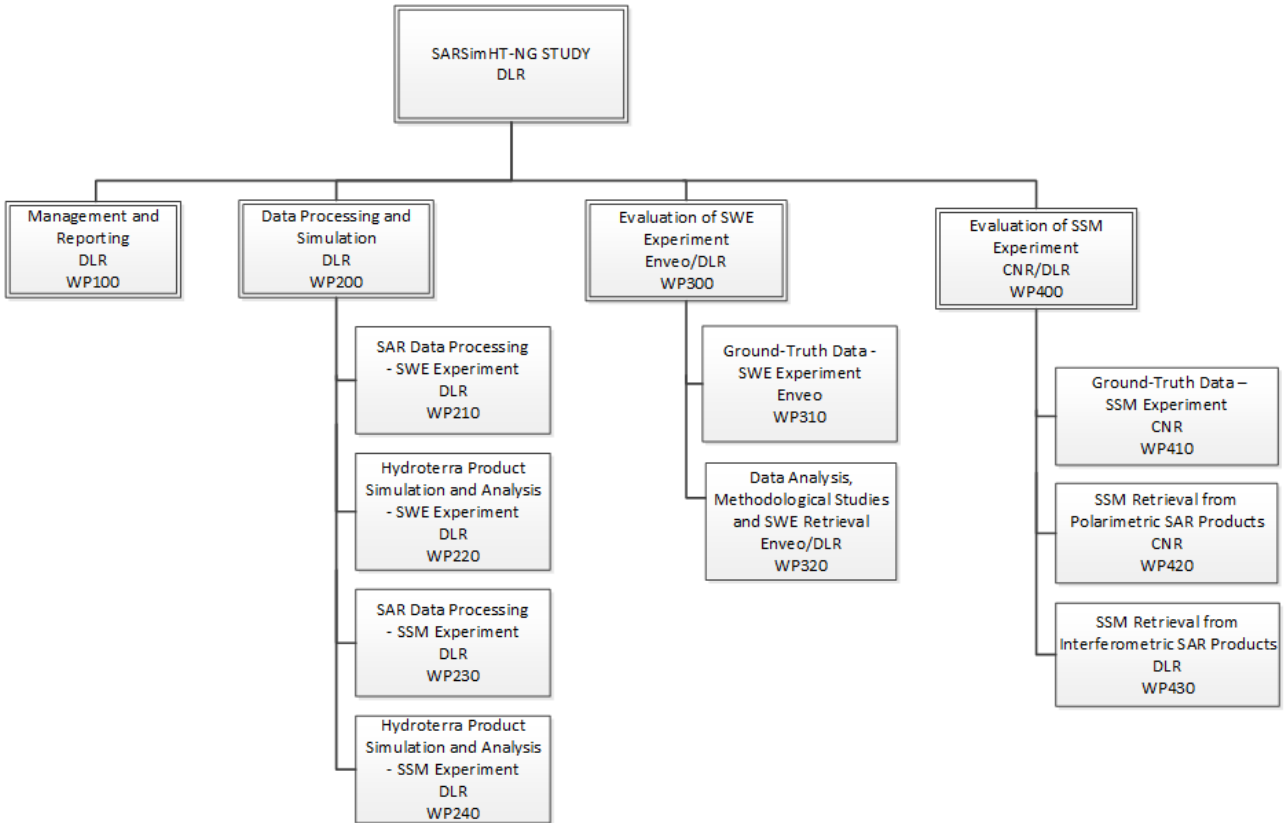
Figure 2-1: SARSimHT-NG – Study work package breakdown structure.

The contents of this report regard the following work packages:

1. WP240: Hydroterra Product Simulation and Analysis – SSM Experiment
2. WP320: Data Analysis, Methodological Studies and SWE Retrieval
3. WP420: SSM Retrieval from Polarimetric SAR Products
4. WP430: SSM Retrieval from Interferometric SAR Products

3 Hydroterra Product Simulation and Analysis – SSM Experiment (WP240)

WP 240 includes the following activities: (1) Simulation of Hydroterra amplitude products from acquired image stacks, (2) Processing of Hydroterra interferometric products, (3) Analysis of simulated Hydroterra products and comparison with conventional SAR products, (4) Evaluation of the effect of temporal decorrelation on Hydroterra products.

Items (1) and (2), i.e. the simulation of Hydroterra Single Look Complex (SLC) images and the processing of interferometric products from these data, have already been described in the contribution to the 'Data Acquisition Report (DAR) of the SSM Experiment' [A3]. SSM stands for Surface Soil Moisture.

Items (3) and (4) are described in the following sections. Information on agricultural fields and crops present in the "Apulian Tavoliere" test site, as provided in the SARSIMHT_D2_DAR_SSM_database [A3], has been used in the course of the investigation.

3.1 Preparing the data analysis

3.1.1 Data quality measures

Three standard quality measures (mean value, contrast and coherence) were used to facilitate a comparative analysis of simulated Hydroterra SAR (integration time of about two hours (long)) in two different qualities, GEO (high resolution (F-SAR)) and HT (low resolution (simulated)), with conventional SAR (integration time of a few seconds (short), nominal F-SAR). See Table 2-1 for reference. Calculated from either SLC images or interferograms, the three measures were determined both for the whole scene and for specific areas, e.g. individual fields.

Mean Value

SLC imagery is converted and stored as image intensity data sets. The mean value μ, in [dB], is calculated using

$$\mu = 10 \log_{10}(E\{I^2\}) , \tag{3-1}$$

where E is the expectation value of the image intensity.

Contrast

The image contrast CV, or the Coefficient of Variation, is expressed as the ratio of the image intensities' standard deviation σ to their mean value μ [6], i.e.

$$CV = \frac{\sqrt{E\{(I^2 - E\{I^2\})^2\}}}{E\{I^2\}} = \frac{\sigma}{\mu} . \tag{3-2}$$

The contrast can be used as a measure to assess the focusing quality in SLC images as outlined in [24]. In this study the focusing qualities of conventional SAR and simulated Hydroterra SAR images were compared.

Interferometric Coherence

The quality of an interferogram can be assessed by means of the interferometric coherence γ, which is defined as the normalized cross-correlation coefficient between two SLC images [16], [25]. i.e.

$$\gamma = \frac{|E\{I_1 \cdot I_2^*\}|}{\sqrt{E\{I_1^2\} \cdot E\{I_2^2\}}} , \tag{3-3}$$

where E is the expectation value and * indicates complex conjugation.

3.1.2   Creation of the simulation database

The starting point of the analysis were the GEO (high-resolution geo-synchronous SAR) and the HT (Hydroterra) simulation data products listed in Table 3-1 (see also the DAR [A3], Section 5.4). These products are part of the data delivery D2.

Table 3-1: Files used to create the simulation database ('xx' denotes the different polarimetric channels hh, hv, vv and vh).

Data product	Description
contrast_ht_xx.png	Contrast of the SLC simulation product (all passes fused)
contrast_slc_xx.png	Contrast of the SLC data product (first pass only)
slc_0104_xx.rat	SLC of the first pass only
slc_ht_0104_xx.rat	SLC of the simulation product
coh_ht_0202_xx.png	Coherency of the interferogram (quicklook image)
coh_ht_0202_xx.rat	Coherency of the interferogram (data, RAT format)

For every simulation product (GEO and HT) there are two SLC images, one with short and one with long integration time. These exist for every polarimetric channel HH, HV, VV, VH. This yields 16 SLC images from which were generated:

- *16 Contrast Images* (named: contrast*.rat); contrast values were calculated block by block using a sliding window. Prior to contrast calculation using equation (3-2), the image blocks were normalised to their individual maximum value, $\bar{b} = b/\max(b)$, where b is a block. The size of a block was chosen to match the image resolution. This is necessary because pixels in the high-resolution data (GEO) are square (0.5m x 0.5m) and those in the low-resolution data (HT) are rectangular (5m x 22.2m). Block sizes given in pixels of 16 x 16 (az x rg) were used in the GEO data and 32 x 8 (az x rg) in the HT data.
- *16 Amplitude Images* (named: amplitude*.rat); image pixel magnitudes were calculated from SLC values. Mean values were calculated using equation (3-1).
- *16 Coherency Images* (named: coherency*.rat); interferometric coherence images were generated using equation (3-3).

This sums up to 48 data products per measurement flight. To work with the ground measurement data base these data products were geocoded to the common geographical grid.

In April (FL01, FL02, FL03) and June 2022 (FL05, FL06, FL07) six flights were performed for the purpose of HT simulation. Thus, the database for the analysis contains 288 geocoded datasets plus 288 header files. For more information, see Table 9-1 in the Appendix.

3.1.3   Creating comparative diagrams

In order to facilitate an efficient comparison between short- and long-integration-time products, it is convenient to plot averaged values of contrast, intensity and coherence of all six flights in the same diagram, with two distinct curves representing:

- short integration quality (blue curve) versus
- long integration quality (red curve).

From 288 data products 24 sets of comparative diagrams were generated representing the six flights and the short- (GEO) and long-integration-time (HT) products. The diagrams of the four related polarimetric channels and the associated 12 quicklook images were then compiled into one PDF file to serve as input for further visual inspection.

This way, the following six PDF files are obtained:

1. High-resolution (GEO) products
    a. *Contrast*:   contrast*GEO*.pdf
    b. *Amplitude*:   amplitude*GEO*.pdf
    c. *Coherence*:   coherency*GEO*.pdf
2. Low-resolution (HT) products
    a. *Contrast*:   contrast*HT*.pdf
    b. *Amplitude*:   amplitude*HT*.pdf
    c. *Coherence*:   coherency*HT*.pdf

The analysis can be performed on the whole scene ('Apulian Tavoliere') as well as on individual farms and fields. A set of six PDFs per field or area of interest is obtained. For more information, see Table 9-3 in the Appendix.

3.2   Simulation data analysis

For this data analysis, a total of 50 Areas of Interest (AoIs) were inspected, including the entire 'Apulian Tavoliere' scene, the Caione farm, the CREA farm and 47 individual fields (including those monitored during the airborne SAR campaign). These AoIs are listed in Table 9-2 in the Appendix.

The following sections detail the results of the analysis for a representative selection of AoIs (see Figure 3-1). These serve as examples for the remaining fields listed in the Appendix (Section 9).
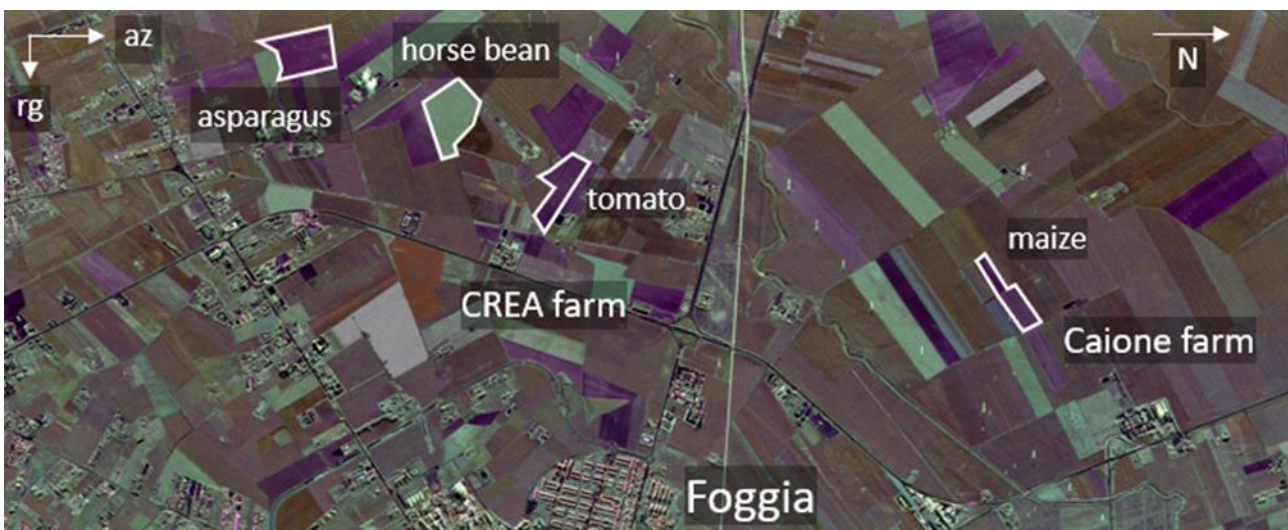
Figure 3-1: High-resolution polarimetric F-SAR C-band image, taken in April (RGB=HH, HV, VV). Situation in April: violet colours indicate bare soil; green colours indicate fields with high vegetation.

3.2.1 Impact on image contrast

A loss of focus quality in Hydroterra data can be expected due to the long azimuth integration time for all objects that move in any way, e.g. in case of vegetation in windy conditions. The higher the vegetation, the more susceptible it is to wind. This can indeed be observed in the simulated geostationary satellite SAR data.

First, the entire scene (C-band, VV polarisation) is considered. In a second step, selected individual fields are examined. Figure 3-2 andFigure 3-3 show the image contrast of FL01 (April) data calculated block by block over the whole scene at high (GEO) and low (HT) resolution and short and long integration times. Dark colours indicate low image contrast. Human-made infrastructure appears white.
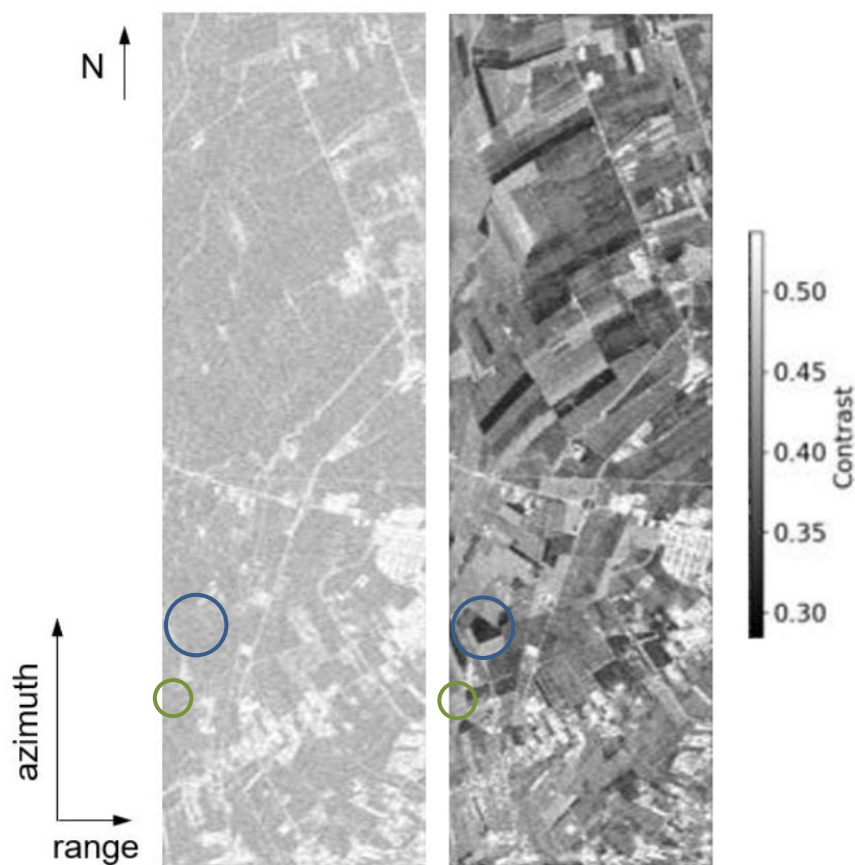
Figure 3-2: Image contrast in FL01; short integration (left) versus long integration (right) in high resolution data (GEO). The contrast value averaged over the scene drops from 0.48 on the left to 0.43 on the right. Circles indicate a field of horse bean (blue) and a field of asparagus (green).

In the high-resolution data (GEO) a decrease in the total contrast from 0.48 to 0.43 is observed, i.e. by 0.05, and in the low-resolution data (HT) this decrease is from 0.51 to 0.48, i.e. by only 0.03. The initial values of 0.48 and 0.51 differ because different resolutions and different sliding window sizes had to be used (see Section 3.1.1 for block size selection). The trend observed here is typical for (simulated) Hydroterra data. Comparing the high- and low-resolution images of the long integrations (right), the contrast drops appear on the same fields - although somewhat blurred due to the lower resolution.
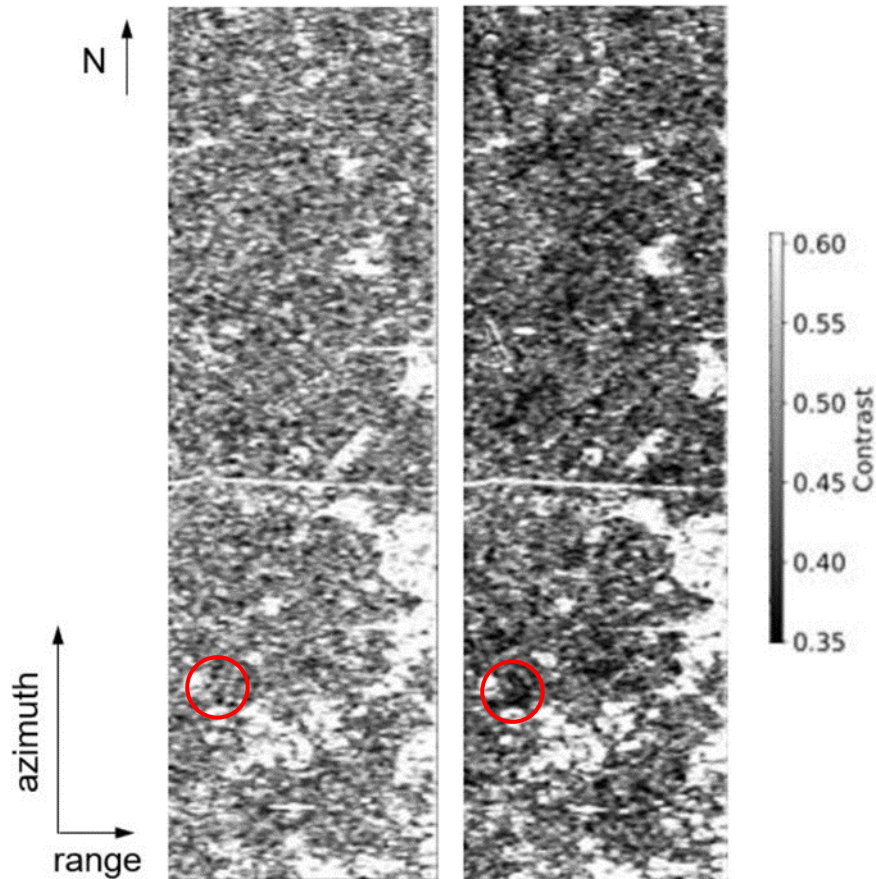
Figure 3-3: Image contrast in FL01; short integration (left) versus long integration (right) in low resolution data (HT). The contrast value averaged over the scene drops from 0.51 on the left to 0.48 on the right. Circles (red) indicate a field of horse bean.

For looking at field-size AoIs the four exemplary fields indicated in Figure 3-1 (horse-bean, asparagus, tomato and maize) were selected. The following plots show the image contrast averaged over the individual AoIs. Their generation is described in Section 3.1.3.

Figure 3-4 shows a comparison of image contrast for a field of horse beans (FIELD_509) and a field of asparagus (FIELD_437) over two seasons (spring - summer). The effect of the vegetation on image contrast can also be observed in the images in Figure 3-2.
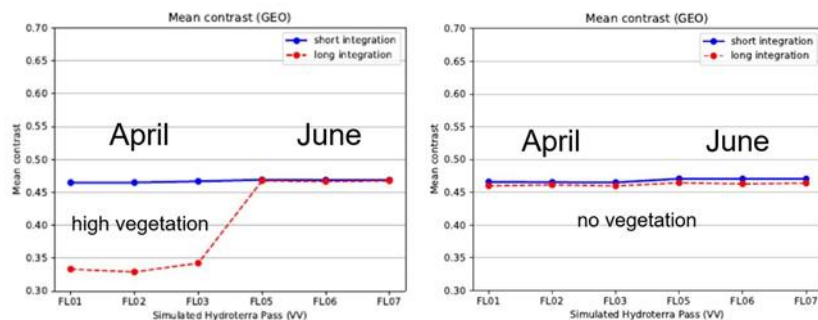
Figure 3-4: Mean image contrast of a horse bean field (FIELD_509) (left) versus an asparagus field (FIELD_437) (right), from April to June, in high-resolution (GEO) data (VV polarisation).
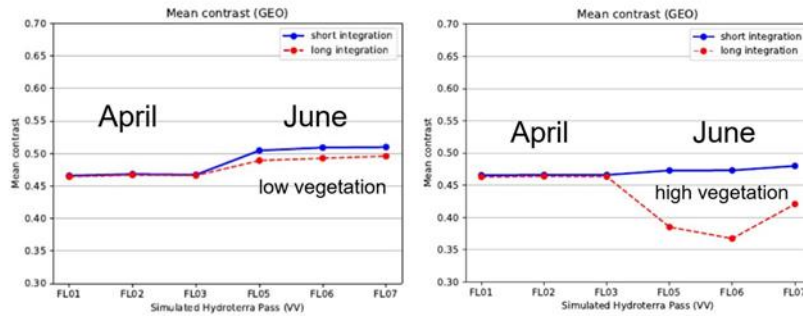
Figure 3-5: Mean image contrast of a field of tomatoes (left) versus a maize field (right), from April to June, in high-resolution (GEO) data (VV polarisation).

Figure 3-5 shows the change in average image contrast for a tomato field (FIELD_043) and a maize field (CA_MA) over the two seasons. Again, the influence of the height of the vegetation present is evident. It can be concluded that in areas with high vegetation the image contrast deteriorates due to defocusing caused by wind-induced movement.

This behaviour is typical of the contrast degradation studied on simulated Hydroterra data. The range between short and long integrations appears to be roughly the same for all four polarisations, but varies somewhat with the type of crop - as might be expected, see Figure 3-6 toFigure 3-9 for details.

Horse Bean
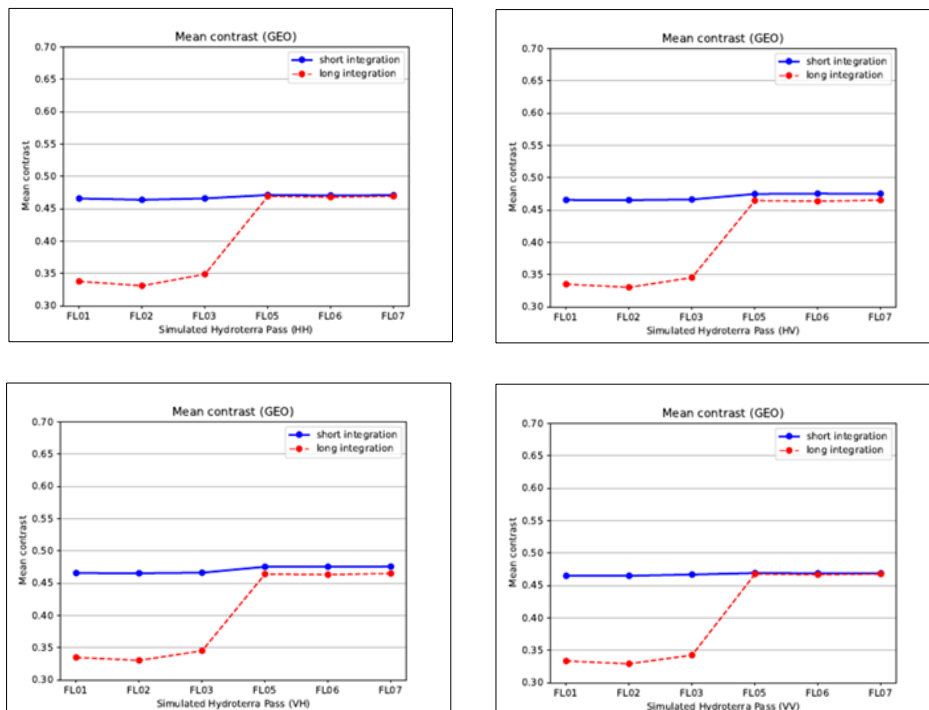
Figure 3-6: Mean image contrast of a horse bean field (FIELD_509) for the different polarisations (HH, HV, VH and VV). High-resolution (GEO) data, from April to June.

Asparagus
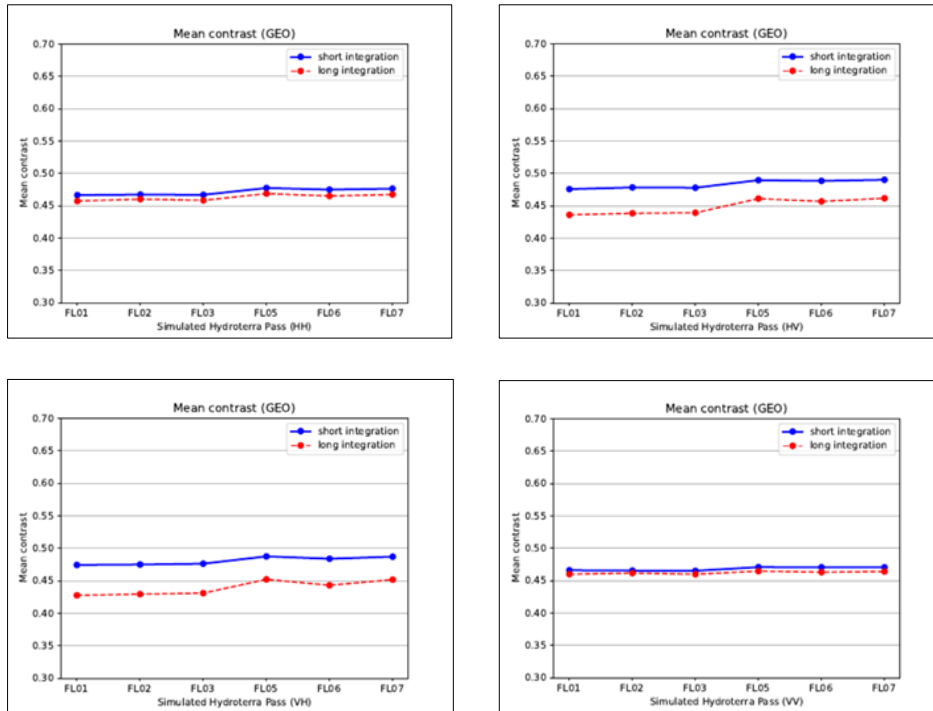
Figure 3-7: Mean image contrast of an asparagus field (FIELD_437) for the different polarisations (HH, HV, VH and VV). High-resolution (GEO) data, from April to June.

Tomato
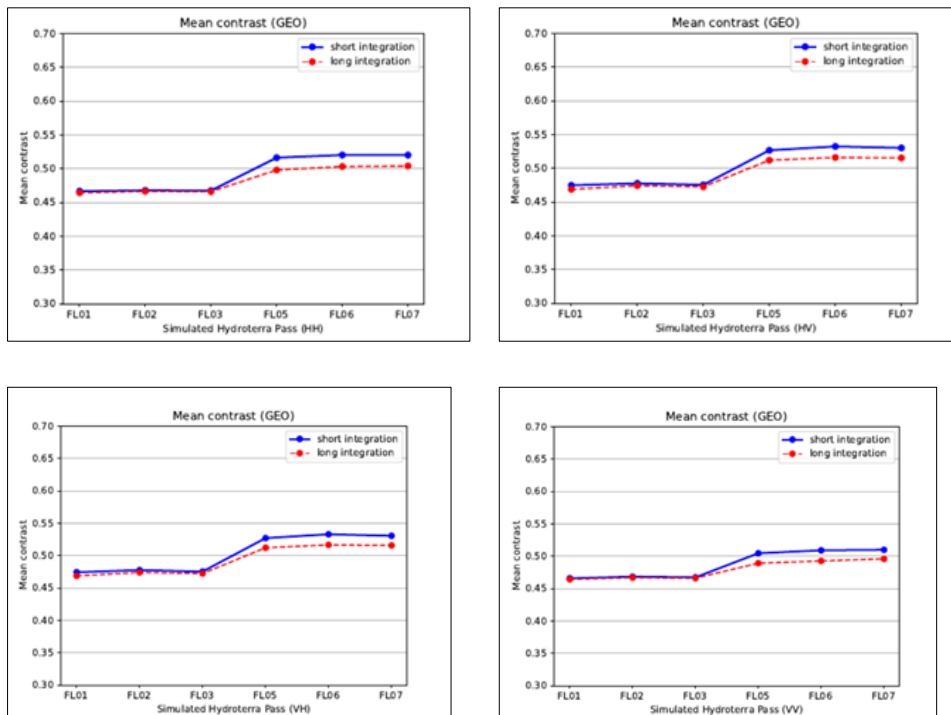
Figure 3-8: Mean image contrast of a tomato field (FIELD_043) for the different polarisations (HH, HV, VH and VV). High-resolution (GEO) data, from April to June.

Maize
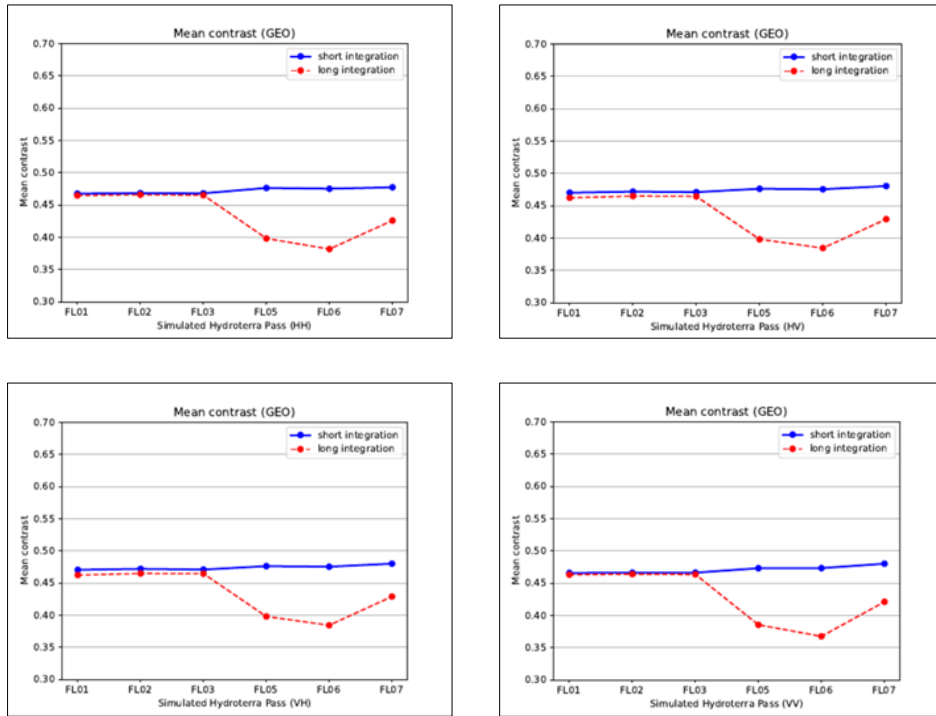
Figure 3-9: Mean image contrast of a maize field (CA_MA) for the different polarisations (HH, HV, VH and VV). High-resolution (GEO) data, from April to June.

For asparagus (see Figure 3-7), larger differences between short and long integrations can be observed in cross polarisation (HV and VH). These differences in HV and VH, although smaller, are also present for low vegetation periods for other crops, e.g. horse bean in June (see Figure 3-6) or maize in April (see Figure 3-9).

Spatial resolution plays a role in this analysis. The number of pixels per field needs to be large in order to reflect correct statistics. The results presented so far have been obtained from high resolution datasets. The effect of low spatial resolution, as would be the case with Hydroterra, is shown below. First, an AoI of the size of a field, i.e. maize (CA_MA), is considered (Figure 3-10 andFigure 3-11). Then, for comparison, the AoI is enlarged to the size of the Caione farm (Figure 3-12 andFigure 3-13).
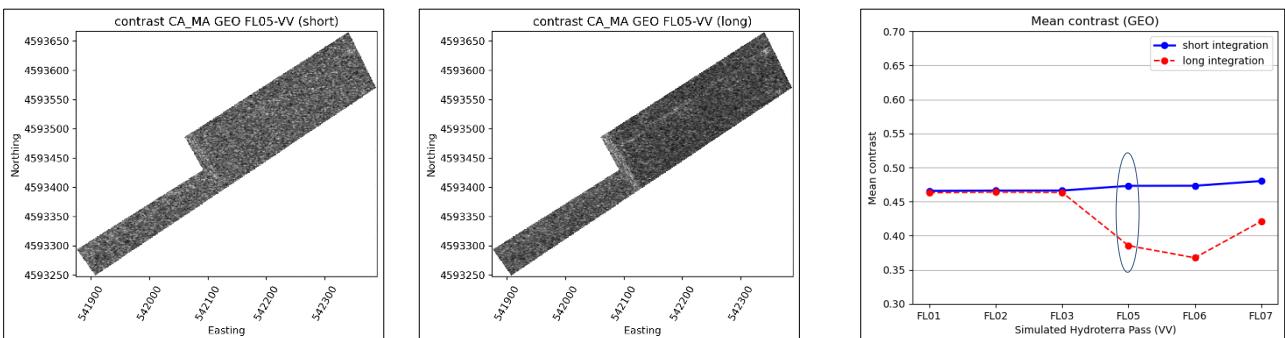
Figure 3-10: Mean image contrast of a maize field (CA_MA) in GEO-SAR quality; FL05, VV polarisation, high resolution. Short integration (left), long integration (centre), comparison of mean image contrast (right).
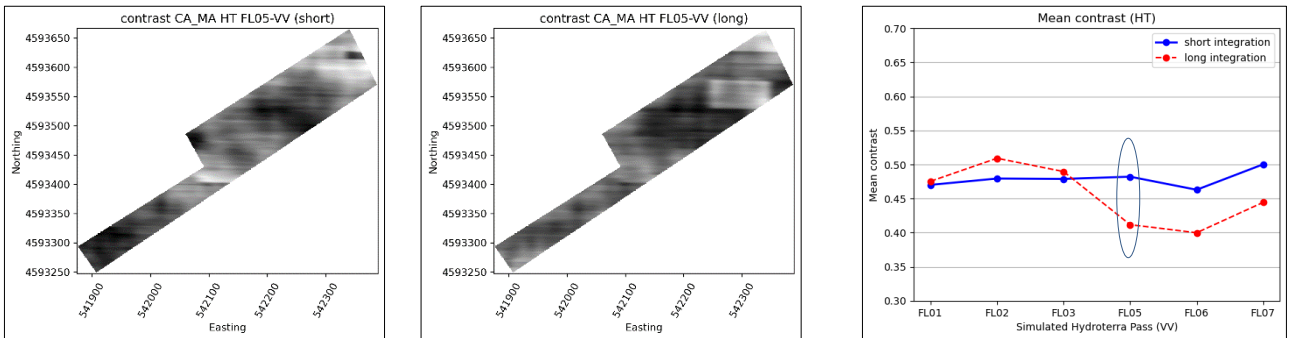
Figure 3-11: Mean image contrast of a maize field (CA_MA) in HT-SAR quality; FL05, VV polarisation, low resolution. Short integration (left), long integration (centre), comparison of mean image contrast (right).
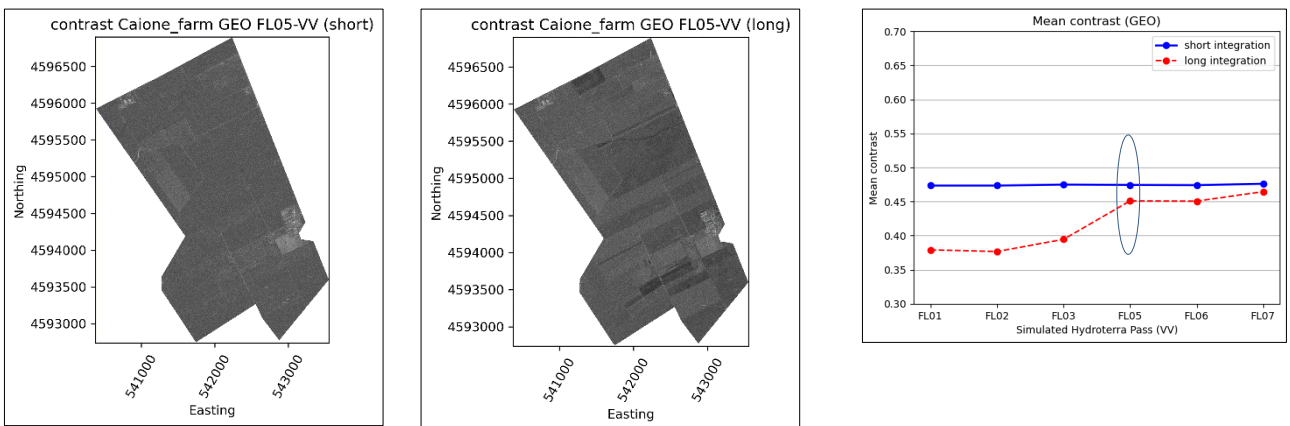
Figure 3-12: Mean image contrast of the Caione Farm in GEO-SAR quality; FL05, VV polarisation, high resolution. Short integration (left), long integration (centre), comparison of mean image contrast (right).
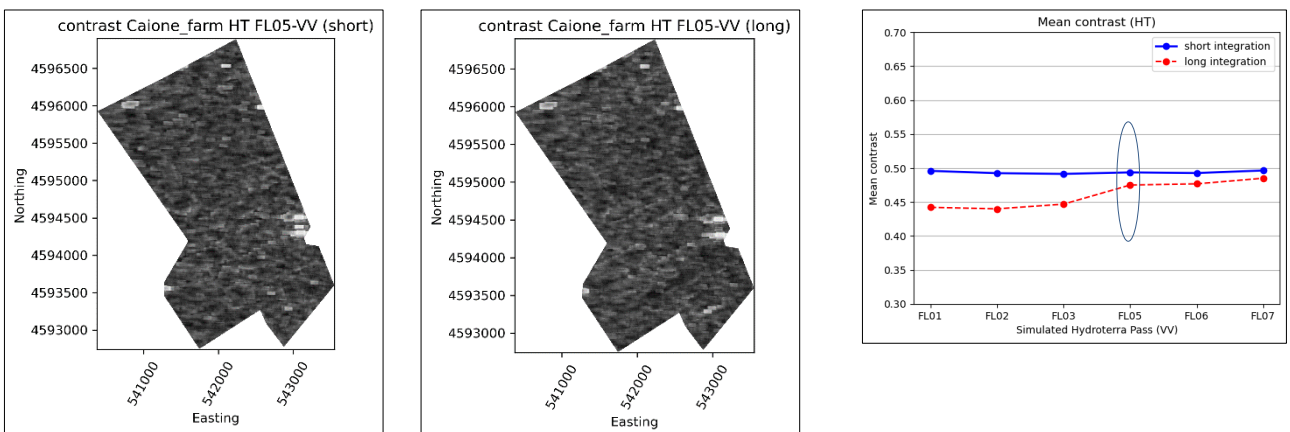
Figure 3-13: Mean image contrast of the Caione Farm in HT-SAR quality; FL05, VV polarisation, low resolution. Short integration (left), long integration (centre), comparison of mean image contrast (right).

The grid size in easting in Figure 3-11 is 100m. The HT simulated slant range resolution is set to 22.2m, which is about 50m in the ground range. There are few pixels only in the best case which can be averaged. This results in unreliable estimates as can be seen in the plot in Figure 3-11. The result is different when the AoI is of the size of the Caione farm (see Figure 3-13). The size of the grid in easting is 1000m, 500m in northing. Hundreds of pixels make mean contrast estimation more reliable.

3.2.2   Impact on image intensity

The effect of different integration times on the mean value of image intensities over an area of interest is shown here for AoIs of different sizes: farm, field and field strip. The Caione farm, the fields CA01_DW and CREA_BS and the field strip CA01_DW_24 were chosen.

For the flights in June the mean values were found to be unaffected by different azimuth integration times (short or long). This is equally true for both the high resolution (GEO) and the low resolution (HT) data. For the flights in April, however, a level gap Δµ of approx. 0.5dB to 1dB, varying with the size of the AoI, between short and long integrations can be observed in case of the Caione farm (see Figure 3-14) and the Caione durum wheat field incl. the field strip 24 (see Figure 3-15). In contrast, the data for the bare soil field CREA_BS do not show this characteristic (see Figure 3-16).
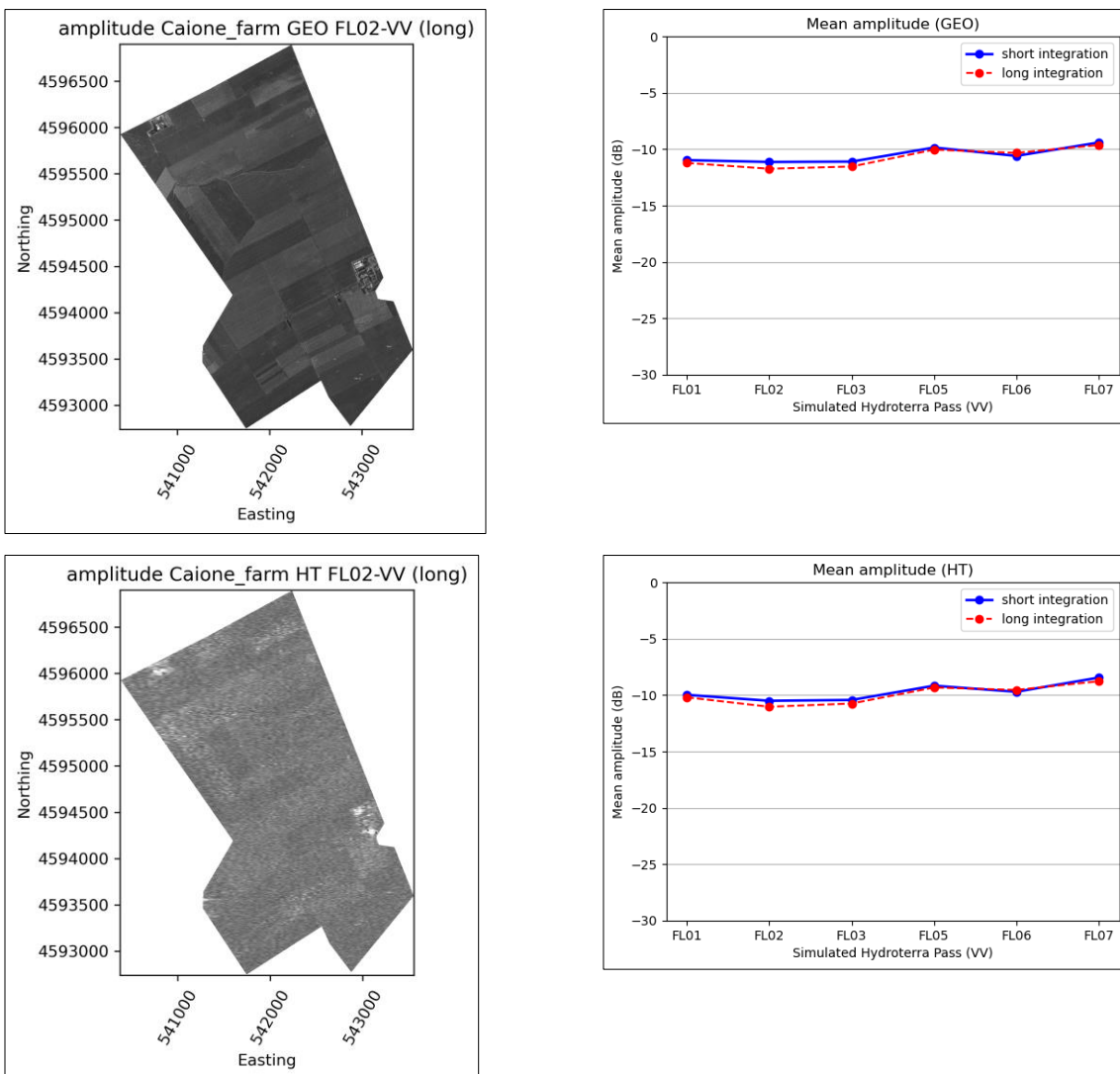
Figure 3-14: CAIONE FARM (AoI) – Mean image intensity values (VV polarisation) of flights FL01, 02, 03 (April) and FL05, 06, 07 (June) plotted for the high (GEO) and low (HT) resolution cases. Note, that the dashed red line indicating long integration, is just below (Δµ ~ -0.5dB) the blue line (short integration) for FL02 in April.
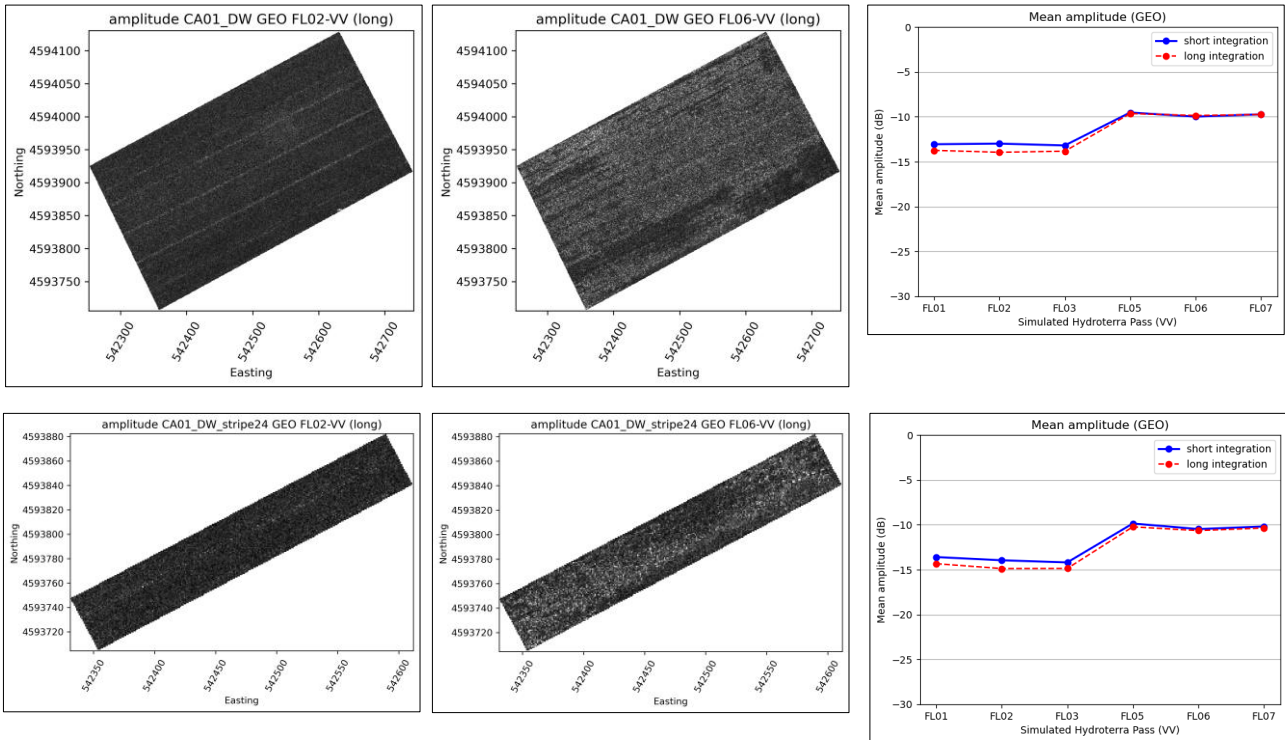
Figure 3-15: Field CA01_DW (top row) and field strip 24 (bottom row) (AoI) – Mean image intensity values (VV polarisation) of flights FL01, 02, 03 (April) and FL05, 06, 07 (June) plotted for the high (GEO) resolution case. Note that the dashed red line, indicating long integration, is well below (Δμ ~ -1dB) the blue line (short integration) for the April flights.
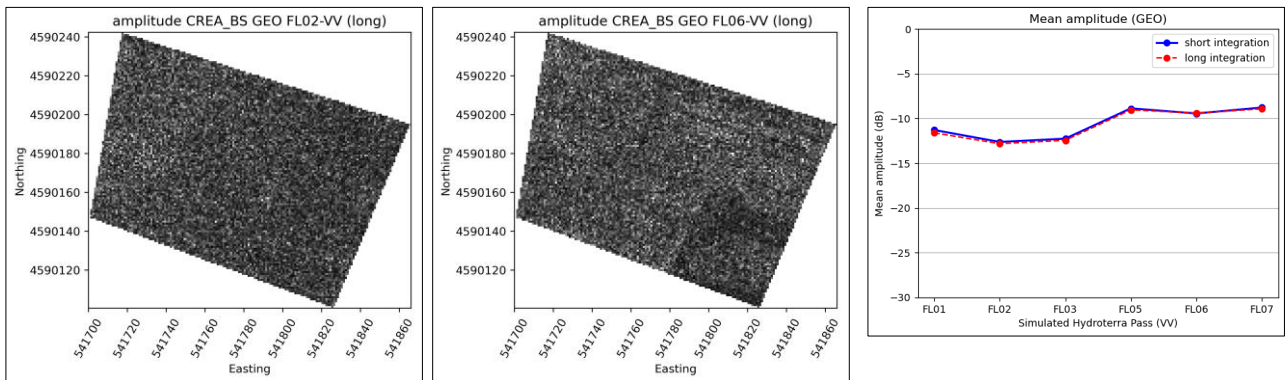
Figure 3-16: Field CREA_BS/QU (AoI) – Mean image intensity values (VV polarisation) of flights FL01, 02, 03 (April) and FL05, 06, 07 (June) plotted for the high (GEO) resolution case. Bare soil in April. Quinoa in June. Note that the blue and the dashed red lines are almost identical.

Wind speed and direction were measured by anemometer during the two missions in April and in June 2022. For flight FL02 on April 28 the wind speed was about 10m/s avg. from North with peaks up to 13m/s. On June 15 for flight FL06 the wind speed was about 5.6m/s avg. from North and gusts up to 8.7m/s. This data is part of the SSM database (see D2: DAR [A3]).

From the results shown in Figure 3-15 andFigure 3-16, it can be concluded that for long azimuth integration times, SAR focusing is slightly degraded for vegetated areas affected by wind-induced movement.

3.2.3 Impact on interferometric coherence

In this section, the effect of long azimuth integration times on interferometric coherence and thus interferogram formation is shown exemplarily for a limited number of different sized AoIs. Diurnal (FL01-FL02 and FL05-FL06) and day-to-day (FL02-FL03, FL03-FL01 and FL06-FL07, FL07-FL05) for both seasons (April, June) are considered. Note, that pixel size becomes critical when an AoI is of the size of a field in the HT case (low resolution). In order to obtain meaningful results for the HT case, both the Caione and CREA farms were selected as minimum size areas. A few fields were irrigated in April and June 2022. The resulting effects on the coherence are shown in the following in high resolution (GEO) only.

Apulian Tavoliere
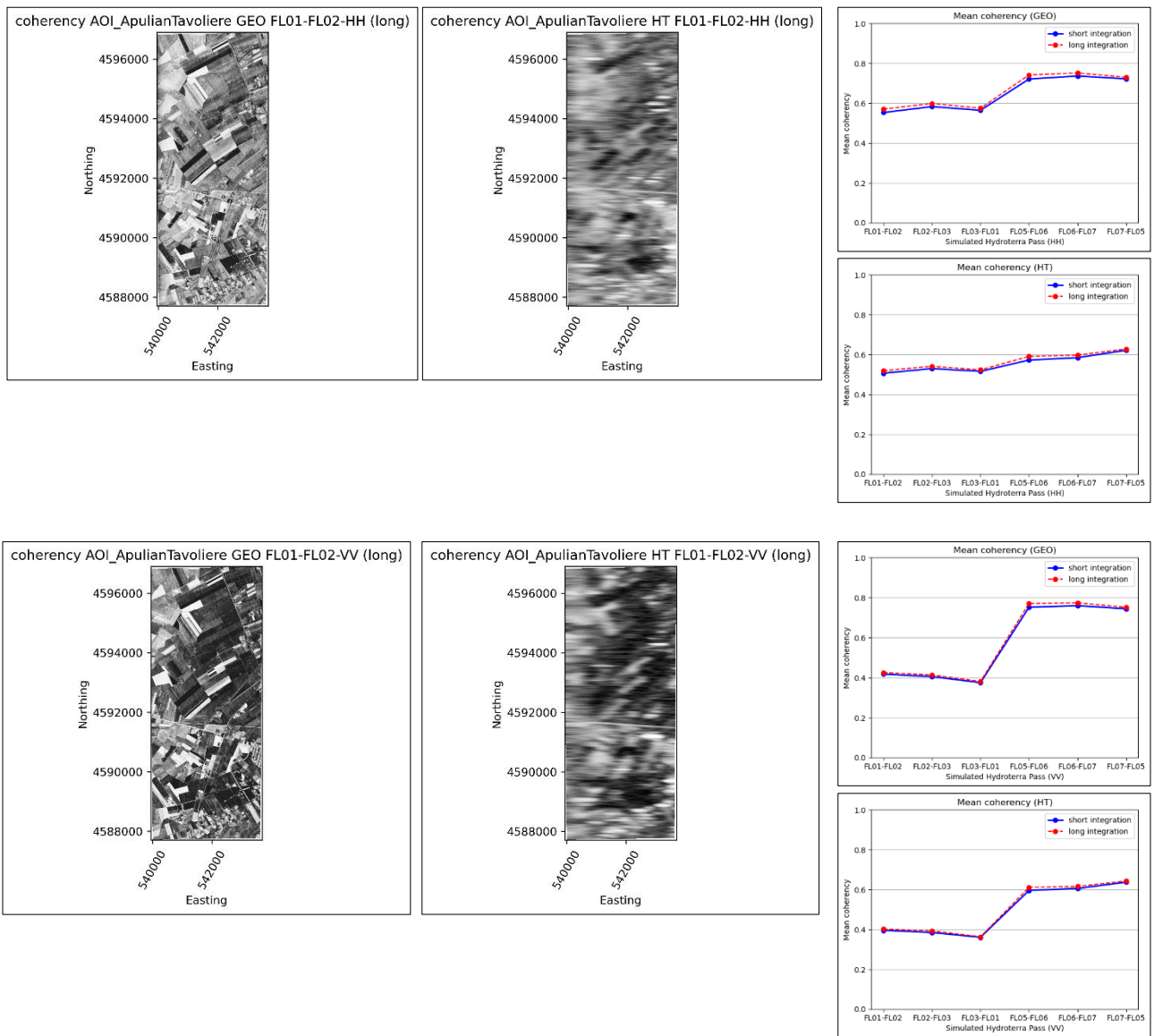
Figure 3-17: Interferometric coherence images of the 'Apulian Tavoliere'-AoI in HH (top) and VV (bottom) polarisation. High resolution (GEO) on the left, low resolution (HT) to the right. Graphs showing mean coherence values of the whole scene per interferogram (FL01-FL02, …, FL07-FL05) and per integration time (short, long) for both GEO and HT cases and HH and VV polarisations. Note the larger seasonal split in VV polarisation.

The plots in Figure 3-17 show that levels of mean coherence are almost the same or only marginally higher in cases of long integrations. Absolute values differ quite a lot between GEO and HT. Additionally, a larger seasonal split can be observed in VV polarisation in both cases.

CREA Farm
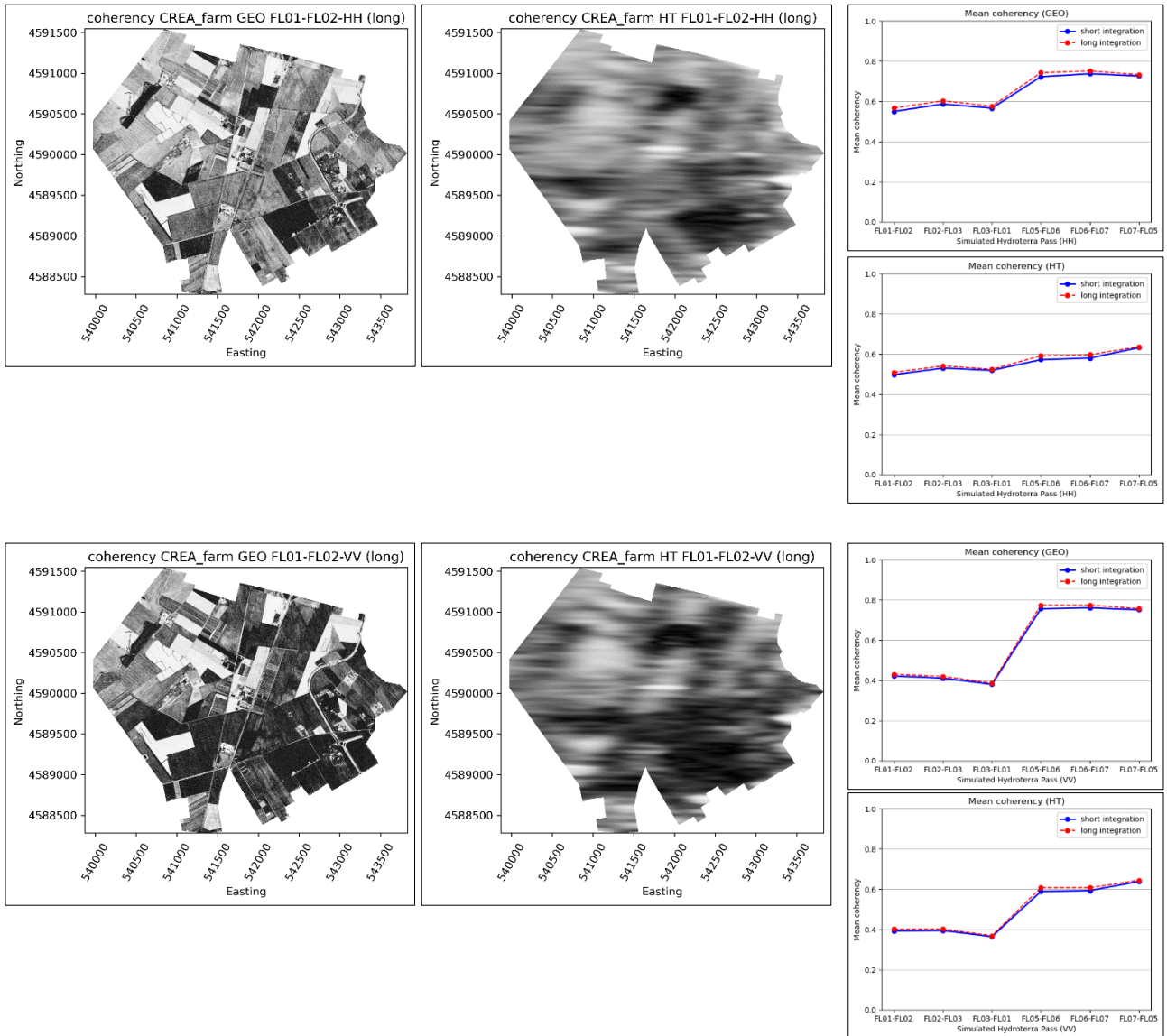
Figure 3-18: Interferometric coherence images of the 'CREA Farm'-AoI in HH (top) and VV (bottom) polarisation. High resolution (GEO) on the left, low resolution (HT) to the right. Graphs showing mean coherence values of the whole scene per interferogram (FL01-FL02, …, FL07-FL05) and per integration time (short, long) for both GEO and HT cases and HH and VV polarisations. Note the larger seasonal split in VV polarisation.

The mean coherence values obtained for the 'CREA Farm', shown in Figure 3-18, show the same behaviour and levels as in the previous case, the 'Apulian Tavoliere' AoI.
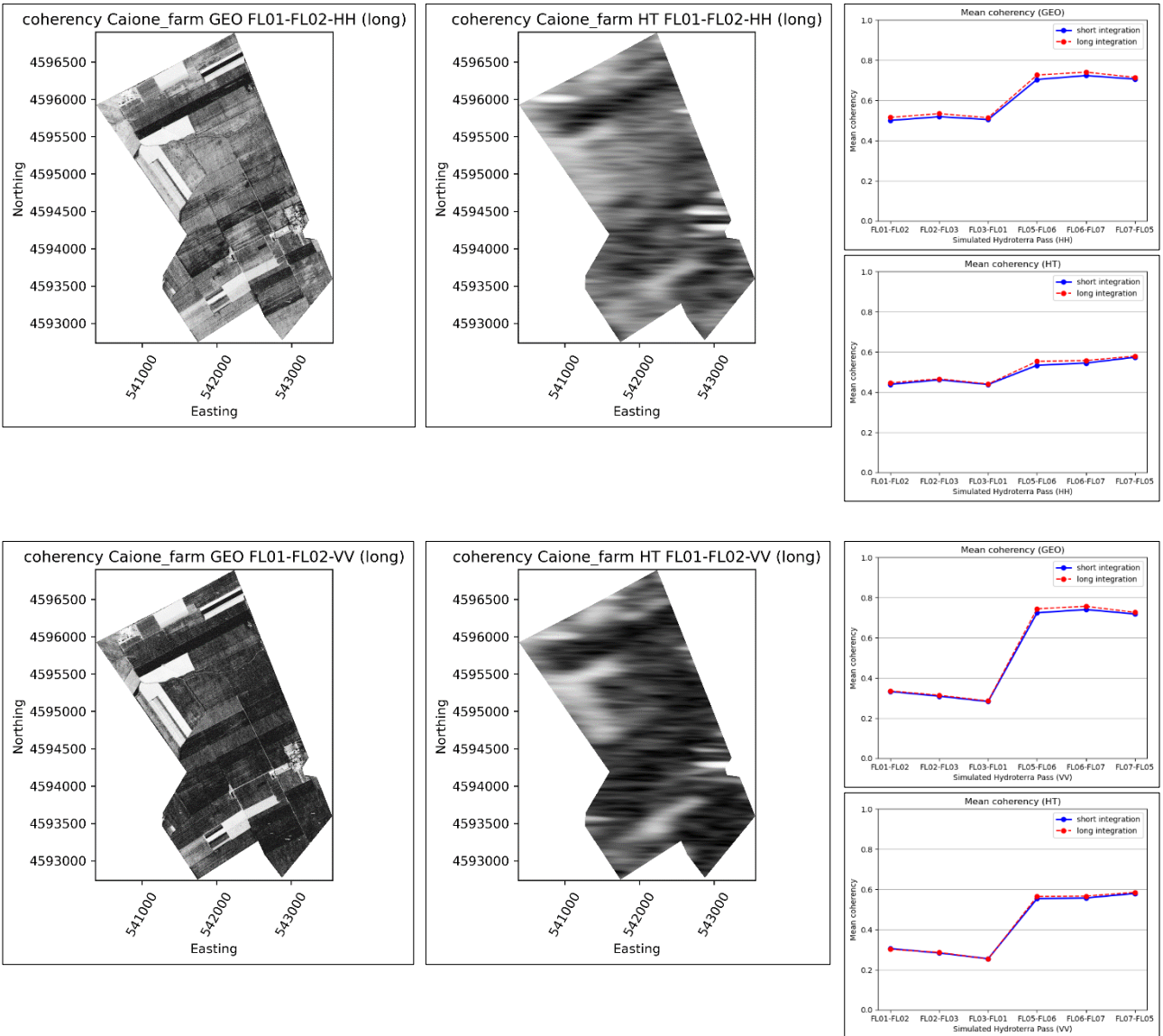
Caione Farm

Figure 3-19: Interferometric coherence images of the 'Caione Farm'-AoI in HH (top) and VV (bottom) polarisation. High resolution (GEO) on the left, low resolution (HT) to the right. Graphs showing mean coherence values of the whole scene per interferogram (FL01-FL02, …, FL07-FL05) and per integration time (short, long) for both GEO and HT cases and HH and VV polarisations. Note the larger seasonal split in VV polarisation.

As shown in Figure 3-19, the mean coherence values obtained in this case show the same behaviour as in the previous cases above. Absolute values differ, very likely due to the kind of land-use in this AoI. In fact, they are lower in both polarisations.

With regard to the objective of this analysis, it can be stated that there is no significant difference in the quality of interferograms obtained from long integrations compared to short integrations.

Irrigation activities

Interferometric coherence, in general, is an indicator of change in a target scenario between two measurements. In the course of the 22HTERRA airborne SAR campaign a dedicated irrigation experiment was executed. Two types of irrigation systems were used, mobile boom and stationary drip. Details are noted in the DAR [A3]. The goal was to monitor the change in SSM and the drying process over two days with radar monitoring. In this section exemplary results of three fields are shown obtained from high resolution and long azimuth integration time (GEO) data products.

Field Caione CA01_DW (mobile boom irrigation, durum wheat in mid boot stage)
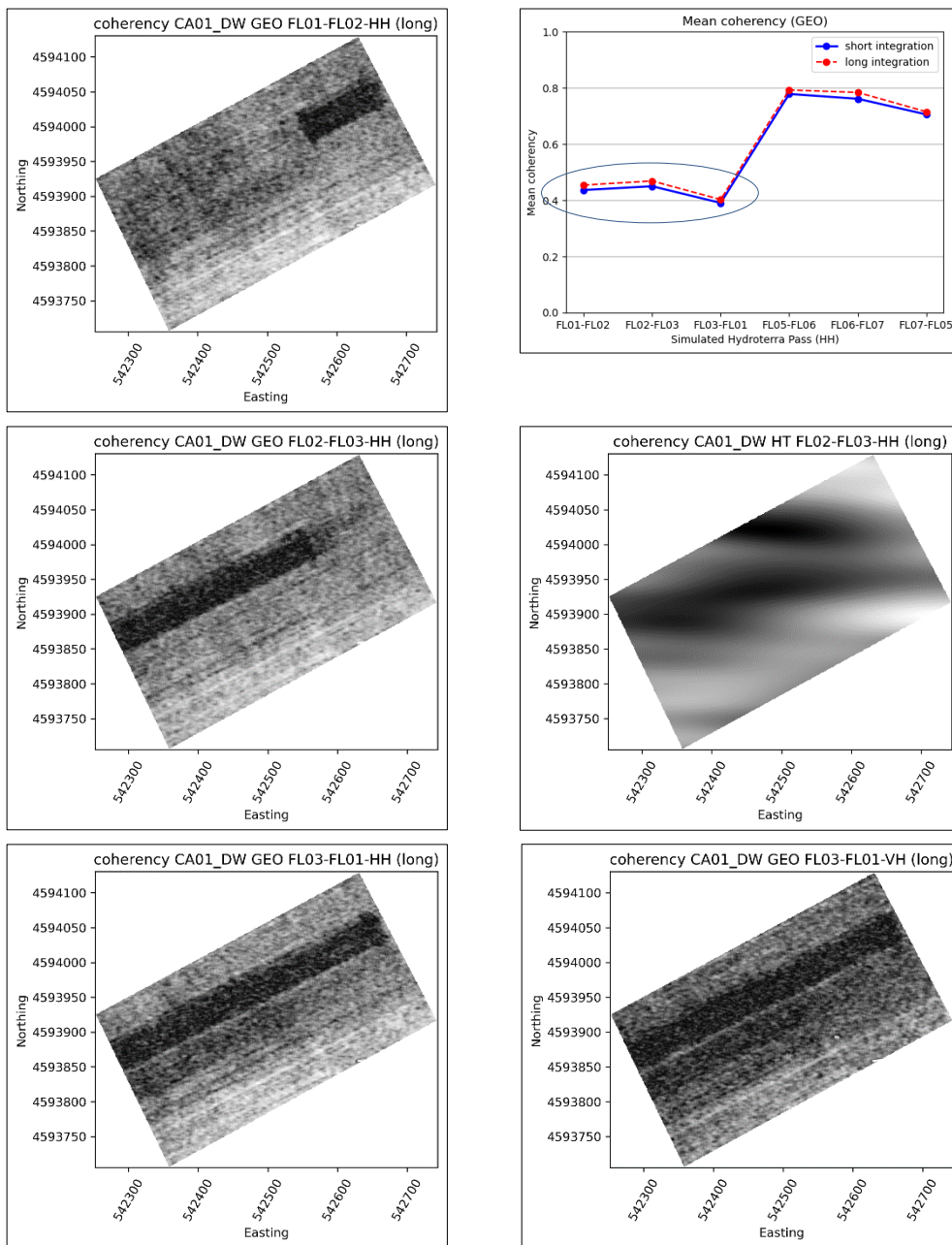
Figure 3-20: Interferometric coherence in GEO product quality of the field 'CA01_DW'. Period April 28-29, 2022. Irrigation with mobile boom system in progress along sub-strip 29 (left column). Top right: Graph showing a drop in mean coherence over 24 hours. Mid right: HT resolution product. Bottom right: VH polarisation for comparison.

Field CREA_DW (mobile boom irrigation, durum wheat in mid boot stage)
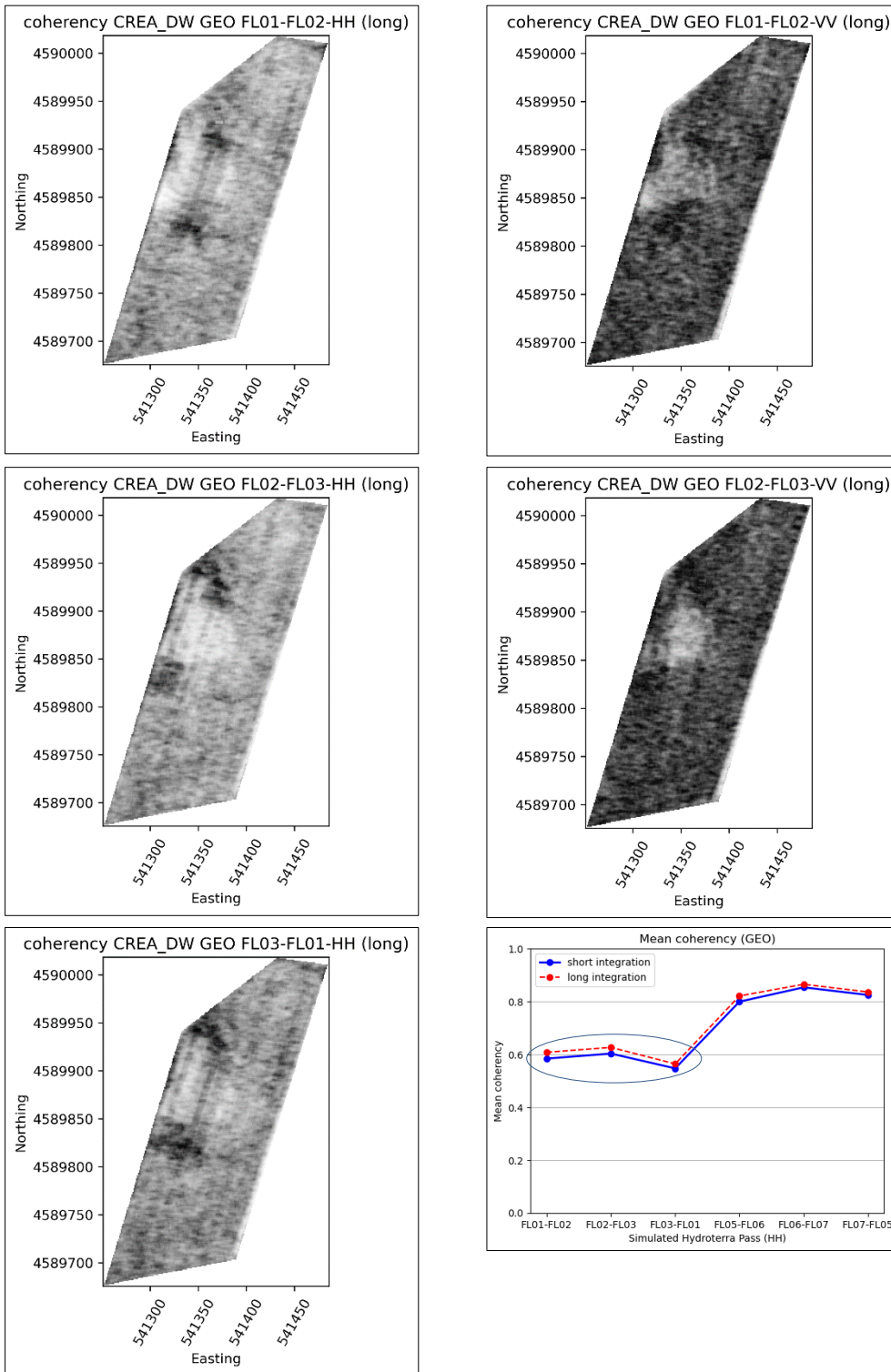
Figure 3-21: Interferometric coherence in GEO product quality of the field 'CREA_DW'. Period April 28-29, 2022. Irrigation with mobile boom system in progress on sub-strips 28 & 29 (left). Top and mid right: VV polarisation for comparison. Bottom right: Graph showing a drop in mean coherence over 24 hours.

Field CREA_BS / CREA_QU (drip irrigation, bare soil in April, quinoa crop in June)
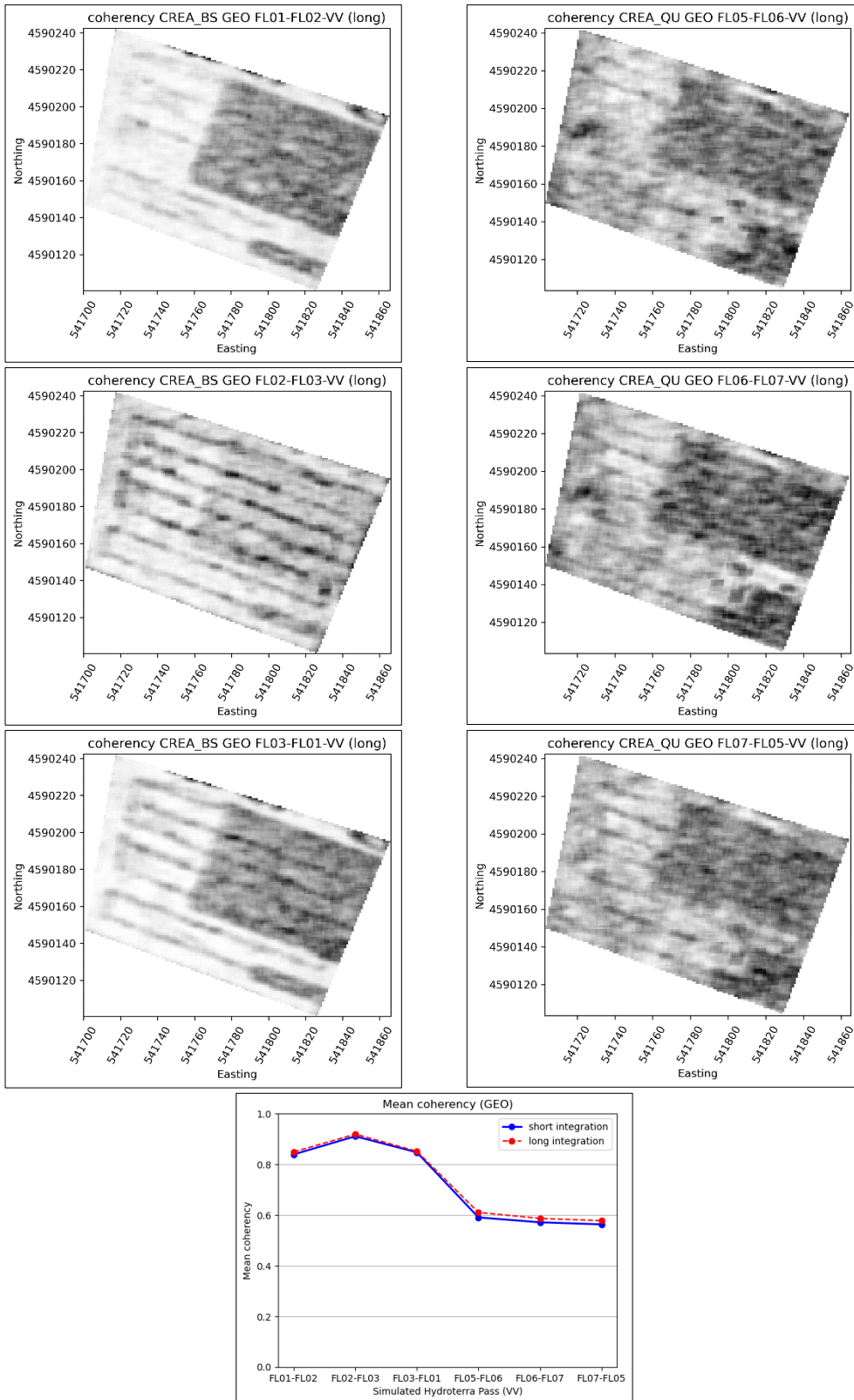
Figure 3-22: Interferometric coherence in GEO product quality of the field 'CREA_BS/QU'. Period April & June, 2022. Drip irrigation was stopped the evening before the first flight, both in April and in June. Left column: CREA_BS, in April. Right column: CREA_QU, in June. Bottom: Graph showing the mean coherence.

The images of interferometric coherence of the field CA01_DW in Figure 3-20 (left column) clearly show the effect of mobile boom irrigation being active during radar measurements. Irrigation was active on field stripe 29 from 9am on April 28 until 7am on April 29.

Figure 3-23: Photograph of the field CA01_DW taken from aircraft during first flight on April 28. The position of a mobile boom irrigation system operating on stripe 29 is indicated.

The adjacent stripes 28, 27 and 24 (to the right in the photo) had been irrigated just 24 to 72 hours before the first flight. The effect of desiccation can be seen in the long-term coherence (FL03-FL01) shown in Figure 3-20 (bottom row).

Interferometric coherence may not always be efficient in detecting ongoing irrigation, as can be seen in Figure 3-21 (left column). The field CREA_DW has an area in which the crop of durum wheat is in a different state to that in the rest of the field (see the photo in Figure 3-24).

Figure 3-24: Photograph of the fields CREA_DW and CREA_BS taken from aircraft during first flight on April 28. The position of the mobile boom irrigation system operating on stripe 28 in the DW field is indicated by a circle. Right next to it in the triangular shaped area (light green colour) the durum wheat crop seems to be sparse. In the bottom half of the photo the bare soil field BS is indicated. Drip irrigation was stopped here at 7pm on April 27.

Regarding drip irrigation the interferometric coherence of the CREA_BS/QU field (Bare Soil in April, QUinoa crop in June) shows different behaviour as can be seen in Figure 3-22. In the case of bare soil coherence values taken short and medium term (FL01-FL02, FL02-FL03) reflect the desiccation of the soil in the field. In June, however, this is barely noticeable. Very likely due to vegetation covering the soil.

Figure 3-25: Photograph of the CREA_QU field on the left of the CREA institute taken in June. Drip irrigation was stopped at 7pm on June 14, the day before the first flight (June 15).

3.3   Summary

In this study, carried out in WP 240, the question of the impact of long azimuth integration times (hours) of a future Hydroterra SAR compared to conventional SAR featuring much shorter integration times (seconds) is addressed. Three standard SAR quality measures (mean value, contrast and interferometric coherence) were used to quantify the effects and thus answer the question. In order to decouple the effects of (i) the long azimuth integration time and (ii) the poor resolution as of a Hydroterra SAR, the study is based on two types of simulated SAR data derived from airborne F-SAR data referred to as GEO-SAR (geosynchronous orbit, high resolution SAR) and HT-SAR (Hydroterra SAR, scenario 4, for reference see [7]). The F-SAR data were collected at the 'Apulian Tavoliere' test site near the city of Foggia in Italy in two missions, the first in April 2022 and the second in June 2022.

Summarizing the study results, it was found that:

a)   Only if the imaged areas are stationary, the image intensity mean values will not be affected by changing azimuth integration times. In case of e.g. wind-induced movement of durum wheat fields or similar, mean values may be reduced. This correlates with wind speed and vegetation height. In this study the field CREA_BS/QU shows the characteristics of a stationary target.

b)   Image contrast is a measure of SAR focusing quality. When long azimuth integration times are used in SAR focusing, image contrast is greatly reduced in all parts of an image that are subject to e.g. wind-induced movement, such as vegetation with a minimum growth height (e.g. durum wheat in April).

c)   Interferometric coherence is hardly influenced by changing azimuth integration times. In this study, no significant differences in the quality of interferograms obtained from long integrations compared to short integrations were observed.

4 Data Analysis, Snow Mass Retrieval and Performance Evaluation of the SWE Experiment (WP320)

4.1 Introduction

This chapter reports on the work performed within WP320 of the SARSimHT-NG project, dealing with the analysis and evaluation of the C- and L-band airborne SAR data that were acquired in March 2021 over the test site Wörgetal in the Austrian Alps. Main objective of this activity is the implementation, application and evaluation of procedures for retrieving the change of snow mass (SWE) over ground due to snowfall events from repeat-pass interferometric (RP-InSAR) data. This activity benefits from the fact that during the Wörgetal campaign two snowfall events of different intensity took place that are spanned by several RP-InSAR acquisitions.

During the Wörgetal field experiment F-SAR data were acquired on seven days (2, 3, 4, 6, 8, 9, 19 March 2021), spanning two major snowfall events: the first event on 5 March yielding snow accumulation (SWE) of 10mm to 15mm w.e., and the second event from 14 to 18 March yielding snow accumulation of 50mm to 70mm w.e. (w.e. = water equivalent), see Figure 4-1. On each of the days with aircraft deployment multiple repeat flights were performed along two tracks, with heading north to south (track 10), respectively south to north (track 11). Details on airborne measurements, field measurements, processing procedures, acquired and processed data inventory and performance, as well as on simulated Hydroterra products are provided in the Data Acquisition Report [A2].

A sequence of different tasks has been performed within WP320, starting with studies on the response of backscatter and interferometric signals to changes in properties of the Alpine snowpack related to accumulation events. Of major interest for the feasibility and performance of RP-InSAR SWE retrieval is the temporal evolution of coherence and the impact of snowfall events at different frequencies. Another critical issue for deriving SWE from temporal changes of InSAR phase is the need for reference phase values at sites with zero SWE accumulation or with known changes in SWE from external sources. For the Wörgetal data set the phase of the corner reflectors (CRs), cleaned of snow, is used as reference. In order to minimize the impact of noise in the CR-phase, repeat-pass pairs with similar squint angles were selected [A2].

Retrievals on the snow accumulated during the two snowfall events (ΔSWE) were performed and evaluated using full resolution F-SAR data and interferograms derived from simulated geosynchronous SAR data, the simulated Hydroterra products.
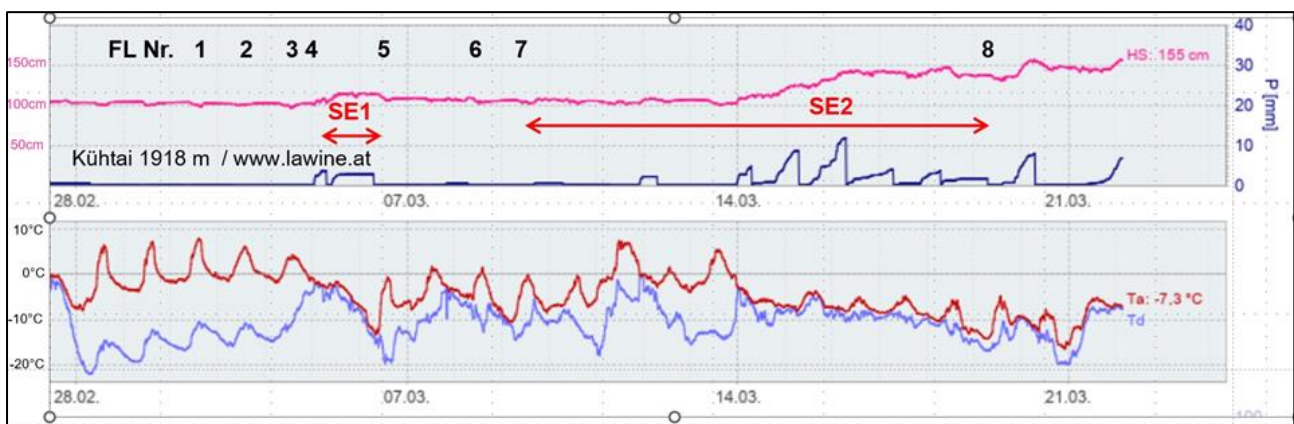
Figure 4-1: Record of the snow station Kühtai (1918m a.s.l., 3km east of Wörgetal), 27.2. to 23.3.2021. HS – snow depth, P – precipitation, Ta – atmospheric temperature, Td – dew point temperature. The flight numbers refer to the dates of the flights. SE1 and SE2 refer to the InSAR time spans for the two snowfall events covered in the SWE retrieval studies.

4.2 Analysis of backscatter intensity and interferometric signals

The signature analysis presented in this section is based on full resolution F-SAR data: The resolution (az x rg) in C-band is 0.5m x 0.5m, in L-band 0.6m x 1.3m; pixel size (az x rg) in C-band 0.2m x 0.3m, in L-band 0.4m x 0.6m [A2]. In order to minimize impacts of topography and related variations of snow depth, the analysis focuses on three sections (RoIs) of Wörgetal with moderate slopes where the ground-based snow measurements were made: Oberer Boden (OB), Mittlerer Boden (MB), Unterer Boden (UB) (see Figure 4-2 andFigure 4-3). The outlines of the RoIs include the transects of in-situ measurements and surroundings, excluding steep slopes. These areas were not affected by surface melt during the F-SAR flights, whereas on steep east- and south-facing slopes transient melt was observed in the snow surface layer on some days around noon due to solar irradiance.
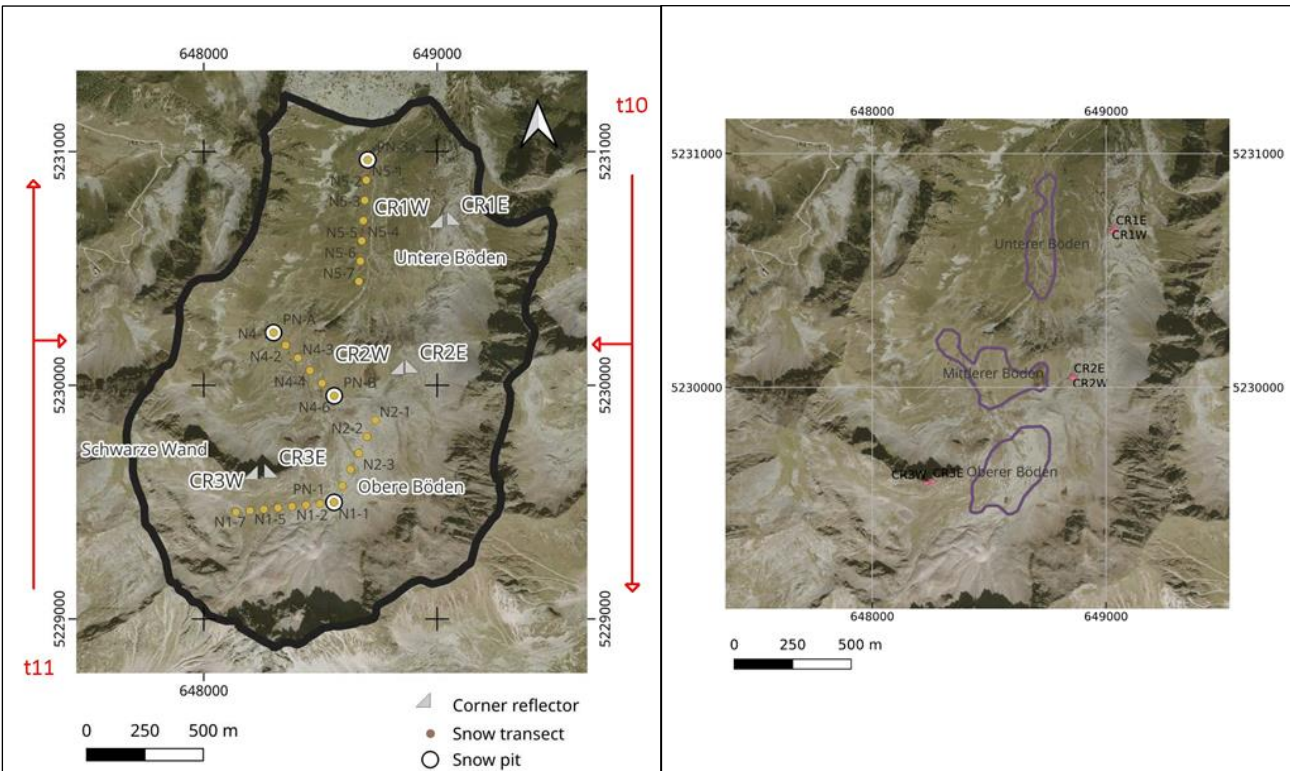
Figure 4-2: Image map of Wörgetal based on airborne photogrammetric data. t10, t11 heading of F-SAR flight tracks. The snow transects (left image) refer to measurements made on 6 March 2021. Right image: Out-lines of RoIs used for evaluation of SWE retrievals.

The RoIs are located in Alpine tundra environment. The main surface cover is Alpine grassland (sedges and grasses) and includes some plots covered by dwarf shrubs (in particular in UB). A small part of these areas is covered by bare soil and debris. Mean topographic elevation and radar incidence angles are specified in Table 4-1. Mean values and standard deviations of in-situ snow depth (SD) and SWE are specified in Table 4-2, including data on total SD and SWE observed on the first two days of the campaign (2 & 3 March 2021), and ΔSD & ΔSWE of fresh snow related snowfall events SE1 and SE2.

The 1st snowfall event, SE1, refers to snowfall on 5 March. The measurements on snow accumulation were performed on the day after (6 March, associated with FL0602 & FL0603), showing a mean snow density of 95kgm^{-3} for the fresh snow, a typical value for dry fresh snow not affected by wind compaction. The mean value for ΔSD of the three sites is 13.7cm, and the mean ΔSWE 13.0mm. There is a minor trend for increase of ΔSD with elevation, observed also for the total snowpack at the beginning

of the campaign. The mean density of the total snowpack, measured in snow pits on 2 and 3 March, was 340kgm^{-3}, typical for metamorphic snow that had been subject to occasional transient melt events.

Table 4-1: RoI elevation, radar look angle and incidence angle (mean value, standard deviation and median, in radar image geometry).

RoI	Elevation [m] a.s.l.	θ_L Track 10	θi mean Track 10	θi Std. dev	θi med Track 10.	θ_L Track 11	θi mean Track 11	θi Std. dev	θi med Track 11
OB	2335	25.8	28.3	8.2	29.9	33.4	37.4	6.0	38.8
MB	2250	28.7	31.8	5.9	32.7	33.8	33.6	5.4	33.7
UB	2095	29.5	32.8	7.2	35.5	38.4	32.1	9.0	31.0
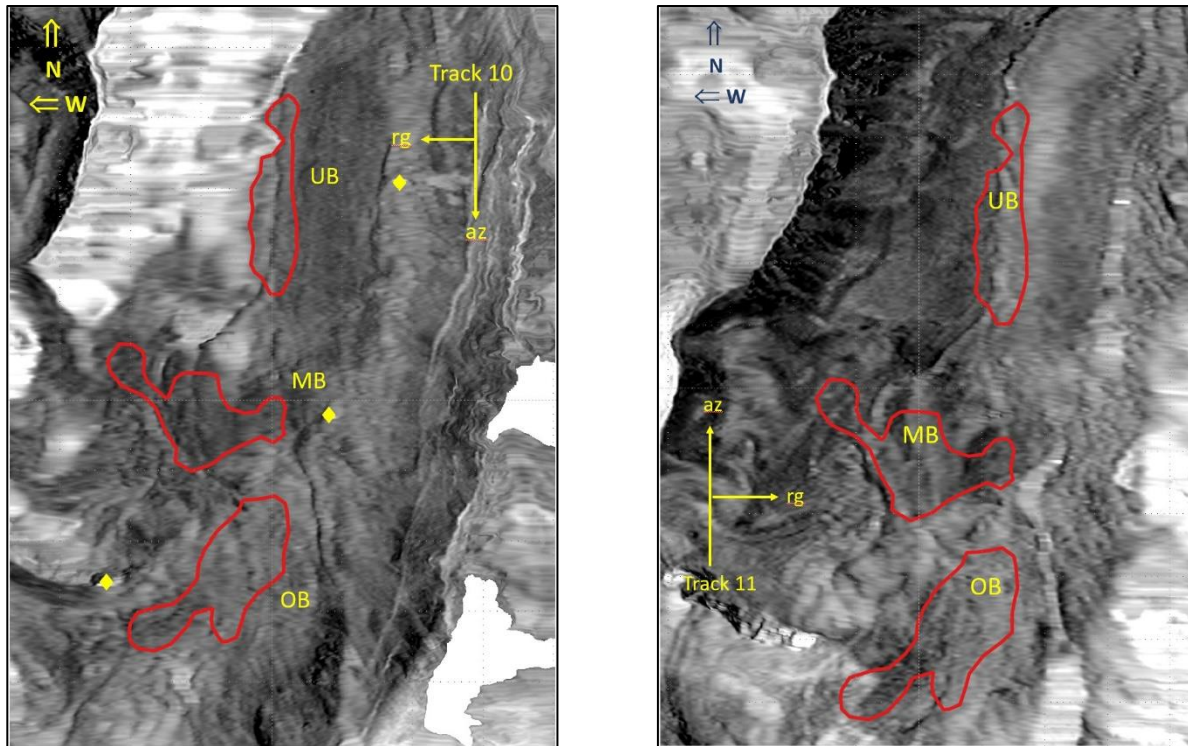
Figure 4-3: Geocoded F-SAR C-band VV intensity images of the Wörgetal test site, track 10 (left), track 11 (right), with outlines of the three RoIs used for signature studies and retrieval tests. OB - Oberer Boden, MB - Mittlerer Boden, UB - Unterer Boden. Corner reflector locations are indicated by ♦.

The 2nd snowfall event, SE2, includes snow accumulating during the days 14 to 18 March, in which the snowfall intensity was highest during the first two days of the period. The measurements on snow accumulation of SE2 were performed on 19 March, the day of the last flights of the campaign (FL0802 & FL0803). The mean ΔSD of the three sites amounts to 44.2cm, and the mean ΔSWE is 64.0mm. The mean density of the accumulated snow is 145kgm^{-3}, which is higher than for SE1. The higher density for the accumulation period of a few days compared to SE1 can mainly be attributed to settlement as the result of creep under the action of overburden, probably partly also due to turbulent exchange processes and radiation at the snow/air interface. ΔSD of SE2 does not indicate any pronounced trend with elevation. The small-scale spatial variability of SD at the individual sites is primarily determined by small-scale topography and terrain roughness.

Table 4-2: RoI snow depth (SD) and SWE (mean values & standard deviation) from in-situ point measurements. SE - snowfall event. SE1: Snowfall on 5 March 2021. SE2: Snow accumulating between 14 and 18 March 2021.

RoI	SD [cm] 2&3 March	SWE [mm]	SD std. dev.	ΔSD SE1 [cm]	ΔSD SE1 std. dev.	SE1ΔSWE [mm]	ΔSD SE2 [cm]	ΔSD SE2 std. dev.	SE2ΔSWE [mm]
OB	140.8	480.1	29.4	15.6	2.1	14.8	43.2	2.3	62.6
MB	127.6	435.1	41.2	13.3	2.4	12.6	46.0	6.8	66.7
UB	116.2	396.2	37.8	12.3	1.1	11.7	42.1	6.2	61.0

4.2.1 Backscatter intensity

Various publications report on studies suggesting the use of backscatter intensity and co-polarized phase difference as input quantities for SWE retrieval. In order to check the suitability of these parameters for retrieving SWE complementary to retrievals from the RP-InSAR data, we checked the signal response to the two snowfall events.

Figure 4-4 shows time series of C- and L-band VV-polarized backscatter intensity of the three RoIs for track 10 and track 11. The data are derived from images in radar geometry, applying a boxcar filter of size 25 x 25 pixel on full resolution data. This results for the averaged image in an L-band pixel size of 10m x 15m and C-band pixels size of 5m x 7.5m (azimuth x range), ENL = 190 (L-band), ENL = 150 (C-band). The backscatter intensities of the RoIs are averages over a few hundred pixels, so that the speckle-related uncertainty is of no concern. For C-band the radiometric, polarimetric and interferometric calibration was checked by means of the corner reflectors [A2]. For L-band the size of the reflectors deployed in Wörgetal (edge length 0.95 m) is rather small. Pre- and post-campaign calibration flights were performed over DLR's calibration site Kaufbeuren [A2].

The C-band VV-polarized data show moderate increase of σ° during the observation period, possibly related to gradually increasing size of scattering elements due to snow metamorphism. Differences in σ° between the individual sites can only partly be attributed to different incidence angles (Table 2-1). The roughness of the ground below the dry snowpack plays a major role. The low σ° values of MB compared to the two other sites can be explained by smooth Alpine grassland and bogs that are covering parts of the area. The C-band σ° time series of track 10 and track 11 show at all sites a moderate increase during the whole period. There is no difference in the temporal evolution between the two tracks, as to be expected according to the stable snow properties and the close temporal coincidence of the two tracks. For L-band the temporal changes of σ° between track 10 and track 11 are divergent. L-VV of track 10 decreases at each of the three sites by 1dB from FL01 to FL04, whereas L-VV of track 11 increases by 1.3dB. At FL05 L-VV of track 10 shows a spike in the time series and track 11 shows a dip. As mentioned above, these differences in the time sequence of L-VV cannot be attributed to temporal changes of snow or ground properties between the two tracks

The polarisation ratios of both frequencies and tracks show very little temporal variability and do not exhibit any clear response to the snow fall events (Figure 4-5). There is an increase of the track 10 C-band VH/VV ratio by 0.8dB for the data spanning the first (weak) snowfall event, but almost zero response to the second (strong) snowfall event. The track 11 data show changes up to 0.3dB.

In summary, the backscatter intensity data are largely unaffected by the snowfall events, supporting the focus on interferometric methods for snow mass retrievals in Alpine terrain.
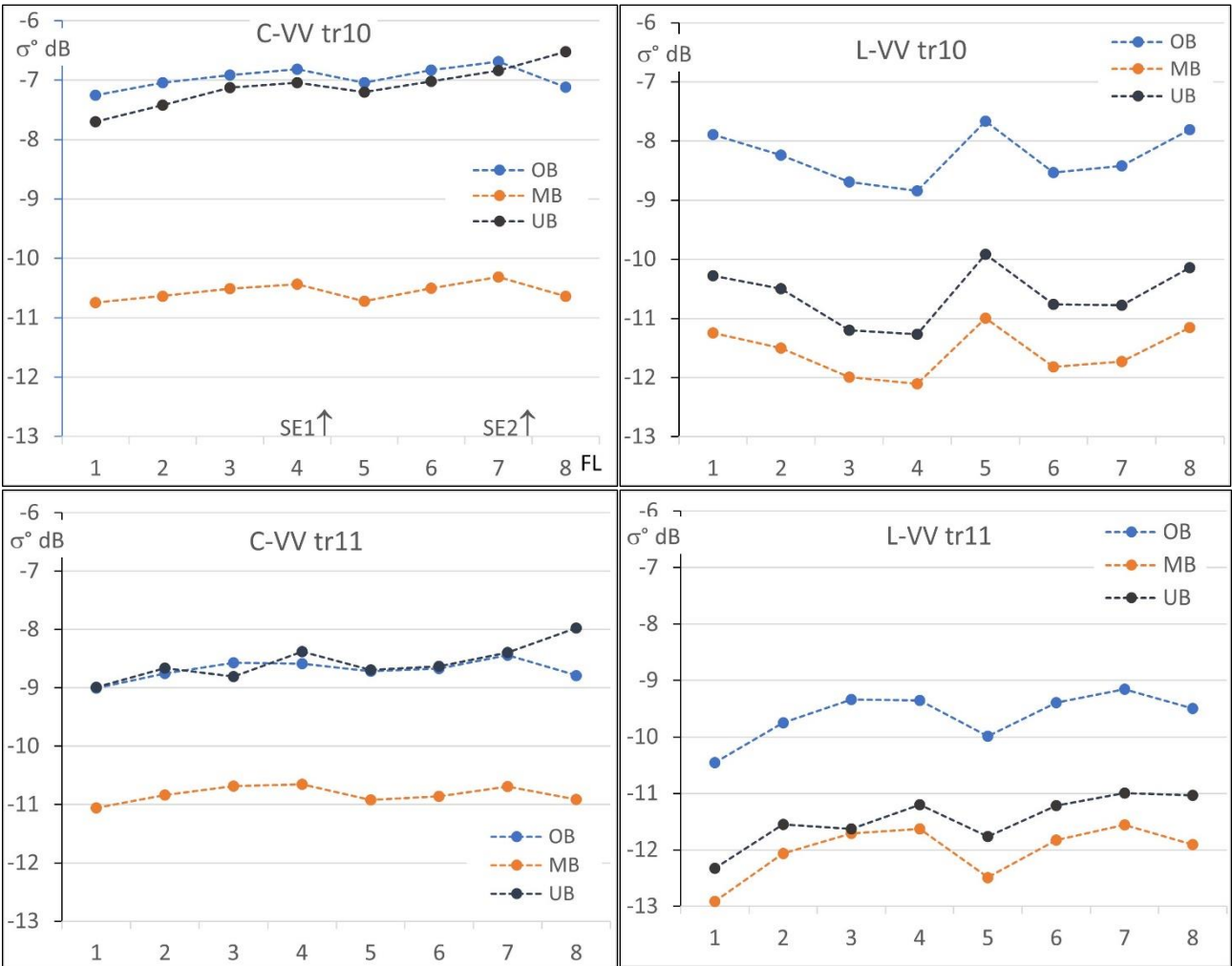
Figure 4-4: Mean σ° (C-band and L-Band, VV polarization) time series for the RoIs derived from data of flights FL01 to FL08, track 10 and track 11. The arrows indicate the occurrence of snowfall events: SE1 between FL04 and FL05, SE2 between FL07 and FL08.
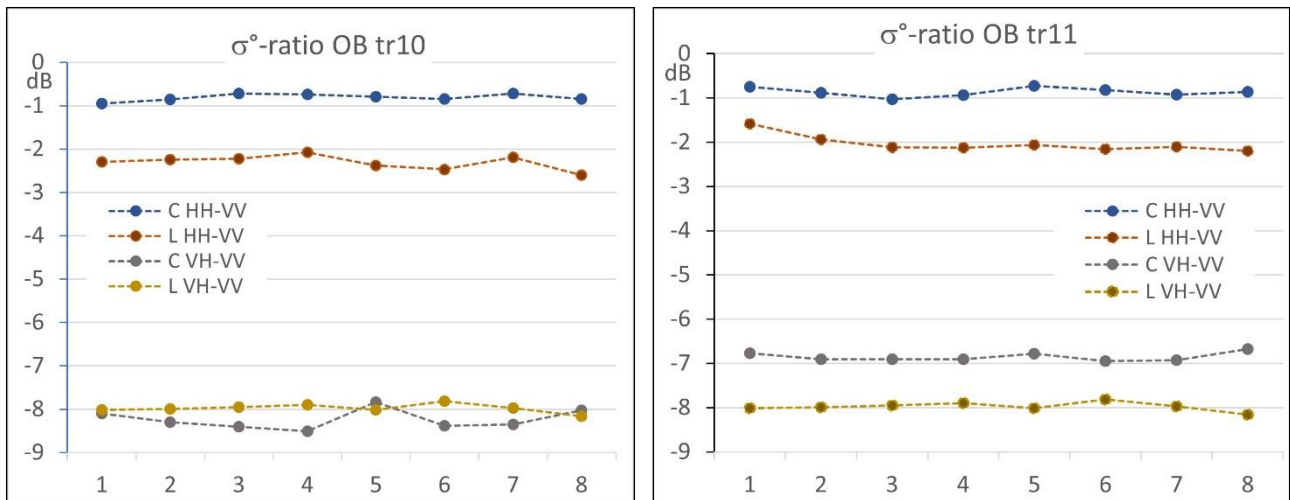
Figure 4-5: Time series of backscatter ratio (in dB) C-and L-band HH/VV and VH/VV channels, track 10 and 11, Oberer Boden.

4.2.2 Co-polarized phase difference

Theoretical and experimental studies show distinct relations between the VV-HH co-polarized phase difference (CPD) and dielectric and structural anisotropy of seasonal snow, as well as the feasibility for estimating the depth of fresh snow using X-band RP-InSAR data [11], [12]. The CPD is linked to the micro-structure of snow arising from the anisotropy of ice grains. Horizontal structures dominate in fresh snow, whereas vertical structures prevail in metamorphic snow.

CPD at C-band frequencies may also show some response to fresh snow deposited upon a seasonal snow pack. In order to check the information content of F-SAR CPD data in respect to SD we computed the complex co-polarized (vvhh) coherence

$$\gamma_{vvhh} = \frac{\langle s_{vv} \cdot s_{hh}^* \rangle}{\sqrt{\langle |s_{vv}|^2 \rangle \cdot \langle |s_{hh}|^2 \rangle}} \tag{4-1}$$

$\langle \dots \rangle$ denotes the expectation value and $*$ the complex conjugate.

We use windows of size 25 x 25 pixel for computing the complex co-pol coherence. The magnitude, $|\gamma_{vvhh}|$ indicates the strength of correlation between VV and HH measurements. Mean values of the RoI C-band phase differences ($\varphi_{CPD} = \varphi_{VV} - \varphi_{HH}$) in track 10 data are shown in Figure 4-6. Increased CPD values are observed for the flights on the day after the two snowfall events, amounting on the average to 0.07rad for SE1 (FL05) and 0.26rad for SE2 (FL08). However, the ΔCPD values of the three sites related to SE2 show a spread that is not in accordance with the observed depth of fresh snow. Besides, an increase of CPD is also observed between FL03 to FL04 without snowfall.

The L-band data show a CPD increase of 0.1rad between FL04 and FL05 and of 0.05rad between FL07 and FL08. In summary, the co-polarized phase difference of both frequencies does not show a consistent relation to snow depth.
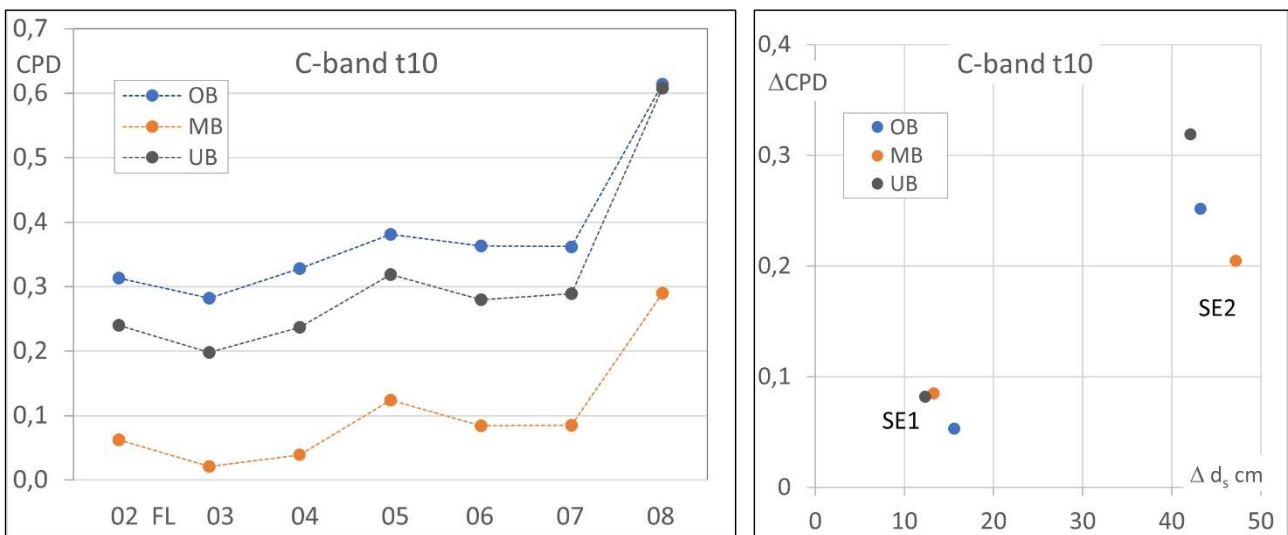
Figure 4-6: Co-polarized C-band phase difference (VV-HH) in radian of the three RoIs. Left: Mean values for the flights FL02 to FL08, track 10. Right: Change in CPD between flights spanning the two snowfall events vs. observed snow depth. SE1 ΔCPD FL05-FL04; SE2 ΔCPD FL08-FL07.

4.2.3   Coherence and temporal decorrelation of RP-InSAR pairs

The coherence estimates shown in this section are based on windows of size 25 x 25 pixels of the full resolution F-SAR data. Due to the large number of looks (C-band ENL = 150, L-band ENL = 190) the estimated coherence has a very small bias [16]. Figure 4-7, Figure 4-8 and Figure 4-9 show mean values of the C-band and L-band coherence magnitude of HH-polarized data for the central section of the test site. The γ_{VV} coherence is slightly higher than γ_{HH}, with mean C-band γ_{VV} exceeding the γ_{HH} magnitude by values ranging from 0.01 to 0.04 and L-band γ_{VV} exceeding the γ_{HH} magnitude by 0.005 to 0.02.
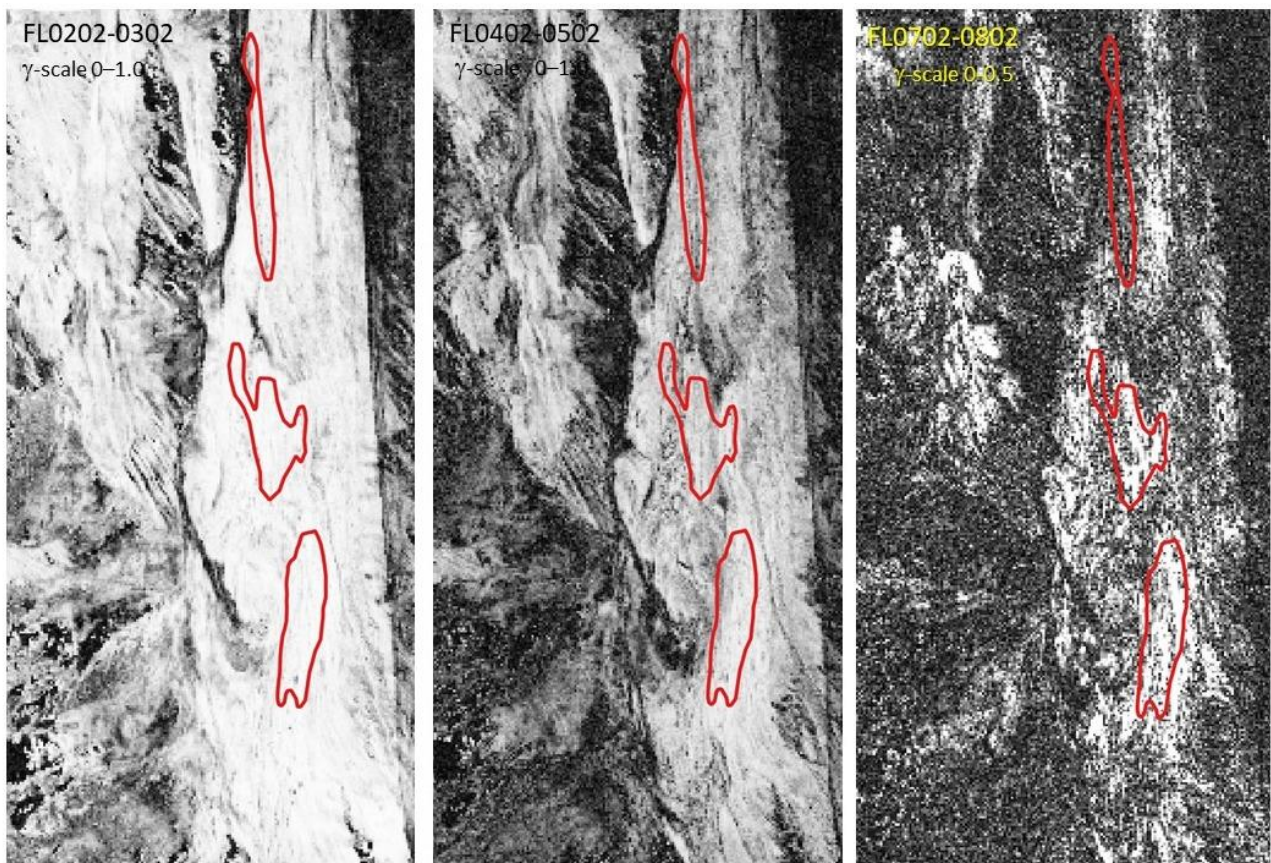
Figure 4-7: F-SAR RP-InSAR coherence magnitude images, C-band HH, radar projection. Track 10, image pairs FL0202-FL0302, FL402-FL0502 (spanning SE1), FL0702-FL0802 (spanning SE2). FL0202-FL0302, FL402-FL0502: grey scale 0 to 1.0; FL0702-FL0802: grey scale 0 to 0.5.

Figure 4-7 and Figure 4-8 show examples for C-band, respectively L-band, of coherence images for an interval without snowfall (FL0202-FL0302, 3 to 5 March 2021) and images spanning the two snowfall events (SE1: FL0402-FL0502, 4 to 6 March 2021; SE2: FL0702-FL0802, 9 to 19 March 2021). As expected, L-band shows higher coherence throughout, with pronounced gain compared to C-band for the data of both snowfall events, in particular SE2. For SE2 (FL0702-FL0802) the grey scale of γ_{HH} in Figure 4-7 has been clipped to 0.0 to 0.5, in order to provide better distinction of low coherence values. Topographic features are evident in the spatial pattern of all coherence images, accentuated by low coherence on backslopes.
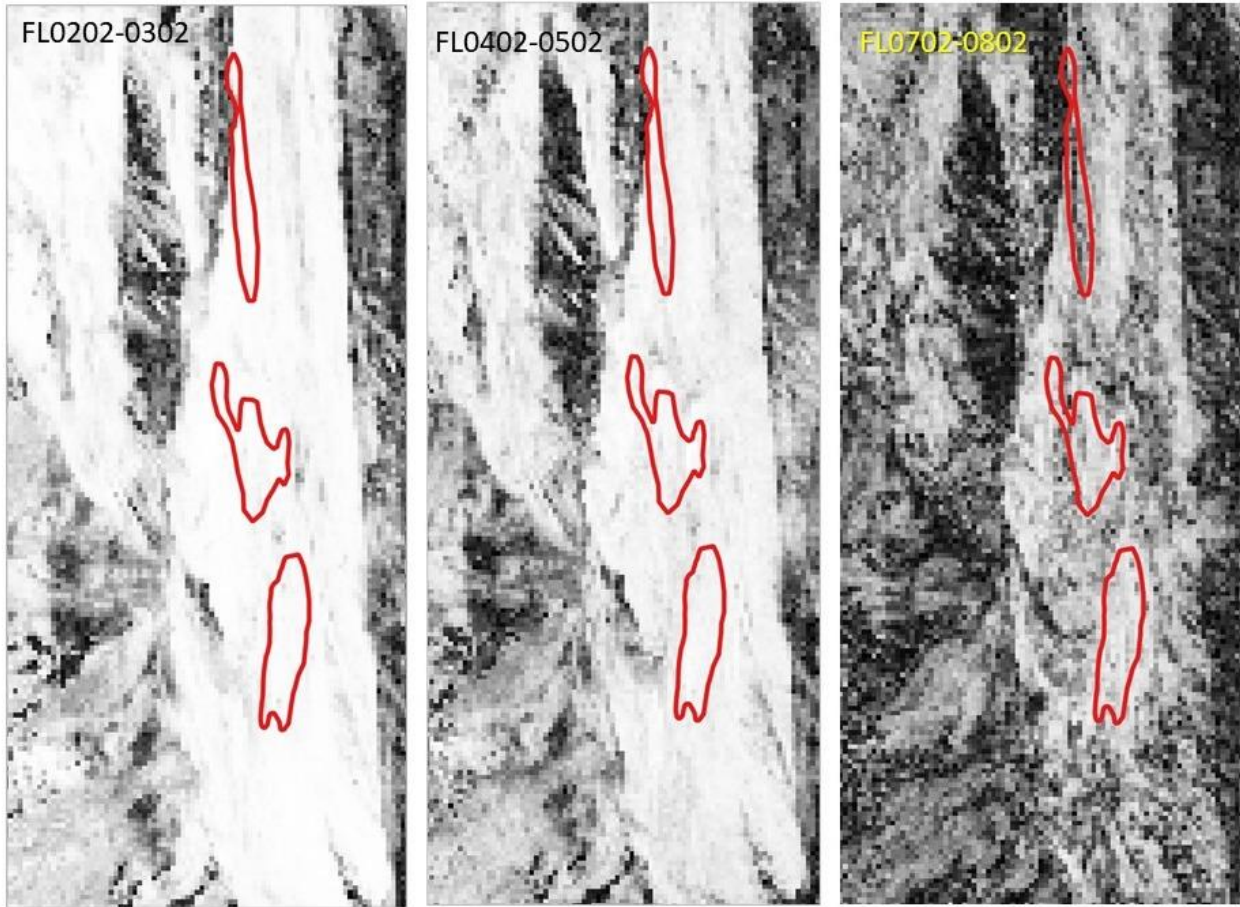
Figure 4-8: F-SAR RP-InSAR coherence magnitude images, L-band HH, radar projection. Track 10, image pairs FL0202-FL0302, FL402-FL0502 (spanning SE1), FL0702-FL0802 (spanning SE2). Grey scale 0 to 1.0.
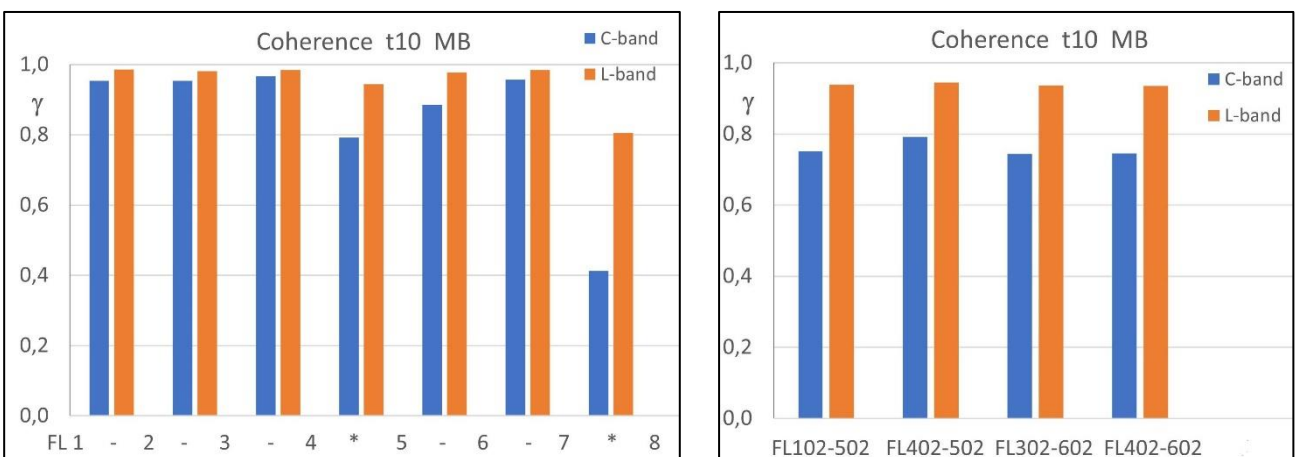
Figure 4-9: Magnitude of total normalized coherence, F-SAR track 10, C-band HH and L-band HH, Mittlerer Boden. Left: Successive repeat pass pairs (FL0102 to FL0202, FL0202 to FL0302, . . .); * refers to snowfall events. Right: Coherence of different image pairs spanning the 1st snowfall event.

In order to check the impact of changes in snow properties on coherence, we focus on data of the RoIs for which topographic effects are of little relevance. Figure 4-9 shows examples of track 10 for the RoI

MB. The γ values of successive flights without snowfall are high, ranging from 0.89 to 0.97 in C-band and from 0.98 to 0.99 in L-band. The lowest C-band magnitude of γ without snowfall (γ = 0.89, FL0502-FL0602) coincides with an image pair of quite different squint angles. The snowfall events between flights cause major decrease of γ, in particular in C-band: γ = 0.80 spanning SE1 and γ = 0.41 spanning SE2. The L-band coherence is much less affected by snowfall: γ = 0.94 for SE1 and γ = 0.80 for SE2. The coherence numbers of OB are similar to those of MB. The coherence of UB is lower, due to impact of bumpy micro- to mesoscale topography.

The coherence data show that in both C-band and L-band the coherence remains high for intervals without snowfall, at least for time spans of a few days. The high degree of F-SAR coherence benefits from the high spatial resolution of the data. The interferograms spanning different intervals between 2 and 8 March 2021, including the snowfall event SE1, show also that the different numbers of snow-free days are of little relevance and the signal is affected by partial decorrelation related to SE1 (happening between FL0402 and FL0502). For SE2 the change in the C-band interferometric phase exceeds the 2π phase ambiguity and the deposited snow causes major temporal decorrelation. L-band shows also for SE2 comparatively high γ-values (except on steep back-slopes), confirming the usefulness of L-band RP-InSAR for obtaining useful estimates of SWE also in case of snowfall events of moderate to high intensity.

4.3 RP-InSAR SWE retrievals and evaluation

4.3.1 RP-InSAR ΔSWE retrieval algorithm

The algorithm for retrieval of SWE from interferometric SAR data exploits the path delay of a radar signal propagating through a snow layer over ground by means of differential interferometry of repeat-pass SAR data (D-InSAR) [13]. A precondition for using the phase delay in the snowpack for the retrieval of SWE is the use of a radar wavelength for which the absorption and scattering losses in the snowpack are small. This is the case for C-band and L-band in dry snow. Other critical issues are the 2π phase ambiguity and the temporal decorrelation of the interferometric phase for which snowfall intensity and melting are decisive factors. The decorrelation problem can be mitigated by using longer wavelengths (L-band rather than C-band) [14].

In case of the Wörgetal campaign the change in SWE (ΔSWE) due to accumulation of fresh snow on top of a dry seasonal snowpack is derived from measurements of the interferometric phase before and after the snowfall. The phase difference is given by

$$\Delta\varphi_s = -2k_i\Delta d_s\left(\cos\theta_i - \sqrt{\varepsilon_s - \sin^2\theta_i}\right) \tag{4-2}$$

where ε_s is the permittivity of the snowpack, θ_i is the local incidence angle, $k_i = 2\pi/\lambda$ the wavenumber in free space and Δd_s the depth of the fresh snow layer. For dry snow the imaginary part of the snow permittivity can be neglected, and the real part can be expressed as a function of the snow density, ρ [15]:

$$\varepsilon_s \simeq \varepsilon_s' = 1 + 1.60\,\rho + 1.86\,\rho^3, \qquad \rho \le 0.40\,\text{g cm}^{-3} \tag{4-3}$$

An estimate for the density of the accumulated snow is needed for computing ε_s and deriving SWE:

$$\Delta d_s = -\Delta\varphi_s\frac{\lambda}{4\pi}\left[1\middle/\left(cos\theta - \sqrt{\varepsilon_s - sin\theta^2}\right)\right] \; ; \; \mathit{\Delta SWE} = \rho\,\Delta d_s \tag{4-4}$$

Snow depth and SWE measurements refer to the vertical direction also on slopes [17]. Therefore, the slope angle, α, needs to be considered for deriving SWE from the observed phase on sloping terrain:

$$\Delta SWE = \Delta\varphi_s \frac{\lambda}{4\pi} \cdot \rho \cdot \frac{1}{\cos\alpha} \cdot \frac{1}{\sqrt{\varepsilon_s - \sin\theta^2} - \cos\theta} \qquad (4\text{-}5)$$

In order to derive the change in phase attributed to changes in snow mass, $\Delta\varphi_s$, from the total phase $\Delta\varphi$ in repeat pass interferograms, it is necessary to account for the reference phase at sites without change in snow mass or with known ΔSWE:

$$\Delta\varphi_s = \Delta\varphi - \Delta\varphi_{ref} \qquad (4\text{-}6)$$

For the Wörgetal data set the phase of the corner reflectors cleaned of snow, $\Delta\varphi_{ref}$, is used as reference. The density of the fresh snow is known from field measurements on the days of flights after the snowfall events: 0.095gcm[-3] for SE1 and 0.145gcm[-3] for SE2. In case of the F-SAR data set possible changes in the atmospheric phase delay, $\Delta\varphi_{atm}$, are of no relevance because the reference phase of a reflector accounts implicitly for possible temporal changes of the atmospheric phase delay. At incidence angles < 40° differences in the density of fresh snow have only a small impact on the sensitivity of the interferometric phase in respect to ΔSWE.

4.3.2 ΔSWE retrieval uncertainty

The total error estimate of ΔSWE needs to account for random and systematic error contributions, including random as well as systematic phase errors of the scene pixel ($\Delta\varphi$) and the reference target ($\Delta\varphi_{ref}$), combined in quadrature:

$$\sigma_{\Delta\varphi s}(x,y) = \sqrt{\sigma^2_{\varphi,ran}(x,y) + \sigma^2_{\varphi,sys}(x,y) + \sigma^2_{\varphi,CR}(x,y)} \qquad (4\text{-}7)$$

The magnitude of the random error can be reduced by increasing the number of looks (window size) of the products, whereas systematic errors are related to phase offsets arising mainly from residual baseline errors. $\sigma_{\varphi,sys}$ varies with the local incidence angle, increasing in steep topography. The reference phase for ΔSWE = 0mm used in the error estimate below is based on the phase of three corner reflectors. The related error $\sigma_{\varphi,CR}$ is a systematic error. The random error for a pixel comprising L resolution elements (looks) can be estimated for high coherence values in dependence of coherence magnitude $|\gamma|$:

$$\sigma_{\varphi,ran} = \frac{1}{\sqrt{2L}} \frac{\sqrt{1-\gamma^2}}{\gamma} \quad [rad], \; for \; L \to \infty \qquad (4\text{-}8)$$

This equation can be used for estimating the statistical uncertainty of φ_s derived from phase images based on a large number of looks (L). For low coherence and a small number of looks the phase error is underestimated, requiring a formulation as proposed in [16].

The systematic errors (phase offsets) in the Wörgetal data set vary with the passes used for deriving a particular interferogram. For $\sigma_{\varphi,CR}$ not only residual baseline errors play a role, but also sidelobes from surrounding terrain, in particular in L-band.

The full equation for retrieving ΔSWE from changes of the RP-InSAR is specified in Eq. 4-2. For incidence angles $\theta_i \le 50°$ and snow density $\rho \le 0.40$gcm[-3] this equation can be approximated by the following linear relation:

$$\Delta SWE = -\Delta\varphi_s \frac{\lambda}{2\pi} \frac{\cos\theta_i}{1.6} \qquad (4\text{-}9)$$

This equation can be used for uncertainty estimation:

$$\sigma(\Delta SWE) = \frac{\lambda}{2\pi} \frac{\cos\theta_i}{1.6} \sqrt{\sigma^2_{\varphi,ran}(x,y) + \sigma^2_{\varphi,sys}(x,y) + \sigma^2_{\varphi,CR}(x,y)} \qquad (4\text{-}10)$$

4.3.2.1 Uncertainty estimates for ΔSWE derived from full resolution F-SAR data

For full resolution F-SAR data the random phase error plays a small role. A window size of 25 x 25 pixels is used for SWE retrieval, with the equivalent number of looks: C-band ENL ≈ 150 (window size 5m x 7.5m), L-band ENL ≈ 190 (10m x 15m). The average coherence of the RoIs of the F-SAR passes used for retrieval is: $|\gamma|$ = 0.8 for C-band SE1, $|\gamma|$ = 0.95 for L-band SE1 and $|\gamma|$ = 0.8 for L-band SE2.

The random errors for full resolution F-SAR data, with window size specified above, are:

- C-band, SE1, $|\gamma|$ = 0.80: $\sigma_{\varphi,ran}$ = 0.043rad, $\sigma(\Delta SWE)$ = 0.21mm

- L-band, SE1, $|\gamma|$ = 0.95: $\sigma_{\varphi,ran}$ = 0.017rad, $\sigma(\Delta SWE)$ = 0.33mm

- L-band, SE2, $|\gamma|$ = 0.80: $\sigma_{\varphi,ran}$ = 0.038rad, $\sigma(\Delta SWE)$ = 0.74mm.

The actual errors in retrieved ΔSWE are higher due to systematic errors which may vary with the steepness of slopes and also along the flight track, a problem for spatially detailed estimation of these errors. As an estimate for $\sigma_{\varphi,CR}$ we use the maximum difference between the phase of individual CRs in track 10. The errors, accounting for $\sigma_{\varphi,ran}$ and $\sigma_{\varphi,CR}$, are:

- C-band SE1: $\sigma_{\varphi,ran}$ = 0.043rad, $\sigma_{\varphi,CR}$ = 0.490rad; total σ_{SWE} = 2.39mm

- L-band SE1: $\sigma_{\varphi,ran}$ = 0.017rad, $\sigma_{\varphi,CR}$ = 0.155rad; total σ_{SWE} = 3.04mm

- L-band SE2: $\sigma_{\varphi,ran}$ = 0.038rad, $\sigma_{\varphi,CR}$ = 0.122rad; total σ_{SWE} = 2.49mm

These errors are rough estimates because possible systematic errors, $\sigma_{\varphi,sys}$, are not taken into account. On level terrain $\sigma_{\varphi,sys}$ may be of similar magnitude as $\sigma_{\varphi,CR}$. For SE1 the mean ΔSWE bias is below these error estimates which can be attributed to spatial averaging. The maximum SE1 bias of individual RoIs is slightly higher (Table 4-5). This can partly be attributed to small-scale spatial variability of SWE, affecting the comparison of in-situ point data with full spatial coverage by the airborne data. The range of the SE2 bias of the individual RoIs, derived from L-band data, is higher.

For satellite-based SWE measurements the reference phase is obtained from sites that are snow-free or for which ΔSWE and/or snow depth data are available from recording stations. In case of snow depth (which is measured by recording stations in many mountain areas) snow density estimates are needed for obtaining SWE estimates. Operational snow process models are able to provide suitable estimates of snow density. For the ΔSWE uncertainty the representativity of the in-situ data, as well as the phase uncertainty at the reference sites, are of importance.

4.3.3 F-SAR repeat pass interferometric SWE retrievals of Wörgetal

In this section SWE retrievals using full resolution C- and L-band HH- and VV-polarized F-SAR data are presented and the performance of the retrieved products is assessed. Due to the C-band 2π phase ambiguity in respect to ΔSWE (32mm at θ_i = 30) and due to the low coherence for SE2, C-band data are used only for SWE retrievals of snowfall event SE1. L-band data are applied for retrievals of both snowfall events. The SWE retrievals below are based on image pairs spanning a single snowfall event. In case of SE1 there are several options, whereas for SE2 two combinations, FL06-FL08 and FL07-FL08, are available.

As evident from the uncertainty estimation addressed above, the accuracy of the CR phase used as reference for ΔSWE = 0mm is a critical factor for performance of the SWE product. We checked the phase of the individual CRs for the available RP-InSAR pairs spanning the two snowfall events. Good performance in this respect can be expected for repeat-pass pairs with optimum correction of motion errors. Image pairs with close agreement of the squint angles facilitate the correction of motion errors [A2]. However, these images are not necessarily the optimum choice in respect to the agreement of the

phase of different reflectors and polarizations within an interferogram. For selecting suitable image pairs for SWE retrieval we use the agreement of the phase between different reflectors and of HH and VV polarizations as indicators. For track 11 only two reflectors (CR1 and CR2) can be used because of problems with CR3 due to reflections from adjoining steep slopes [A2].

The CR reference phases of the image pairs selected for SWE retrieval are specified in Table 4-3. The CR phase was obtained from full resolution images. For the selected C-band pairs (FL0302-FL0602 and FL0103-FL0105) the difference between the HH and VV CR phase is ≤ 0.024rad, supporting the choice of these scenes for SWE retrieval. For L-band the differences are larger (≤ 0.055rad) which can be attributed to higher phase uncertainty due to the comparatively small reflector size in respect to the L-band wavelength.

Table 4-3: CR reference phase for F-SAR repeat-pass image pairs selected for ΔSWE retrievals of snow events SE1 and SE2. C-band data are not used for SE2 because of the 2π phase ambiguity.

Event	Track 10				Track 11			
	C-HH	C-VV	L-HH	L-VV	C-HH	C-VV	L-HH	L-VV
SE1	FL0302-FL0602		FL0302-FL0602		FL0103-FL0503		FL0103-FL0503	
SE1	-2.881	-2.905	-0.552	-0.590	1.828	1.830	-0.920	-0.898
SE2			FL0602-FL0802				FL0703-FL0803	
SE2	-	-	3.069	3.084	-	-	2.720	2.775
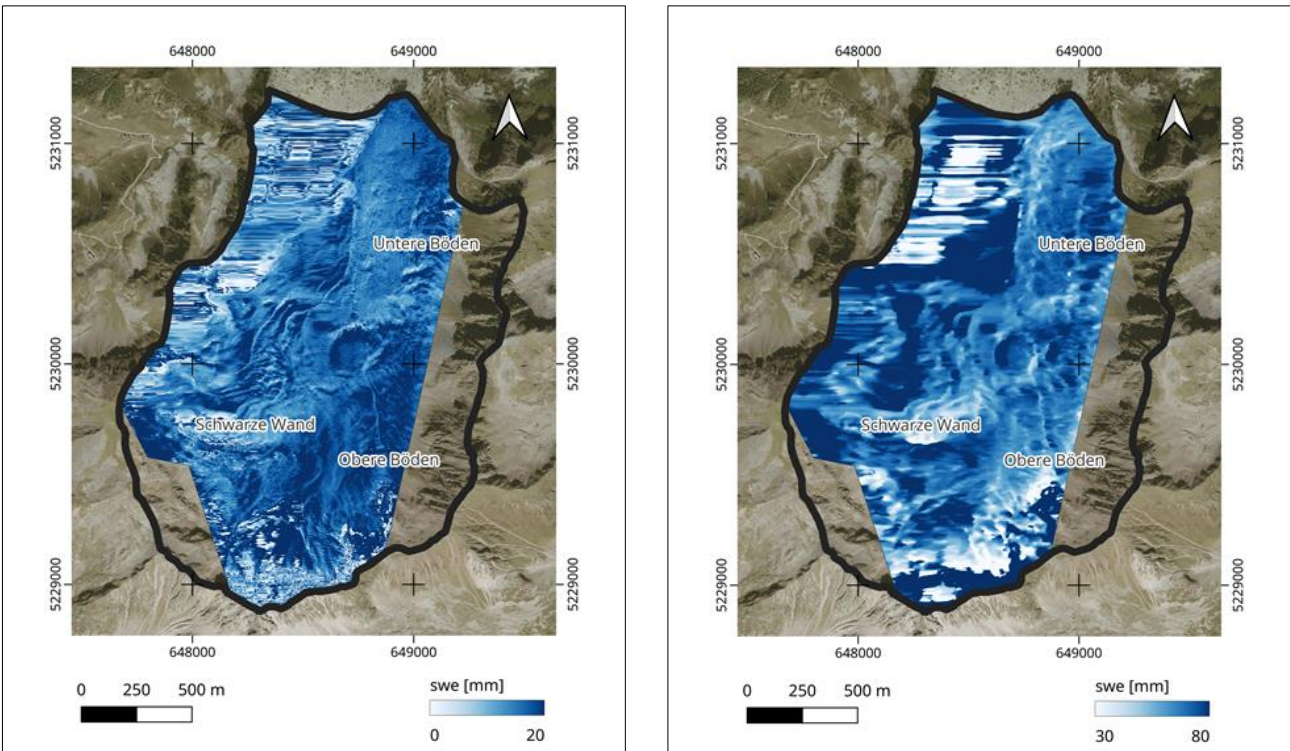
Figure 4-10: Maps of snow accumulated during the snowfall events SE1 and SE2 derived from F-SAR data of track 10. Left: based on C-band VV InSAR data of 4 and 8 March 2021 (FL0402-FL0602), colour scale: 0 ≤ ΔSWE ≤ 20 mm. Right: based on L-band VV data of 7 and 19 March 2021 (FL0702-FL0802). Colour scale: 30 ≤ ΔSWE ≤ 80 mm. The black line encloses the Wörgetal test site.

Figure 4-10 shows examples for ΔSWE maps retrieved from data of track 10 for the two snowfall events, for SE1 derived from C-band data and for SE2 derived from L-band data. On steep slopes the retrieved ΔSWE data are affected by low coherence and phase noise whereas on level terrain the spatial variability of ΔSWE is comparatively low, in accordance with the field observations.

The analysis of the performance of the ΔSWE retrievals below refers to the RoIs. The spatial variability of the depth of fresh snow within these areas is small (Table 4-2). Therefore, the mean values of ΔSWE of these sites, derived from data of the two frequencies and polarizations, are compared with the field data (Table 4-4, Figure 4-11 andFigure 4-12).

Table 4-4: ΔSWE [mm] in the Wörgetal RoIs for the two snowfall events, derived from F-SAR RP-InSAR data. The mean value of computed ΔSWE is based on data of the three RoIs from both tracks. The flights used for the retrievals are specified in Table 4-3.

Event	Channel	ΔSWE [mm] Track 10			ΔSWE [mm] Track 11			Mean	Mean
		OB	**MB**	**UB**	**OB**	**MB**	**UB**	Comp.	In situ
SE1	C-HH	11.7	12.8	12.7	14.6	16.0	15.4	13.9	13.0
SE1	C-VV	11.5	12.5	12.5	14.7	16.1	15.6	13.8	13.0
SE1	L-HH	11.4	9.1	10.4	14.4	14.4	16.6	12.7	13.0
SE1	L-VV	11.1	9.4	10.8	14.0	13.9	16.4	12.6	13.0
SE2	L-HH	67.9	67.8	72.0	54.5	63.1	61.4	64.5	63.4
SE2	L-VV	69.1	69.0	74.0	56.5	64.8	62.7	66.0	63.4
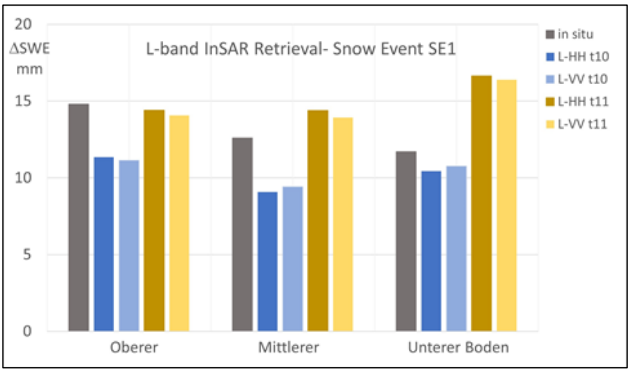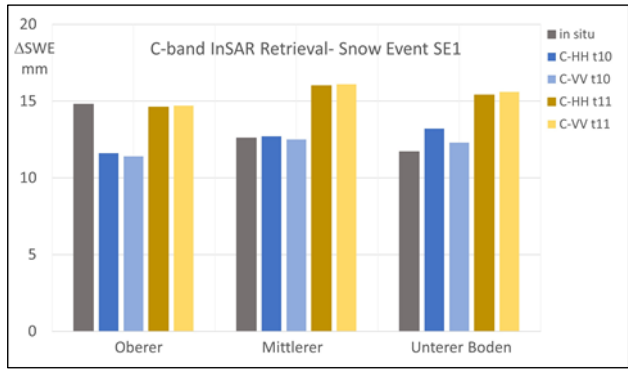
Figure 4-11: Bar chart of mean SWE values of the Wörgetal RoIs, snow event SE1, retrieved from F-SAR C-band and L-band data, track 10 and 11, and mean values of in-situ point measurements along transects.
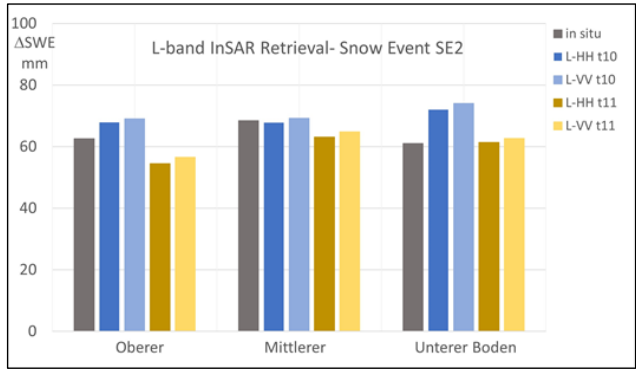
Figure 4-12: Bar chart of mean SWE values of the Wörgetal RoIs, snow event SE2, retrieved from F-SAR L-band data, track 10 and 11, and mean values of in-situ point measurements along transects.

The comparisons of the RP-InSAR based ΔSWE values and the mean SWE of the field measurements at the three sites show good agreement, matching the input requirements for snow process models and hydrology models. The differences between mean in-situ and computed ΔSWE values, based on the data of both tracks and polarizations, and the maximum differences for individual RoIs and tracks are specified in Table 4-5.

Table 4-5: Comparison of observed and computed ΔSWE, mean values of the 3 RoIs; track 10 and track11. The computed ΔSWE is derived from full resolution F-SAR data, HH and VV polarizations. Max. bias is the maximum deviation of computed ΔSWE of any individual RoI and tracks from in situ mean values.

Event	Mean in-situ ΔSWE [mm]	Channel	Comp. ΔSWE [mm]	Bias (computed in-situ) [mm]	Max. bias of individual RoI [mm]
SE1	13.0	C-band	13.8	0.8	-3.2/+3.8
SE1	13.0	L-band	12.7	-0.3	-3.5/+4.8
SE2	63.4	L-band	65.2	1.8	-8.1/+13.0

Differences in retrieved and observed ΔSWE are arising, on one hand, from uncertainties in the differential phase $\Delta\varphi_s$ of accumulated snow, on the other hand, also from the different spatial patterns of in-situ point measurements compared to the area-extended computed ΔSWE. Considering the sensitivity of $\Delta\varphi_s$ in respect to SWE, the requirements on the accuracy of the phase are high. The mean sensitivity over the RoIs is 4.76mm w.e./rad for C-band and 19.51mm w.e./rad for L-band. Because of the large number of looks and high coherence the error of the interferometric phase of the F-SAR RP-InSAR data is small (Section 4.3.2). Consequently, the phase of the corner reflectors, $\Delta\varphi_{ref}$, used as reference for ΔSWE = 0mm, is a greater source of error than the phase uncertainty of the multi-look snow pixels.

The differences in retrieved ΔSWE between HH and VV polarizations are insignificant (Table 4-4). The differences in mean ΔSWE of SE1 between C-band and L-band are also small. There are differences on the order of some mm in ΔSWE between the two tracks. For SE1 the mean ΔSWE of track 11 exceeds ΔSWE of track 10 by 3mm (C-band) and by 4mm (L-band). For SE2 the mean L-band ΔSWE of track 10 exceeds ΔSWE of track 11 by 8mm. Considering the different sign of the computed versus in-situ ΔSWE difference between SE1 and SE2 for L-band track 10 and track 11 ΔSWE (Figure 4-12) and the equality of the sign for C-band and L-band biases of SE1 ΔSWE for track 10 and track 11 (Figure 4-11), this difference is probably caused by biases in the reference phase between track 10 and track 11. Variations in the reference phase between the tracks are also evident in other repeat-pass pairs that we analysed.
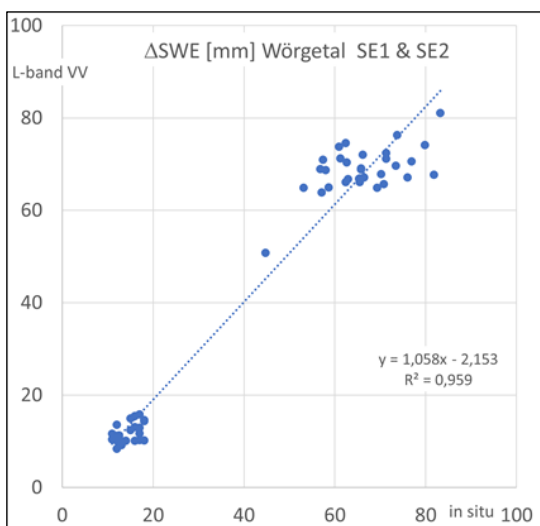
Figure 4-13: ΔSWE retrieval, F-SAR L-band VV, versus in-situ measurements along transects, snowfall events SE1 and SE2. ···· regression line.

Figure 4-13 shows computed ΔSWE values, derived from L-band VV data, for the snowfall events SE1 and SE2 in comparison to in-situ observations along transects in the three RoIs. Because of the low spatial variability of snow depth at each event, the data are forming two clusters which are spread out along the same regression line versus the field observations.

4.4 RP-InSAR SWE retrievals using simulated geosynchronous SAR data

The analysis of coherence, phase and SWE retrievals presented in this section is based on simulated Hydroterra products which account for the resolution, sampling, number of samples and NESZ of the Hydroterra system [A2]. The simulated Hydroterra products with the following specifications are used:

- Single look resolution: (az x rg): 5m x 22.1326m
- Pixel size (az x rg): 2.9335m x 19.1849m
- Interferometric product, 8 x 2 processing window, ENL 8.137

For the simulated Hydroterra products we use the acronym: HT01x01. The raster of these data is largely expanded in azimuth because of the large difference in azimuth and range resolution. For visualization (Figure 4-14 andFigure 4-15) we use the simulated HT04x01 product (4x1 pixels, az x rg) and simulated geosynchronous SAR products with F-SAR resolution.

Simulated interferometric Hydroterra products were computed from C-band F-SAR data for the following flight combinations [A2]:

- Flight 01 – Flight 05, time lag 4 days, spanning SE1 (mean ΔSWE = 13mm)
- Flight 02 – Flight 08, time lag 16 days, spanning SE1 and SE2 (mean ΔSWE = 77mm)
- Flight 03 – Flight 04, time lag 6 h, no snowfall
- Flight 06 – Flight 07, time lag 1 day, no snowfall

The combination FL02-FL08 shows almost complete decorrelation, due to intense snowfall. The snowfall amount exceeds the 2π phase ambiguity almost 3-fold. The full resolution C-band F-SAR data, which are spanning SE2 (ΔSWE = 64mm), show also major decorrelation and are affected by 2π phase ambiguity, not feasible for SWE retrieval. Therefore, the evaluation of SWE retrieval using simulated HT data is based on the FL01-FL05 interferometric product.

4.4.1 Uncertainty estimates of ΔSWE derived from simulated geosynchronous data

The error estimates for ΔSWE need to account for random and systematic phase errors of the scene pixel and the reference target (Eqs. 4-7 & 4-10). The random errors for HT01x01 data with ENL = 8.137 based on the formulation presented in [16] are:

- $|\gamma|$ = 0.4: $\sigma_{\varphi,ran}$ = 0.74rad, $\sigma(\Delta$SWE) = 3.60mm
- $|\gamma|$ = 0.6: $\sigma_{\varphi,ran}$ = 0.42rad, $\sigma(\Delta$SWE) = 2.04mm
- $|\gamma|$ = 0.8: $\sigma_{\varphi,ran}$ = 0.19rad, $\sigma(\Delta$SWE) = 0.92mm

The total error of ΔSWE is obtained by adding the random and systematic errors of the scene pixel and the reference pixel in quadrature (Eq. 4-10). For the F-SAR analysis presented in Section 4.3 the reflector phase is used as reference for ΔSWE = 0mm. In case of reflectors only the systematic phase error is of relevance for the reference target. Using the same CR C-band phase error as for RP-InSAR SE1 ($\sigma_{\varphi,CR}$ = 0.49rad) yields the following total error of ΔSWE:

- $|\gamma|$ = 0.4: $\sigma_{\varphi,tot}$ = 0.89rad, $\sigma(\Delta$SWE) = 4.33mm
- $|\gamma|$ = 0.8: $\sigma_{\varphi,tot}$ = 0.53rad, $\sigma(\Delta$SWE) = 2.58mm

This shows that also for ΔSWE retrievals using geosynchronous SAR the quality of the reference phase is critical. If reference data of sites with known ΔSWE are available, the phase uncertainty of the reference corresponds to the random errors specified above in case of perfect removal of atmospheric and topographic phase components.

4.4.2 SWE retrievals and performance

The performance analysis for the SWE retrievals refers to the same RoIs as used for RP-InSAR SWE retrievals. The analysis is performed for snowfall SE1 because the snow amount of SE2 exceeds the 2π ambiguity more than twofold and the coherence is very low.

The coordinate axes of the simulated HT products of both tracks are aligned in range (x-axis) and azimuth (y-axis) direction [A2] which means that the orientation of tracks 10 and 11 differ from each other. In order to facilitate comparisons between the two tracks and with RP-InSAR data shown in Sections 4.2 and 4.3, we changed the orientation for the simulated HT images shown in Figure 4-14 and Figure 4-15 to match the orientation of the geographic coordinates. These images are not geocoded, but are flipped, respectively mirrored simulated HT images. The HT04x01 format is used in the figures for visualization. The statistical analysis for coherence, phase and SWE is based on the HT01x01 products.
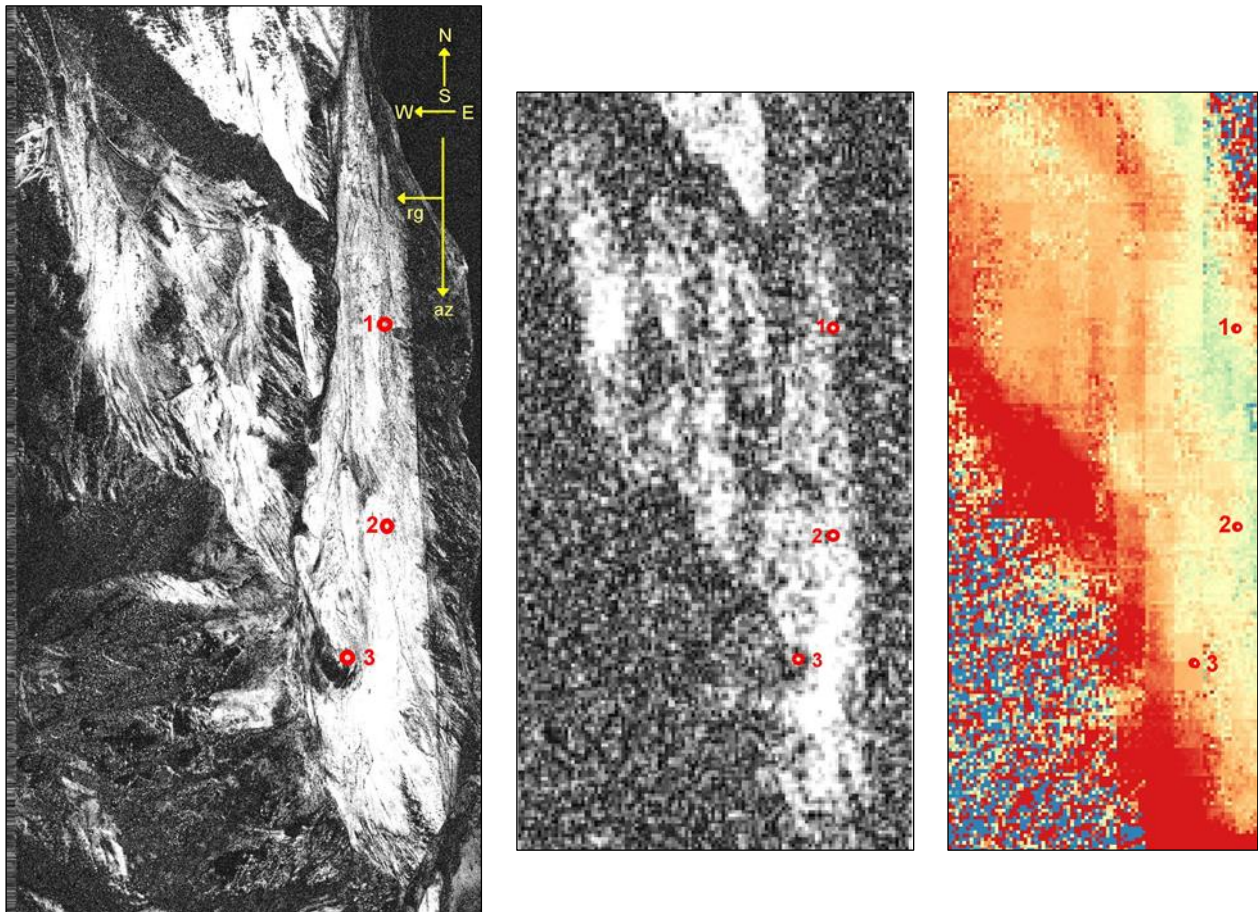
Figure 4-14: Simulated geosynchronous SAR images over Wörgetal, derived from F-SAR C-band VV data track 10 of flights FL0102 and FL0502. Left to right: (i) Coherence of high resolution simulated geosynchronous SAR products, grey scale $0 \leq |\gamma| \leq 0.8$; (ii) and (iii) image format HT04x01; (ii) Coherence grey scale $0 \leq |\gamma| \leq 0.8$; (iii) Repeat-pass phase, colour scale $-1.5 \leq |\varphi| \leq 1.5$ rad. The red points show corner reflector locations. Range (rg) and azimuth (az) correspond to the x-and y-axis of the simulated HT products.

Figure 4-14 shows simulated geosynchronous coherence images and a phase image, derived from F-SAR track 10 data of the flights FL0102 and FL0502 and Figure 4-15 shows coherence and phase images, derived from F-SAR track 11 data of the flights FL0103 and FL0503. The colour scales of both phase images are shifted by 1rad in order to match the shift in the frequency distribution of the phase.

Because the resolution of the HT01x01 data does not allow for accurate estimation of the corner reflector phase, the CR phase values of the simulated F-SAR high resolution products are used as reference for zero ΔSWE. For track 10 the mean HH, respectively VV, phase values of CR2 and CR3 are used as reference. For these two reflectors the HH-VV phase values show close agreement whereas for CR1 the HH and VV numbers do not match well. For track 11 mean values of CR1 and CR2 are used because the phase signal of CR3 is affected by reflection from adjoining steep slopes. The mean values of the following CR phase values are used as reference for zero ΔSWE:

- Track 10 CR2: φ_{HH} = -2.41, φ_{VV} = -2.37;   CR3: φ_{HH} = -2.77, φ_{VV} = -2.67rad
- Track 11 CR1: φ_{HH} = 1.67, φ_{VV} = 1.80;   CR2: φ_{HH} = 1.64, φ_{VV} = 1.76rad
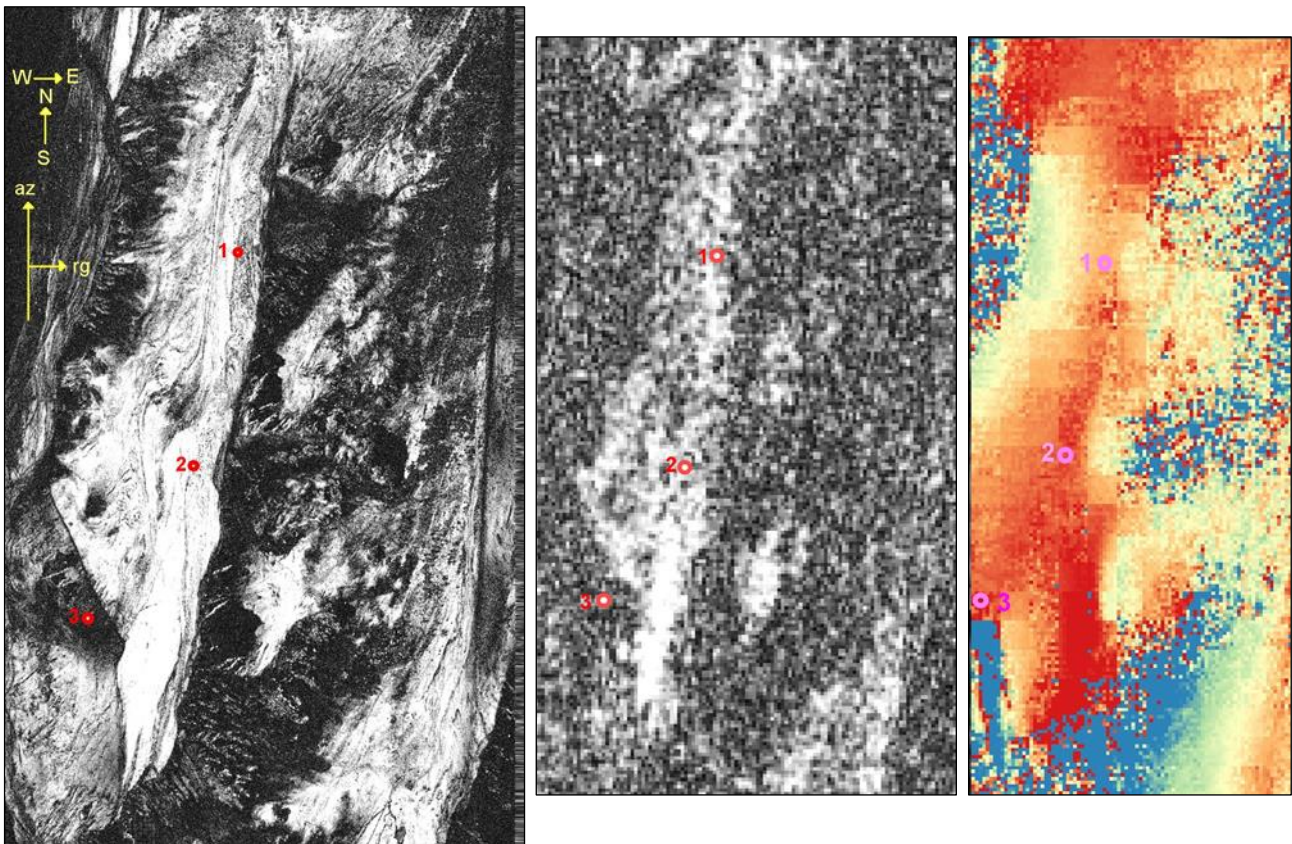
Figure 4-15: Simulated geosynchronous SAR images over Wörgetal, derived from F-SAR C-band VV data track 11 of flights FL0103 and FL0503. Left to right: (i) Coherence of high resolution simulated geosynchronous SAR products, grey scale $0 \leq |\gamma| \leq 0.8$. (ii) and (iii) image format HT04x01; (ii) Coherence grey scale $0 \leq |\gamma| \leq 0.8$; (iii) Repeat-pass phase, colour scale $-2.5 \leq |\varphi| \leq 0.5$rad.

The mean values and standard deviation of coherence and phase in Table 4-6 and Table 4-7 are based on areas covered by 500 to 700 pixels in HT01x01 data for the different RoIs and tracks, which explains the lower phase variance compared to the error estimates for single pixels. The lower coherence and larger phase variance of Unterer Boden (UB) can be explained by the higher roughness of the terrain compared to MB and OB. The coherence of the simulated data for track 11 is slightly lower than for track 10, an impact of the difference in terrain illumination. The coherence of the VV-polarized data is slightly higher than the coherence of the HH-polarized data, as observed also for the original F-SAR data. The computed and in-situ ΔSWE values agree well. The mean ΔSWE values of the three RoIs agree within 0.4mm for track 10 and within 2.6mm for track 11:

- In-situ $\langle\Delta SWE\rangle$ = 13.0mm, HT track 10 $\langle\Delta SWE\rangle$ = 12.6mm, HT track 11 $\langle\Delta SWE\rangle$ = 15.6mm.

The differences for individual RoIs range for track 10 from underestimation of 2.6mm for OB to overestimation of 1.7mm for UB and show for track 11 overestimation ranging from 1.6mm for OB to 4.0mm for MB. The standard deviations of HT ΔSWE for OB and MB, referring to the computed mean values, are smaller than the standard deviations of the in-situ point measurements, an indication for spatial smoothing by the processing procedure.

Table 4-6: Mean values and standard deviation of coherence, phase (rad) and ΔSWE (mm) of the Wörgetal RoIs for snowfall event SE1, derived from simulated Hydroterra data HT01x01, FL01-FL05, track 10. SWEobs.: in-situ mean ΔSWE.

Site	Channel	$\langle COH \rangle$	σ_{COH}	$\langle \varphi \rangle$	σ_φ	$\langle \Delta SWE \rangle$	$\sigma_{\Delta SWE}$	ΔSWEobs.
OB	C-HH	0.57	0.10	-0.10	0.13	12.30	0.64	14.8
OB	C-VV	0.61	0.11	-0.15	0.13	12.06	0.64	14.8
MB	C-HH	0.53	0.08	-0.01	0.10	12.34	0.48	12.6
MB	C-VV	0.56	0.08	-0.06	0.13	12.10	0.62	12.6
UB	C-HH	0.25	0.11	0.23	0.41	13.35	1.95	11.7
UB	C-VV	0.28	0.09	0.27	0.31	13.54	1.47	11.7

Table 4-7: Mean values and standard deviation of coherence, phase (rad) and ΔSWE (mm) of the Wörgetal RoIs for snowfall event SE1, derived from simulated Hydroterra data HT01x01, FL01-FL05, track 11.

Site	Channel	$\langle COH \rangle$	σ_{COH}	$\langle \varphi \rangle$	σ_φ	$\langle \Delta SWE \rangle$	$\sigma_{\Delta SWE}$	ΔSWEobs.
OB	C-HH	0.31	0.06	-1.85	0.28	16.13	1.27	14.8
OB	C-VV	0.37	0.04	-1.95	0.26	16.58	1.17	14.8
MB	C-HH	0.46	0.09	-1.73	0.23	16.26	1.08	12.6
MB	C-VV	0.49	0.08	-1.88	0.15	16.96	0.71	12.6
UB	C-HH	0.37	0.11	-1.08	0.35	13.39	1.67	11.7
UB	C-VV	0.41	0.11	-1.24	0.29	14.16	1.39	11.7

Whereas the ΔSWE retrieval accuracy within the RoIs matches well the observational requirements for snow monitoring and hydrology, the performance is less reliable on steep slopes. This can mainly be attributed to topographic effects in the low-resolution data, showing low coherence and imperfect elimination of topographic phase on steep slopes with rugged topography.

The incidence angle at the RoIs for the simulated data are prescribed by the F-SAR data that are used as basis for HT image simulation. The mean incidence angles of the RoIs range from 29.9° to 35.5° for track 10 and from 31.0° to 38.8° for track 11. For a geosynchronous satellite at 10°E location the incidence angle on a horizontal surface at the test site is 56°. On one hand, the sensitivity of Δφ in terms of ΔSWE increases with the incidence angle, for example by about 50% from 30° to 60° incidence angle. On the other hand, the phase noise and the uncertainty of topographic phase correction increase towards slanting incidence, in particular in complex terrain.

5 SSM Retrieval from Polarimetric SAR Products (WP420)

This section analyses the polarimetric SAR data collected in spring 2022 at the agricultural test site 'Apulian Tavoliere', located west of the city of Foggia in Italy. The SAR data consist of stripmap C- and L-band SAR time series and simulated Hydroterra products. To support the C- and L-band SAR acquisitions executed by DLR and the scientific analysis of the data set, two experimental campaigns were organised and performed by CNR-IREA in collaboration with CREA-CI on 28-29 April and 15-16 June.

The document provides an insight into the possibilities of monitoring surface soil moisture (SSM) using i) L- and C-band SAR data from Low Earth Orbit (LEO), such as those provided by the upcoming ROSE-L and Sentinel-1 NG missions, and ii) geosynchronous SAR observations.

In particular, the following issues are discussed:

- How does the sensitivity of L- and C-band SAR data to SSM change from medium to high incidence angles?
- What is the capability of hyper-temporal SAR acquisitions to monitor sub-daily surface processes induced by irrigation practices?
- What is the impact of a long integration time on the monitoring of SSM changes?

5.1 SAR and ground data overview

During the campaigns of 28-29 April and 15-16 June, four F-SAR measurement flights were flown each time. Two per day, one in the morning and one in the afternoon. Detailed information can be found in the DAR [A3].

For three out of four flights, a stack of 12 stripmap SAR data sets was acquired with a spatial baseline of zero metres and a temporal baseline of approx. 10 minutes. The fourth flight was performed with four acquisitions. For each campaign, the time interval between flights was five hours between the first and second flights, 24 hours between the first and third flights, and 19 hours between the second and third flights. During the second mission in June, there was a 20-minute gap in each batch due to a hardware malfunction in the data recorder. In addition, only 11 stripmap images were acquired during the first flight in June. The off-nadir angle ranges from approximately 23° to 58°. The total number of polarimetric SAR images, the temporal frequency and the start and end time of the SAR acquisitions are summarised in Table 5-1.

For each campaign and frequency, a master acquisition was identified whose geometry serves as a reference for stack co-registration. After SAR data focusing, four calibrated Single Look Complex (SLC) stacks, already co-registered for SAR interferometry, are available. In C-band, the resolutions are 50cm (30cm pixel size) in slant range and 50cm (20cm pixel size) in azimuth. In L-band, the resolutions are 130cm (60cm pixel size) in slant range and 60cm (40cm pixel size) in azimuth. The acquired data sets were further processed. All SLC data were detected, multi-looked (2x5 rg x az), and geocoded to map geometry at 1m pixel size. A further 3x3 boxcar filter was applied. The geocoded products have a resolution of ~3m in C-band and ~7m in L-band.

For each campaign, the interferometric coherence of all acquisitions was computed with respect to the first pass acquisition. Coherence was estimated using a Gaussian window with a kernel size of 21x21 and a SIGMA parameter of 5x5. Coherence maps were geocoded to the same map geometry of the backscatter intensity.

Three interferometric stacks from the first three flights at C-band were used to simulate Hydroterra acquisitions. The fourth flight was merely an add-on and its acquisitions were not used for Hydroterra simulation. Hydroterra single look complex products are supplied as radiometrically calibrated beta-nought coefficients. They have a spatial resolution of 22m x 5m and a pixel size of 19m x 2.9m (rg x az) approximately. The SLC was detected and raised to the power of two to obtain the backscatter

coefficient, divided by the sine of the incidence angle to perform the beta-nought to sigma-nought conversion, multi-looked by a factor of 1x12 (rg x az), and geocoded using the available DEM. Considering an angle of 40° at mid-swath, the ground range resolution cell is approximately 34m x 34m. Simulated geosynchronous SAR (GEO) products with F-SAR resolution were also generated.

Crop maps for April and June are shown in Figure 5-1. Detailed SSM and vegetation biomass measurements were collected on selected fields in the CREA and Caione farms. In particular, wheat and bare fields were monitored in April, while maize, sunflower, quinoa and alfalfa fields were monitored in June.

Continuous SSM data were measured by 6 ground stations installed in the monitored fields, while gridded SSM data were collected by portable sensors four times during each campaign. Irrigation was applied to selected fields before and during the flights to ensure spatial and temporal variability of SSM within and between fields. Information on irrigation timing, amount of water applied, leaf wetness and wind speed is also available. A detailed description of the SAR acquisition, image processing and soil data collection is given in [A3].

As shown in Figure 5-1, wheat is the main winter crop in the area and was therefore selected for in-depth analysis. In addition, a crop with a different canopy structure, i.e. maize, and therefore a different radar response is investigated.

Table 5-1: Summary of the number of C- and L-band stripmap SAR images, temporal frequency and start and end acquisition times for each campaign.

	April, 28 morning	April, 28 afternoon	April, 29 morning	April, 29 afternoon	June, 15 morning	June, 15 afternoon	June, 16 morning	June, 16 afternoon
N images	12	12	12	4	11	12	12	4
temporal frequency (minutes)	10	10	10	18 (on average)	10	10	10	17 (on average)
start - end acquisition times (local time)	09:42:56 - 11:40:01	14:46:12 - 16:37:56	09:50:07 - 11:43:18	14:39:17 - 15:33:42	09:51:45 - 11:42:06	14:48:16 - 16:45:25	09:34:46 - 11:36:28	14:42:14 - 15:33:21
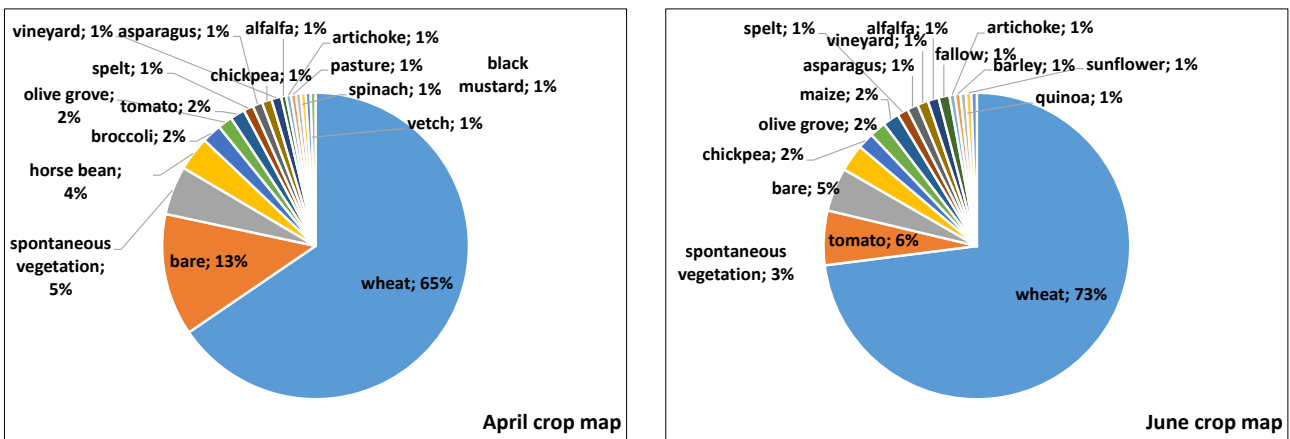
Figure 5-1: Percentage of different crops in April (194 fields in total) and in June (174 fields in total) crop maps.

5.2   Sensitivity analysis of L- and C-band intensity to SSM over wheat fields

To investigate the sensitivity of L- and C-band SAR data to SSM, all stripmap images and gridded SSM measurements collected over one CREA and two Caione wheat fields (CA01 and CA02) during the April flights are used. Each wheat field was divided into four stripes and irrigated on different dates, i.e. April, 26, 27, 28 and 29 for the CREA field and April, 24, 27, 28 and 29 for the Caione fields. Stripes are labelled according to the date of irrigation. The stripes on the CREA field were partially irrigated due to the shorter working length of the mobile boom system. Wheat plants were all at the booting stage but with different plant densities, i.e. 350 plants/m² in the Caione plots and 270 plants/m² in the CREA plot. The water content of the vegetation averaged over the four stripes was 496.8 ± 109.1 g/m², 378.7 ± 189.3 g/m² and 332.6 ± 178.4 g/m² in CA2, CA1 and CREA plots, respectively. Figure 5-2 shows the L-HH intensity over the CREA, CA01 and CA02 wheat fields, imaged at 40.0°, 49.8° and 47.2° angles of incidence. Irrigated areas (brightest areas) are visible along the stripes in the CREA field. Solar panels obscure the bright field located in the upper left corner. An example of gridded SSM measurement locations is also shown on the top right.
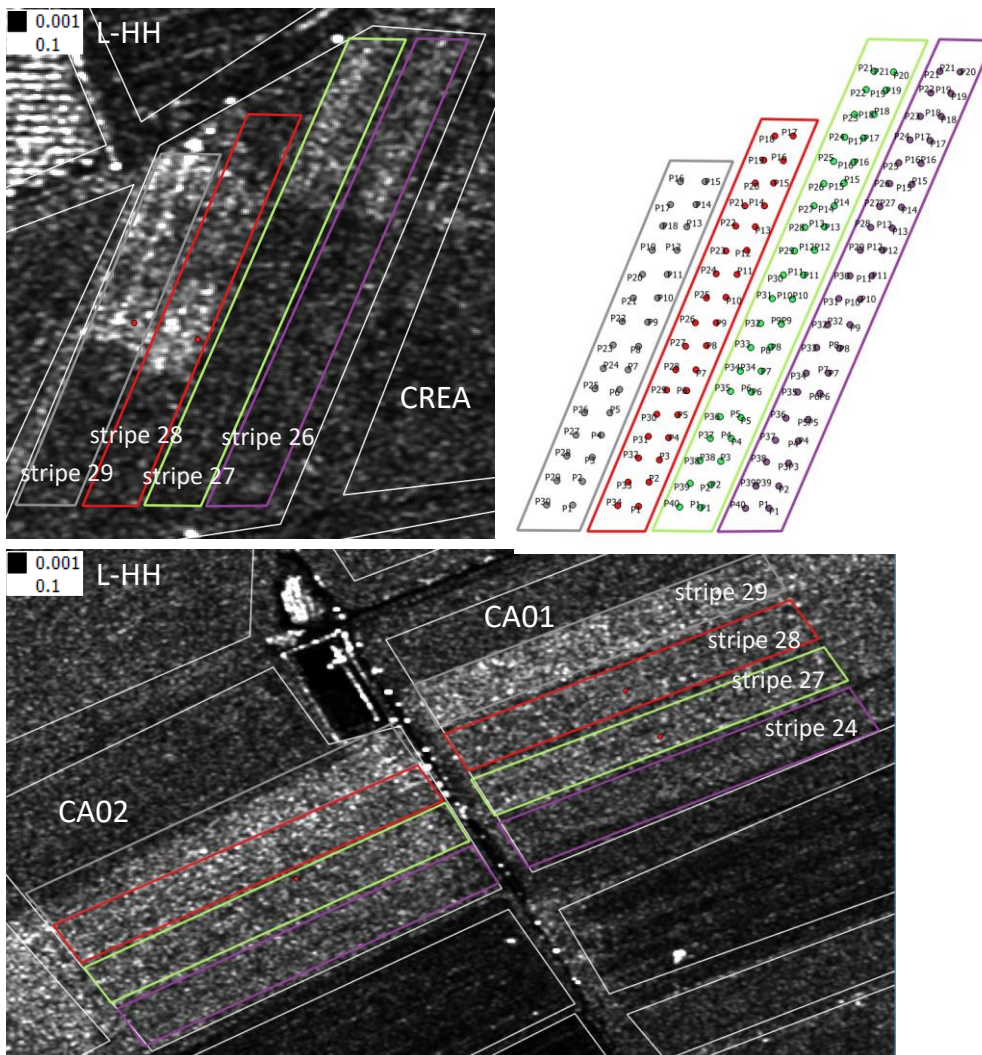
Figure 5-2: L-band HH intensity on 29 April at 14:39 of CREA (upper left panel) and CA02 and CA01 (lower panel) wheat fields. The stripes are labelled according to the irrigation date, i.e. 26 or 24 April (purple line), 27 April (green line), 28 April (red line) and 29 April (grey line). Five red dots indicate the locations of the ground stations. Upper right panel: an example of grid SSM measurements over the CREA field stripes.

5.2.1   Medium incidence angle

In the CREA field, SSM measurements were taken four times during the flights along stripes 26 and 27, and twice along stripes 28 and 29, i.e. not during the irrigation days. Figure 5-3 shows the box plots of the SSM values per date, morning and afternoon, and per stripe, divided into wet (irrigated) and dry (non-irrigated) areas.
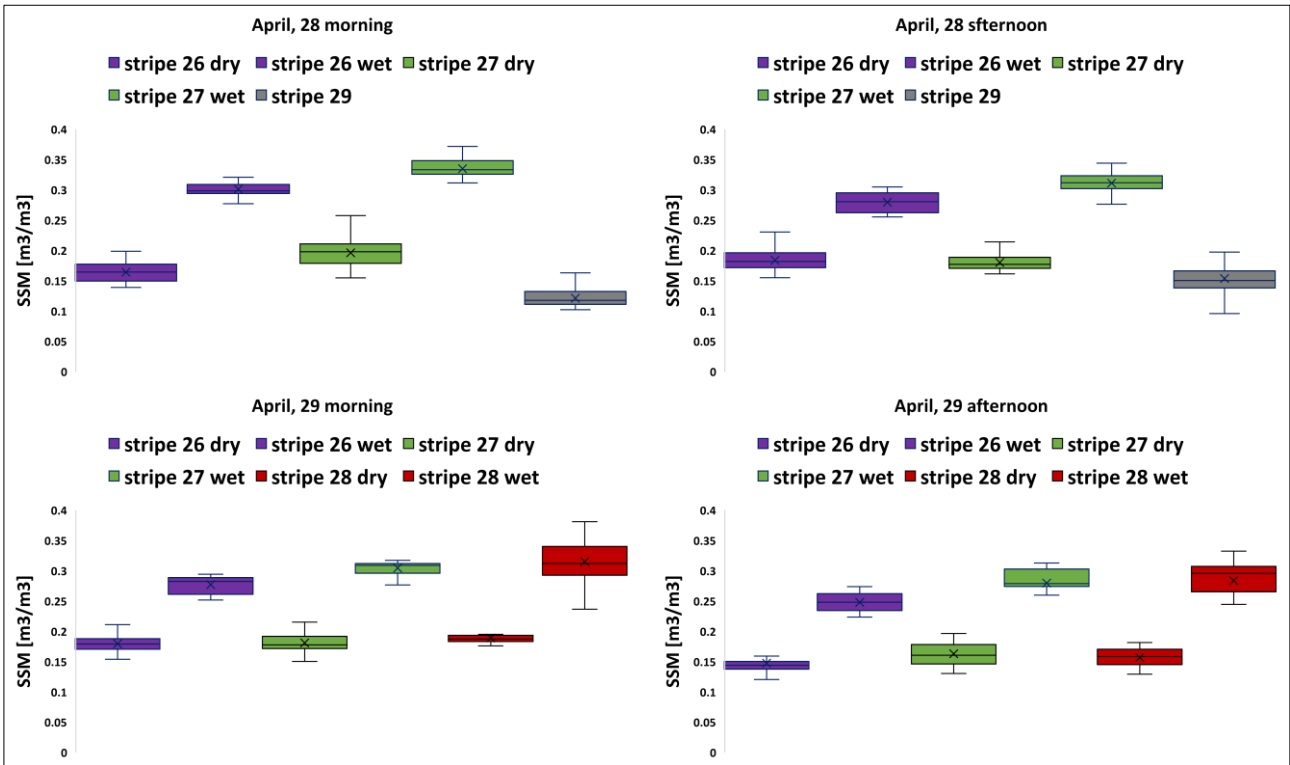
Figure 5-3: Box plots of SSM measurements over the CREA wheat field per date along the stripes divided in wet and dry areas. Median (black line) and mean (black cross) are indicated.

SAR acquisitions and SSM measurements were matched in time. The C- and L-band polarimetric SAR intensities were averaged over the wet and dry areas and plotted as function of the corresponding SSM mean in the scatterplots in Figure 5-5 andFigure 5-4, respectively. In the C-band and at 40° incidence, backscatter at VH and HH polarisation shows similar sensitivity to SSM in terms of slope **s** and correlation coefficient **R** (s=15.86 dB/(m³/m³), R=0.85 and s=14.83 dB/(m³/m³), R=0.83, respectively) and half that for VV polarisation (s=7.61 dB/(m³/m³), R=0.71). It can be seen that the VV backscatter is attenuated by the crop canopy by about 2dB compared to the HH backscatter. Conversely, at L-band, VV backscatter sensitivity to SSM (s=40.15 dB/(m³/m³), R=0.96) is higher than HH (s=24.75 dB/(m³/m³), R=0.94), while VH backscatter shows an intermediate sensitivity (s=31.88 dB/(m³/m³), R=0.94). VV backscatter is slightly attenuated with respect to HH at an SSM of 0.15m³/m³, while it is about 2dB higher than HH at an SSM of 0.30m³/m³. This can be explained by the fact that soil changes affect the L-band backscatter more than vegetation.

Figure 5-5: Sensitivity of C-band intensity at HH (top left), VV (top right) and VH (bottom left) polarisation to SSM at 40° incidence. The linear fit equation and the coefficient of determination are reported.
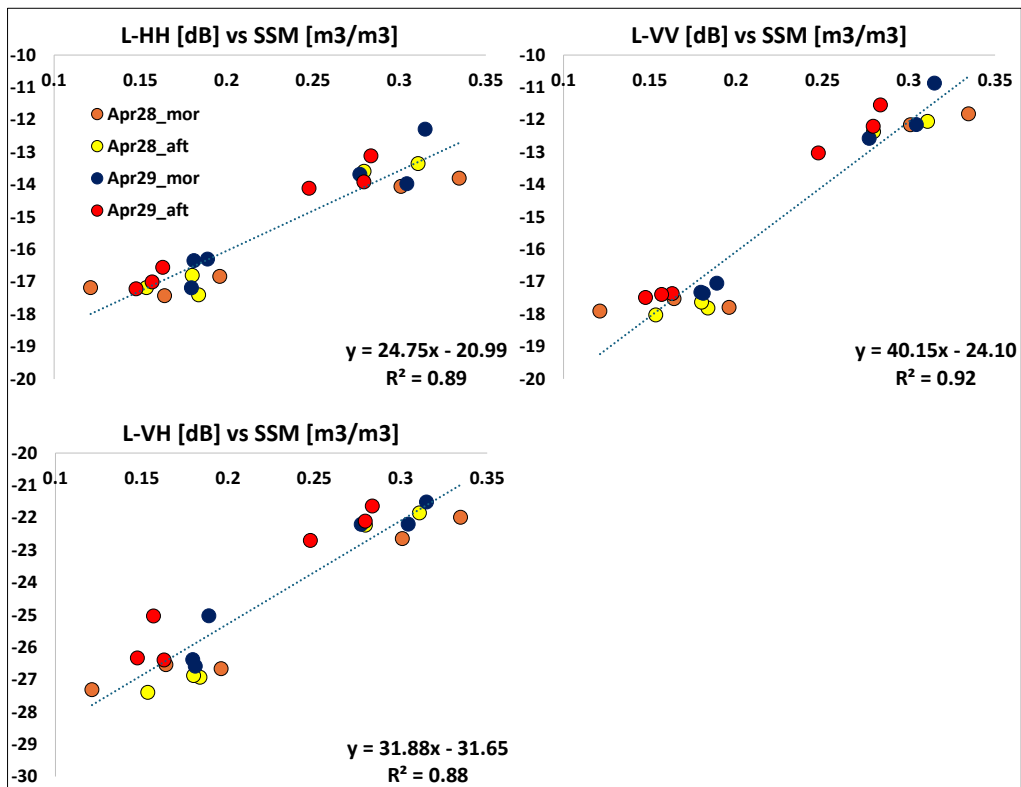
Figure 5-4: Sensitivity of L-band intensity at HH (top left), VV (top right) and VH (bottom left) to SSM at 40° incidence. The linear fit equation and the coefficient of determination are reported.

5.2.2 High incidence angle

In the Caione fields, CA01 and CA02, irrigation was completed by 7:00 am on 28 April and on 29 April, therefore the stripes were uniformly wet or dry during the F-SAR flights. Figure 5-6 shows the SSM measurements along the CA02 stripes. CA01 had the same SSM distribution because the irrigation schedule was the same in both Caione fields.

The SAR acquisitions and SSM measurements of CA01 and CA02 were matched in time. However, due to some delays in the ground data collection activities on the morning of 28 April, the SSM collection along stripes 24 and 27 at CA01 and CA02 started after the morning F-SAR flights and finished later than the afternoon F-SAR flights along stripe 24. On 29 April the SSM collection on stripe 27 started later as well. Therefore, SSM measurements collected over stripes 24 and 27 are not included in the sensitivity analysis.
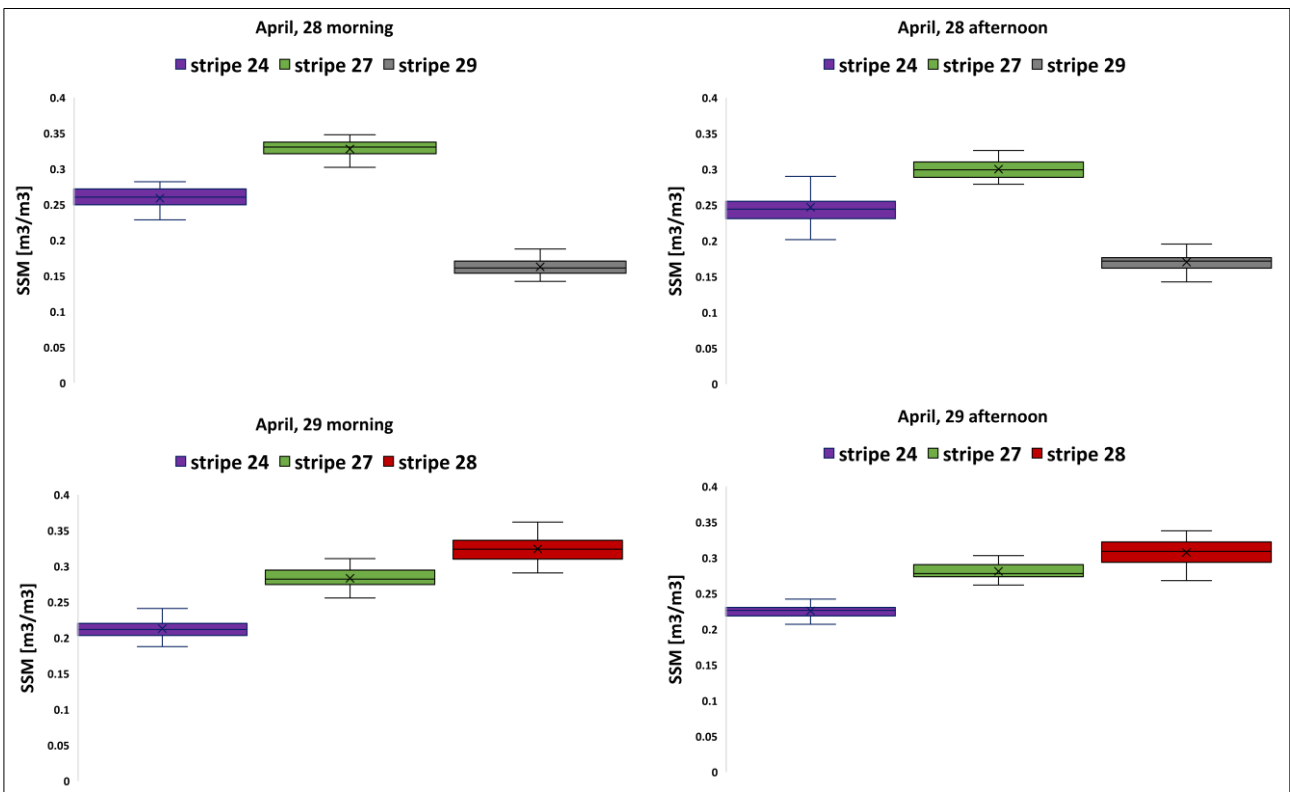
Figure 5-6: Box plots of SSM measurements over the CA02 wheat field per date along the stripes.

Figure 5-8 andFigure 5-7 are the same as Figure 5-5 andFigure 5-4 above but at 47.2° mean angle of incidence for CA02 and 49.9° mean angle of incidence for CA01. Backscatter sensitivity to SSM is generally reduced with respect to 40° incidence in C- and L-band and all polarisations. In C-band, HH and VH polarisations have comparable sensitivity. However, VV shows a slightly higher sensitivity, although the scattering of the observations is also larger. Moreover, HH and VV backscatter reach comparable values, especially for wet SSM conditions. At L-band, the backscatter sensitivity to SSM is preserved for all polarisations, although it is reduced with respect to the case of the medium angle of incidence, i.e. s=24.82 dB/(m³/m³), R=0.95 at VV pol, s=25.24 dB/(m³/m³), R=0.95 at VH pol and s=18.05 dB/(m³/m³), R=0.99 at HH pol. The VV backscatter is attenuated compared to the HH backscatter by approx. 4dB.
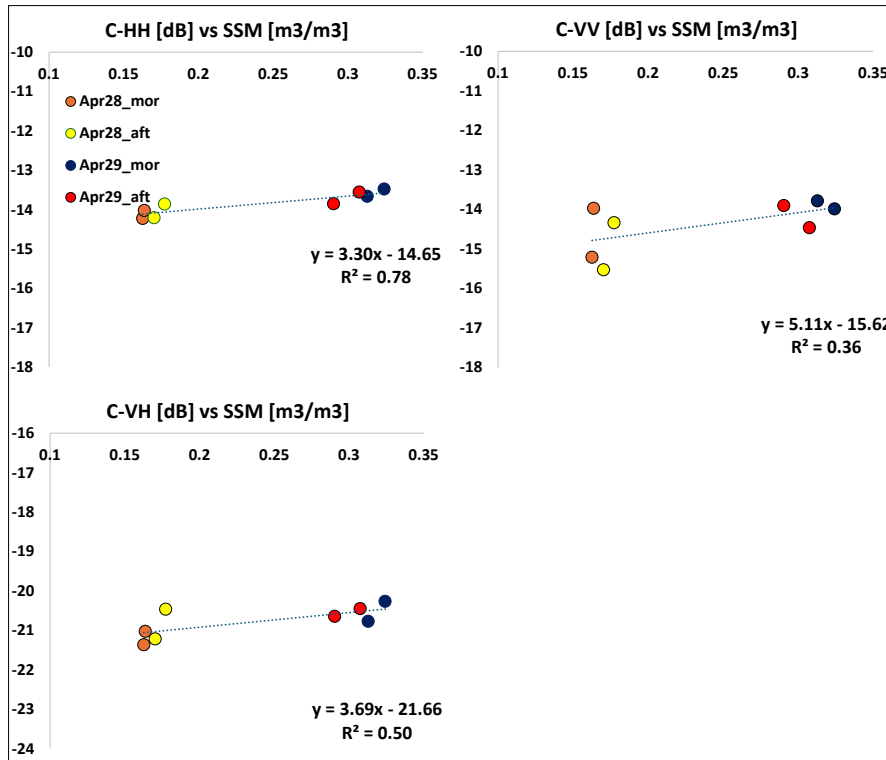
Figure 5-8: Sensitivity of C-band intensity at HH (top left), VV (top right) and VH (bottom left) polarisation to SSM between 47.2° and 49.9° incidence. The linear fit equation and the coefficient of determination are reported.
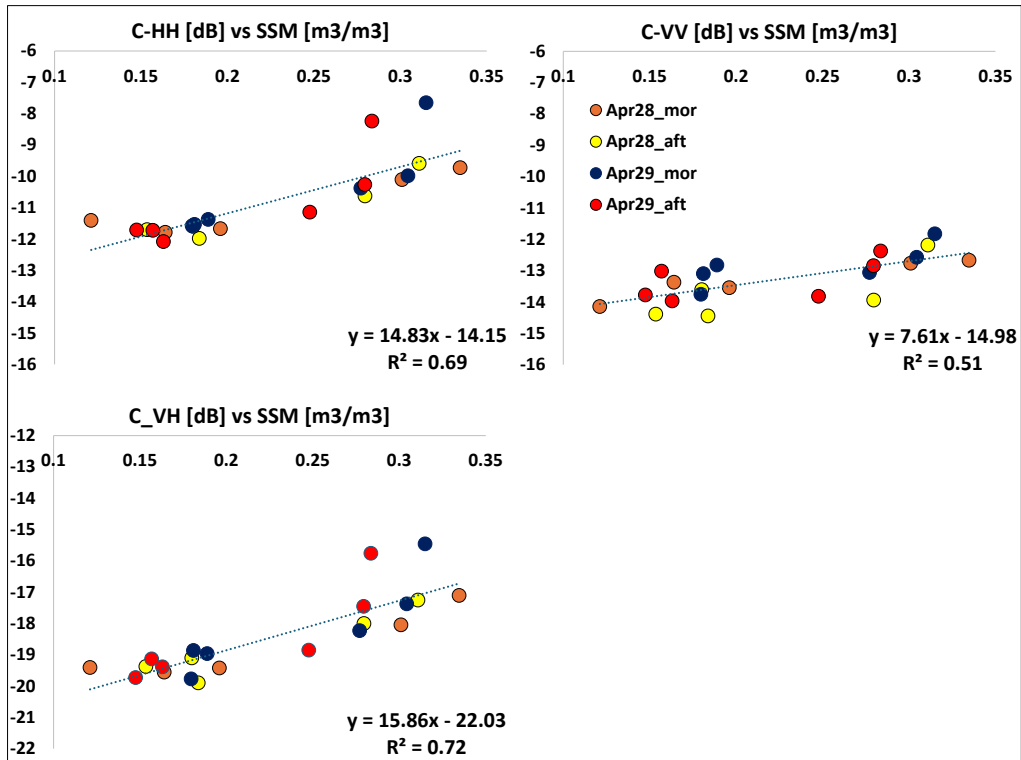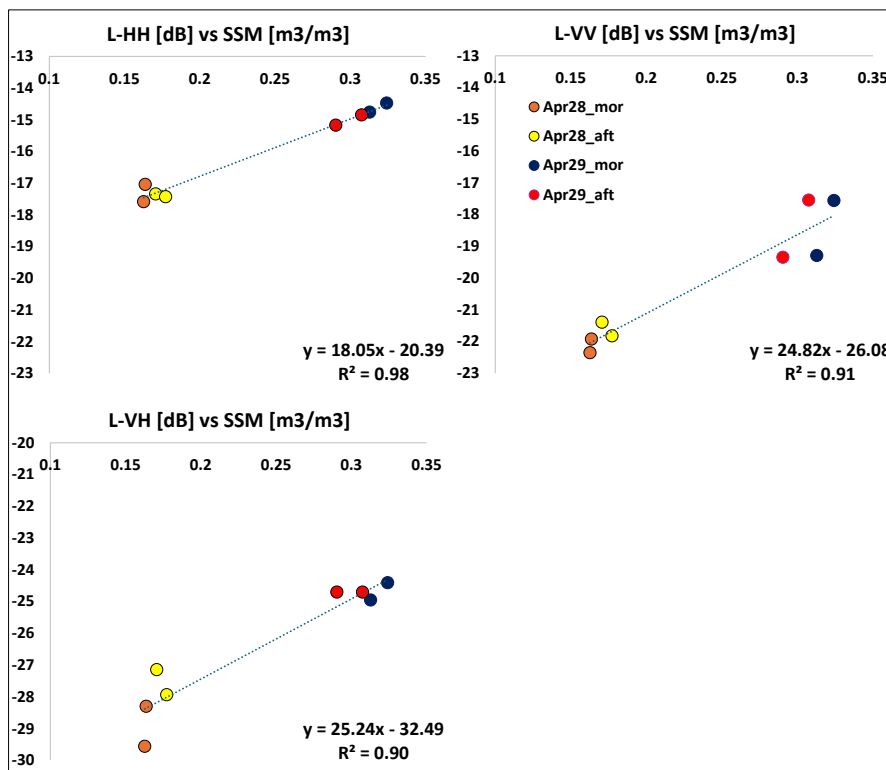

Figure 5-7: Sensitivity of L-band intensity at HH (top left), VV (top right) and VH (bottom left) polarisation to SSM between 47.2° and 49.9° incidence. The linear fit equation and the coefficient of determination are reported

5.2.3 Interpreting the sensitivity to SSM

To better interpret the sensitivity to SSM as shown in Figure 5-5 andFigure 5-4, Figure 5-8 andFigure 5-7, the influence of the wheat canopy on the SAR observations is first examined. Figure 5-9 (top panels) shows an analysis of the radar response of wheat in C- and L-band as a function of angle of incidence. Eight to ten wheat fields distributed over the 'Apulian Tavoliere' experimental site with an area greater than 2ha and imaged at 30°, 40° or 50° mean angle of incidence were identified and their backscatter was averaged. The mean backscatter from the stripmap SAR acquisition on 28 April at 10:03, in particular, is shown in Figure 5-9. The inter-field standard deviation is also shown. Winter wheat is rain-fed in the region, therefore the selected fields had similar soil moisture conditions, which can be quantified, for example, by the level measured by the temporary ground station at CREA stripe 29, which was not irrigated on 28 April, i.e. 0.135m³/m³. In C-band, wheat backscatter at HH and VH decreases by about 2dB from 30° to 50° incidence angle (see Figure 5-9, upper left panel). However, the rate of decrease from 30° to 50° is less than expected over bare ground. For example, the effect predicted by the IEM soil scattering model [27] for a soil surface with an SSM of 0.135m³/m³ and a roughness (vertical height standard deviation) of 0.9cm is approximately 5.5dB at HH pol. Such a reduced decrease indicates an increasingly important role of volume scattering at high angles of incidence, with an associated decrease in sensitivity to SSM, as shown in Figure 5-8, left panel. At VV, double bounce and volume scattering actually cause an increase in backscattering from 30° to 50° (e.g. [28], [29], [30]). Under these circumstances, the sensitivity to SSM below the crop will also decrease. However, until volume scattering dominates, there is still sensitivity to SSM due to the double bounce and attenuated soil contributions [31], as shown in Figure 5-8, right panel.

For comparison, Figure 5-9, lower left panel, shows the C-band backscatter averaged over bare fields. Two fields with an extent of more than 2ha per angle of incidence were selected. It can be seen that HH, VV and VH decrease with increasing angle of incidence, VV is slightly higher than HH (about 1dB at 50°) and at 50° is about 4dB lower than at 30°. For wheat, on the other hand, VV is about 1dB higher at 50° than at 30°.

In L-band (Figure 5-9, upper right panel), the backscattering always decreases with the angle of incidence, as it does for bare soil (Figure 5-9, lower right panel). Vegetation induced attenuation increases more at VV than at HH, as expected for crops with a vertical structure. In fact, HH backscatter decreases by about 3dB from 30° to 50°, while VV decreases by about 4dB. Conversely, VV backscatter is slightly higher than HH backscatter over bare soil, with a higher rate of decrease (about 7dB between VV backscatter at 30° and VV backscatter at 50°). This suggests that at high angles of incidence, volume scattering contributes to the total backscatter also at L-band.

Figure 5-10 corresponds to Figure 5-9, but for the mean coherence. At C-band (Figure 5-10, upper left panel), the coherence at HH polarisation and 30° incidence decreases to about 0.8 after 20 minutes from the first SAR acquisition, probably due to the wind effect on the wheat canopy (wind speed was 9m/s). At the same time, however, coherence decreases strongly from near to far range for all polarisations, and more so for VV than for HH. Conversely, in L-band (Figure 5-10, upper right panel), coherence remains stable at all polarisations and angles of incidence. For bare soil (Figure 5-10, bottom), high coherence (>0.95) is observed at all radar frequencies and polarisations.
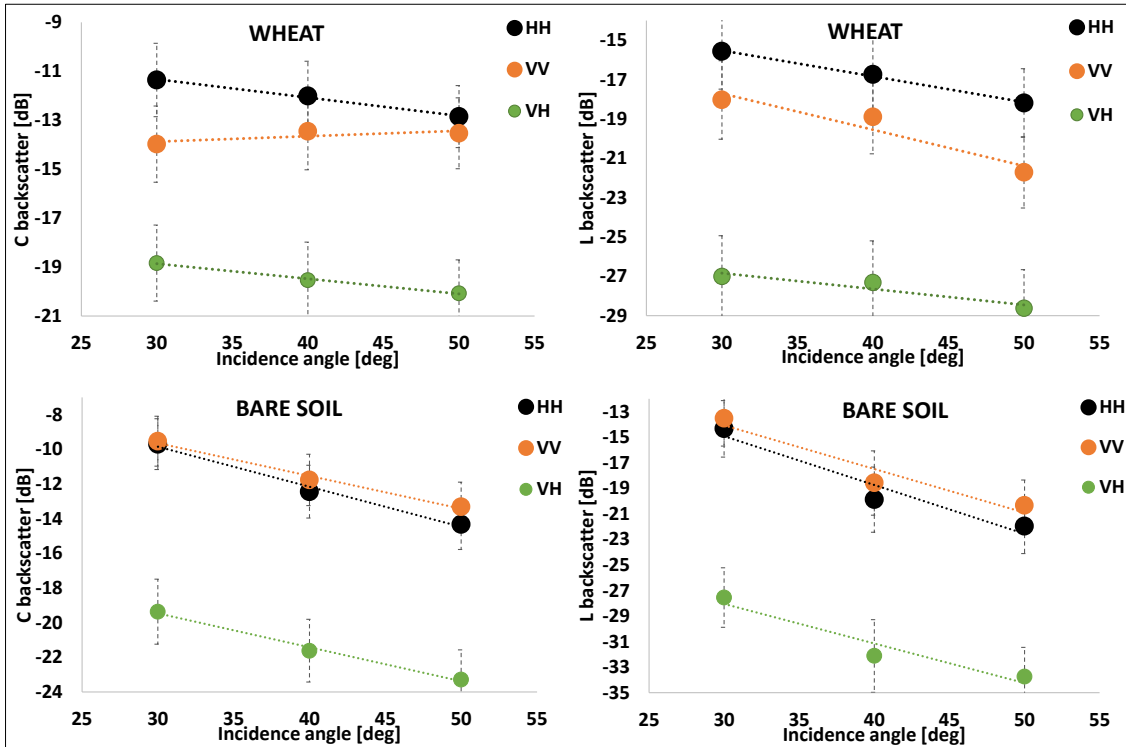
Figure 5-9: C-band (left panels) and L-band (right panels) backscatter averaged over wheat fields (top panel) and bare fields (bottom panel) at HH (black dots), VV (orange dots) and VH (green dots) as a function of the angle of incidence. The error bars correspond to the related standard deviation. The linear fit lines are shown.
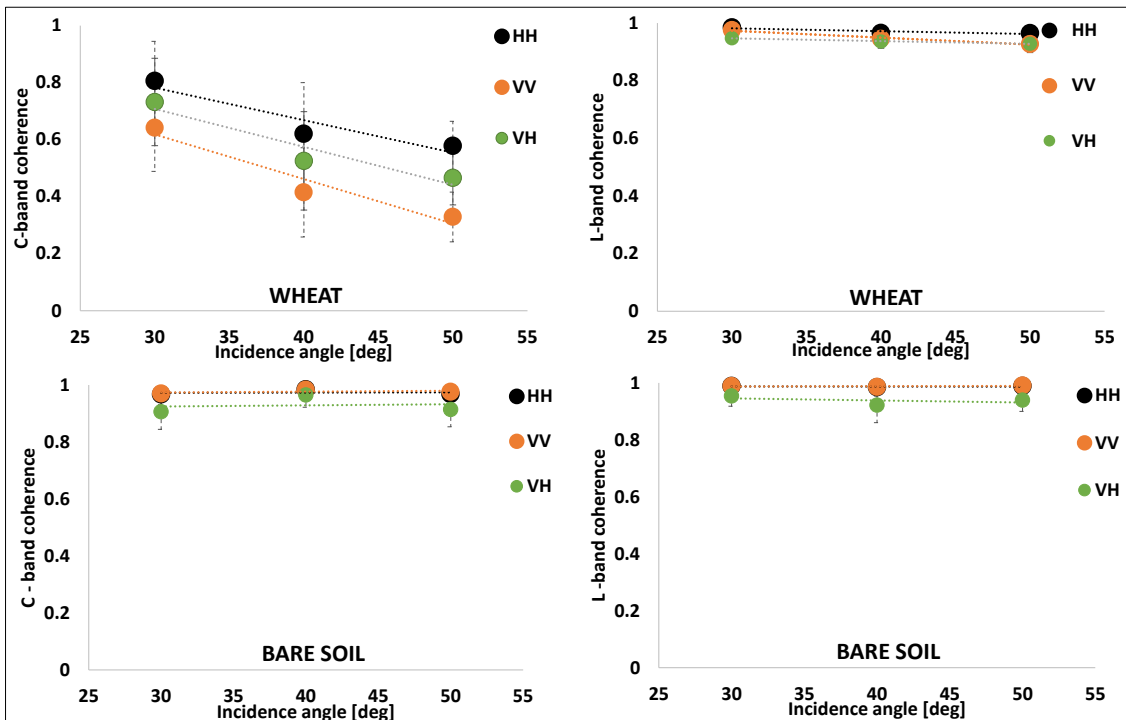
Figure 5-10: C-band (left panel) and L-band (right panel) coherence averaged over wheat fields (top panel) and bare fields (bottom panel) at HH (black dots), VV (orange dots) and VH (green dots) as a function of the incidence angle. The error bars correspond to the related standard deviation. The linear fit lines are shown.

5.3   Sensitivity analysis of L- and C-band intensity to SSM over maize fields

5.3.1   High incidence angle

The sensitivity analysis of C- and L-band intensity to SSM is presented using the stripmap images and gridded SSM measurements collected over the Caione maize fields (CA_MA and CA_MA_4) monitored during the June flights. Figure 5-11 shows the C-HH intensity over CA_MA and CA_MA_4, imaged at 48.1° and 50.3° incidence angles. The CREA maize field at approx. 43° incidence angle is not included in the sensitivity analysis due to the reduced SSM variability measured during the June campaign, e.g. 0.02m³/m³.

CA_MA was divided into three stripes (CA_MA_1, CA_MA_2 and CA_MA_3), all irrigated on 13 and 14 June. Conversely, CA_MA_4 was not irrigated on these days. The maize plants were all at an early stage (i.e. stem elongation phase) and the vegetation water content was homogenous, i.e. 369.3 ± 56.0g/m² on average. The gridded SSM measurement locations are also shown in Figure 5-11. SSM measurements were collected four times during the flights along the stripes. Figure 5-13 shows the box plots of the SSM values per day, morning and afternoon, and per stripe.
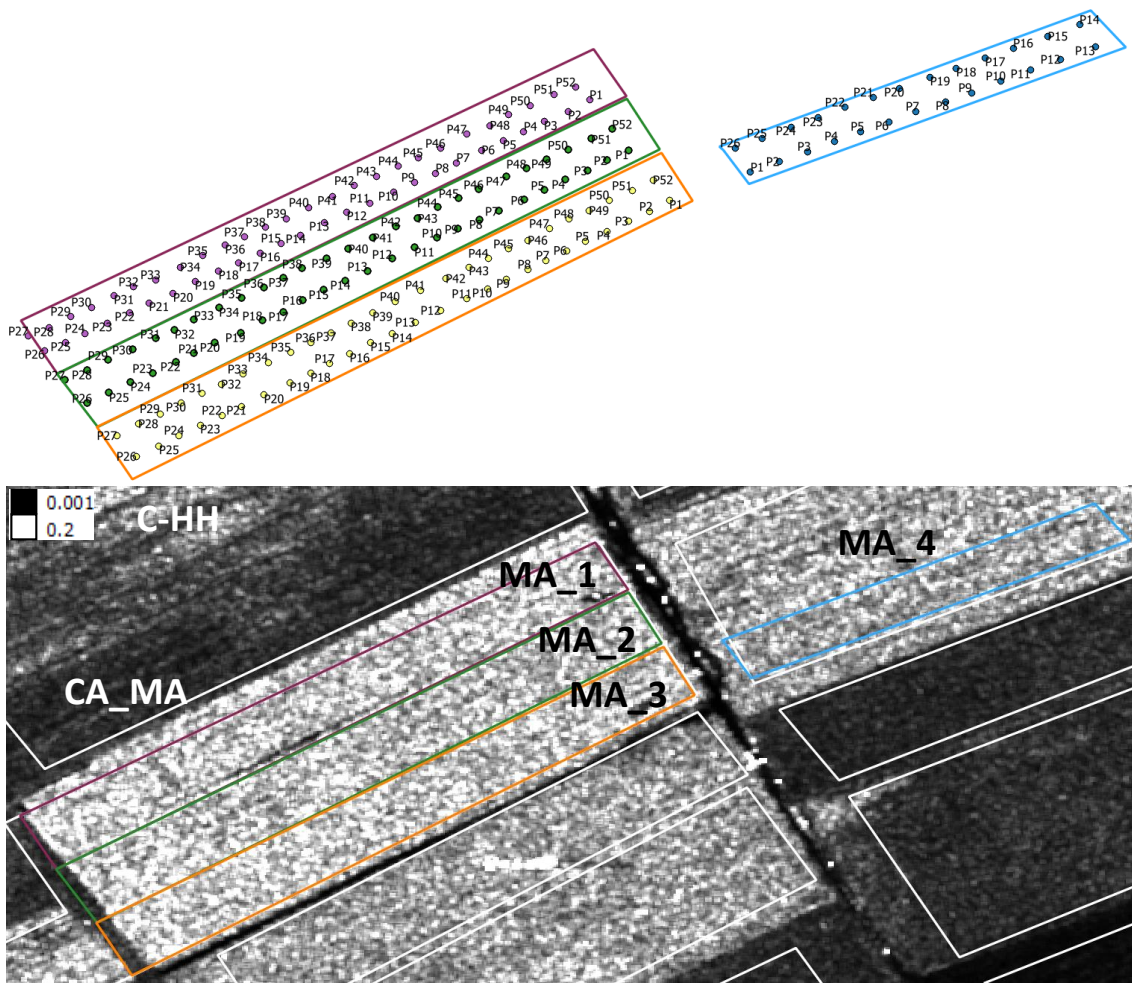
Figure 5-11: Gridded SSM measurement locations are shown (top panel). C-band HH intensity on 16 June at 14:42 of the CA maize fields divided in stripes MA_1, MA_2, MA_3, and MA_4, (bottom panel).
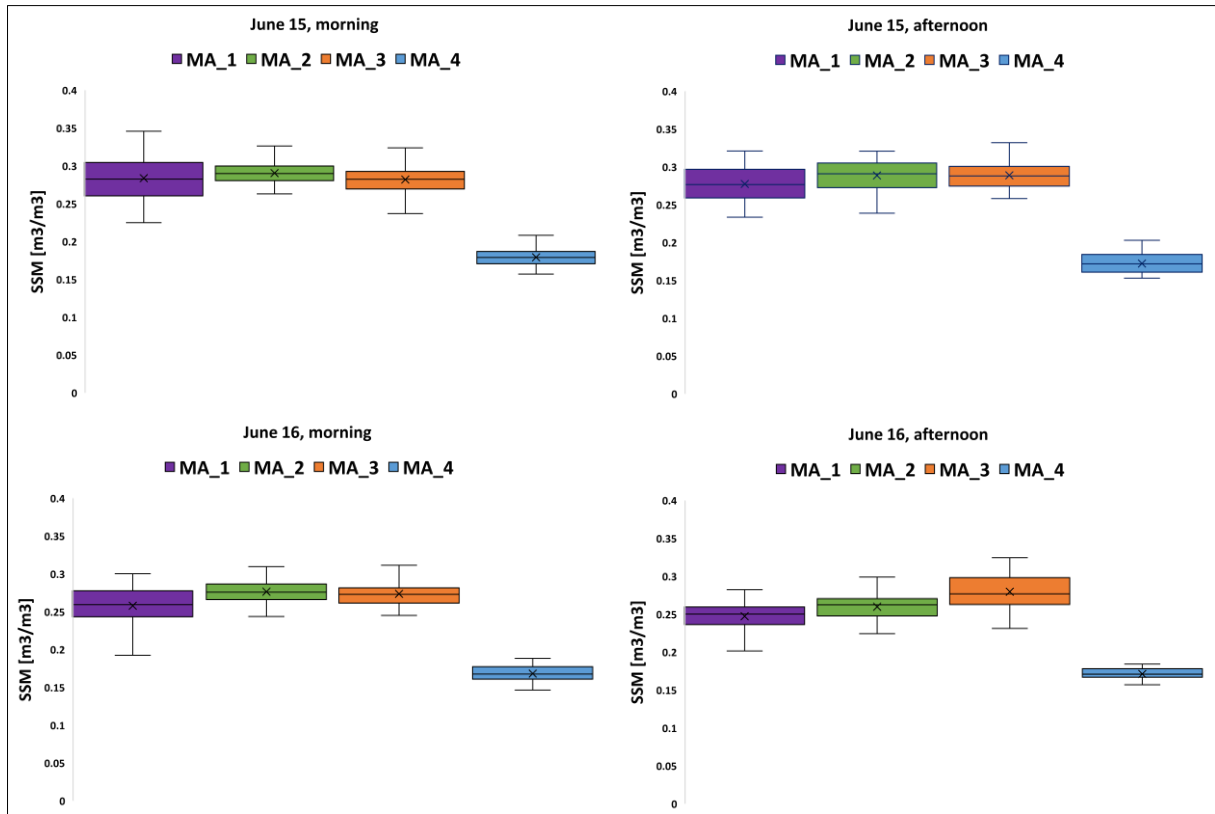
Figure 5-12: Box plots of SSM measurements of the Caione maize stripes per date.
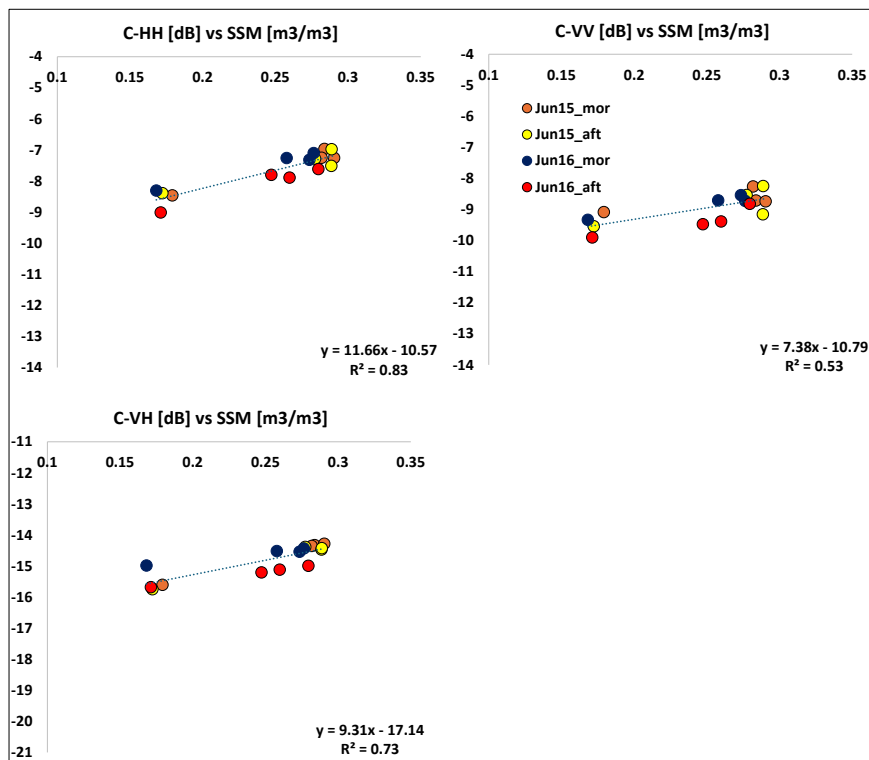
Figure 5-13: Sensitivity of C-band intensity at HH (top left), VV (top right) and VH (bottom left) polarisation to SSM of maize stripes. The linear fit equation and the coefficient of determination are reported
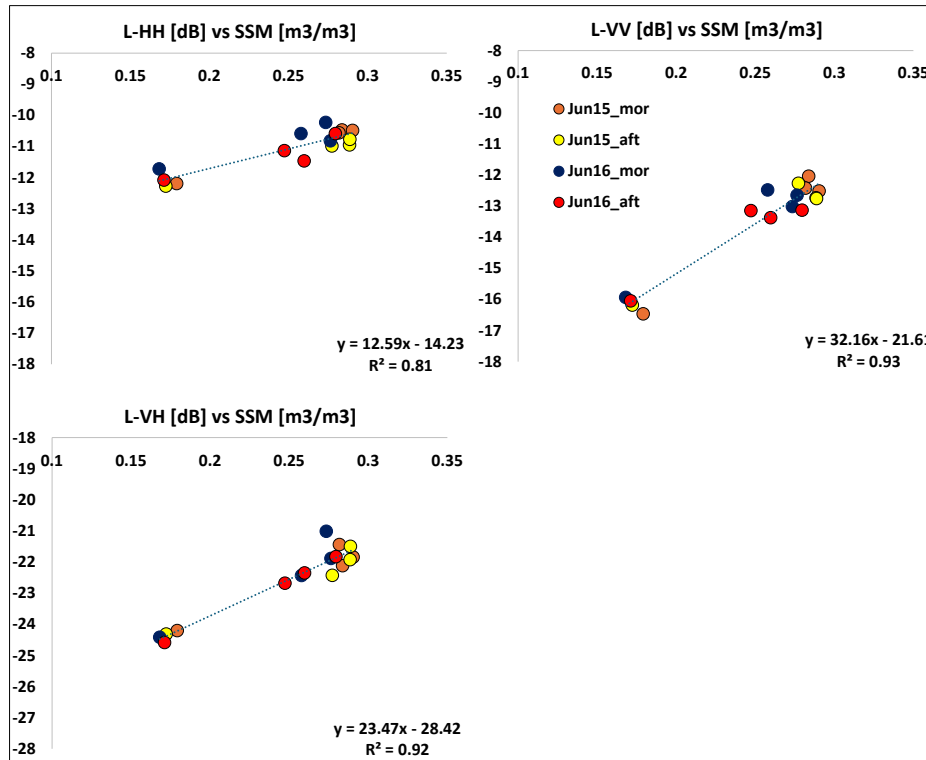
Figure 5-14: Sensitivity of L-band intensity at HH (top left), VV (top right) and VH (bottom left) polarisation to SSM of maize stripes. The linear fit equation and the coefficient of determination are reported.

SAR acquisitions and SSM measurements were matched in time. In C-band, backscatter at all polarisations is significantly correlated with SSM (see Figure 5-13), with higher sensitivity at HH than VV and intermediate sensitivity at VH (i.e. s=11.66 dB/(m³/m³), R=0.91 and s=7.38 dB/(m³/m³), R=0.73 and s=9.31 dB/(m³/m³), R=0.85, respectively). It can be seen that the VV backscatter is attenuated by about 1.3dB on average compared to the HH backscatter. At L-band, VV backscatter sensitivity to SSM (s=32.16 dB/(m³/m³), R=0.97) is higher than HH (s=12.59 dB/(m³/m³), R=0.90), while VH backscatter shows an intermediate sensitivity (s=23.47 dB/(m³/m³), R=0.96), see Figure 5-14.

5.4   Summary of the sensitivity analysis

For wheat crops, the dataset shows that at C-band, the higher the angle of incidence, the greater the vegetation effect on the radar response, which reduces the sensitivity to SSM. However, sensitivity to SSM still holds at high angles of incidence as long as volume contribution does not prevail. The best sensitivity is found at HH polarisation and medium incidence angles, whereas at high angles of incidence no significant differences between polarisations are observed. Sensitivity to SSM is preserved at L-band and 40°-50°, especially at VV. The VH channel shows sensitivity to SSM at both C-band and 40° and L-band and 40°-50°.

For maize crops, in C-band, backscatter is found to be sensitive to SSM, especially at HH, although the fields were imaged at a high angle of incidence. It should be emphasised that this is mainly due to the fact that the crops were at an early stage and therefore the vegetation cover (and biomass) was low. In L-band, VV is very sensitive to SSM. The VH channel also shows sensitivity to SSM, especially at L-band.

5.5 Hyper-temporal SAR acquisitions to monitor sub-daily leaf wetness and soil moisture changes

5.5.1 Irrigation interception

At CREA, stripe 28, a ground station measuring SSM and leaf wetness every 15 minutes was installed. The leaf wetness sensor detects any water on the leaf surface and for how long the canopy is wet, thus providing information about water interception. Between 09:45 and 10:00 the mobile sprinkler passed over the station. The F-SAR passes started at 9:42 and ended at 11:40 in the morning. Figure 5-15 shows a focus area of 30m × 4.5m (blue rectangle) around the station (red dot) located in stripe 28 (red polygon) as imaged by the first four L-VV images on 28 April. The area around the station was completely wet between 9:53 and 10:14.

The time series of C-band (top panel) and L-band (bottom panel) backscatter averaged over the area around the station and acquired during the morning flight of 28 April are shown in Figure 5-16.

While irrigation was ongoing, the presence of leaf wetness was recorded between 09:45 and 10:00, which started to decrease at 10:15 and disappeared after one hour (Figure 5-16, right panel). A delayed increase in SSM was measured between 10:00 and 10:15 from 0.13m³/m³ to 0.31m³/m³, which decreased slightly to 0.286m³/m³ at the end of the morning flight (Figure 5-16, left panel).

All plots suggest that the backscatter behaviour can be divided into two parts.

First, from 9:53 to 10:14 (after the first four SAR acquisitions), the C-band backscatter increased by about 4dB at both HH and VV (Figure 5-16, upper left panel). The initial attenuation difference between VV and HH of approximately 1dB can also be observed. At VH (Figure 5-16, top right panel), the C-band backscatter increased by approximately 5dB (Figure 5-16, top right panel).

This means that until water was present "on" the leaves at 10:15, the total C-band backscatter perceived the water on the leaves as a positive (isotropic) backscatter contribution, which added to a typical (differential) backscatter of wheat plants.

In the second part, as leaf wetness decreased and soil wetness reached a stable value, the VV backscatter became increasingly more attenuated than the HH backscatter (up to 3dB at the last morning F-SAR pass), and thus the HH/VV ratio increased. VH decreased to a stable value of about -17dB.

This temporal behaviour can be explained by the fact that, while the water on the leaves evaporated, the water in the soil was absorbed by the plants causing the rise of differential attenuation between C-VV and -HH (HH/VV). It has been previously observed that the HH/VV radar ratio, particularly around 40° incidence, is a good indicator of canopy biomass due to the strong attenuation of the vertically polarised wave by the vertically oriented wheat stems on both the forward and return propagation paths [30]. Overall, the changes in C-band backscatter between the first and last morning acquisitions are approx. 2.6dB and 1dB at HH and VV, respectively, from dry to wet SSM conditions, as expected from the sensitivity analysis in Figure 5-5. On the other hand, in the same interval, the HH/VV ratio went from about 1dB to 3dB.

At L-band, VV and HH backscatter (Figure 5-16, bottom left panel) increased by up to 7dB and 5dB, respectively, and VH (bottom right panel) by up to 6dB until 10:14. The rapid increase of VV compared to HH suggests that the L-band backscatter was more sensitive to the changing water content in the soil. In the second part, after the SSM jump, all polarisations reached a stable value. VV remained higher than HH by 2dB. The changes in backscatter between the first and the last acquisition in the morning are approx. 3.5dB and 6dB at HH and VV, respectively. This is consistent with the sensitivity analysis in Figure 5-4.
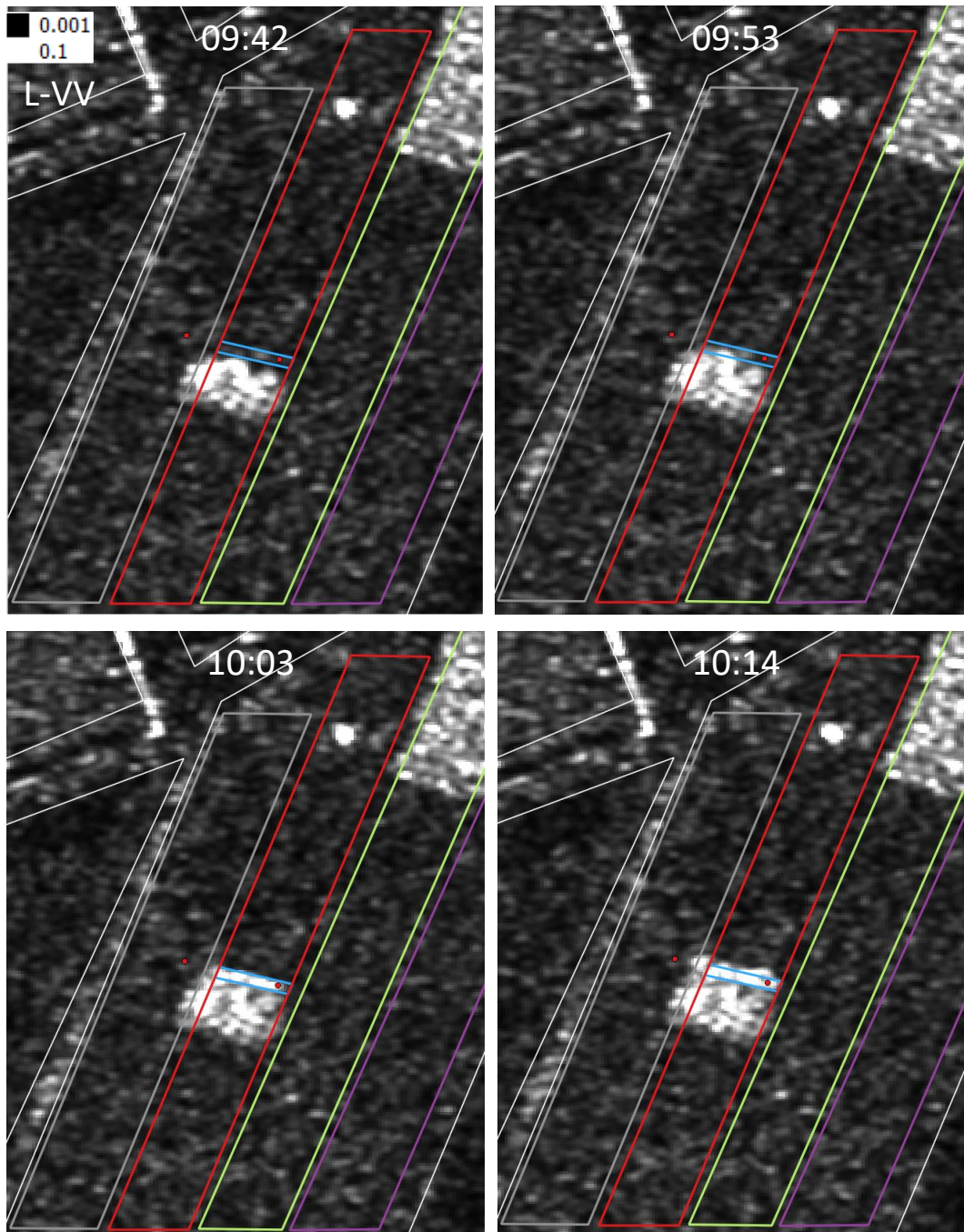
Figure 5-15: L-VV intensity acquired on 28 April at 9:42 (top left), 9:53 (top right), 10:03 (bottom left) and 10:14 (bottom right) over the CREA wheat field. The red dots are the locations of the temporary ground stations at stripes 28 (red polygon) and 29 (grey polygon). The area of interest around the station is indicated by the light blue rectangle.
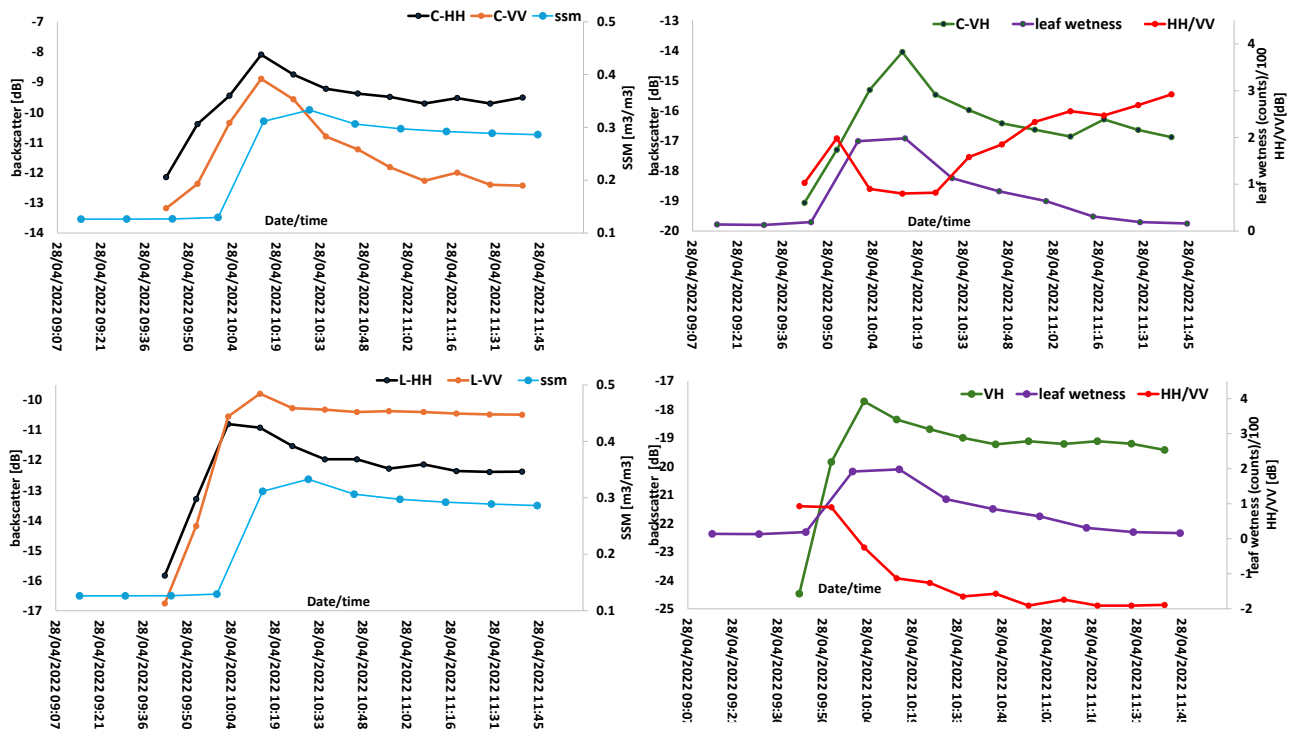
Figure 5-16: C-VV and HH backscatter (left top panel), C-VH backscatter and HH/VV (right top panel), L-VV and HH backscatter (left bottom panel) and L-VH backscatter and HH/VV (right bottom panel) averaged over an area of 30m × 4.5m around the ground station. SSM values (blue line) and leaf wetness counts (purple line) are also shown.

5.5.2 Sub-daily SSM changes in a wheat field at medium angle of incidence

5.5.2.1 Intensity

In this section, the irrigated stripes 28 and 29 of the CREA wheat field are analysed (Figure 5-2, top panel).

Irrigation started at 9:00 and ended at 15:00 on 28 April. On the same day, the F-SAR passes started at 9:42 and finished at 11:40 and started at 14:46 and finished at 16:37. Irrigation on CREA stripe 29 started at 9:00 and ended at 15:00 on 29 April, while F-SAR passes started at 9:50 and ended at 11:43 and started at 14:39 and ended at 15:33. The 00:00:00 (hms) time stamp in the following plots corresponds to 09:42:56 on 28 April, the start time of the F-SAR master acquisition (see Table 5-1).

As a result, the stripmap images showed increasing SSM wetness along the stripes. In both stripes, the ground stations (red dots in Figure 5-15) recorded the increase in SSM due to the overflight of the sprinkler boom at 10:15 on stripe 28 and at 09:15 on stripe 29. The stripes 28 and 29 were completely wet within approx. 5 and 29 hours from the first flight. An example of the temporal behaviour of SSM before and after irrigation, as measured by the station in stripe 28, is shown in Figure 5-16, left panel.

Based on the rate of SSM change measured by the ground stations, the SSM increase and subsequent drying of the irrigated portions along stripes 28 and 29 were simulated and are shown in Figure 5-17,Figure 5-18,Figure 5-19 andFigure 5-20. Figure 5-17 shows the temporal behaviour of C- and L-band backscatter averaged over the irrigated part of stripe 28 during the April F-SAR flights. The scatterplots of C- and L-band backscatter versus SSM are shown in Figure 5-18. Figure 5-19 andFigure 5-20 show the same as Figure 5-17 andFigure 5-18, but for stripe 29.

All figures indicate that the hyper-temporal SAR flights allow tracking of the sub-daily incremental changes in SSM during irrigation. The best sensitivity is observed at C-HH (e.g. s=21.85 dB/(m³/m³),

R=0.99 for stripe 28) and C-VH (e.g. s=20.77 dB/(m³/m³), R=0.99 for stripe 28) and L-VV (e.g. s=34.69 dB/(m³/m³), R=0.96 for stripe 28).
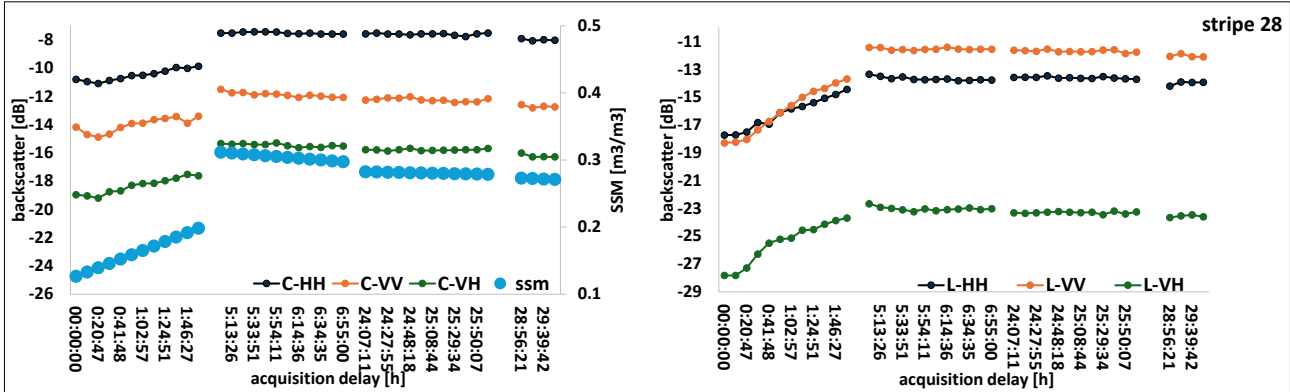
Figure 5-17: Temporal behaviour of C-VV (orange line), HH (black line) and VH (green line) backscatter (left) and L-VV (orange line), HH (black line) and VH (green line) backscatter (right) averaged over the irrigated part of stripe 28. The temporal behaviour of the simulated SSM values (blue line) of the stripe during irrigation is also shown.
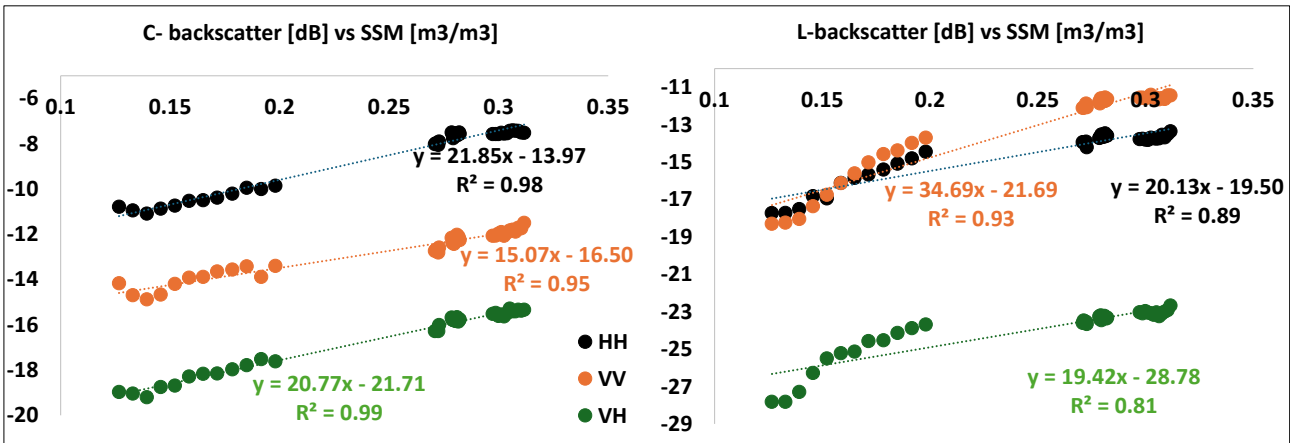
Figure 5-18: Scatterplots of C-backscatter vs. SSM (left) and L-backscatter vs. SSM (right). Linear fit equations and coefficients of determination are given.
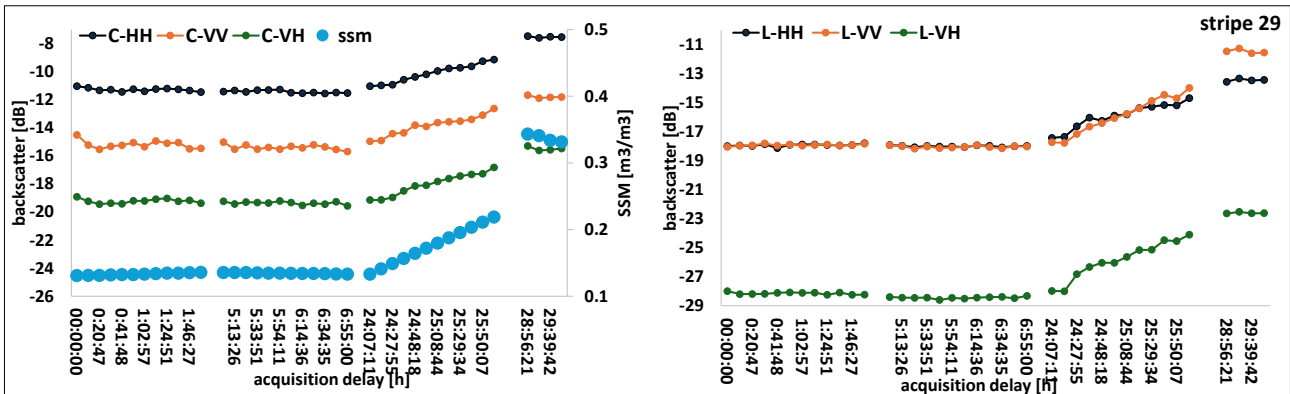
Figure 5-19: Temporal behaviour of C-VV (orange line), HH (black line) and VH (green line) backscatter (left) and L-VV (orange line), HH (black line) and VH (green line) backscatter (right) averaged over the irrigated part of stripe 29. The temporal behaviour of the simulated SSM values (blue line) of the stripe during irrigation is also shown.
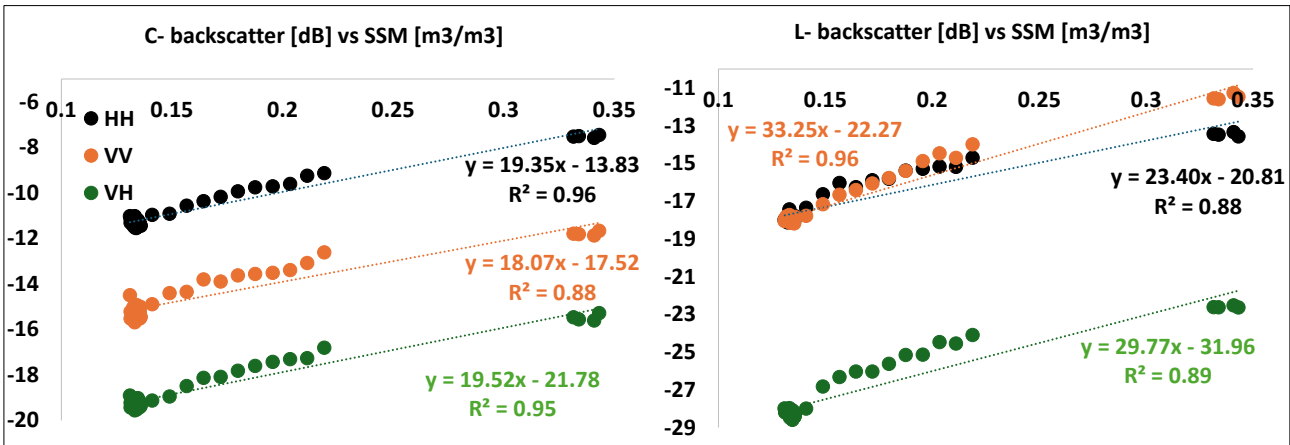
Figure 5-20: Scatterplots of C-backscatter vs. SSM (left) and L-backscatter vs. SSM (right). Linear fit equations and coefficients of determination are given.

5.5.2.2 Backscatter ratios and coherence

Figure 5-21 shows the scatterplots between the backscatter ratio and the SSM ratio over stripes 28 and 29. The backscatter ratio is evaluated between the subsequent SAR observations with respect to the
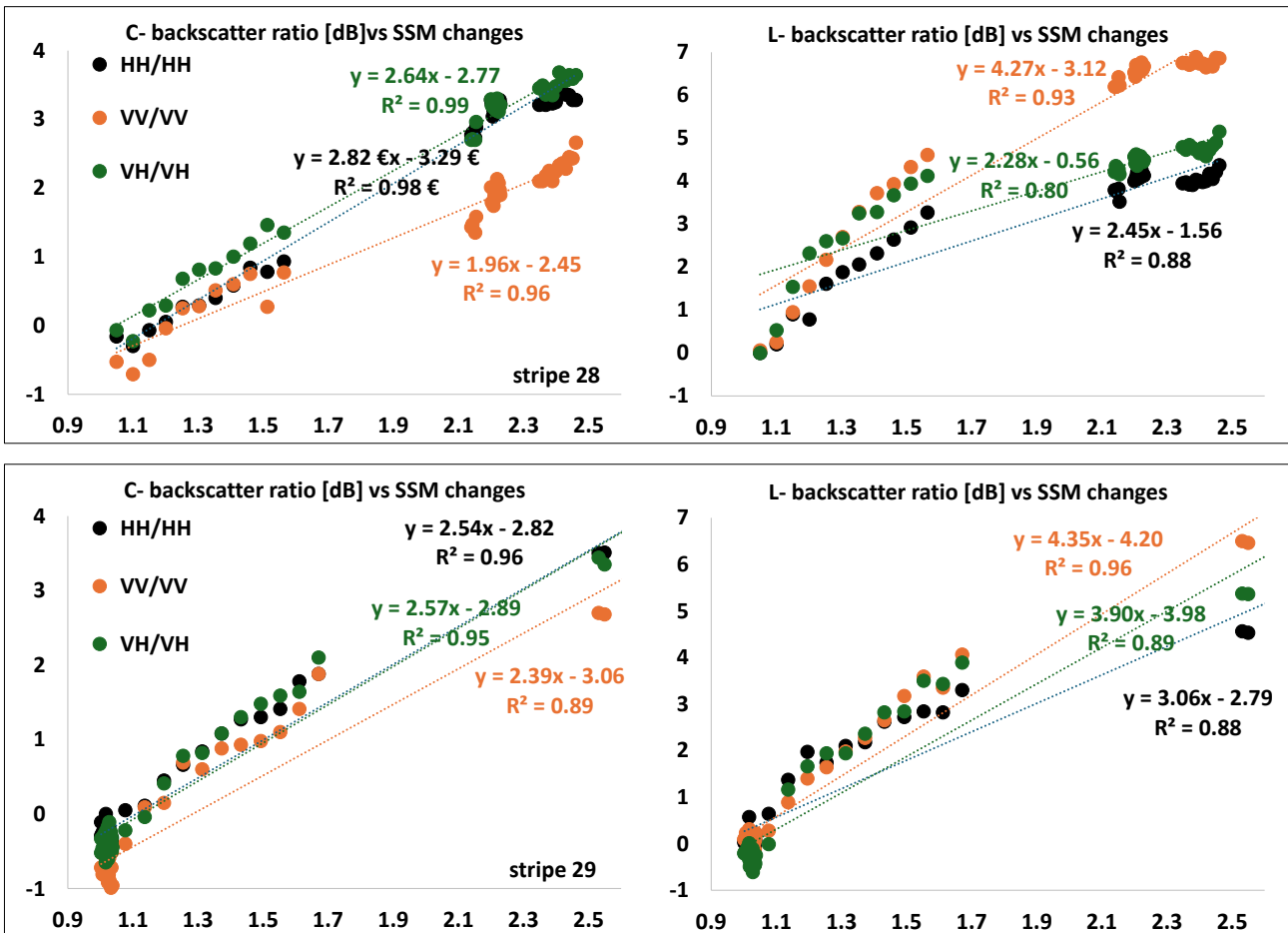
Figure 5-21: Scatterplots of C- (left) and L- (right) backscatter ratio vs. SSM ratio of stripe 28 (top panel) and stripe 29 (bottom panel). Linear fit equations and coefficients of determination are reported.

first SAR observation. For the backscatter, C-HH and C-VH show better sensitivity to SSM changes than C-VV, whereas at L-band, VV shows the highest sensitivity.

Figure 5-22 and Figure 5-23 show the temporal behaviour of C- and L-band coherence (top panel) and their scatterplots with respect to SSM change over stripes 28 and 29, respectively. Coherence was computed with respect to the first F-SAR acquisition pass. While the backscatter ratios increased as the soils became wet, the coherence decreased at all frequencies and polarisations. HH and VH coherence show the best sensitivity to SSM changes at both C- and L-band.

As an example, Figure 5-24 compares the VV coherence and backscatter ratios at C- and L-band. At C-band, the coherence is strongly affected by temporal decorrelation, most likely due to the strong wind present during SAR data acquisition. Therefore, little sensitivity to SSM is shown. In this respect, the backscatter ratio is more robust to changes in vegetation geometry and shows good sensitivity to changes in SSM. Conversely, in L-band, where the effect of temporal decorrelation is low, the coherence tracks changes in SSM due to irrigation well. The L-band backscatter ratio is as well clearly affected by the soil wetness status.
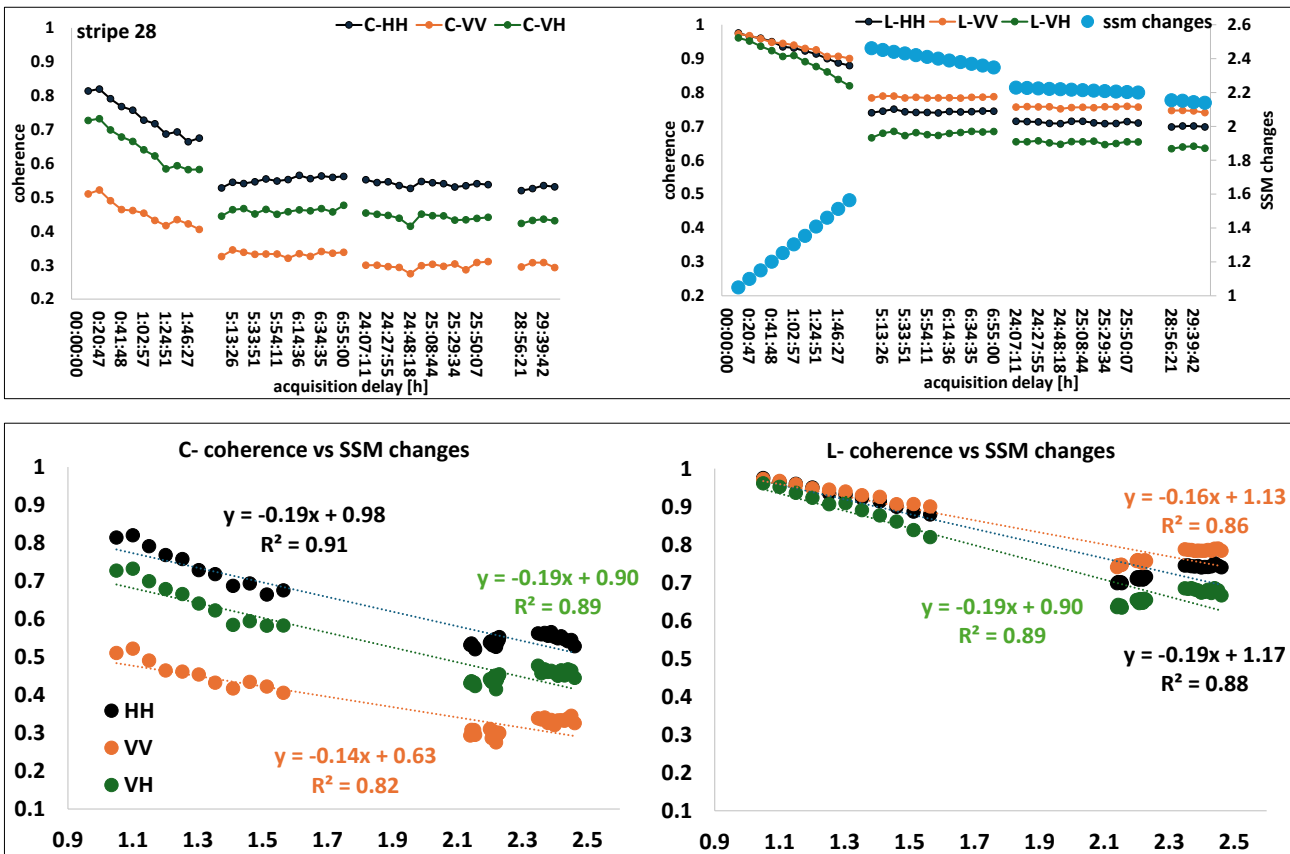
Figure 5-22: Top panel: Temporal behaviour of C-VV (orange line), HH (black line) and VH (green line) coherence (left panel) and L-VV (orange line), HH (black line) and VH (green line) coherence (right panel) averaged over the irrigated part of stripe 28. The temporal behaviour of simulated SSM changes (blue line) while the stripes were irrigated is also shown. Bottom panel: Scatterplots of C-coherence vs. SSM (left) and L-coherence vs. SSM changes. Linear fit equations and coefficients of determination are given.

Figure 5-23: Top panel: Temporal behaviour of C-VV (orange line), HH (black line) and VH (green line) coherence (left panel) and L-VV (orange line), HH (black line) and VH (green line) coherence (right panel) averaged over the irrigated part of stripe 29. The temporal behaviour of simulated SSM changes (blue line) while the stripes were irrigated is also shown. Bottom panel: Scatterplots of C-coherence vs. SSM (left) and L-coherence vs. SSM changes. Linear fit equations and coefficients of determination are given.
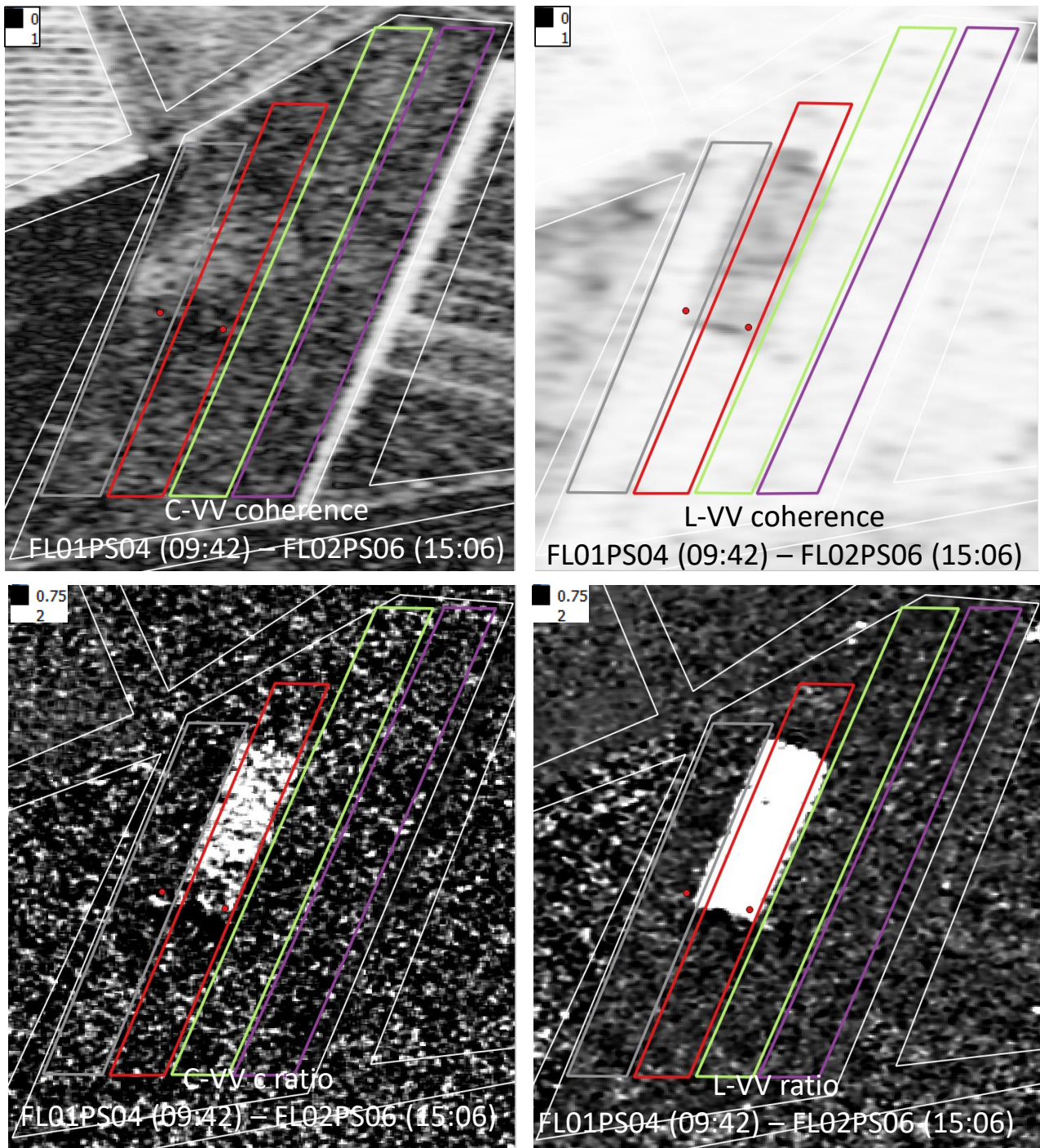
Figure 5-24: C-VV (top, left) and L-VV (top, right) coherence of stripe 28 between the first pass (PS04) on 28 April morning (FL01) and the third pass (PS06) on 28 April afternoon (FL02). Bottom: C-VV and L-VV ratios (red polygon).

5.5.2.3 Optimal polarisation for maximum contrast between wet and dry soils

The polarimetric properties of the radar response have been examined by computing the polarisation that maximises the contrast between irrigated and non-irrigated areas, i.e. the optimal polarimetric matched filter (PMF). For this purpose, the method proposed by Swartz et al. (1988) [32] to optimise the contrast between two different land cover types in the same radar image has been adapted to the temporal domain. The non-irrigated area consists of the strip before irrigation, whereas the irrigated target consists of the area during or after irrigation.

Figure 5-25 compares the temporal behaviour of the backscatter ratios of stripes 28 and 29 with respect to the PMF. It can be seen that during steady soil conditions or transitional phases, co- and cross-polarisations contribute approximately equally to the PMF. Conversely, when the dry-to-wet transition is completed, the optimum contrast SAR feature can be approximated by HH and VH in C-band and by VV in L-band.

Figure 5-25: Temporal behaviour of backscatter ratios in C- (left) and L-band (right), i.e. HH/HH (black line), VV/VV (orange line) and VH/VH (green line) of stripe 28 (top panel) and stripe 29 (bottom panel). The polarimetric matched filter (PMF) is shown in red.

5.5.3 Sub-daily SSM changes in a wheat field at high angle of incidence

5.5.3.1 Intensity

The irrigation of CA01 stripe 28 started at 9:00 on 27 April and ended at 07:00 on 28 April. Therefore, stripe 28 was completely wet during the F-SAR flights. Figure 5-26 shows the temporal behaviour of C- and L-band backscatter. An SSM decrease of 0.03m³/m³ was measured by the ground station between the first and the last F-SAR acquisition. An overall decrease in co- and cross-polarisation backscatter was also observed (1 dB or less).
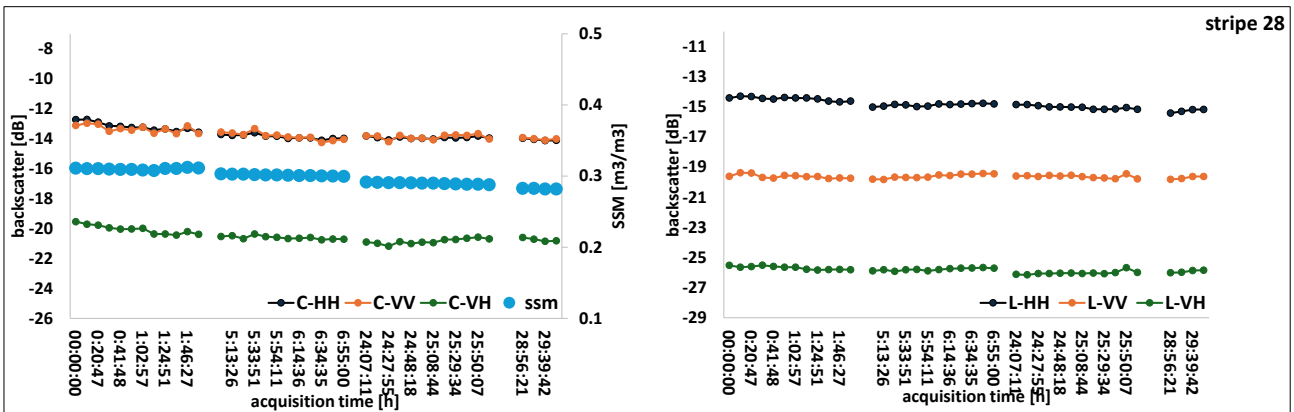
Figure 5-26: Temporal behaviour of C-VV (orange line), HH (black line) and VH (green line) backscatter (left) and L-VV (orange line), HH (black line) and VH (green line) backscatter (right) averaged over the irrigated part of stripe 28. The temporal behaviour of the SSM values (blue line) measured by the ground station located in stripe 28 is also shown.

Conversely, the irrigation of CA01 stripe 29 started on 28 April at 9:00 and ended on 29 April at 07:00. In this case, an increase of backscatter was recorded on 29 April. Figure 5-27 is the same as Figure 5-26, but for stripe 29. No ground station was installed in stripe 29. However, in order to have SSM values to assess the backscatter sensitivity, the SSM measurements collected by portable probes are reported as references in Figure 5-27. On 28 April, stripe 29 was sampled in its dry soil state, while on 29 April the SSM measured at stripe 28 is used as stripe 29 was not sampled. Scatterplots (see Figure 5-28) between backscatter and SSM confirm that at C-band a limited sensitivity is observed (an increase of about 1dB
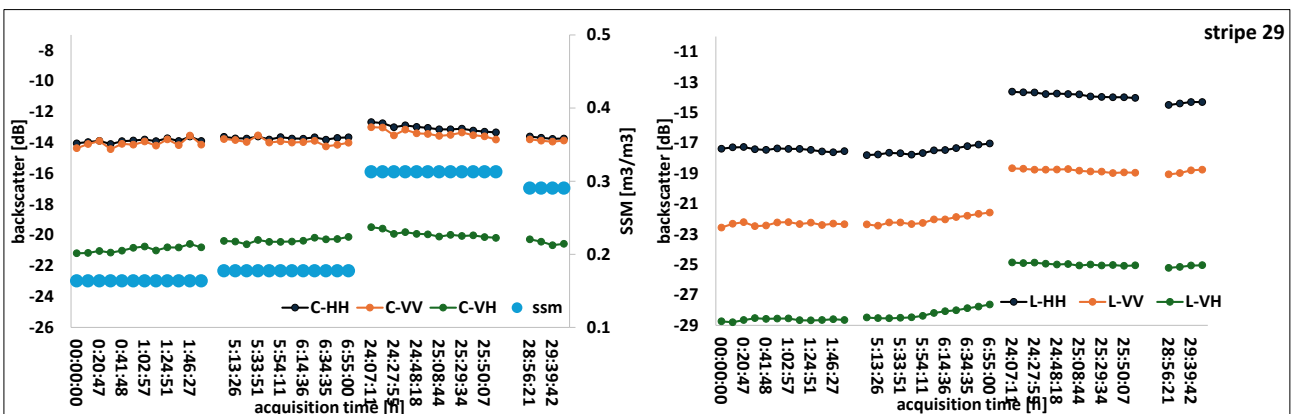
Figure 5-27: Temporal behaviour of C-VV (orange line), HH (black line) and VH (green line) backscatter (left) and L-VV (orange line), HH (black line) and VH (green line) backscatter (right) averaged over the irrigated part of stripe 29. The temporal behaviour of the SSM values (blue line) measured by portable probes is also shown.

from wet to dry soil conditions and a significant correlation between 0.73 and 0.83 are found). At L-band, however, a significant sensitivity to SSM is observed at all polarisations (an increase of about 3dB from wet to dry soil conditions and a correlation of 0.98 are found).
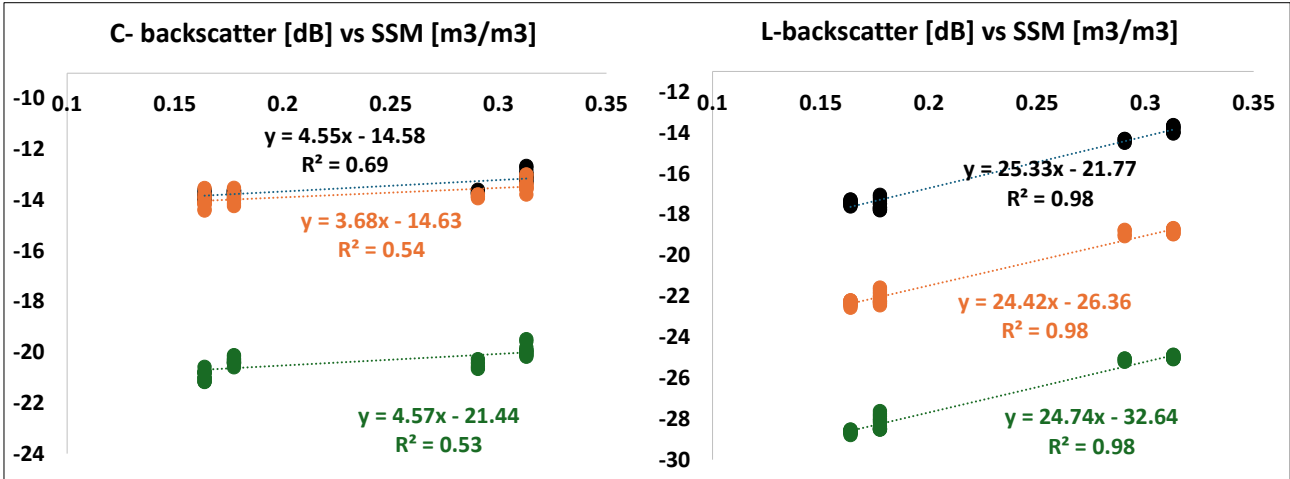
Figure 5-28: Scatterplots of C- (left) and L-band (right) backscatter vs. SSM. HH (black), VV (orange) and VH (green). Linear fit equations and coefficients of determination are reported.

5.5.3.2 Backscatter ratios and coherence

Figure 5-29 shows the scatterplots of the intensity changes with respect to the SSM changes. Only stripe 29 is presented, where the status of soil wetness changes due to irrigation. Comparing Figure 5-29 and Figure 5-21, it can be noted that the sensitivity of backscatter changes to SSM changes is reduced at a higher incidence angle, while it is preserved at L-band.
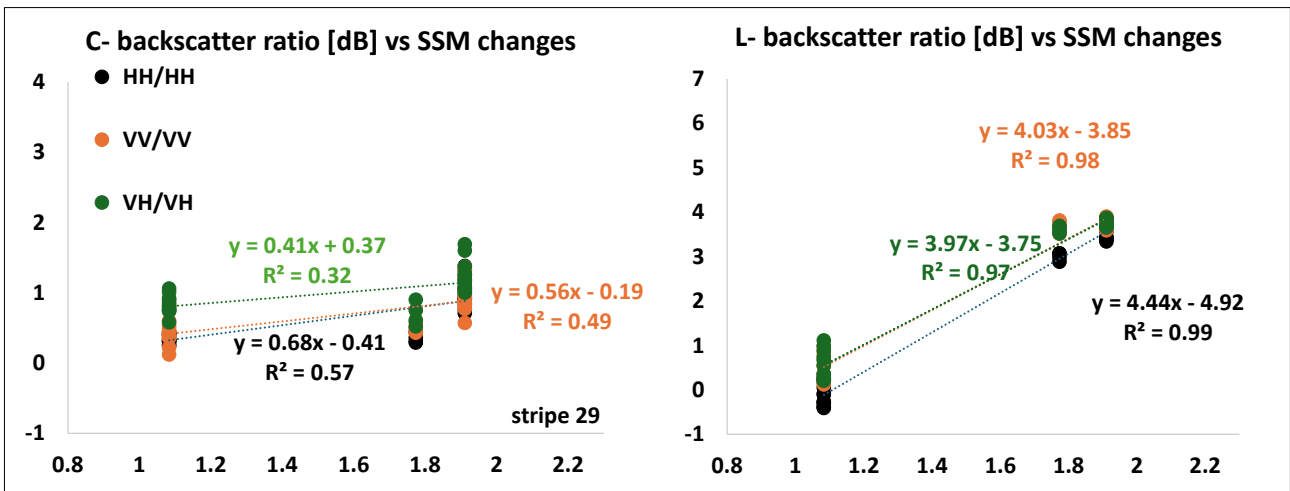
Figure 5-29: Scatterplots of C- (left) and L-band (right) backscatter ratios vs. SSM changes of stripe 29. Linear fit equations and coefficients of determination are given.

In terms of coherence, significant decorrelation is observed for stripe 28, which has experienced limited changes in soil moisture, especially in the morning of 28 April, probably due to the effect of wind on vegetation. Conversely, in L-band the wind effect on the coherence is reduced (Figure 5-30).
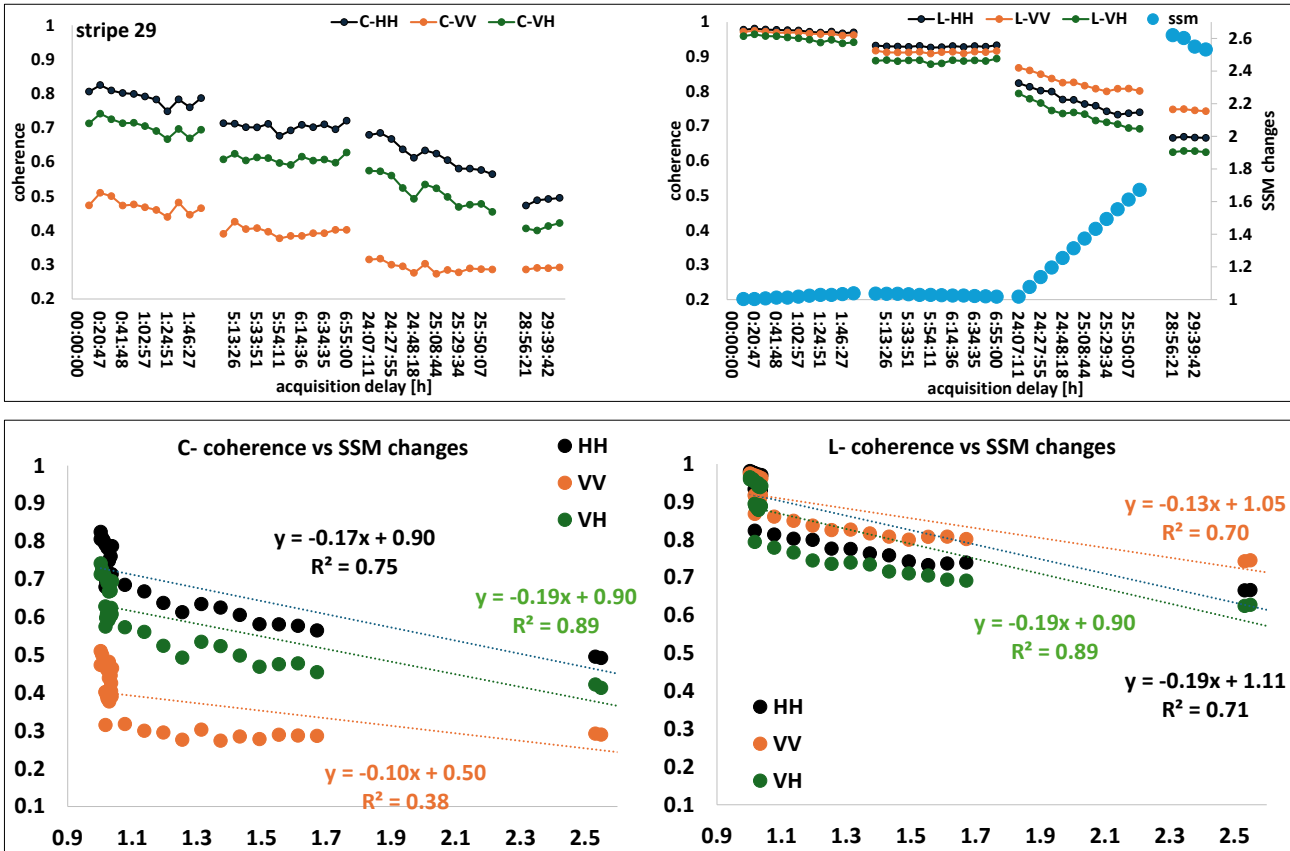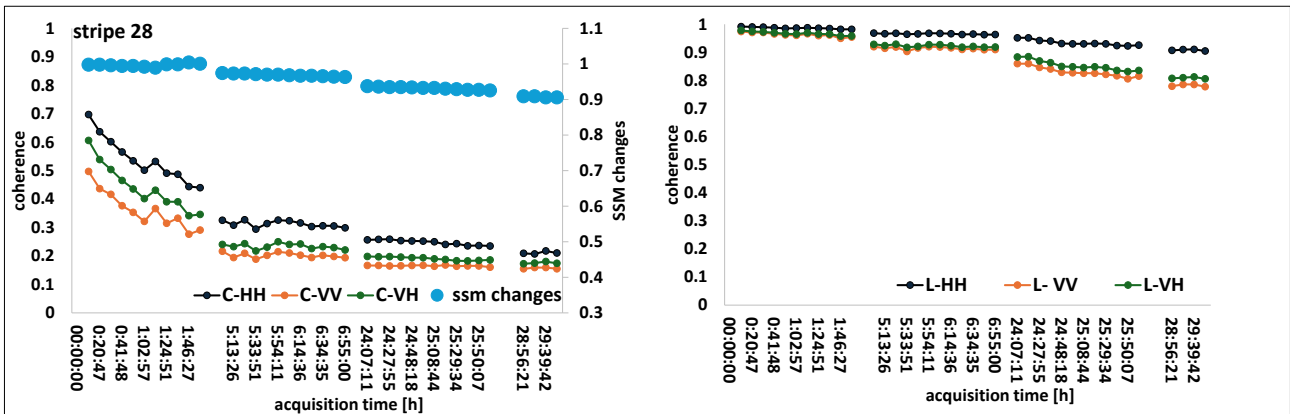
Figure 5-30: Temporal behaviour of C-VV (orange line), HH (black line) and VH (green line) coherence (left panel) and L-VV (orange line), HH (black line) and VH (green line) coherence (right panel) averaged over stripe 28. The temporal behaviour of the SSM changes (blue line) measured by the ground station at stripe 28 is also shown.
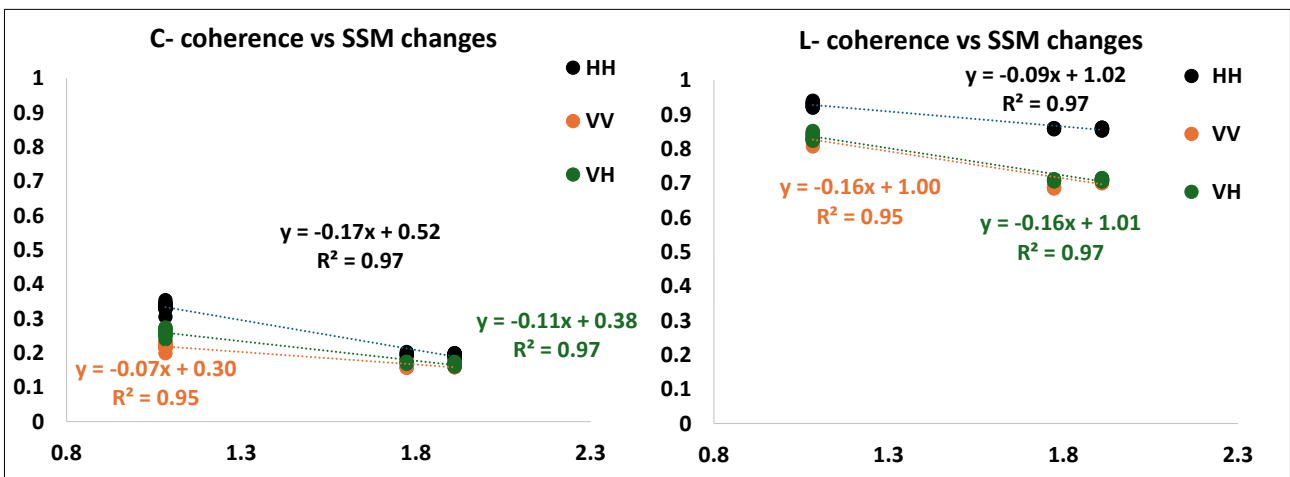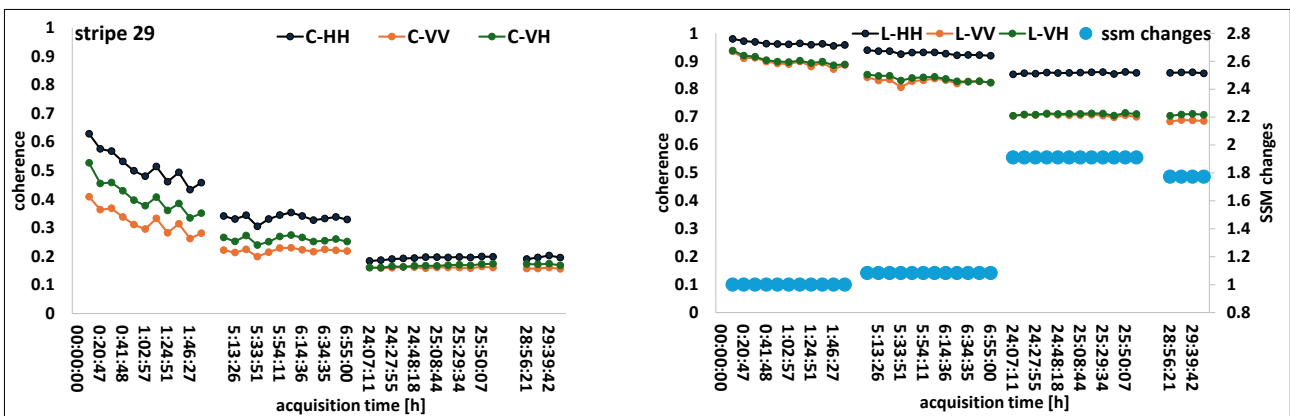
Figure 5-31: Top panel: Temporal behaviour of the C-VV (orange line), HH (black line) and VH (green line) coherence (left panel) and L-VV (orange line), HH (black line) and VH (green line) coherence (right panel) averaged over stripe 29. The temporal behaviour of the SSM changes (blue line) measured by portable probes is also shown. Bottom panel: Scatterplots of C-coherence vs. SSM (left) and L-coherence vs. SSM changes. Linear fit equations and coefficients of determination are given.

For stripe 29, Figure 5-31 (top panel) shows a rapid decrease in C-band coherence on 28 April during the morning and a further decrease around noon, which are not related to changes in the SSM. At the same time, little decorrelation is observed in L-band. After irrigation, a further decrease in coherence can be seen in C-band (more in HH and VH than in VV), while in L-band the decrease is more pronounced in VV and VH polarisation.

The scatterplots shown in Figure 5-31 (bottom panel) do not include the acquisitions in the morning of 28 April because of the rapid decline in the C-band coherence induced by wind.

5.5.3.3   Optimal polarisation for maximum contrast between wet and dry soils

Figure 5-32 shows the temporal behaviour of the backscatter ratios in relation to the PMF for both stripes 28 and 29. At stripe 28, a decrease in the backscatter ratios can be observed as a result of the dry-out process. In contrast, at stripe 29, an increase in the backscatter ratios is evident after 24 hours (i.e. on the morning of 29 April). Both co- and cross-polarisation contribute to the PMF in both C- and L-band.
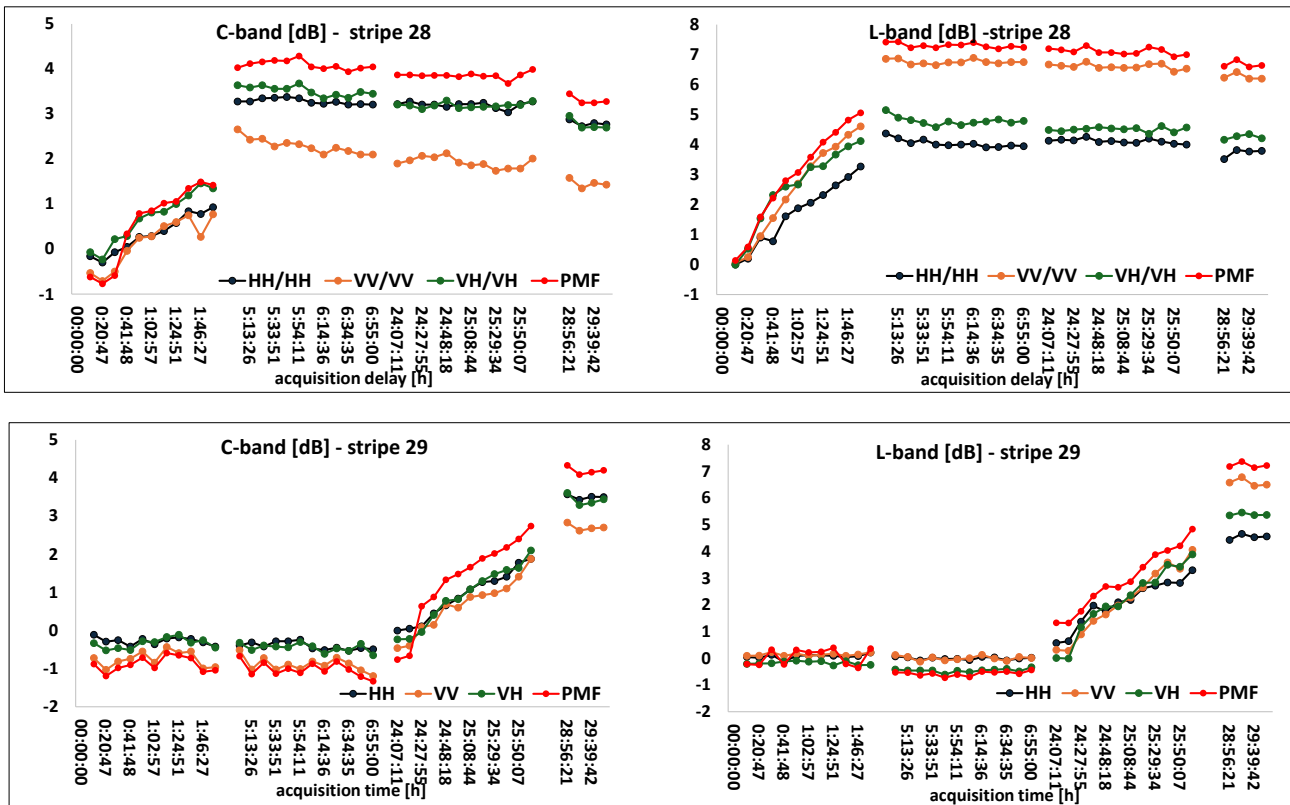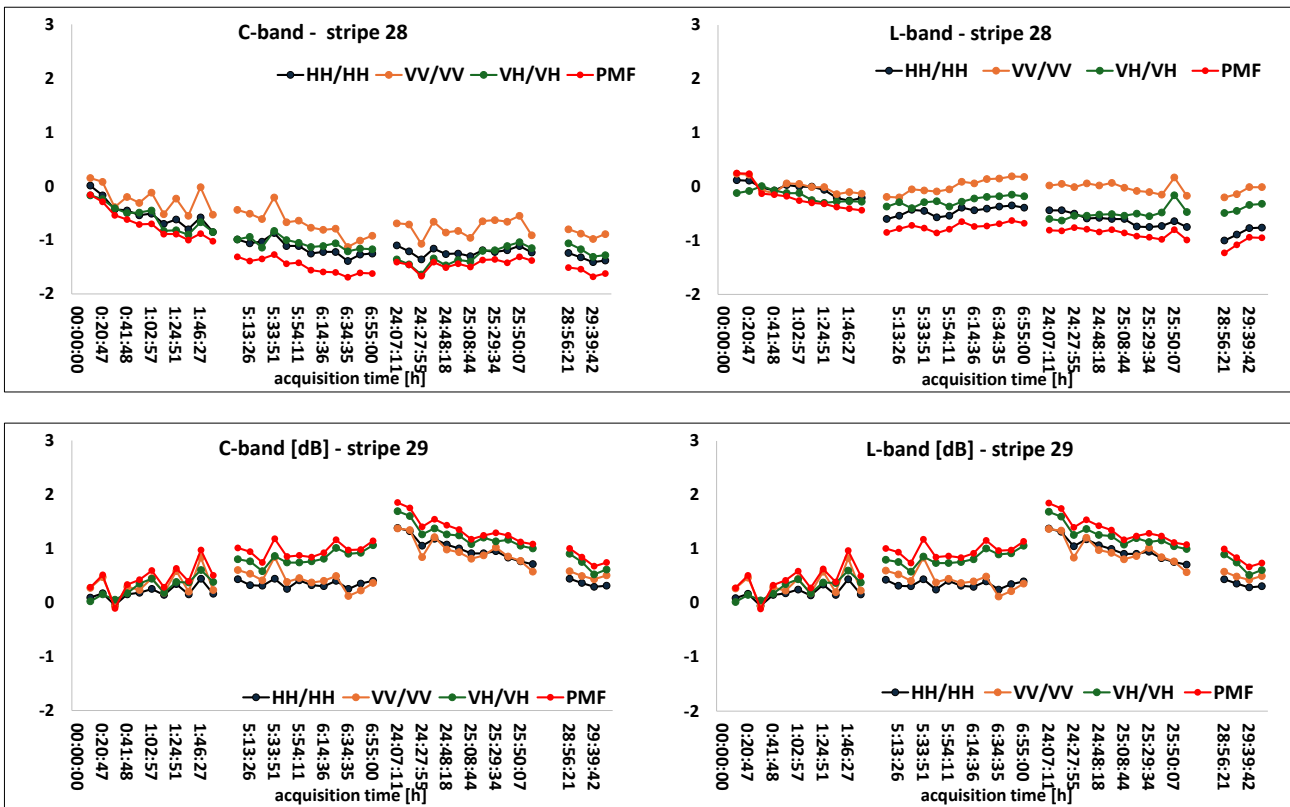

Figure 5-32: Temporal behaviour of C- (left) and L-band (right) backscatter ratios, i.e. HH/HH (black line), VV/VV (orange line) and VH/VH (green line) of stripe 28 (top panel) and stripe 29 (bottom panel). The polarimetric matched filter (PMF) is shown in red.

5.5.4   Sub-daily SSM changes in a bare field

The CREA bare soil field was irrigated on 26 and 27 April. During the April campaign the soil desiccation process was monitored here (see Figure 5-33). Since the backscatter sensitivity to SSM over bare soil is quite well known, the following section focuses on the effects on coherence.
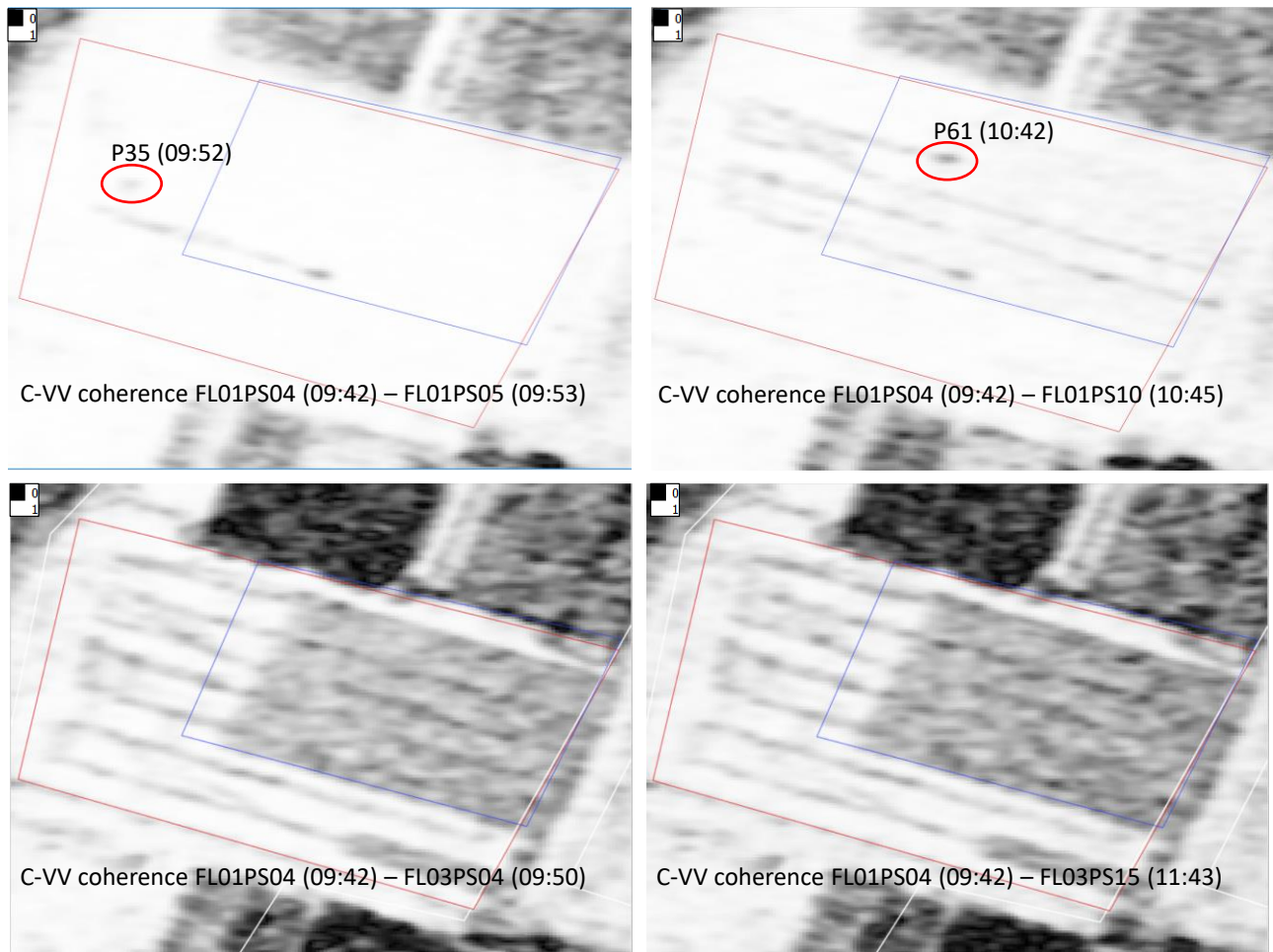
Figure 5-33: C-VV coherence after 10 minutes (top left), after one hour (top right), after 24 hours (bottom left) and after 26 hours (bottom right). FL01 means flights on 28 April morning and FL03 means flights on 29 April morning. The red polygon marks the bare ground and the blue polygon marks the irrigated part. P35 and P61 are the locations of the SSM samples taken at 9:52 and 10:42 on 28 April. Their GPS coordinates are listed in the SARSimHT-NG soil moisture database, see the DAR [A3] for reference. A decorrelation effect along the path tread by the ground team is visible.

5.5.4.1 Coherence

As an example, Figure 5-33 shows the temporal evolution of the C-VV coherence over the bare ground at 10 minutes, one hour, 24 and 26 hours after the first F-SAR acquisition. It is evident that there is a remarkable temporal decorrelation of the irrigated area with respect to the remaining non-irrigated area. It is also interesting to note that C-VV is sensitive to changes in soil roughness. Indeed, the path covered by the ground team during the gridded SSM measurements can be inferred from the temporal decorrelation induced by the roughness change. As an example, the time at which the SSM measurements were taken at locations P35 and P61 is shown.

In Figure 5-34 the scatterplots of C- and L- band coherence versus the SSM changes measured by the ground station are shown. It can be seen that the C-band coherence is more sensitive to SSM drying than the L-band coherence.
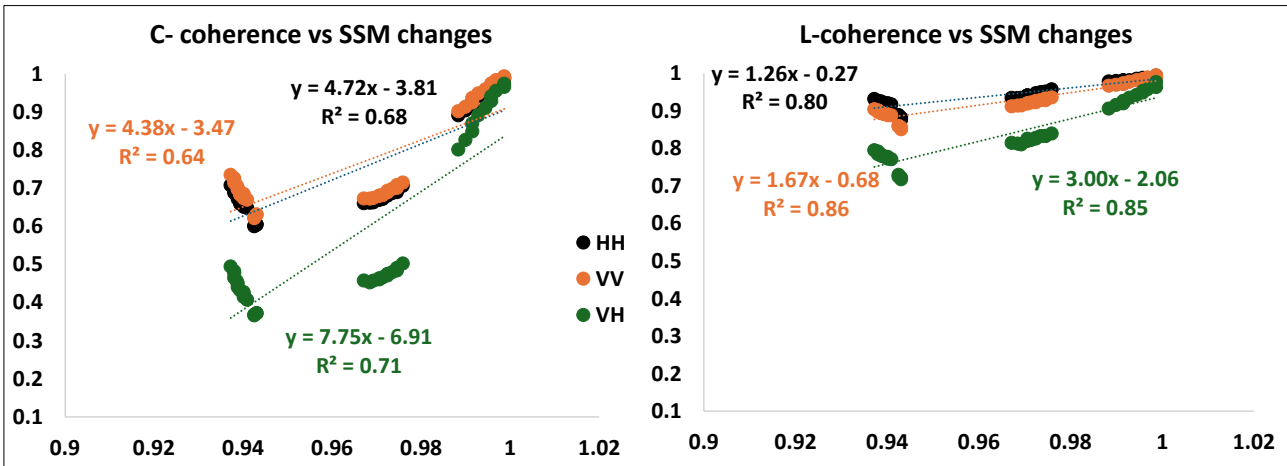
Figure 5-34: Scatterplots of C-coherence vs. SSM changes (left) and L-coherence vs. SSM changes (right). Linear fit equations and coefficients of determination are given.

5.6 Summary of fast surface process monitoring

The surface processes caused by irrigation, such as the interception of water by vegetation and the increase in soil moisture, take place on a time scale of tens of minutes or hours. The hyper-temporal F-SAR observations make it possible to record leaf wetness and changes in soil moisture with a fine temporal resolution. The presence of water on the leaves influences the radar response by making a positive contribution that transiently affects all polarisations in the C-band. The L-band backscatter is more sensitive to the SSM changes in the soil.

At medium angles of incidence, both C- and L-bands are sensitive to SSM changes during irrigation of wheat crops, especially for C-HH and L-VV. Cross-polarised backscatter, both in the C- and L-band, reacts to the increasing wetness in the soil as well. The C-band coherence is more sensitive to changes in vegetation than to changes in SSM, while the backscatter ratio retains its dependence on SSM. Conversely, L-band coherence can track SSM changes due to irrigation under vegetation. The polarimetric SAR configuration that comes closest to the optimal contrast between irrigated and non-irrigated areas is C-HH, C-VH and L-VV.

At high angles of incidence, the ability of C-band to monitor SSM changes over vegetated fields is reduced. L-band, on the other hand, is less affected by vegetation.

For bare soil, C-band coherence is affected by SSM as well as by changes in soil roughness.

5.7 SSM retrieval

5.7.1 Sub-daily SSM from C-band SAR time series

Examples of SSM retrieval using the sub-daily C-band SAR time series are presented in this section. A short-term change detection (STCD) approach has been adopted [33]. Its rationale is summarised below.

The main concept underlying the STCD approach is that SSM changes occur on relatively short time scales (e.g. a few days), whereas the other surface parameters affecting radar backscatter (e.g. soil roughness, canopy structure and vegetation biomass) are usually characterized by significantly longer time scales (e.g. some weeks). As a result, dense SAR time series are expected to track changes in SSM only, since other parameters affecting radar backscatter can be considered constant. SMOSAR ("Soil MOisture retrieval from multi-temporal SAR data" [33]) is the software implementing the STCD algorithm. The main physical approximations implemented in SMOSAR are:

- First, STCD applies to bare or vegetated soils dominated by attenuated surface scattering over which an adequate sensitivity to SSM is observed. In other words, surfaces dominated by volume scattering with little or no sensitivity to soil moisture (SM) are masked using the approach developed by [34].

- Second, SMOSAR exploits the approximation that the backscatter ratio between two successive SAR acquisitions (or data) depends only on the ratio between the surface reflection coefficients, $\alpha_{PP}(\varepsilon, \vartheta)$, of the two acquisitions (or data), which can be mathematically expressed as:

$$\frac{\sigma_{i+1}^0}{\sigma_i^0} \approx \left|\frac{\alpha_{PP}^{i+1}(\varepsilon, \vartheta)}{\alpha_{PP}^i(\varepsilon, \vartheta)}\right|^2 \approx \frac{SSM^{i+1}}{SSM^i} \, , \tag{5-1}$$

where i identifies the index in a time series, ε is the relative dielectric constant of the soil, ϑ the incidence angle, *PP* the polarisation.

For VV polarisation, $\alpha_{PP}(\varepsilon, \vartheta)$ is

$$|\alpha_{VV}(\varepsilon, \vartheta)| = \left|\frac{(\varepsilon-1)(sin^2\vartheta - \varepsilon(1+sin^2\vartheta))}{\left(\varepsilon\cos\vartheta + \sqrt{\varepsilon - sin^2\vartheta}\right)^2}\right| \, . \tag{5-2}$$

For each acquisition (or datum), the quantitative retrieval of $\alpha_{PP}(\varepsilon, \vartheta)$ and then SSM is based on equation (5-1). More precisely, $\alpha_{PP}(\varepsilon, \vartheta)$ is the solution of a stochastic underdetermined linear system whose maximum likelihood solution $(\vec{\alpha}_{PP}^*)$ can be expressed, according to [35], as:

$$\vec{\alpha}_{PP}^* = \alpha_{min} \cdot max\left(\frac{1}{\hat{S}_{iN}}\right) \cdot [\hat{S}_{1N}, \hat{S}_{2N}, \dots \hat{S}_{NN}], \ i = 1, \dots, N \tag{5-3}$$

where N is the number of images in the SAR time series $\hat{S}_{iN} = \sqrt{(\sigma_0)_{doy(i)}/(\sigma_0)_{doy(N)}}$, and α_{min} is an estimate of the minimum reflection coefficient among the N SAR images. An estimate can be obtained at low resolution (e.g. ~40km) using additional information such as SSM operational products (e.g. from SMOS, SMAP, ASCAT, etc.) (e.g. [36]), or by using a calibration curve expressing SAR observations versus SSM values at low resolution [33], or by using the measured soil moisture, which is the option chosen in this study.

Two study cases are discussed: i) Stripe 28 of the CREA wheat field imaged at 40° incidence and ii) stripe 29 of the CA01 wheat field imaged at 50° incidence. In particular, the C-VV F-SAR observations are used.

Two aspects are evaluated: i) The effect of temporal frequency on the monitoring of sub-daily SSM changes and ii) the effect of the increased angle of incidence on SSM retrieval.

Figure 5-35, on the left, shows the comparison of the time series of SSM observed over stripe 28 of CREA wheat and the SSM retrieved from the hyper-temporal F-SAR time series. The minimum value of the observed SSM was used to calculate α_{min}. The SSM time series was obtained by inverting eq. (5-2), where the $\alpha_{PP}(\varepsilon, \vartheta)$ time series was retrieved by eq. (5-3). The true SSM time series is well reproduced with a slight underestimation after the jump due to the irrigation. An RMSE of 0.039m³/m³ and a correlation of R=0.97 are obtained. For comparison, the SSM values retrieved from four F-SAR acquisitions (mean temporal revisit of 14 hours, i.e. the first SAR acquisition per flight), are shown. It can be seen that subsampling the SAR observations reduces the capability to monitor rapid changes in the SSM, i.e. the RMSE increases to 0.07m³/m³. In particular, the SSM time series after the SSM jump is further underestimated.

Figure 5-35, on the right, shows the comparison of the time series of SSM observed over stripe 29 of CA01 wheat and the SSM retrieved from the hyper-temporal F-SAR time series. The increasing influence of vegetation on the radar response, as already observed in Section 5.5.3, results in a deterioration of the retrieval metrics, i.e. RMSE is 0.07m³/m³ and R is 0.73. In particular, the wetness conditions are underestimated.
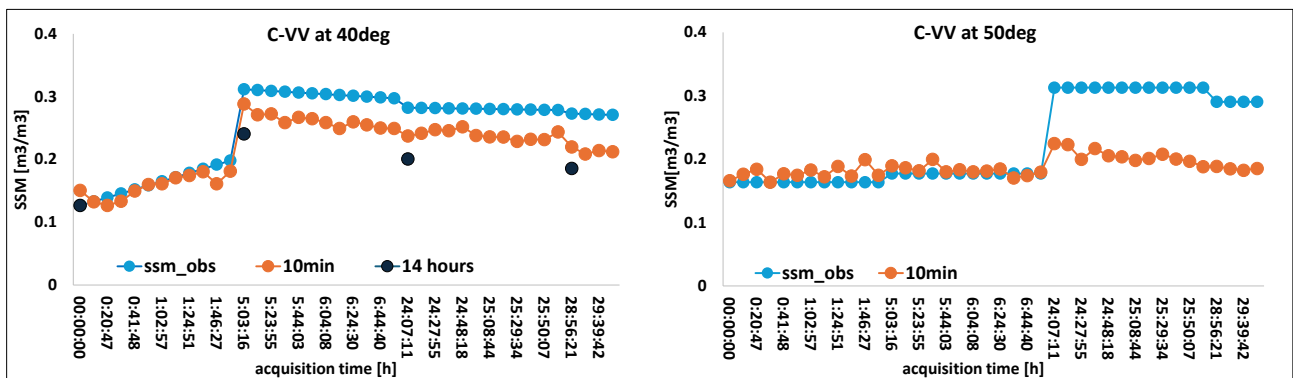
Figure 5-35: Comparison of the observed SSM time series (blue dots) of CREA wheat imaged at 40° incidence (left) and CA01 wheat field imaged at 50° incidence (right) with the SSM retrieved from F-SAR observations acquired every 10 minutes (orange dots) and from four F-SAR images acquired at an average time interval of 14 hours.

5.7.2 SSM from GEO and simulated Hydroterra products

Figure 5-36 compares the GEO F-SAR images and the simulated Hydroterra images over the monitored CREA wheat field. The images correspond to observations on 28 April morning (FL01-PS04), 28 April afternoon (FL02-PS04) and 29 April morning (FL03-PS04). The high spatial resolution GEO F-SAR images show SSM changes in stripe 28 (red polygon) and stripe 29 (grey polygon) due to irrigation (top row). Conversely, the reduced spatial resolution of the Hydroterra images (bottom row) prevents the correct separation of irrigated and non-irrigated areas.

Examples of sub-daily C-band SSM maps have been derived using the SMOSAR code according to eq. (5-1) and are shown in Figure 5-37. The SSM variations of the irrigated parts of stripes 28 and 29 can be seen in the SSM maps derived from the GEO F-SAR images (top row). Conversely, the SSM spatial patterns are not reproduced by the Hydroterra imagery (bottom row).
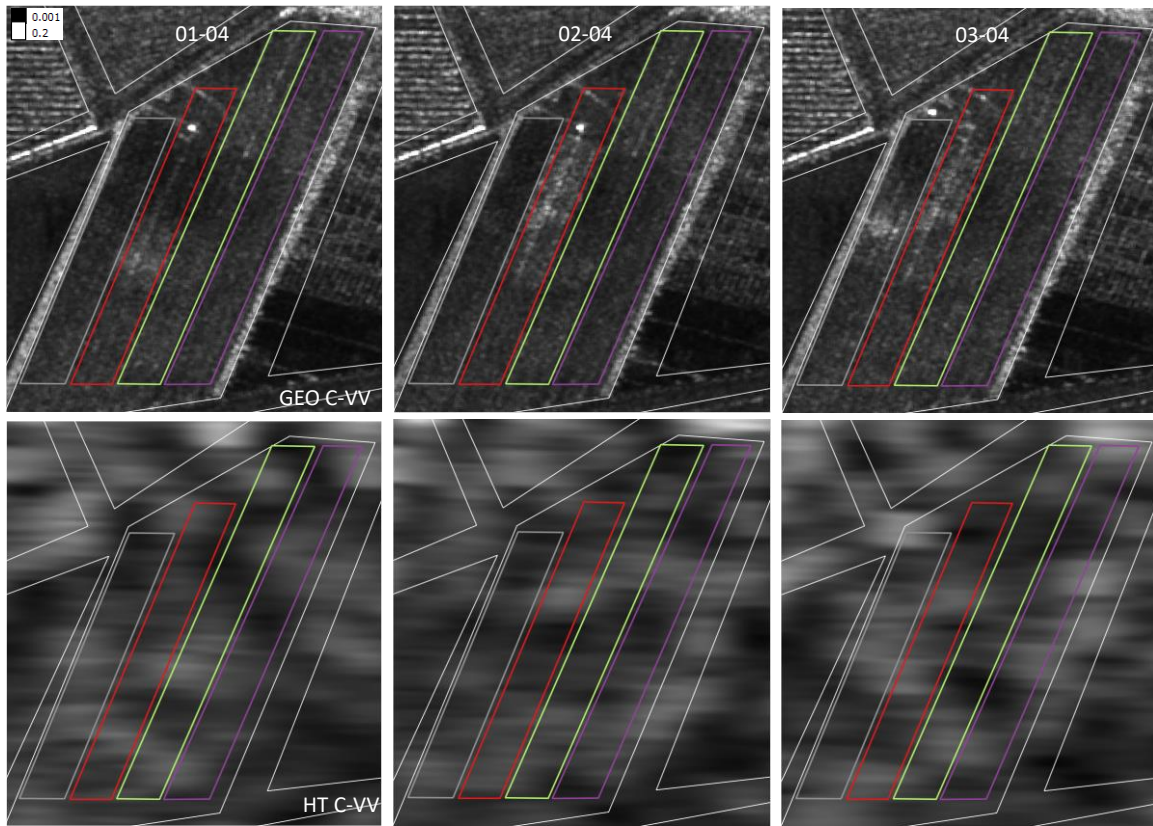
Figure 5-36: CREA wheat stripes imaged by the GEO F-SAR images (top panels) and the simulated Hydroterra images (bottom panels).
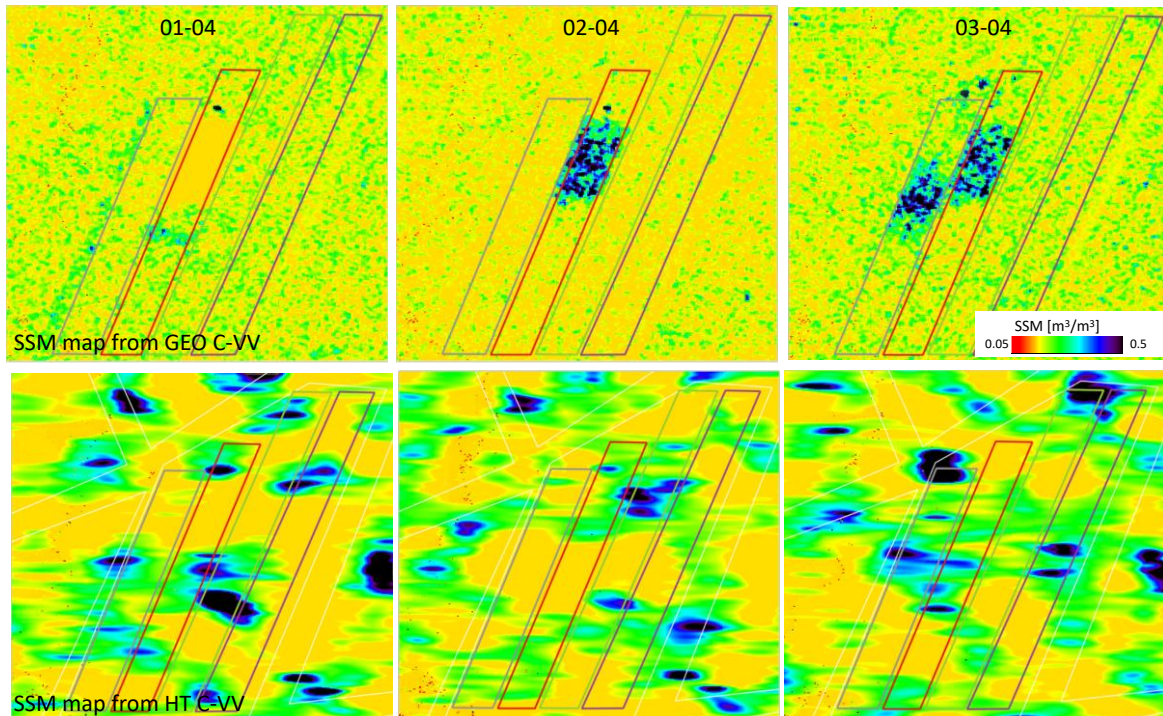
Figure 5-37: SSM maps of the CREA wheat stripes derived from the GEO F-SAR images (top panels) and the simulated Hydroterra images (bottom panels).

5.8   Summary of SSM retrieval

An STCD SSM retrieval approach was applied to the hyper-temporal F-SAR C-band and VV polarisation images, which were acquired every 10 minutes. The high temporal frequency allows monitoring the changes in SSM caused by irrigation, which usually last in a time frame of hours. Reducing the temporal sampling of SAR observations to 14 hours degrades the accuracy (RMSE) of the SSM retrieval from $0.039 m^3/m^3$ to $0.07 m^3/m^3$.

Even for hyper-temporal F-SAR images, the increase in the angle of incidence affects the retrieval performance due to the stronger influence of vegetation. Indeed, the RMSE increases to $0.07 m^3/m^3$.

For the simulated geosynchronous images, the long integration time does not prevent the monitoring of the SSM changes due to irrigation. The main effect comes from the reduced spatial resolution of the Hydroterra images, where the wet-dry soil patterns are blurred.

6 SSM Retrieval from Interferometric SAR Products (WP430)

6.1 Introduction

In this chapter the impact of soil moisture on repeat-pass interferometric SAR observables, including the coherence, phase, and phase-triplets is investigated. The potential to retrieve soil moisture from bare and vegetated areas is analysed. Two types of radar products are compared: The high-resolution F-SAR data provides a baseline to compare with the low-resolution simulated Hydroterra data. Over the last years, different approaches for soil moisture retrieval from SAR have been proposed, including the use of backscatter time series [18], polarimetry [19], [20], and interferometry [21], [22]. The use of interferometric techniques recently gained significant interest. This study uses the physical DInSAR model from [21]. The model explicitly models the expected interferometric coherence and phase between two zero-baseline repeat-pass acquisitions at different times based on the difference in soil moisture.

This report is structured as follows: Section 6.2 provides a short overview of the physical model and explains how the measured soil moisture values are transformed to the expected interferometric parameters. Section 6.3 covers the details related to the 22HTERRA campaign data (DAR [A3]), defines the relevant time periods and image areas, discusses the estimation of coherence and phase-triplets from the SLC data, and explains the ground measurement pre-processing. Individual fields are analysed in Section 6.4. Soil moisture retrieval is covered in Section 6.5. General findings and limitations are discussed in Section 6.6. Section 7.3 concludes the investigation.

6.2 Interferometric Soil Moisture Model

This section summarizes the main assumptions and equations of the model from [21] used in this report. The soil is modelled as a homogeneous lossy dielectric medium with no vegetation on top. Electromagnetic waves travel from the sensor to the ground through the air, enter the soil, propagate through the medium, and get reflected from scatterers in the soil back to the sensor. The medium has a complex relative dielectric coefficient ε_r that depends on the soil composition and moisture. The dielectric coefficient affects the propagation of electromagnetic waves, which can be described by the soil's complex vertical wavenumber k_z'.

A change in soil moisture between two acquisitions leads to a difference in the dielectric coefficients and the vertical wavenumbers. The model evaluates the resulting differences and predicts a decrease in coherence and a non-zero interferometric phase.

6.2.1 Soil Moisture to Dielectrics

The measured volumetric soil moisture m_v must first be converted to the complex relative dielectric coefficient ε_r to evaluate the forward model. We use the empirical model from [23] for this purpose, following the approach in [21]. The conversion for the C-band is performed using the equation for 6GHz. Note that this frequency does not perfectly match the F-SAR C-band centre frequency of 5.3GHz but no significant difference is expected. The soil texture (sand, silt, and clay contents) also affects the dielectric coefficient. The texture can be obtained from ground measurements and is part of the conversion equation. Note that the soil moisture has a more significant effect on ε_r than the soil texture. The conversion is given by:

$$
\begin{aligned}
real \quad &= (1.993 + 0.002 \cdot sand + 0.015 \cdot clay) \\
&+ (38.086 - 0.176 \cdot sand - 0.633 \cdot clay) \cdot m_v \\
&+ (10.720 + 1.256 \cdot sand + 1.522 \cdot clay) \cdot m_v^2 \\
imag \quad &= (-0.123 + 0.002 \cdot sand + 0.003 \cdot clay) \\
&+ (7.502 - 0.058 \cdot sand - 0.116 \cdot clay) \cdot m_v \\
&+ (2.942 + 0.452 \cdot sand + 0.543 \cdot clay) \cdot m_v^2 \\
\varepsilon_r \quad &= real - j \cdot imag
\end{aligned}
\tag{6-1}
$$

where $real$ and $imag$ are the magnitudes of the real and imaginary parts of ε_r, respectively. The resulting ε_r is a complex number with a negative imaginary part. The real part has a larger magnitude. Note that the soil texture components ($sand$, $clay$) range between 0 and 100, while m_v ranges between 0 and 1.

6.2.2 Wave Propagation

While the wave propagates through the air, its wavenumber k and angular frequency ω are given by

$$k = \frac{2\pi}{\lambda} \tag{6-2}$$

$$\omega = 2\pi f \tag{6-3}$$

where λ is the wavenumber and f is the radar frequency. The wavenumber in the air can be separated into the vertical k_z (z-axis) and the horizontal k_x (x-axis) components given the incidence angle θ_{inc}.

$$k_z = k \cos \theta_{inc} \tag{6-4}$$

$$k_x = k \sin \theta_{inc} \tag{6-5}$$

Then, the wave equation (in the Fourier domain) in the air is given by

$$k_x^2 + k_z^2 = \omega^2 \varepsilon_0 \mu_0 \tag{6-6}$$

with dielectric vacuum permittivity ε_0 and magnetic vacuum permeability μ_0. Here, we assume the total air dielectrics ε is close to the vacuum dielectrics ε_0.

When the wave enters the soil, its propagation direction changes, affected by the total soil dielectrics ε'. In the soil, the wave equation is given by

$$k_x'^2 + k_z'^2 = \omega^2 \varepsilon' \mu_0 \tag{6-7}$$

The horizontal boundary condition states

$$k_x' = k_x \tag{6-8}$$

Furthermore, the total soil dielectrics ε' is a product of the relative soil dielectrics and the vacuum dielectrics:

$$\varepsilon' = \varepsilon_r \varepsilon_0 \tag{6-9}$$

With this, we can obtain an expression for the vertical wavenumber k_z' in the soil

$$k_x^2 + k_z'^2 = \omega^2 \varepsilon_r \varepsilon_0 \mu_0 \tag{6-10}$$

$$k_z' = \sqrt{\omega^2 \varepsilon_r \varepsilon_0 \mu_0 - k_x^2} \tag{6-11}$$

Note that ε_r and k_z' are complex numbers with a negative imaginary part.

6.2.3 Interferometric Coherence and Phase

The expected interferometric coherence and phase are computed in several steps. First, the measured soil moisture values $m_{v,1}$ and $m_{v,2}$ from two acquisitions 1 and 2 are converted to the dielectric coefficients $\varepsilon_{r,1}$ and $\varepsilon_{r,2}$ using the relation in Section 6.2.1. Then, the vertical wavenumbers $k_{z,1}'$ and $k_{z,2}'$ are obtained using (6-11). Following the model and assuming a uniform vertical distribution of scatterers and uniform moisture in the soil, the expected value of the interferogram $I_{1,2}$ of pixels p_1, p_2 is:

$$I_{1,2} = \mathbb{E}[p_1 p_2^*] = \frac{1}{2j \cdot k_{z,1}' - 2j \cdot k_{z,2}'^*} \tag{6-12}$$

where $\mathbb{E}$ represents the expected value and $*$ denotes the complex conjugate.
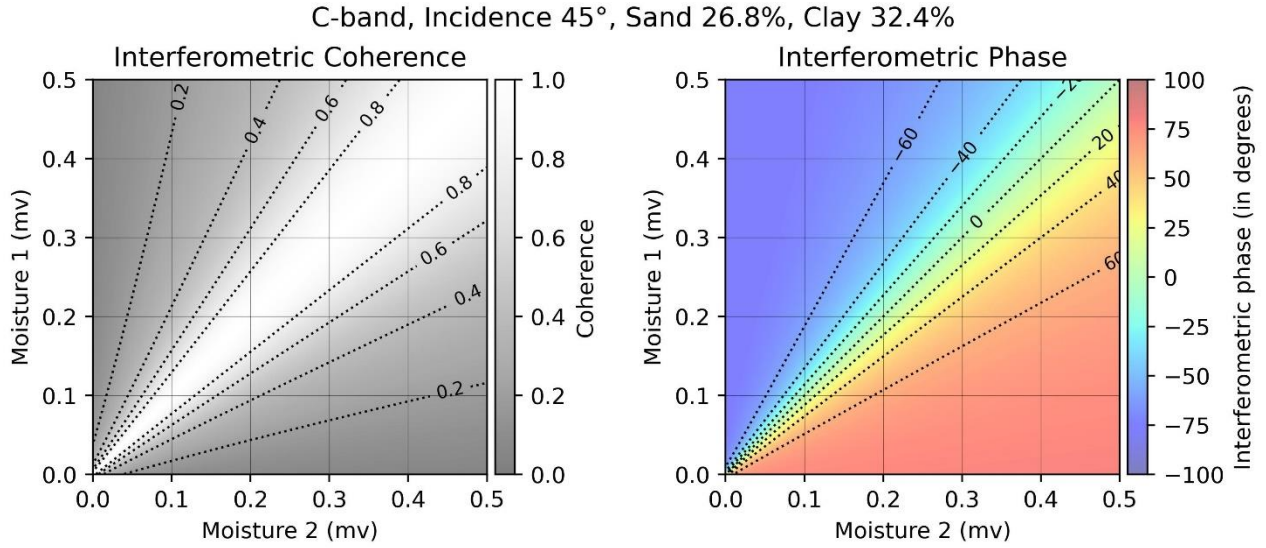
Figure 6-1: Model interferometric coherence and phase for different soil moisture combinations. C-band, incidence angle of 45°, soil texture with 26.8% sand and 32.4% clay.

The complex coherence $\gamma_{complex}$ is given by

$$\gamma_{complex,1,2} = \frac{I_{1,2}}{\sqrt{I_{1,1} I_{2,2}}} = \frac{2j\sqrt{\Im(k'_{z,2})\Im(k'_{z,1})}}{k'^*_{z,2} - k'_{z,1}} \tag{6-13}$$

where $\Im(a)$ denotes the imaginary part of a. To simplify notation, we denote the coherence magnitude with γ and the interferometric phase with φ:

$$\gamma_{1,2} = |\gamma_{complex,1,2}| \tag{6-14}$$

$$\varphi_{1,2} = \arg(\gamma_{complex,1,2}) \tag{6-15}$$

Both the coherence and the interferometric phase are non-linear with respect to the change in soil moisture. Figure 6-1 shows the model interferometric coherence and phase at C-band for different soil moisture combinations $m_{v,1}$ and $m_{v,2}$. The incidence angle does not have a large effect and is fixed to 45° here, matching the figures in [21].

6.2.4 Phase-Triplets

While comparing the observed and predicted coherence is straightforward, the observed interferometric phase requires calibration. In contrast to space-borne systems, the flight path of F-SAR is affected by wind, adding additional phase residuals and uncertainties, making precise calibration more challenging. Alternatively, phase-triplets can be formed using the information from three different acquisitions. The main advantage is that the triplets do not require phase calibration and are not affected by phase offsets. We combine the phases of the three acquisition pairs to form a triplet $\varphi_{1,2,3}$ from acquisitions 1, 2, and 3. The following expressions are equivalent (modulo 2π):

$$\varphi_{1,2,3} = \varphi_{1,2} + \varphi_{2,3} - \varphi_{1,3} \tag{6-16}$$

$$\varphi_{1,2,3} = \varphi_{1,2} + \varphi_{2,3} + \varphi_{3,1} \tag{6-17}$$

$$\varphi_{1,2,3} = \arg(\gamma_{complex,1,2} \cdot \gamma_{complex,2,3} \cdot \gamma^*_{complex,1,3}) \tag{6-18}$$

$$\varphi_{1,2,3} = \arg(\gamma_{complex,1,2} \cdot \gamma_{complex,2,3} \cdot \gamma_{complex,3,1}) \tag{6-19}$$

Since the interferometric phase is non-linear with respect to the change in soil moisture, the triplets are expected to be non-zero when there is a change in moisture.

6.3 Campaign Data Overview and Pre-processing

The data to be analysed consists of SAR SLC images and soil moisture ground measurements. This section summarizes the data properties and describes the pre-processing steps required for further analysis.

6.3.1 Time Periods

The 22HTERRA campaign was performed in two missions: Four flights in April 2022 and four more flights in June 2022. For details refer to the Data Acquisition Report [A3]. The last flights of every mission were short and no long integration products were simulated for two flights. The following time periods are covered in this report:

- APR-28-AM: Flight 1 on 28 April in the morning
- APR-28-PM: Flight 2 on 28 April in the afternoon
- APR-29-AM: Flight 3 on 29 April in the morning
- APR-29-PM: Flight 4 (short) on 29 April in the afternoon
- JUN-15-AM: Flight 5 on 15 June in the morning
- JUN-15-PM: Flight 6 on 15 June in the afternoon
- JUN-16-AM: Flight 7 on 16 June in the morning
- JUN-16-PM: Flight 8 (short) on 16 June in the afternoon

6.3.2 Image Areas

Several fields at CREA and Caione farms have been intensively monitored during the campaign. Soil moisture was recorded at specific points during or shortly after the F-SAR flights. The following image areas that cover the monitored fields are used in this report:

- APR-CREA-BS: Bare soil field at the CREA farm in April (same field as JUN-CREA-QU)
- APR-CREA-DW: Durum wheat field at the CREA farm in April
- APR-CAIONE-DW: Two adjacent durum wheat fields at the Caione farm in April
- JUN-CREA-SF: Sunflower field at the CREA farm in June
- JUN-CREA-QU: Quinoa field at the CREA farm in June (same field as APR-CREA-BS)
- JUN-CREA-MA: Maize (corn) field at the CREA farm in June
- JUN-CAIONE-AA: Alfalfa field at the Caione farm in June
- JUN-CAIONE-MA: Two adjacent maize (corn) fields at the Caione farm in June

6.3.3 SLC Spatial Resolution and Multi-look Window

Three types of SLC images are available:

- F-SAR: high-resolution, short integration time
- GEO-SAR: high-resolution, long integration time (simulated product)
- Hydroterra: low-resolution, long integration time (simulated product)

F-SAR and GEO-SAR images have the same resolution, pixel dimensions, and coordinate system. The processed resolution in azimuth and range is 0.5m x 0.5m, and the pixel spacing is 0.2m x 0.3m. Several F-SAR passes are available for every flight. In this study, the master F-SAR pass within each flight is used for analysis. The simulated Hydroterra SLCs cover the same geographical area as F-SAR and GEO-SAR but have a lower resolution. The processed Hydroterra resolution in azimuth and range is 5.0m x 22.1m, and the pixel spacing is 2.9m x 19.2m.

Spatial averaging (i.e. multi-looking) is required to estimate the interferometric coherence and phase. For F-SAR and GEO-SAR, the high resolution allows the use of a small multi-look window, preserves spatial details, and avoids averaging data from adjacent fields. A multi-look window of 14 x 10 pixels in azimuth and range is used, resulting in a window size of 2.9m x 3m and 34 independent looks.

Due to the low resolution, a larger spatial window is required for the simulated Hydroterra data. We use a multi-look window of 14 x 2 pixels (41.1m x 38.4m) in azimuth and range, equivalent to 14 independent looks. At this resolution, we expect more pixels where different fields or soil moisture values are mixed together. The coherence estimation is biased for low values when the number of looks is small. However, increasing the multi-look window to lower the bias is not feasible since it would further reduce the spatial resolution.

6.3.4 Interferometric Coherence

The complex interferometric coherence $\gamma'_{complex,1,2}$ is estimated from N pixels within the multi-look window taken from SLC images 1 and 2:

$$\gamma'_{complex,1,2} = \frac{\sum_{n=1}^{N} p_{1,n} p_{2,n}^*}{\sqrt{\sum_{n=1}^{N} |p_{1,n}|^2 \cdot \sum_{n=1}^{N} |p_{2,n}|^2}} \tag{6-20}$$

where $p_{i,n}$ represents the n-th pixel within the multi-look window of the SLC image i and $*$ denotes the complex conjugate. The coherence magnitude $\gamma'_{1,2}$ is given by:

$$\gamma'_{1,2} = |\gamma'_{complex,1,2}| \tag{6-21}$$

Figure 6-2 compares the F-SAR coherence in different polarizations between APR-28-AM and APR-29-AM. HH shows the highest coherence values overall and is selected as the main polarization for further analysis. VV shows very low coherence over vegetated areas, with values often reaching below 0.4. HV coherence is in between HH and VV. This is an interesting observation, as the HV coherence is usually expected to be the lowest over vegetated areas. In general, vegetated fields show low coherence, while bare surfaces and artificial objects show higher coherence in all polarizations.

In June, the F-SAR coherence is significantly higher overall as shown in Figure 6-3. Both HH and VV polarizations show high coherence. The HV coherence is lower than HH and VV but still higher than any polarization in April.

Figure 6-5 compares the coherence for F-SAR, GEO-SAR, and Hydroterra data in HH polarization between APR-28-AM and APR-29-AM. F-SAR and GEO-SAR coherence is very similar, and different fields are clearly visible. Hydroterra coherence is noisier, and it is more difficult to recognize individual fields. However, the spatial patterns are still similar to F-SAR.

Some interesting details can be seen in high-resolution data. Figure 6-4 shows the observed F-SAR coherence between 28 April and 29 April mornings over a bare field. A part of the field was irrigated and appears as an area with lower coherence. The black points indicate positions where ground measurements were repeatedly taken during the campaign. Note the tracks with lower coherence following the points. The passing of the ground teams to perform the measurements can explain the lower coherence along the tracks. The disturbances in soil roughness increase the decorrelation and soil compaction can

affect the relative soil moisture content. This example illustrates the high sensitivity of coherence to different changes over time, not necessarily related to soil moisture.
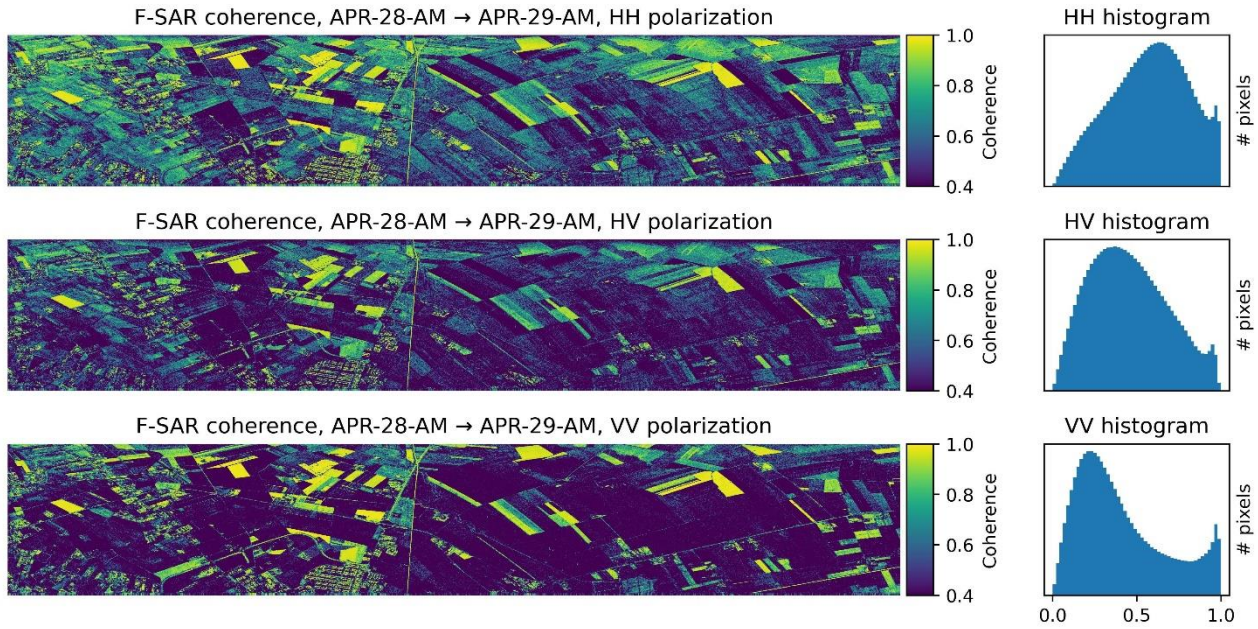
Figure 6-2: F-SAR coherence in April for different polarizations: HH (top), HV (middle), and VV (bottom). The time difference between the acquisitions is 24 hours (APR-28-AM to APR-29-AM).
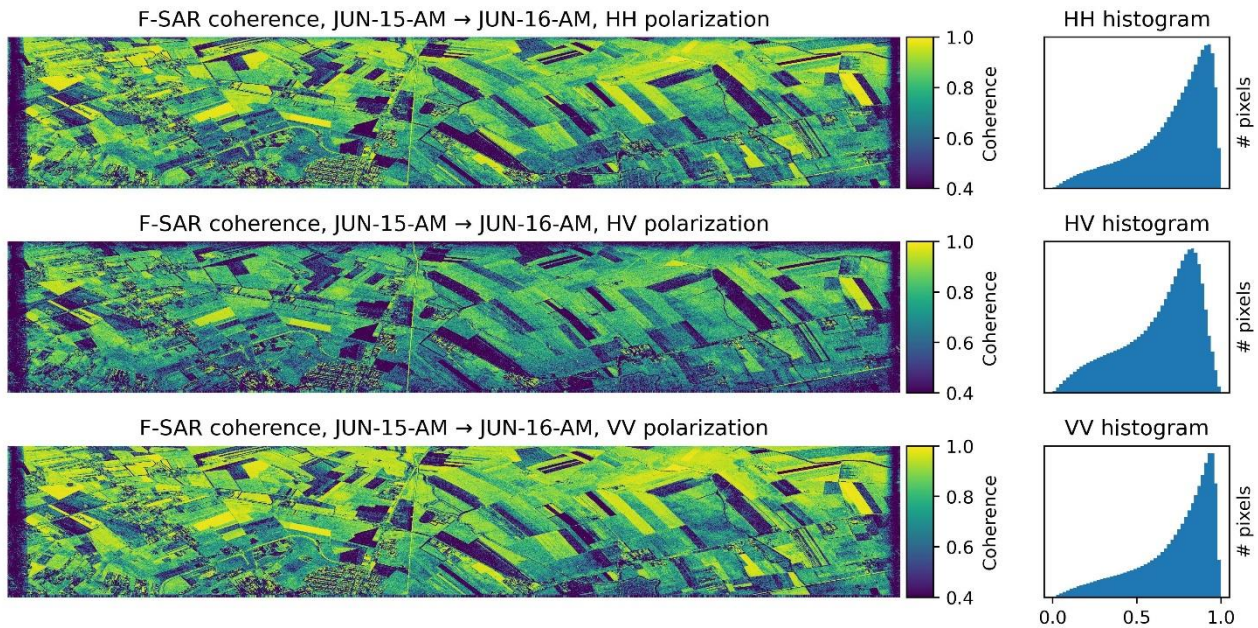
Figure 6-3: F-SAR coherence in June for different polarizations: HH (top), HV (middle), and VV (bottom). The time difference between the acquisitions is 24 hours (JUN-15-AM to JUN-16-AM).
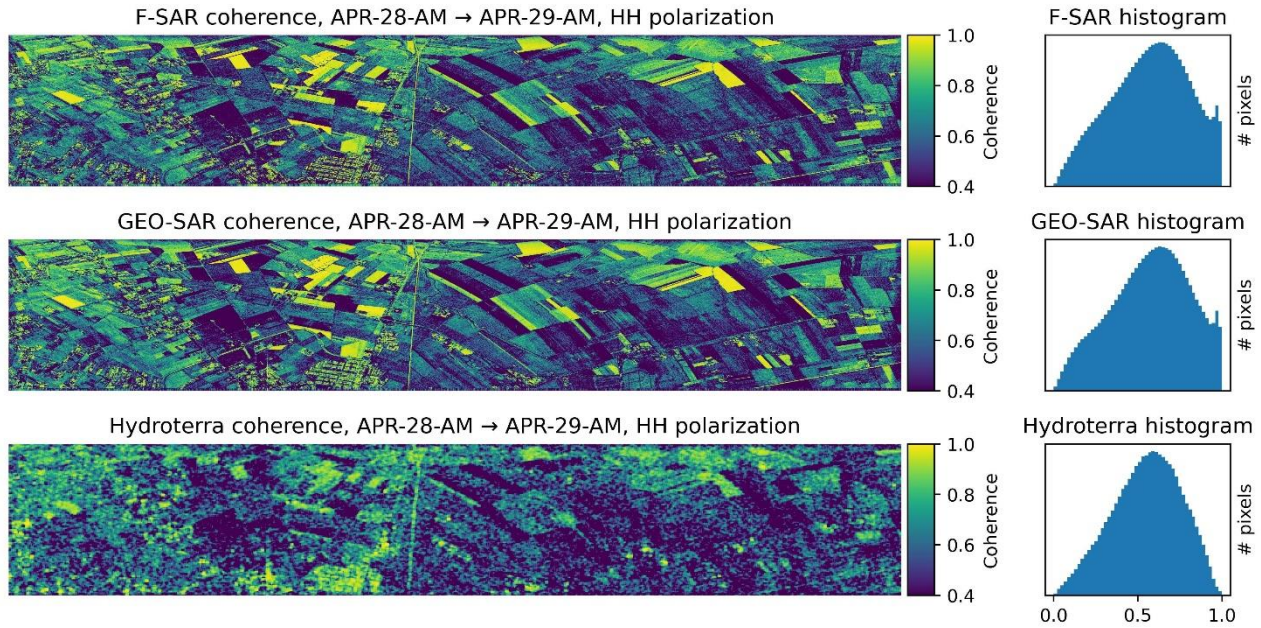
Figure 6-5: Coherence comparison between F-SAR (top), GEO-SAR (middle), and Hydroterra (bottom). The time difference between the acquisitions is 24 hours (APR-28-AM to APR-29-AM).
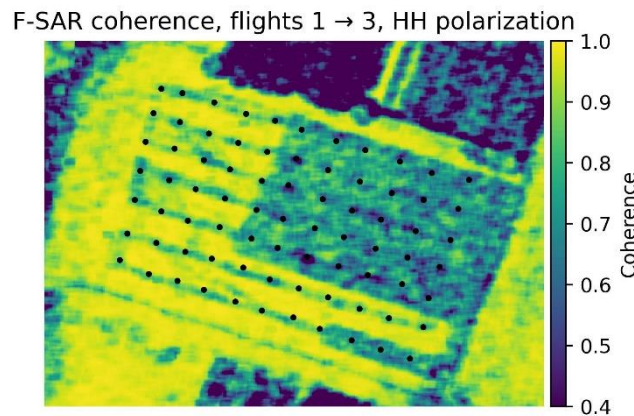
Figure 6-4: Observed F-SAR coherence over the APR-CREA-BS field. Black dots indicate ground measurement positions

6.3.5 Interferometric Phase and Phase-Triplets

The multi-looked interferometric phase $\varphi'_{1,2}$ is given by:

$$\varphi'_{1,2} = \arg\left(\gamma'_{complex,1,2}\right) \tag{6-22}$$

Figure 6-6 compares the multi-looked interferometric phase for F-SAR, GEO-SAR, and Hydroterra data in HH polarization between APR-28-AM and APR-29-AM. F-SAR and GEO-SAR phases show some differences. In the areas with low coherence, the phase is very noisy. The Hydroterra phase shows the same spatial patterns as GEO-SAR but is noisier, and individual fields are difficult to recognize.

A phase-triplet $\varphi'_{1,2,3}$ is formed from three multi-looked interferometric phases:

$$\varphi'_{1,2,3} = \varphi'_{1,2} + \varphi'_{2,3} - \varphi'_{1,3} \tag{6-23}$$

Figure 6-7 compares the phase-triplets for F-SAR, GEO-SAR, and Hydroterra data in HH polarization formed from the three long flights in April. Areas with low coherence (noisy phases) show noisy triplets in all images. The triplets are relatively small for the areas where the coherence is high. Detailed analysis for individual fields can be found in Section 6.4. The triplet distribution shows a clear peak centred around zero. The triplet variance (spread around the peak) is similar for F-SAR and GEO-SAR, with GEO-SAR variance being slightly smaller. The Hydroterra triplets are noisier and show a larger spread around zero in the histogram.
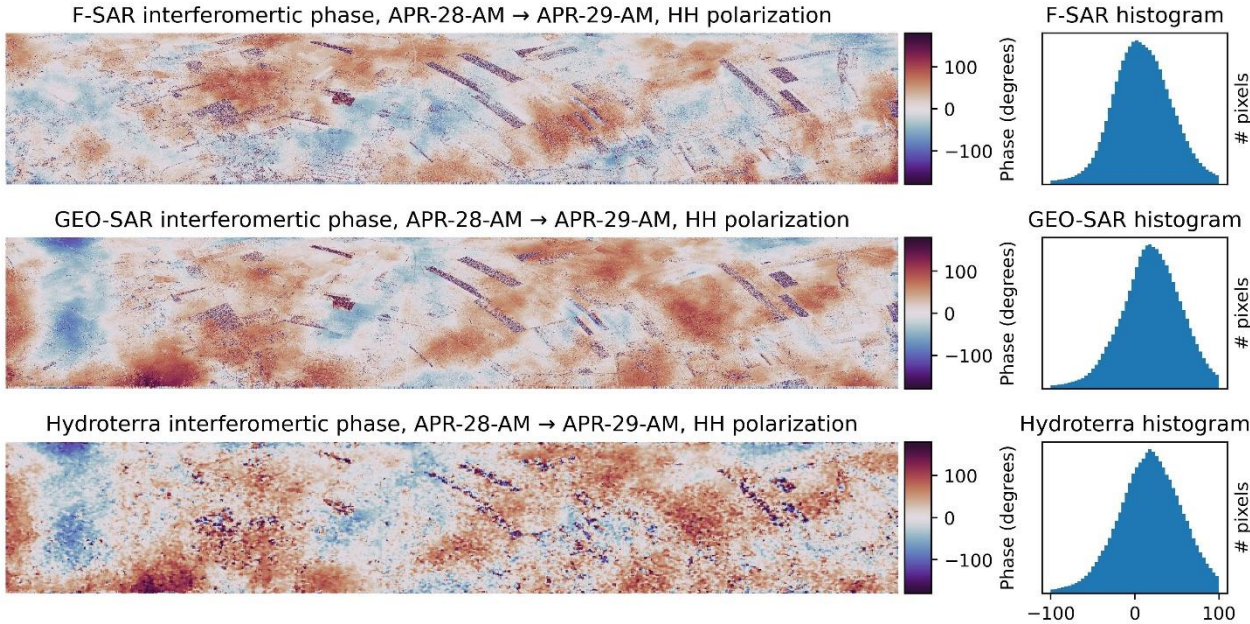
Figure 6-6: Multi-looked interferometric phase comparison between F-SAR (top), GEO-SAR (middle), and Hydroterra (bottom). The phase is not calibrated and only relative differences are meaningful. The time difference between the acquisitions is 24 hours (APR-28-AM to APR-29-AM).
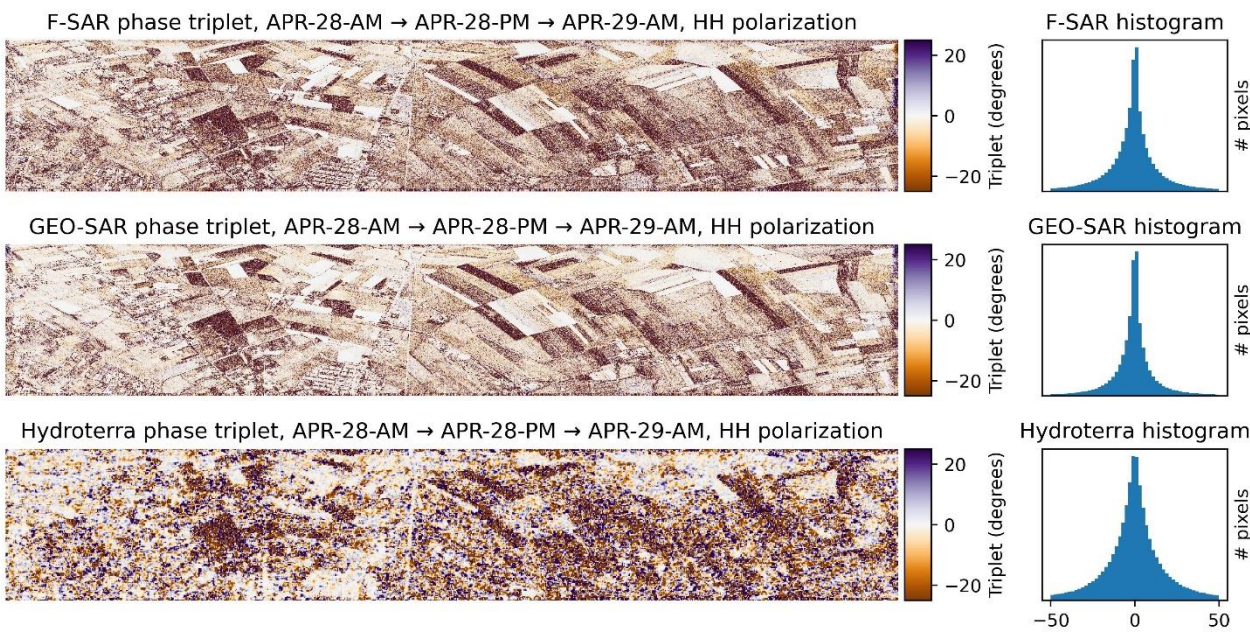
Figure 6-7: Phase-triplet comparison between F-SAR (top), GEO-SAR (middle), and Hydroterra (bottom). The triplets are formed from three acquisitions in April (APR-28-AM, APR-28-PM, and APR-29-AM).

6.3.6   Ground Measurements Preprocessing

The soil moisture ground measurements [A3] are available as points, while the SLC data is provided as a raster. To simplify the analysis in the following sections, we transform the point measurements to a raster in the same coordinate system as the F-SAR data.

First, the point coordinates are converted from longitude-latitude to northing-easting, matching the EPSG:32633 (WGS84 / UTM zone 33N) coordinate system of geocoded F-SAR products (GTC-LUT). Then, azimuth-range coordinate values are obtained using the F-SAR look-up tables.

Points are grouped into the time periods (see Section 6.3.1) corresponding to the individual flights. In the next step, points in close proximity to each other are interpolated onto a raster using linear interpolation. This step creates soil moisture maps in F-SAR / GEO-SAR SLC coordinates for each time period. Figure 6-8 shows the geocoded soil moisture points and the interpolated moisture map for the APR-CREA-BS region on APR-28-AM. The interferometric model can now be applied to the moisture maps to predict the expected interferometric parameters for each valid pixel.
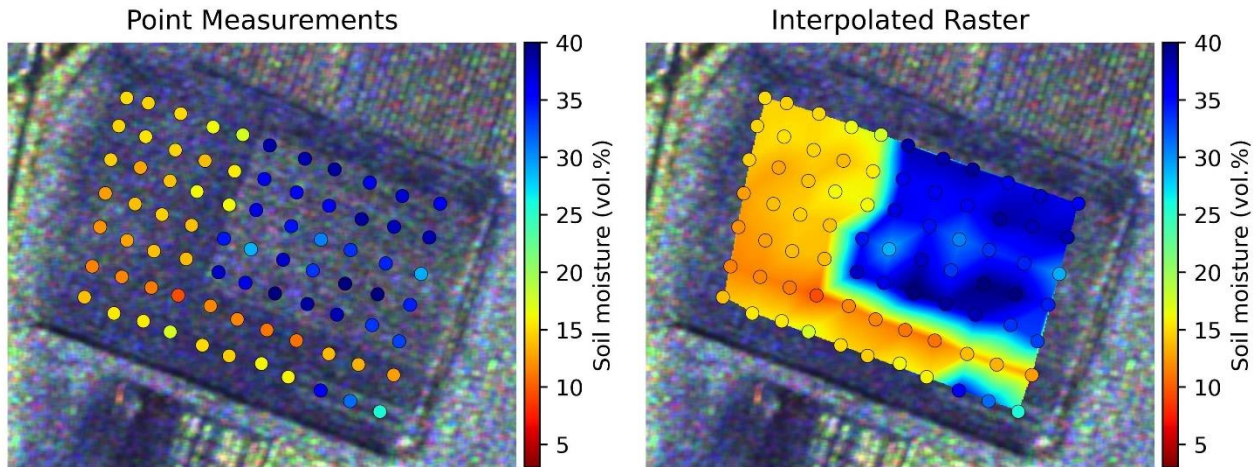
Figure 6-8: Soil moisture point measurements (left) are interpolated to the F-SAR raster (right) with linear interpolation. The background is a Pauli RGB image. Measurements obtained on APR-28-AM.

6.4 Analysis of Individual Fields

6.4.1 Bare Soil Field (APR-CREA-BS)
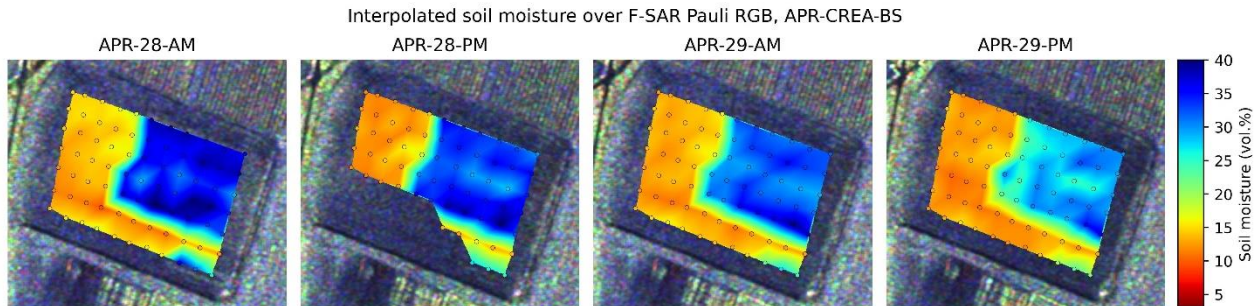
Figure 6-9: Interpolated soil moisture over the APR-CREA-BS bare field for the four flights in April. The background is a Pauli RGB image

Figure 6-9 shows the soil moisture time series over the bare soil field in April. A section of the field was irrigated before the campaign using drip irrigation and a decrease in soil moisture over 10 vol.% is observed in some parts of the field. No simulated Hydroterra data is available for the last time period (APR-29-PM), therefore, the analysis focuses on the first three time periods.

Figure 6-10 compares the modelled and the observed coherence magnitudes. Based on the soil moisture changes, the model predicts a decreased coherence for some sections of the field. The irrigated area is better seen in the F-SAR coherence image. Hydroterra coherence is lower than the F-SAR coherence. Both the F-SAR and Hydroterra coherence are lower than model predictions in the irrigated areas. According to the model, this would require a larger change in soil moisture than indicated by the ground measurements.

Figure 6-10: Comparison of the modelled and observed coherence, APR-CREA-BS field, 24 hours between acquisitions. Top: F-SAR; Bottom: Hydroterra.

Figure 6-11 shows the modelled and the observed interferometric phase. Without calibration, only the relative values are meaningful. The Hydroterra phase is noisier than F-SAR. The model predicts an interferometric phase of tens of degrees for some parts of the field, but the spatial patterns do not match the observed phase well.
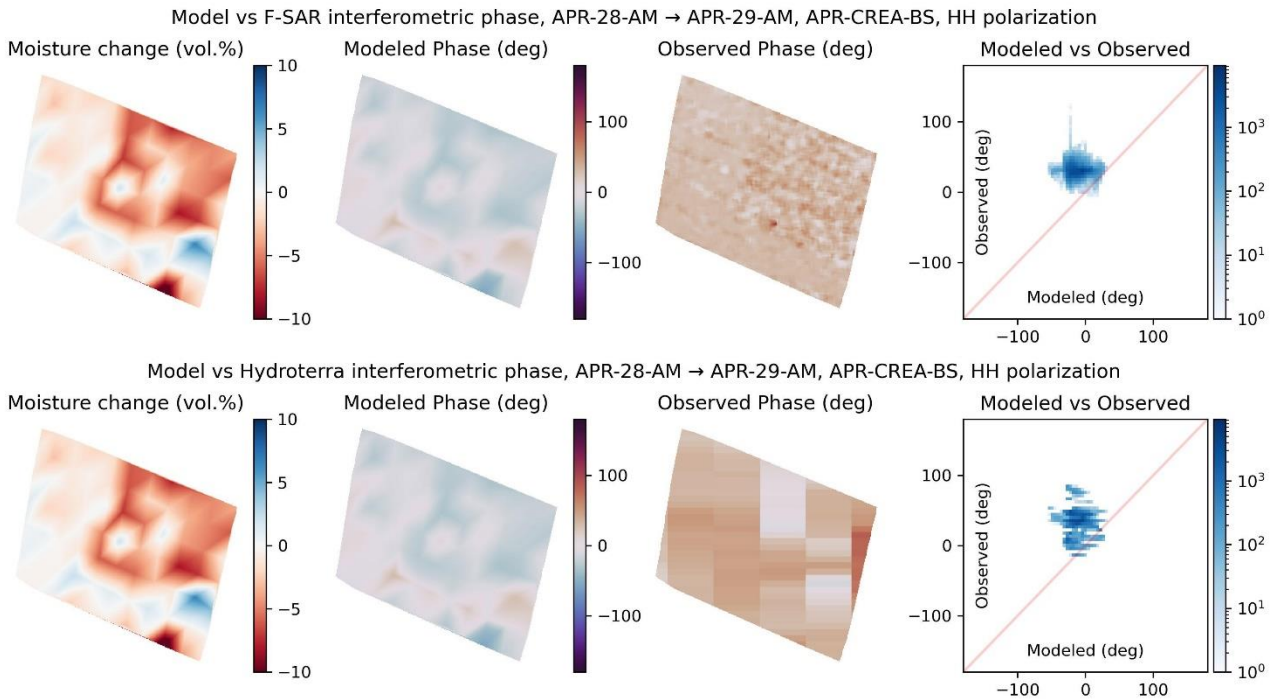
Figure 6-11: Comparison of the modelled and observed interferometric phase, APR-CREA-BS field, 24 hours between acquisitions. The phase is not calibrated, and only the relative values are important. Top: F-SAR; Bottom: Hydroterra.
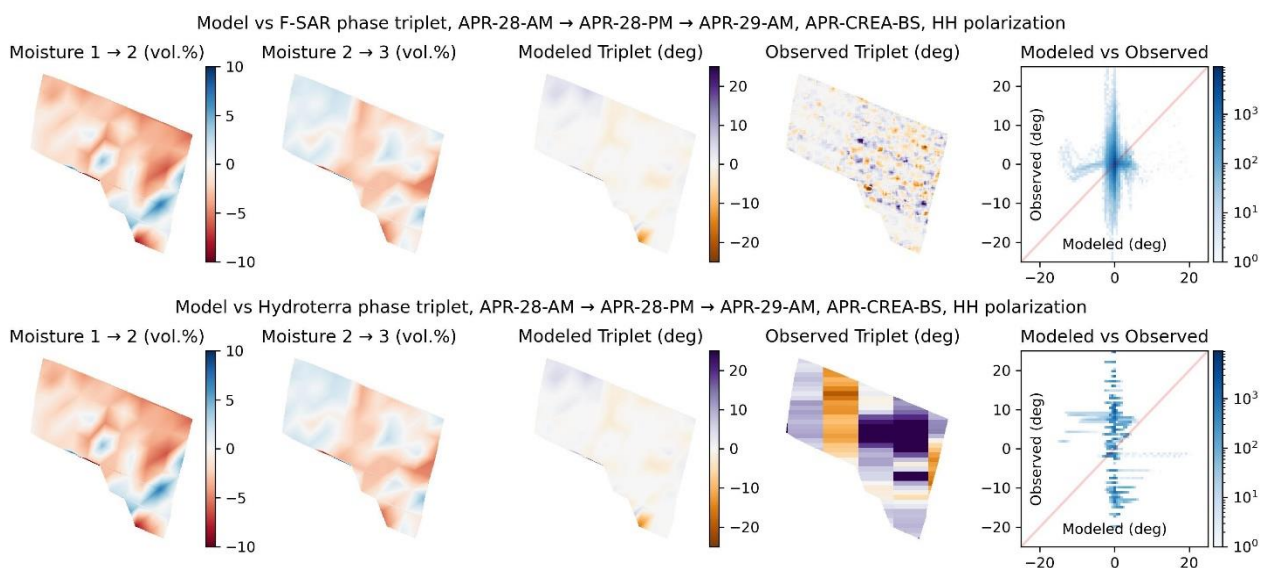
Figure 6-12: Comparison of the modelled and observed phase triplets using the three acquisitions in April, APR-CREA-BS field. Top: F-SAR; Bottom: Hydroterra.

The phase-triplets shown in Figure 6-12 do not require phase calibration. The triplets predicted by the model are relatively small, with most values ranging between -5 and 5 degrees. F-SAR triplets show more variation in the irrigated area where coherence is lower. Hydroterra triplets are very noisy, and no clear spatial pattern is visible. A larger number of looks might be required to reduce the noise. However, the spatial resolution would be insufficient to differentiate dry and irrigated areas over the APR-CREA-BS field.

6.4.2 CREA Durum Wheat Field (APR-CREA-DW)
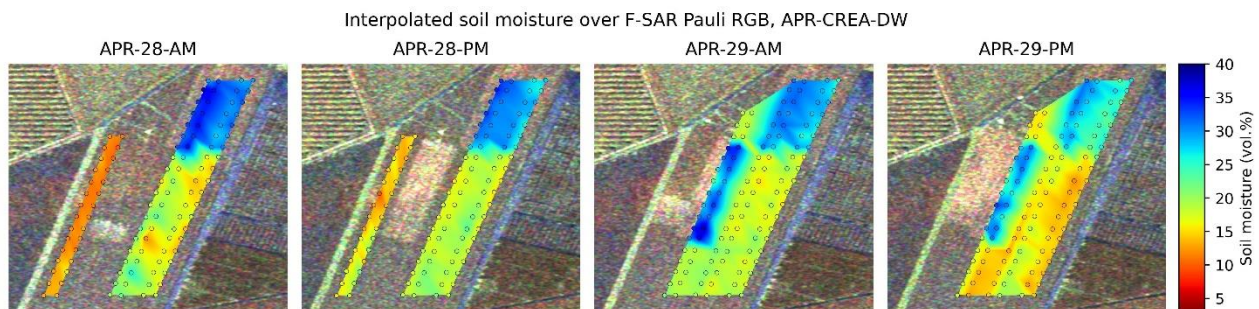
Figure 6-13: Interpolated soil moisture over the APR-CREA-DW wheat field for the four flights in April. The background is a Pauli RGB image.

Figure 6-13 shows the soil moisture time series over the APR-CREA-DW field. The field was irrigated with a mobile boom during the campaign, and irrigation progress is visible as brighter areas in the Pauli RGB images (background).

The dense soil moisture measurements are only available before or after the irrigation. For example, the stripes that were irrigated on 29 April are only measured on 28 April and vice versa. Therefore, interferometric coherence and phase-triplets cannot be modelled for some areas for each time period combination. Especially the spatial patterns over the most interesting stripes irrigated during the campaign cannot be modelled: either the dense ground measurements before or after irrigation are missing. While there are a few permanent ground stations in the area, the distance is too large to interpolate the measurements.

Figure 6-14 shows the APR-CREA-DW field's modelled and observed coherence. Two stripes irrigated before the campaign are covered. While the model predicts high coherence for most parts of the field, the observed coherence is significantly lower for F-SAR and Hydroterra data. This is the decorrelation effect from the vegetation covering the field that is not considered by the model. The observed F-SAR coherence is closer to the modelled coherence than the Hydroterra coherence, which is generally very low. Spatial patterns predicted by the model are not visible in both cases.

Similar to the coherence, no agreement between the model and the observed triplets is observed, as shown in Figure 6-15. Low coherence results in noisy interferometric phases and noisy triplets. While the model predicts low triplets of a few degrees, the observed values have a larger range of tens of degrees.

Figure 6-14: Comparison of the modelled and observed coherence, APR-CREA-DW field, 24 hours between acquisitions. Top: F-SAR; Bottom: Hydroterra.
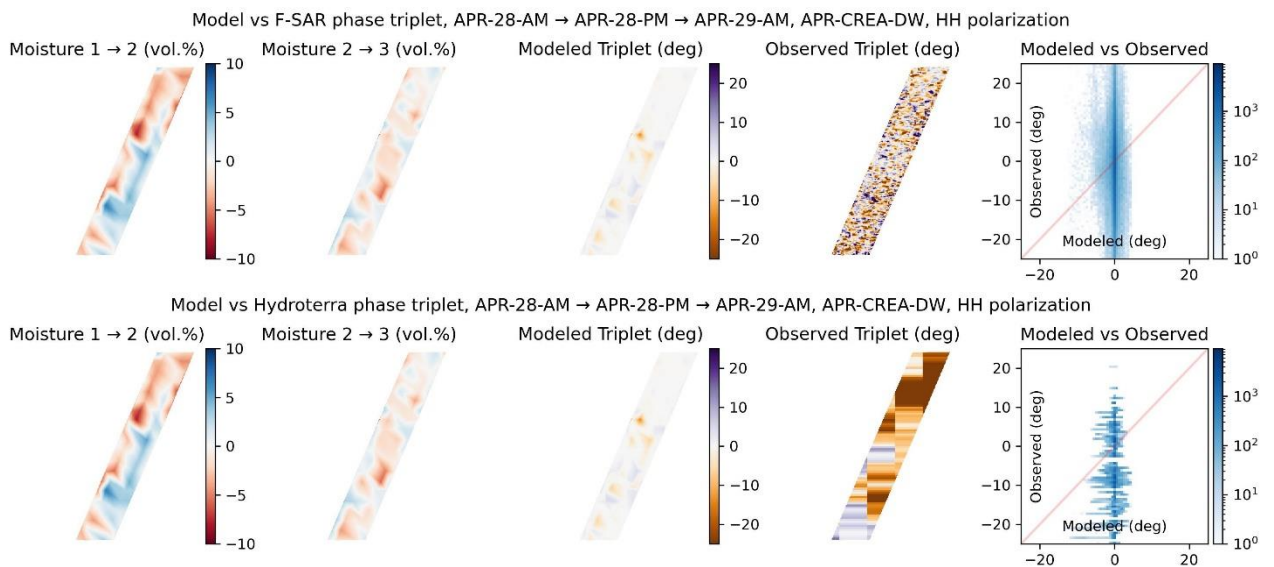
Figure 6-15: Comparison of the modelled and observed phase triplets using the three acquisitions in April, APR-CREA-DW field. Top: F-SAR; Bottom: Hydroterra.

6.4.3 Caione Durum Wheat Fields (APR-CAIONE-DW)
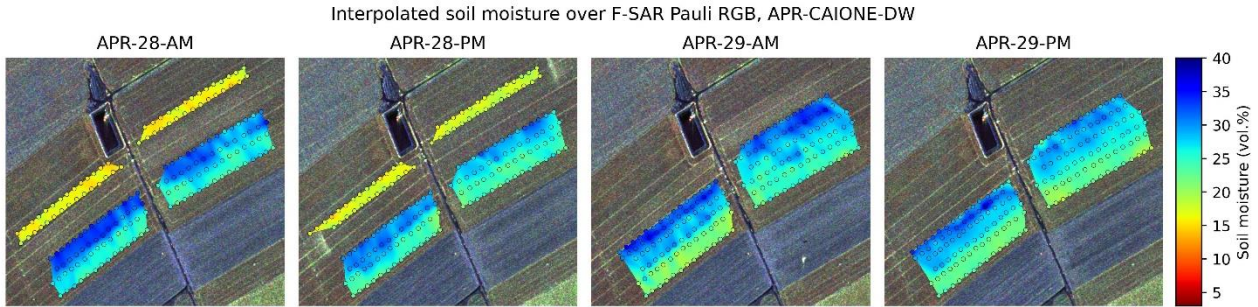
Figure 6-16: Interpolated soil moisture over the APR-CAIONE-DW wheat field for the four flights in April. The background is a Pauli RGB image.

Two adjacent durum wheat fields at the Caione farm were monitored in April. Similar to the APR-CREA-DW field, some stripes were irrigated during the campaign. Dense ground measurements are only available either before or after irrigation as shown in Figure 6-16.

The results for the coherence (Figure 6-17) and phase-triplets (Figure 6-18) are similar to the APR-CREA-DW field. Vegetation introduces strong decorrelation resulting in noisy phase-triplets and low coherence.
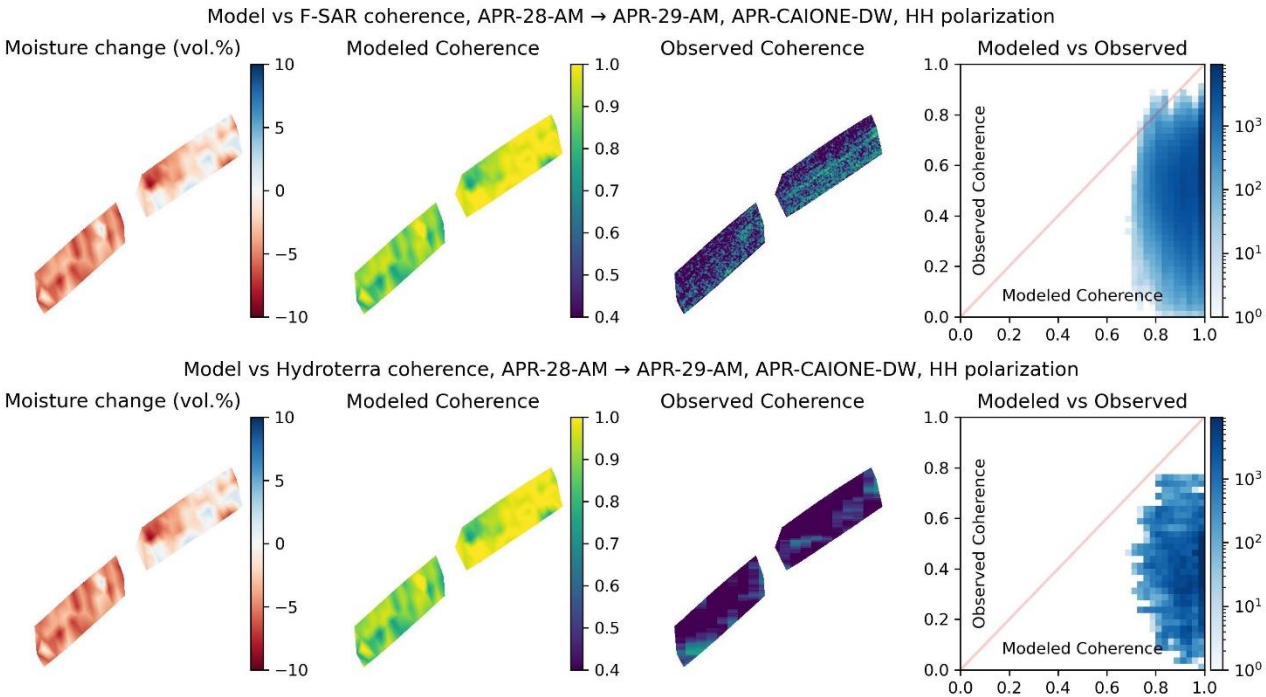
Figure 6-17: Comparison of the modelled and observed coherence, APR-CAIONE-DW fields, 24 hours between acquisitions. Top: F-SAR; Bottom: Hydroterra.
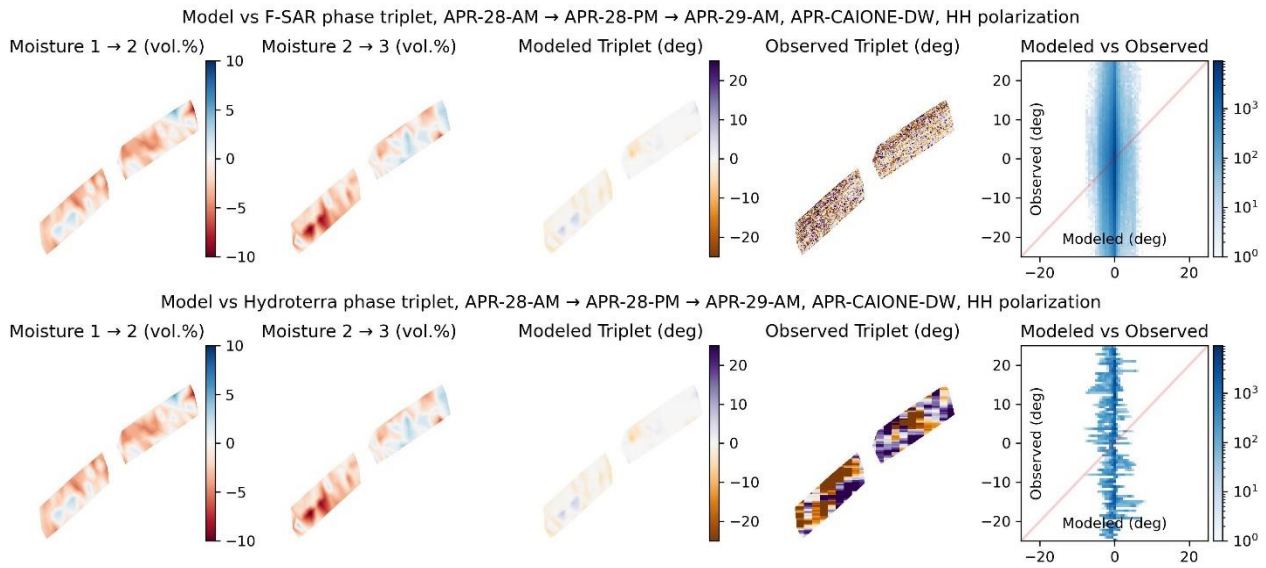
Figure 6-18: Comparison of the modelled and observed phase triplets using the three acquisitions in April, APR-CAIONE-DW field. Top: F-SAR; Bottom: Hydroterra.

6.4.4 Quinoa Field (JUN-CREA-QU)
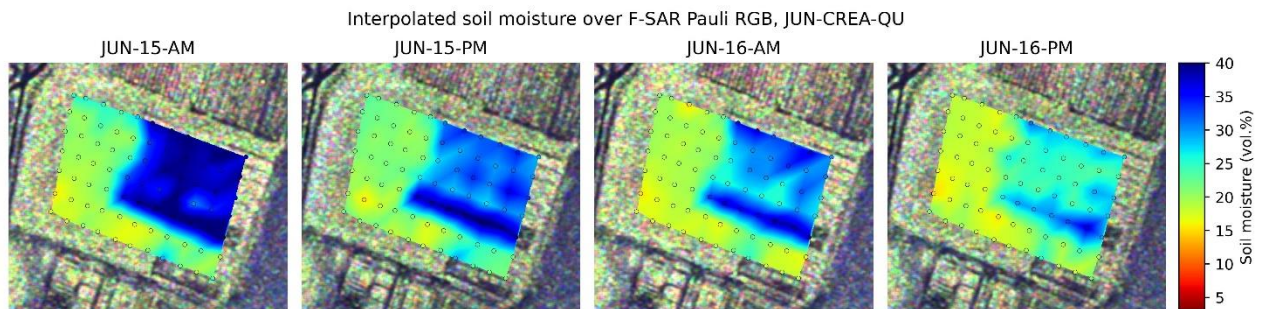
Figure 6-19: Interpolated soil moisture over the JUN-CREA-QU quinoa field for the four flights in June. The background is a Pauli RGB image.

The JUN-CREA-QU quinoa field monitored in June is the same field as APR-CREA-BS, now with vegetation growing on top. Similar to the first part of the campaign in April, part of the field was irrigated and is drying out, as shown in Figure 6-19.

Figure 6-20 shows the modelled and the observed coherence. The model predicts decreased coherence in the centre and at the edges of the field due to changes in the soil moisture. The irrigated part of the field is partially visible in the F-SAR coherence image as an area with low coherence. However, the coherence is also lower than the model predictions in dry parts of the field due to vegetation. Hydroterra coherence does not show the same spatial patterns as the F-SAR data, and the irrigated part of the field is not visible.

Figure 6-21 compares the modelled and observed triplets. Neither F-SAR nor Hydroterra triplets match the model. The irrigated part of the field is visible as an area with larger triplet values for F-SAR. No clear spatial patterns are observed for Hydroterra data.
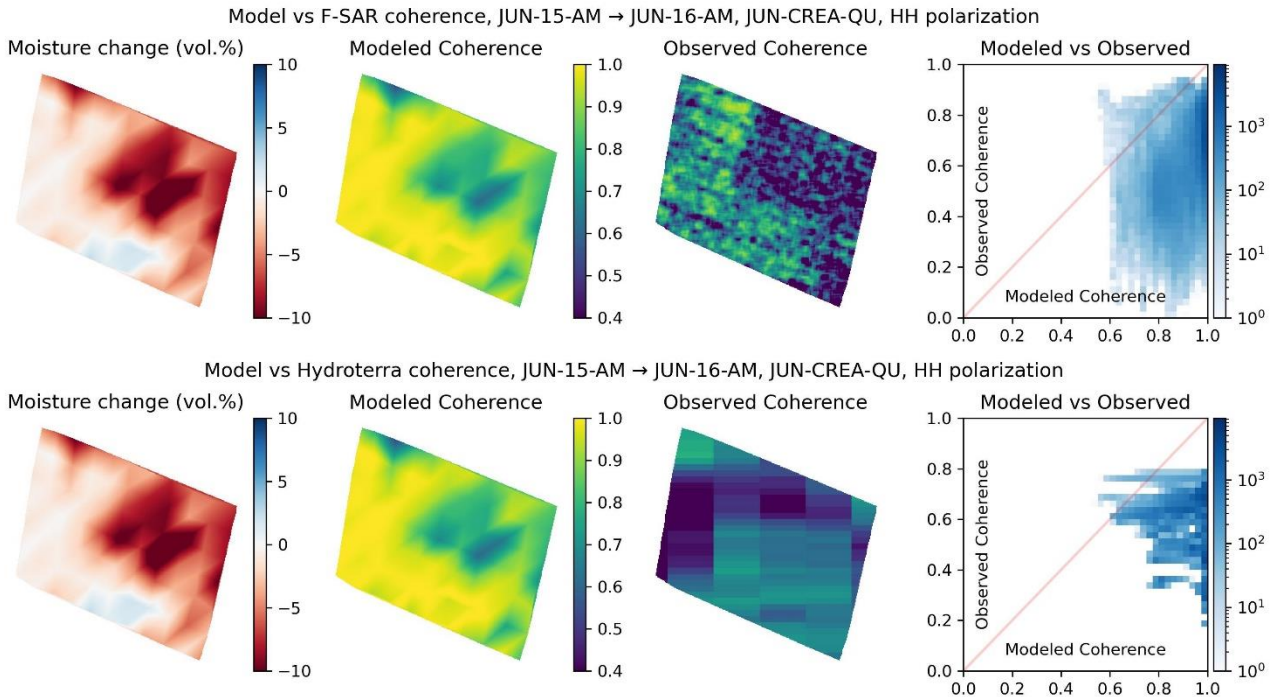
Figure 6-20: Comparison of the modelled and observed coherence, JUN-CREA-QU field, 24 hours between acquisitions. Top: F-SAR; Bottom: Hydroterra.
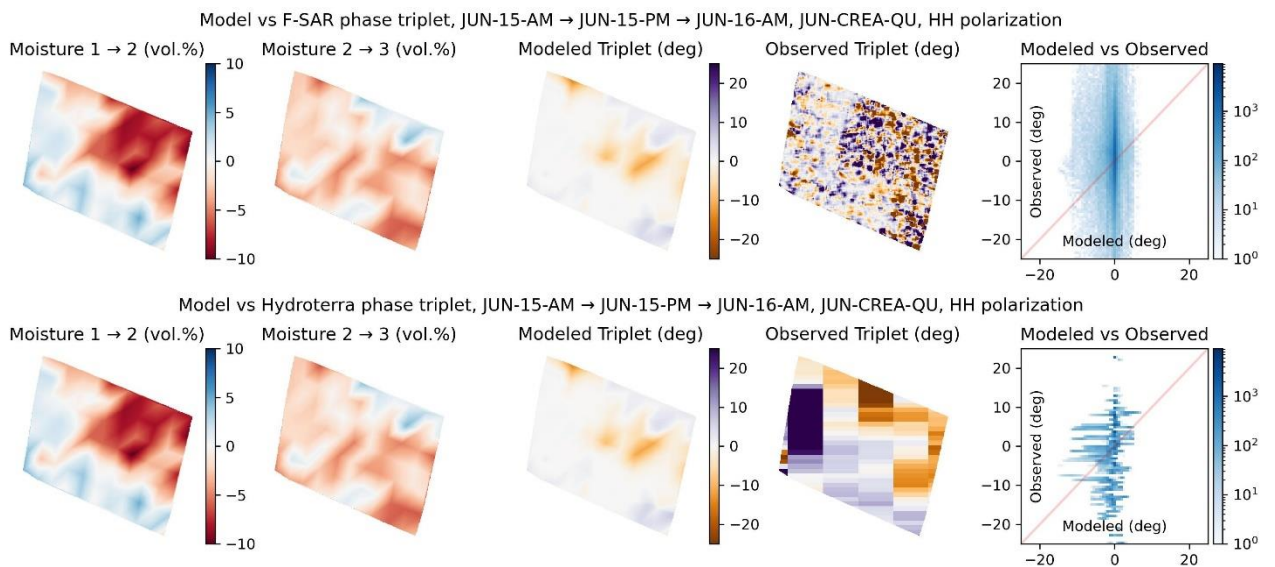
Figure 6-21: Comparison of the modelled and observed phase triplets using the three acquisitions in June, JUN-CREA-QU field. Top: F-SAR; Bottom: Hydroterra.

6.4.5 Sunflower Field (JUN-CREA-SF)
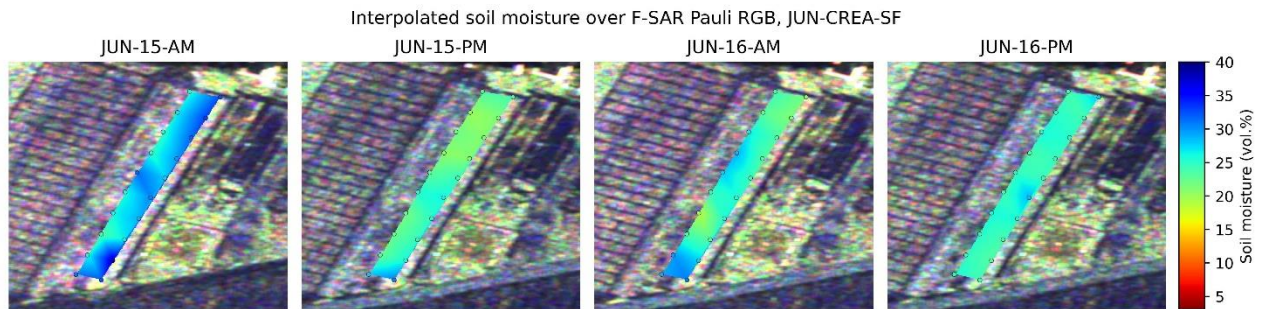
Figure 6-22: Interpolated soil moisture over the JUN-CREA-SF sunflower field for the four flights in June. The background is a Pauli RGB image.
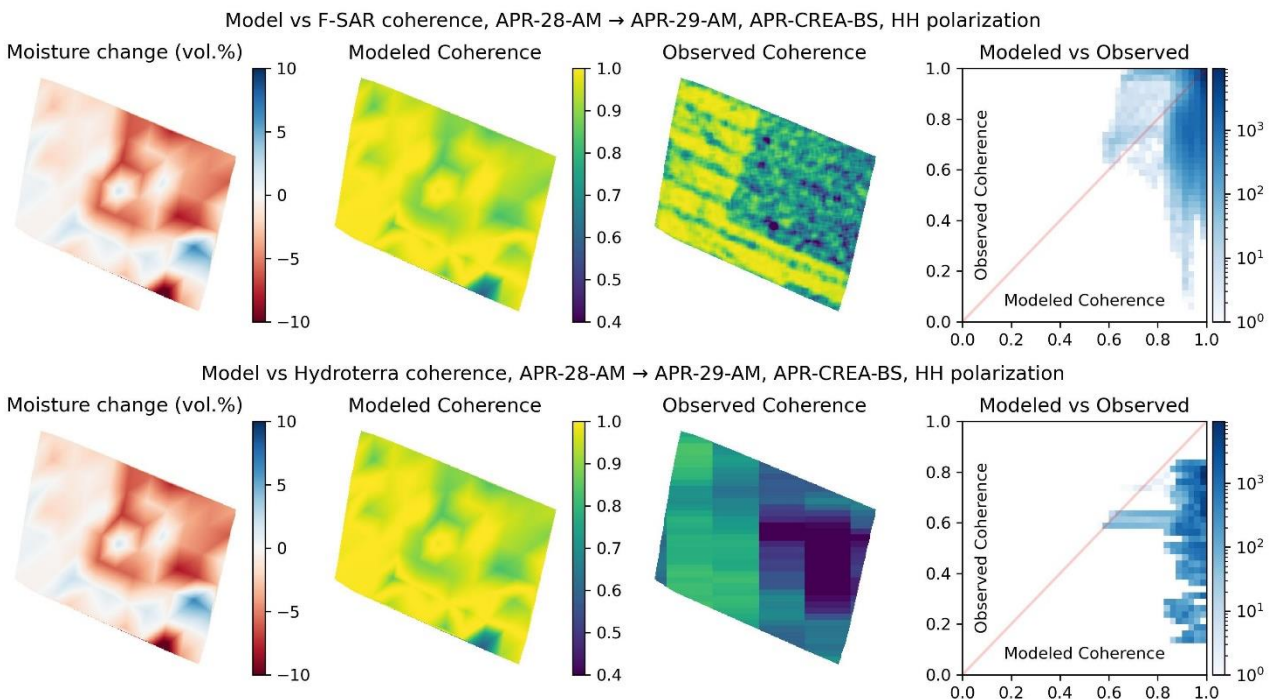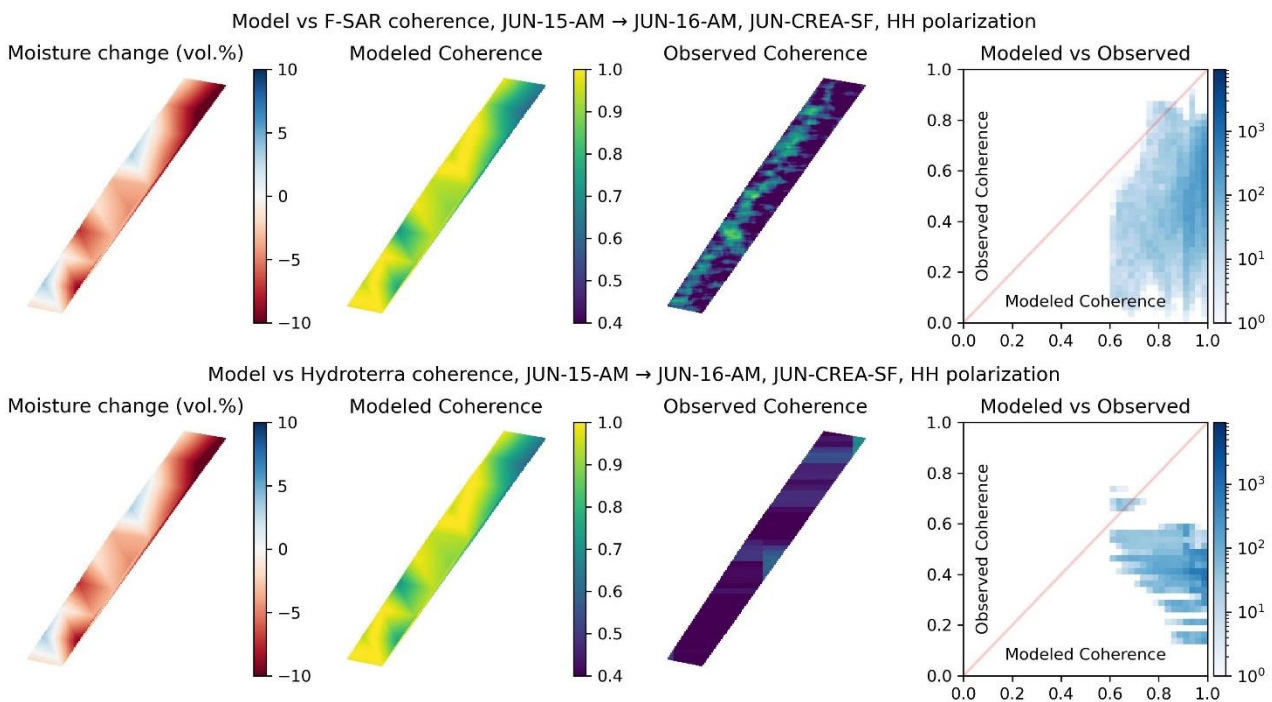

Figure 6-23: Comparison of the modelled and observed coherence, JUN-CREA-SF field, 24 hours between acquisitions. Top: F-SAR; Bottom: Hydroterra.

The JUN-CREA-SF sunflower field shows decreasing soil moisture throughout the campaign (Figure 6-22). The vegetation introduces additional decorrelation, resulting in low F-SAR and Hydroterra coherence that does not match the model.

6.4.6 CREA Maize Field (JUN-CREA-MA)
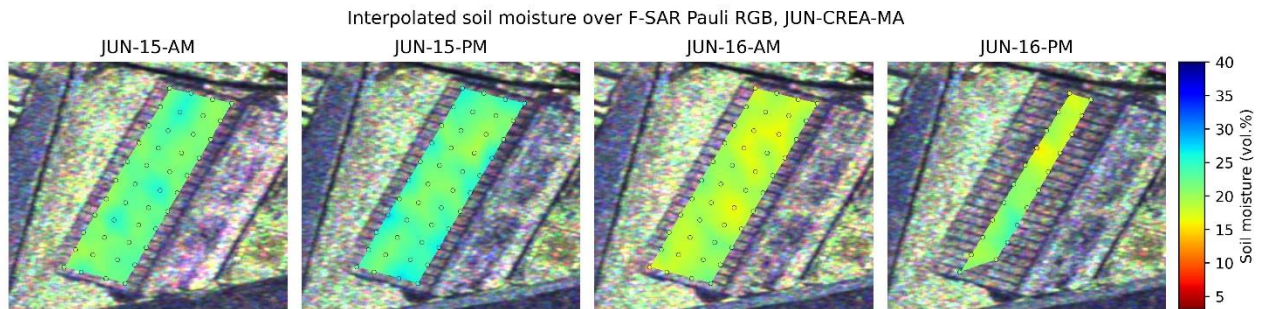
Figure 6-24: Interpolated soil moisture over the JUN-CREA-MA maize field for the four flights in June. The background is a Pauli RGB image
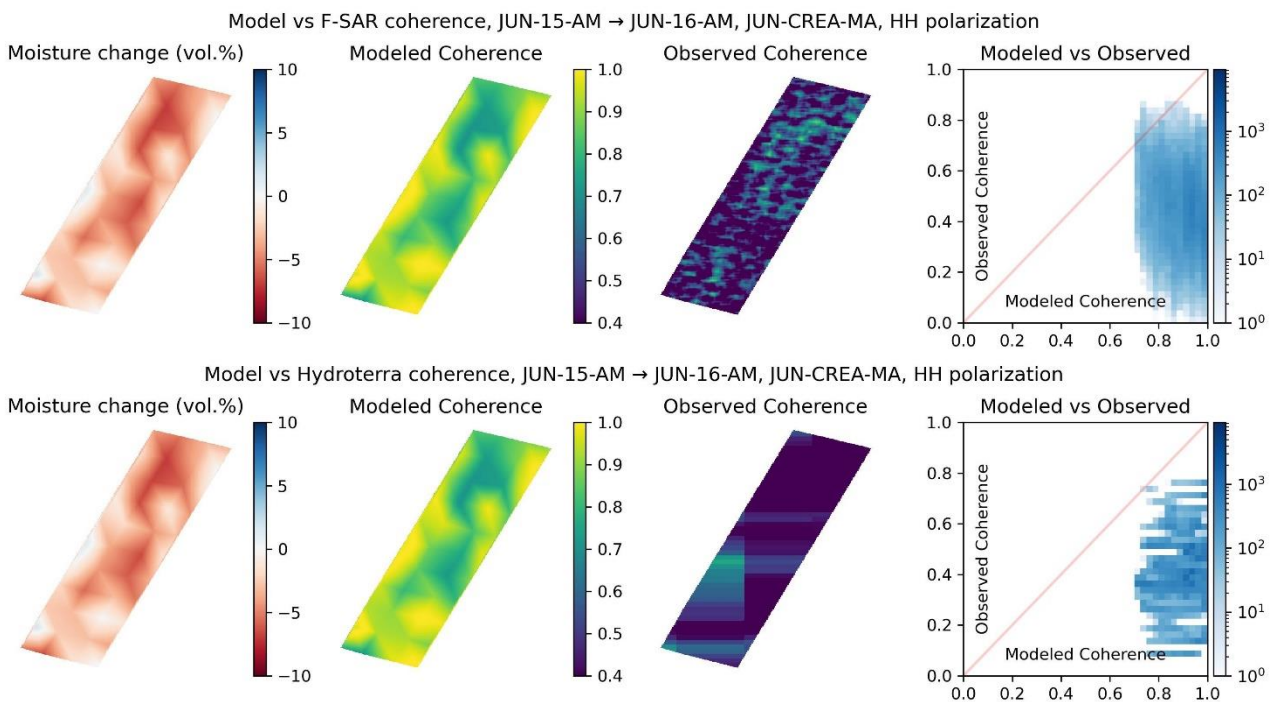
Figure 6-25: Comparison of the modelled and observed coherence, JUN-CREA-MA field, 24 hours between acquisitions. Top: F-SAR; Bottom: Hydroterra.

The JUN-CREA-MA maize field shows a change of soil moisture of a few percent (Figure 6-24). Low coherence is observed (Figure 6-25) for F-SAR and Hydroterra.

6.4.7 Caione Maize Field (JUN-CAIONE-MA)
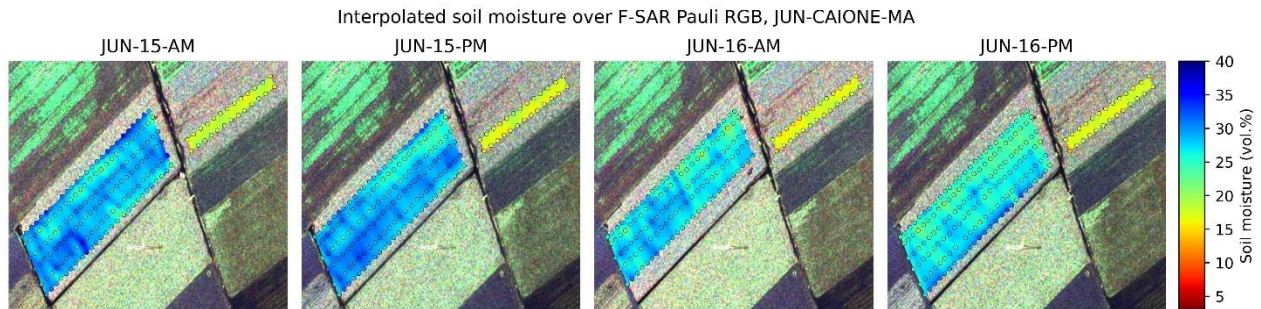
Figure 6-26: Interpolated soil moisture over the JUN-CAIONE-MA maize fields for the four flights in June. Three adjacent strips on one field and an additional strip on a neighboring field were monitored. The background is a Pauli RGB image.
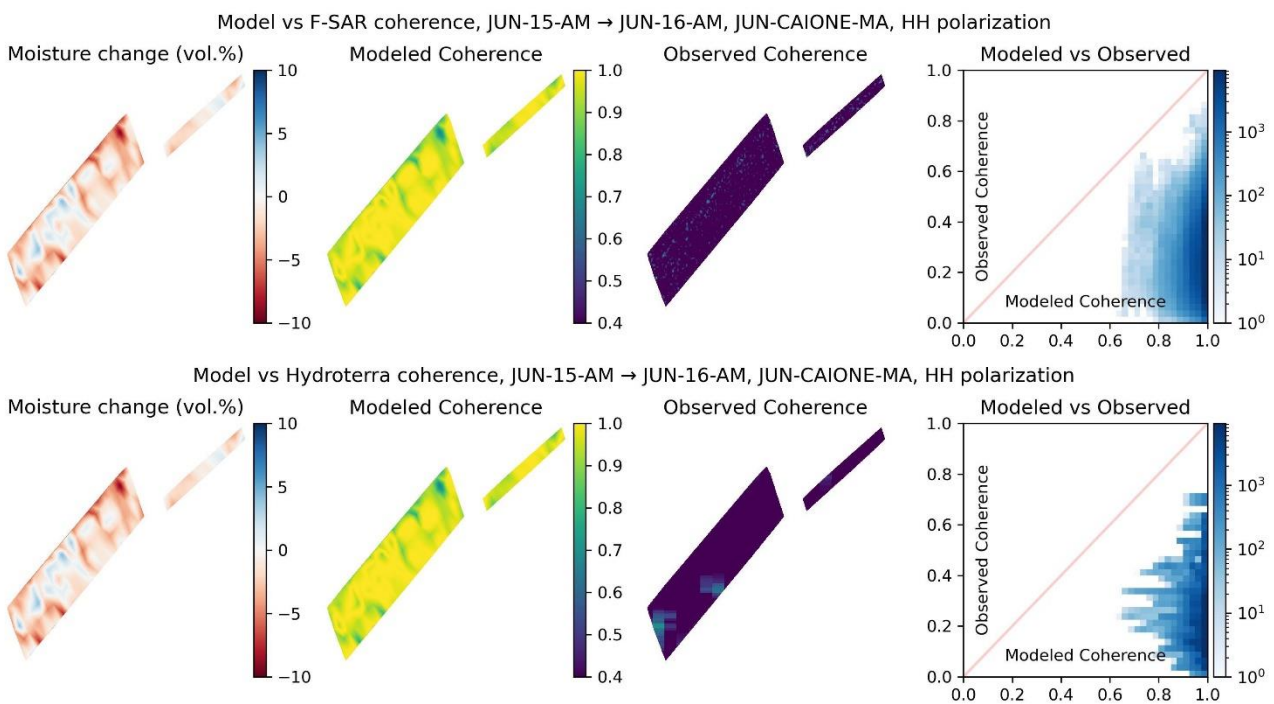
Figure 6-27: Comparison of the modelled and observed coherence, JUN-CAIONE-MA field, 24 hours between acquisitions. Top: F-SAR; Bottom: Hydroterra.

Additional JUN-CAIONE-MA maize fields were monitored at the Caione farm. The soil moisture time series is shown in Figure 6-26. The fields show very low coherence (most values below 0.4), even lower than the JUN-CREA-MA field.

| | SARSimHT-NG – Simulation of Hydroterra SAR System Performance in the Mediterranean and the Alps Based on Experimental Airborne SAR Data

D3: Final Report | Doc.: DLR-HR-TR-SARSimHT-NG-03

Issue: 1.1

Date: 12.09.2024 |

6.4.8 Alfalfa Field (JUN-CAIONE-AA)
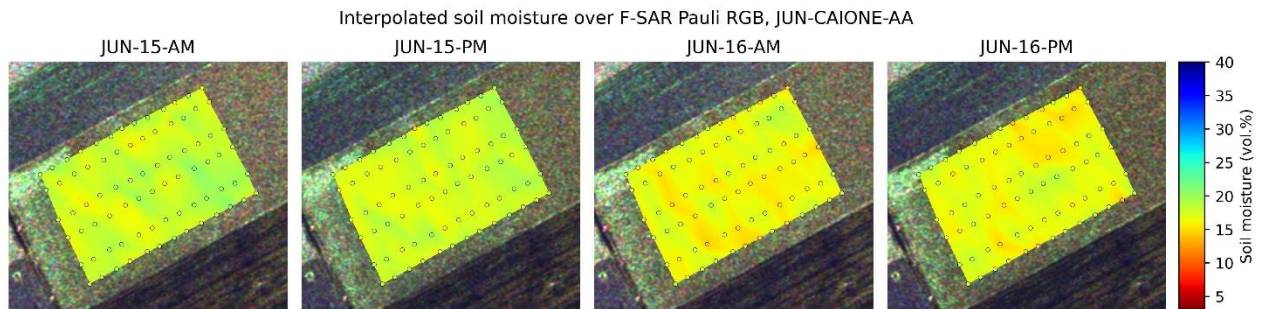
Figure 6-28: Interpolated soil moisture over the JUN-CAIONE-AA alfalfa field for the four flights in June. The background is a Pauli RGB image.
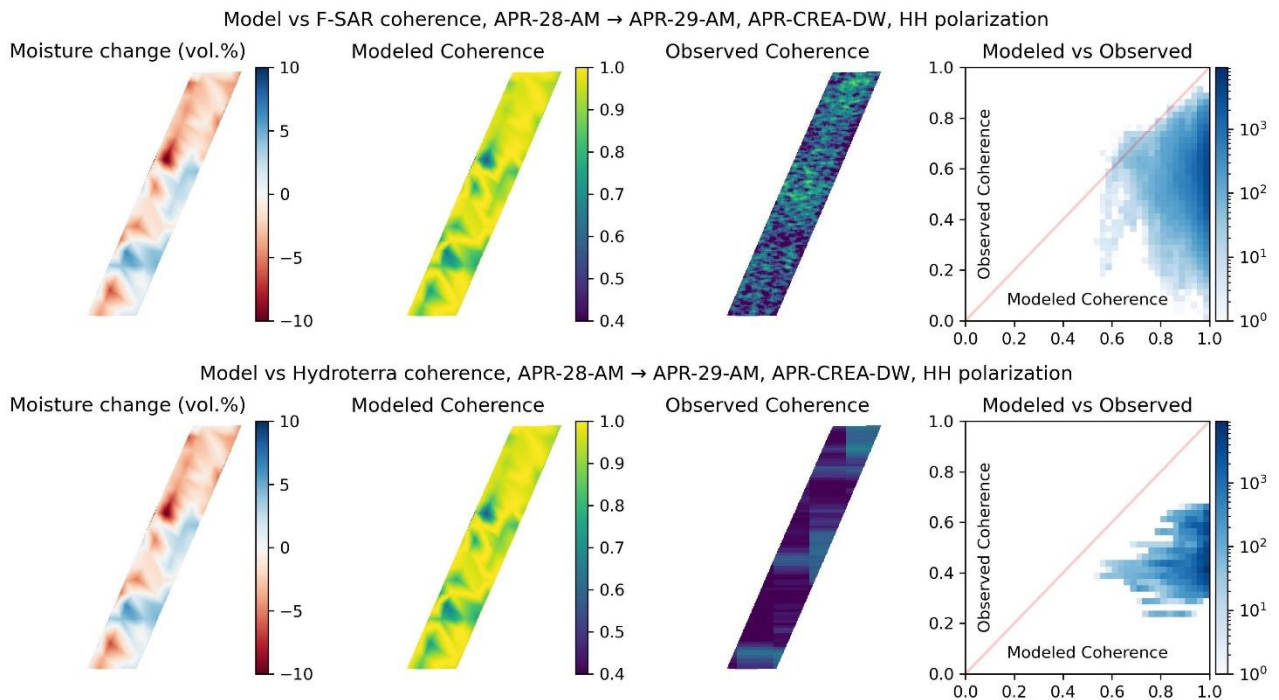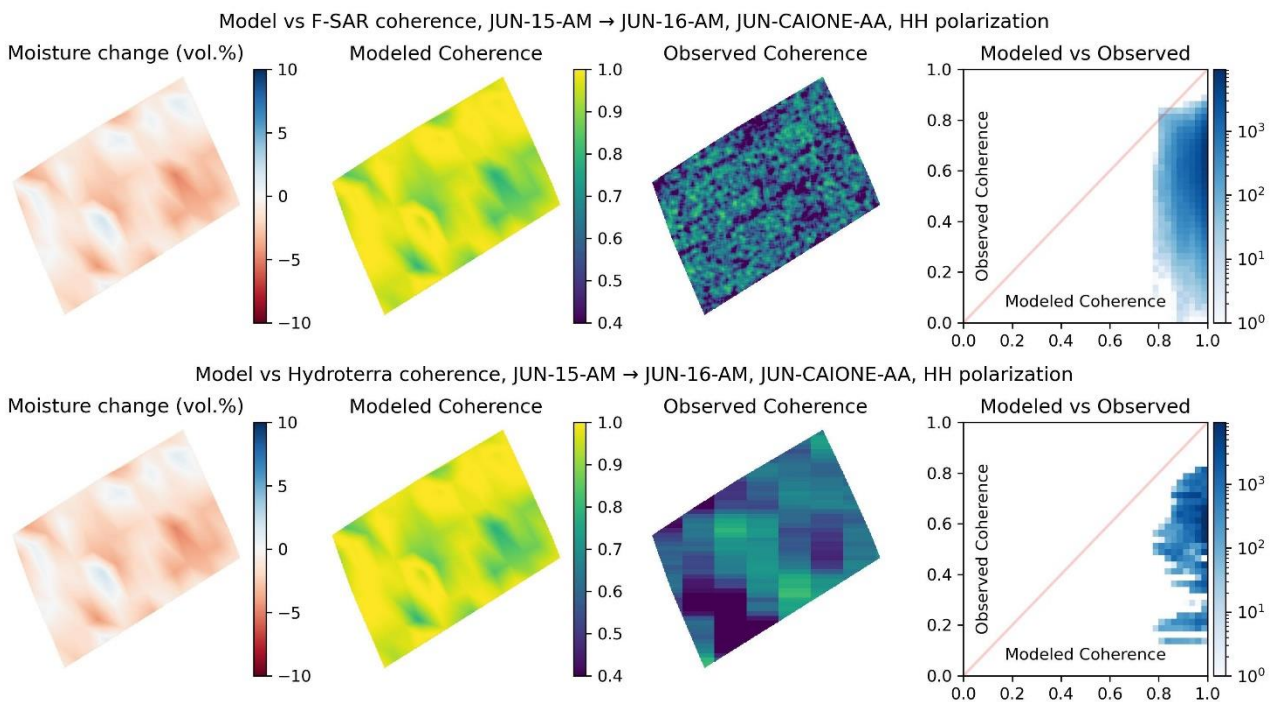

Figure 6-29: Comparison of the modelled and observed coherence, JUN-CAIONE-AA field, 24 hours between acquisitions. Top: F-SAR; Bottom: Hydroterra.

The JUN-CAIONE-AA alfalfa field shows a minimal decrease in soil moisture (Figure 6-28). The vegetation introduces additional decorrelation as shown in Figure 6-29.

6.5   Soil Moisture Retrieval

6.5.1   Model Inversion

Soil moisture can be estimated from several acquisitions by inverting the model. The general idea is to find soil moisture values that produce coherence and triplet values similar to the observed values. We follow the approach from [21] and use both the coherence magnitude and the triplets for the inversion. The goal is to minimize the following loss L:

$$L = \sum_{n>m>k} \left|\varphi_{n,m,k} - \varphi'_{n,m,k}\right|^2 + \sum_{n>k} \left|\gamma_{n,k} - \gamma'_{n,k}\right|^2 \tag{6-24}$$

where $\varphi'_{n,m,k}$, $\gamma'_{n,k}$ are the observed and $\varphi_{n,m,k}$, $\gamma_{n,k}$ are the modelled triplets and coherence, respectively.

This optimization problem can be solved iteratively using gradient descent. First, the soil moisture values are initialized either randomly or at expected values (if available). Then, in every iteration, the soil moisture values are passed through the physical model to obtain the predicted values $\varphi_{n,m,k}$ and $\gamma_{n,k}$.

The predicted values are then compared with the observed values $\varphi'_{n,m,k}$ and $\gamma'_{n,k}$ to compute the loss L. Automatic differentiation is then applied to obtain the gradients of the current soil moisture values with respect to L. The gradients are used to adjust the soil moisture values to make the loss L smaller. This process is repeated until convergence, producing soil moisture values that best fit the observed coherence and triplet values.

There are several points to keep in mind regarding the minimization process. Firstly, methods based on gradient descent can get stuck in a local minimum if the optimization problem is not convex. Therefore, it might be necessary to re-run the minimization several times with different starting conditions to find the global minimum. Secondly, the phases and phase differences should always be expressed in the interval $[-\pi, \pi]$. Thirdly, the soil moisture values should be constrained to a physically valid range (e.g. 0% to 100%) during the optimization. Lastly and most importantly, one of the soil moisture values must be known and fixed to that value (see details in [21]). Otherwise, there can be several solutions that reconstruct the observed interferometric parameters well.
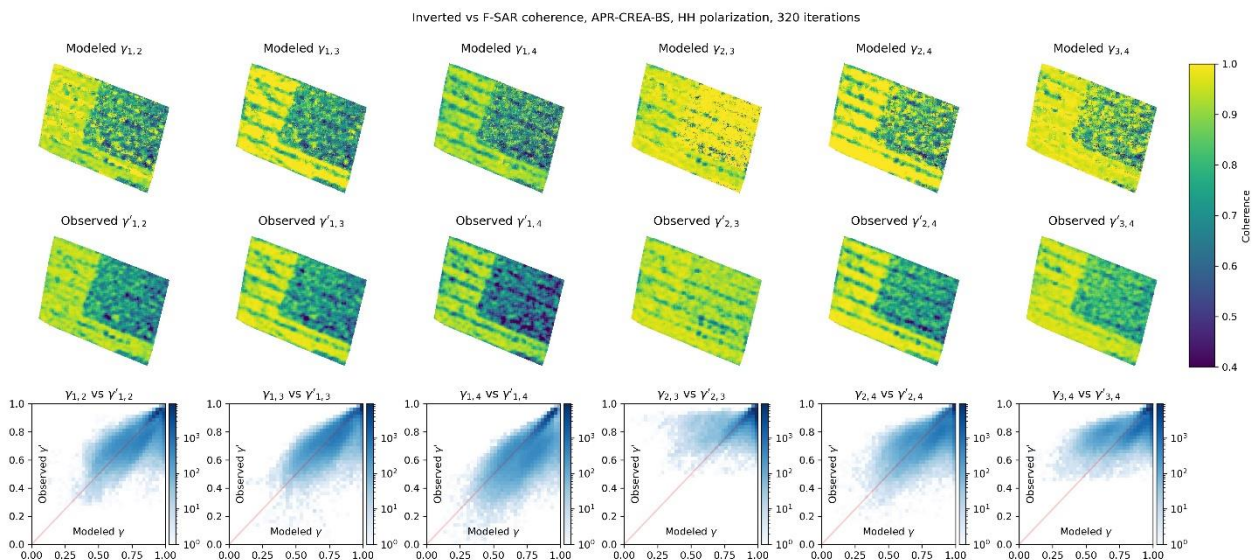
Figure 6-30: Comparison of inverted modelled coherence (top row) and observed F-SAR coherence (middle row). Each column represents one acquisition pair, ranging from (1, 2) on the left to (3, 4) on the right.

6.5.2 Retrieval from F-SAR Data

We first estimate soil moisture from the F-SAR data to validate the inversion algorithm. The APR-CREA-BS bare field is chosen for inversion to minimize the effects of vegetation. All four flights in April are used, resulting in 6 coherence pairs and four triplets for each pixel. The algorithm then has to find four soil moisture values that best model the observed coherence and triplets. Each pixel is inverted independently of the others.

One of the soil moisture values is required to be known during the inversion. We use the ground measurements on APR-28-AM as the known value, while the other measurements in April are used for validation. Furthermore, the algorithm requires initial soil moisture values. Since the moisture on APR-28-AM is already used in the inversion, all moisture values are initialized with it. During the inversion, the algorithm solves an optimization problem and iteratively adjusts the initial values to minimize the difference between the observed and modelled triplets and coherence magnitudes.

Figure 6-30 shows the modelled and observed coherence values after 320 iterations. The algorithm successfully finds moisture values that produce coherence values close to the observed ones, as shown in the histograms in the bottom row. Figure 6-31 shows the observed and modelled triplets. Similar to the coherence, the modelled triplets agree well with the observed values.
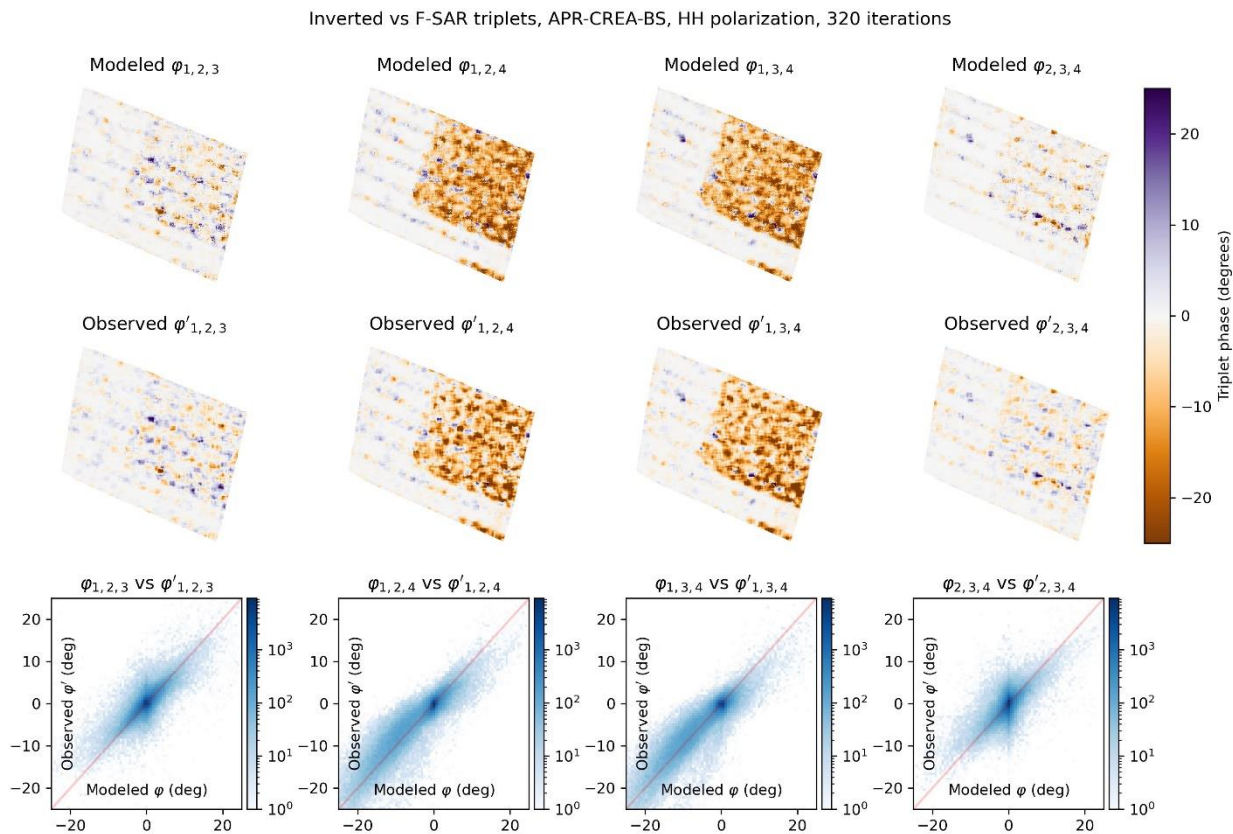
Figure 6-31: Comparison of inverted modelled triplets (top row) and observed F-SAR triplets (middle row). Each column represents one triplet, ranging from (1, 2, 3) on the left to (2, 3, 4) on the right.

Figure 6-32 shows the retrieved soil moisture values and compares them to the ground measurements. Note that the first retrieved value for APR-28-AM is fixed and is identical to the ground measurements. The results are noisier in the areas with low coherence and deviate more from the measured values. The model interprets low coherence as a strong change in soil moisture and tries to increase the difference

between the predicted soil moisture values. Some form of spatial averaging or regularization can be helpful here. In the dry areas with little change and high coherence, the retrieved values are more stable, and the predictions match the observations well.

We observe two types of deviation in the wet areas that are drying over time. Some pixels show an overestimation of soil moisture, while others show a small underestimation. The two over- and under-estimation clusters are best seen for measured moisture above 20 vol.% in the right histogram ($m_{v,4}$ on APR-29-PM) in the bottom row of Figure 6-32. One cluster shows an overestimation, while the other shows a small underestimation. These results are common in image areas with coherence significantly lower than the expected coherence decrease predicted by the forward model.

Generally, the inverted spatial patterns are consistent with the measured soil moisture. This result is expected since the spatial patterns during the first acquisition are similar to all others. In fact, using the first known soil moisture directly as a prediction for the others (without any inversion) produces results of similar quality. A longer time series (e.g. several days) that covers the time before and after irrigation (or a rain event) would be more interesting to invert.
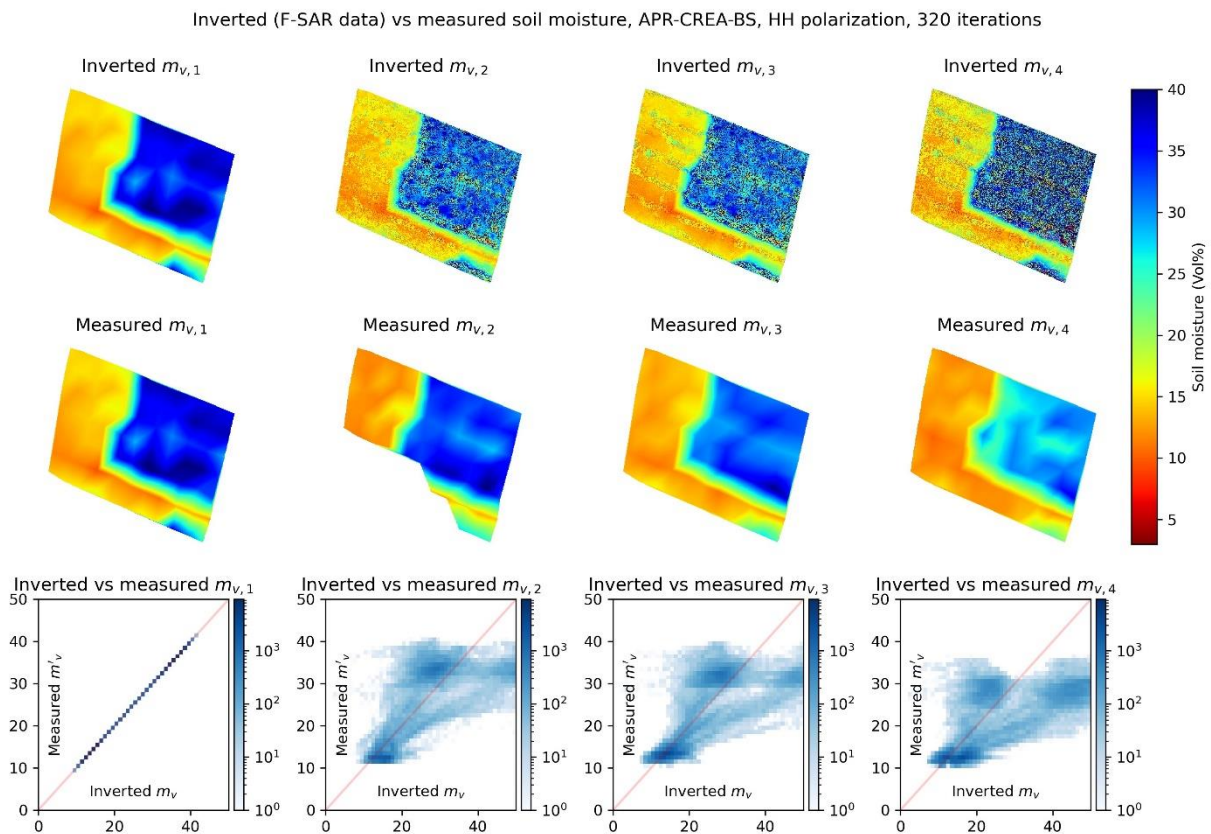
Figure 6-32: Comparison of inverted (top row) and measured (middle row) soil moisture. Each column represents one time period (or flight), ranging from APR-28-AM on the left to APR-29-PM on the right. The first moisture value (APR-28-AM) is fixed to the measured value during the inversion.

6.5.3 Retrieval from Simulated Hydroterra Data

The simulated Hydroterra SLCs are only available for three flights in April. Since there are too many changes on the ground, combining flights between April and June is not feasible. Therefore, only one phase-triplet and three coherence pairs can be formed. With one soil moisture value required to be known and fixed, two others can be inverted. While this inversion setup has even fewer changes in soil moisture than with four F-SAR flights, we provide the results for completeness.

Figure 6-33 shows the observed and inverted coherence magnitudes and the single triplet. The inversion algorithm has more difficulties in finding soil moisture values to approximate the observed Hydroterra coherence in comparison to F-SAR. The observed coherence is low in some parts of the image in every acquisition pair. Large differences in soil moisture between each acquisition are required to model this. With the first moisture value fixed, one other moisture value has to be larger, while the third value has to be smaller.

Note, that the soil moisture was measured at a finer spatial resolution than the observed Hydroterra coherence. Therefore, there are different measured moisture values within one Hydroterra pixel. This variability leads to different inverted coherence values for the same observed coherence, appearing as noisy results in some image areas.

The reconstructed phase-triplets show a better agreement with the observed triplet values. The spatial patterns match the observed data, and the triplet histogram in the bottom row on the right of Figure 6-33 shows clear correlation.
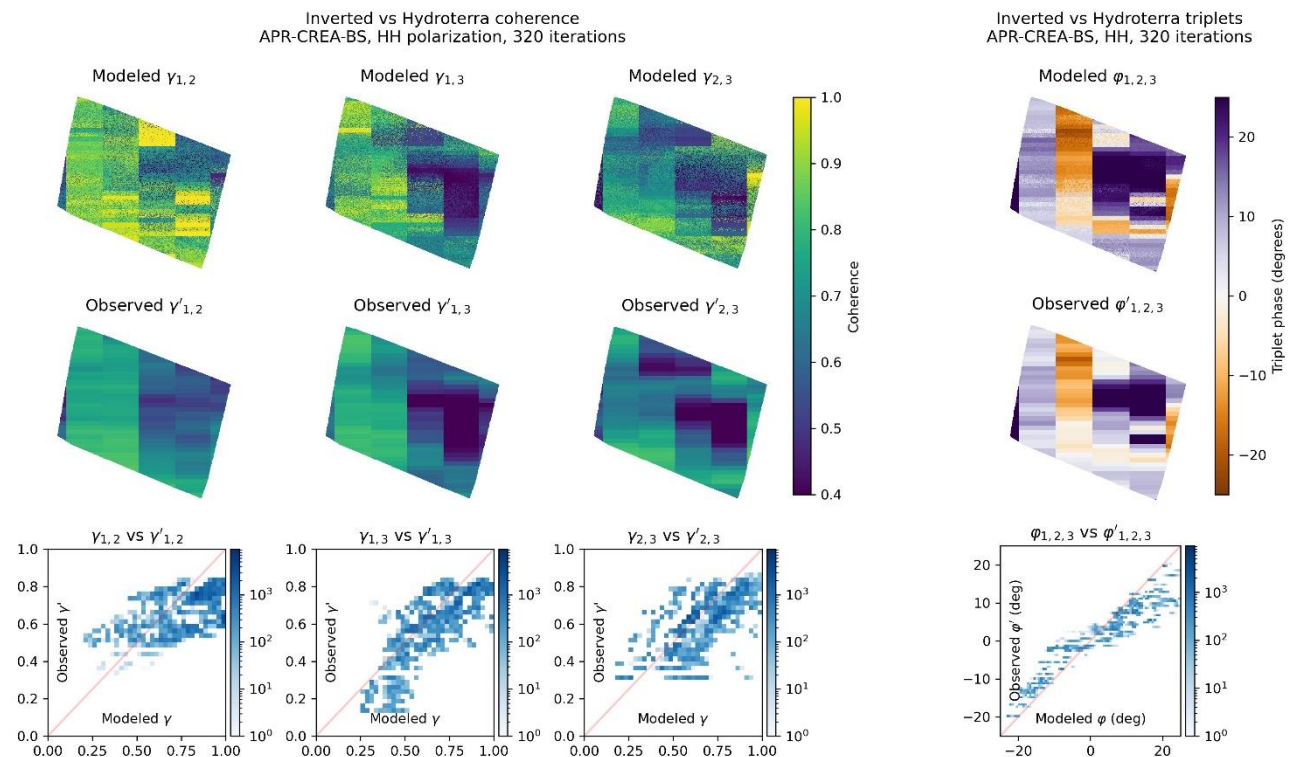
Figure 6-33: Comparison of the inverted interferometric parameters (top row) and the observed Hydroterra parameters (middle row). The first three columns show the coherence for each acquisition pair: (1, 2), (1, 3), and (2, 3), from left to right. The last column shows the single phase-triplet (1, 2, 3).

Figure 6-34 shows the inverted soil moisture from the simulated Hydroterra data. The first value (left column) is fixed to the observed values. Compared to F-SAR, the moisture inverted from the simulated

Hydroterra data appears to be noisier, having a larger variance around the observed values. The spatial moisture patterns match the observations, which is expected, given the limited changes in moisture within 24 hours.
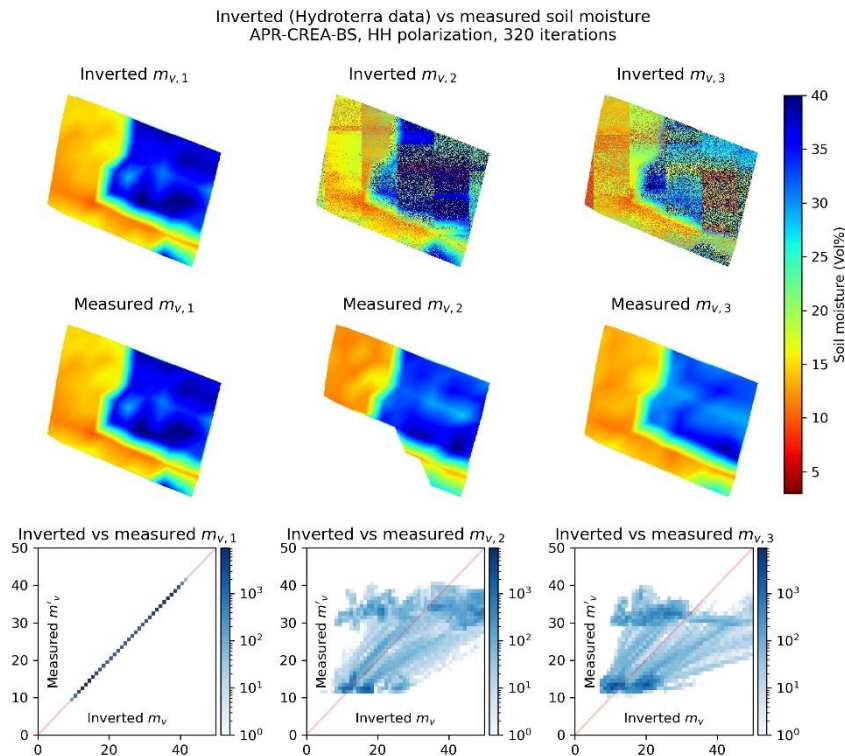
Figure 6-34: Comparison of the inverted (top row) and measured soil moisture (middle row). Each column represents one time period (or flight): APR-28-AM (left), APR-28-PM (centre), and APR-29-AM (right). The first moisture value (APR-28-AM) is fixed to the measured value during the inversion.

6.6 Discussion

6.6.1 Model Limitations

The physical model has several limitations when applied to the real-world scenarios.

Firstly, the model assumes constant soil moisture at every depth and a uniform scatterer density in the vertical direction. These assumptions are reasonable for C-band, where the penetration into the soil is assumed to be small but may be problematic for longer wavelengths.

Secondly, the inversion requires one soil moisture value to be known. This requirement limits the practical applicability of the model. In addition, the moisture values should be measured at the correct depth to match the dielectric constant seen by the radar. Precise measurements may be difficult since the penetration depth changes with the soil moisture.

Lastly, and more importantly, the model does not consider the decorrelation effects of the vegetation on top of the field. Interferometric coherence and phase changes are solely attributed to changes in soil moisture. While this might be of lesser concern at L-band, we see strong vegetation effects at C-band. Therefore, the model is only applicable to areas with no or very low vegetation. For most crops, the observed decorrelation is significantly higher than the model predictions.

6.6.2 Hydroterra Resolution

Compared to F-SAR, the simulated Hydroterra data has a significantly lower resolution and more noise. This fact makes the soil moisture estimation at the field scale challenging, especially when the fields are small. There is a trade-off in the spatial resolution and accuracy of the estimated interferometric parameters. A small spatial multi-look window is preferred if the fields are small or the soil moisture changes significantly within a small distance (e.g. due to irrigation). A large multi-look window lowers the coherence bias but may mix fields with different crop types or irrigation practices.

7 Conclusions

7.1 Snow Mass Retrieval and Performance Evaluation of the SWE Experiment

The main objective of the work presented in Section 4 of this report is concerned with the implementation, testing and evaluation of procedures for retrieving the snow mass (SWE) accumulating during specific time intervals by inversion of repeat-pass interferometric SAR (RP-InSAR) data. The remote sensing data for this study are based on multiple C- and L-band repeat-pass SAR acquisitions along two tracks, acquired by the airborne F-SAR system over the test site Wörgetal, Stubaier Alpen, on 7 days between 2 and 19 March 2021. The data are spanning two snow fall events of different intensity, with mean snow accumulation (ΔSWE) amounting to 13mm on 5 March for snowfall event SE1 and to 64mm between 14 and 18 March for snowfall event SE2. Ground-based snow measurements on physical snow properties and stratification were performed in snow pits; snow depth and SWE were measured along transects. The in-situ measurements spread across three comparatively level sections of Wörgetal, with mean elevations of 2095m, 2250m and 2335m above sea level. The analysis of backscatter and interferometric signatures and the evaluation of ΔSWE retrievals focus on these sections (RoIs), on one hand, for achieving direct comparisons with in-situ data, on the other hand, because signatures on steep lateral slopes are affected by topography-related noise. The RoIs were not affected by surface melt during the F-SAR flights, whereas on steep east- and south-facing slopes transient melt of the snow surface layer was observed on some days around noon.

The analysis of backscatter and interferometric signatures and the generation and evaluation of ΔSWE retrievals were performed for full resolution F-SAR data and for simulated Hydroterra (HT) products. In both cases the phase of corner reflectors, cleaned of snow, is used as reference for zero snow accumulation in order to determine the snowfall-related change in phase. Uncertainty estimates show that the reference phase is a critical factor for the performance of the retrieved ΔSWE, whereas the impact of random phase noise can effectively be reduced by increasing the estimation windows.

For intervals without snowfall the coherence of the full resolution F-SAR data is high, both in C-band and L-band. The coherence benefits from estimation windows with large number of looks using the high-resolution data. The interferograms of different time intervals between 2 and 8 March 2021, spanning snowfall event SE1, show that the inclusion of snow-free days is of little relevance for the coherence: The partial temporal decorrelation in these interferograms can largely be attributed to the accumulated snow. The mean C-band RoI coherence $|\gamma|$ of data spanning SE1 decreases in C-band to 0.75 compared to ≥ 0.9 for the period without snowfall, whereas L-band coherence remains above 0.9. For SE2 the change in the C-band interferometric phase exceeds the 2π phase ambiguity and the associated differential change in the propagation path through the snowpack causes major temporal decorrelation. L-band shows also for data spanning SE2 comparatively high coherence (except on steep back-slopes). The mean $|\gamma|$ for the two upper RoIs is 0.85, for the lower RoI (with rough terrain) $|\gamma|$ is 0.6. This confirms the usefulness of L-band RP-InSAR for obtaining useful estimates of SWE also in case of snowfall events of moderate to high intensity.

The differences of computed minus observed RP-InSAR ΔSWE of individual RoIs range for SE1 for C-band track 10 from -3.2mm to +0.9mm, for C-band track 11 from -0.2mm to +3.8mm, for L-band track 10 from -3.5mm to -0.9mm, for L-band track 11 from -0.6mm to +4.8mm. For SE2 the corresponding numbers range for L-band track 10 from +1.7mm to +13.0mm, for L-band track 11 from -7.1mm to +1.0mm. The differences between HH and VV polarisation are very small. The mean computed ΔSWE of the three RoIs, based on data of both tracks, agrees well with the mean in-situ SWE. The differences in mean ΔSWE (computed – in-situ) are +0.8mm for C-band SE1, -0.3mm for L-band SE1, and +1.8mm for L-band SE2. L-band shows lower sensitivity of the phase in respect to SWE, but offers in comparison to C-band a major extension of the measurement range for ΔSWE and is less susceptible to temporal decorrelation.

Geosynchronous SAR systems, offering frequent repeat observation capability, can help to overcome constraints of temporal decorrelation and 2π phase ambiguity. The related analysis of coherence and phase and the feasibility study on SWE retrievals is based on simulated C-band Hydroterra products which account for the resolution, pixel size, number of samples and NESZ of the proposed Hydroterra system [A2]. The resolution of this product differs in azimuth x range (5m x 22.13m). This has an impact on the representation of topographic features (mountain slopes, ridges, etc.), depending on the orientation of these features in respect to the radar coordinates. For the SWE feasibility study presented here this is of minor concern because the analysis focuses on three RoIs with moderate topography.

The low resolution of the simulated HT products is not suitable for obtaining reliable phase numbers of the corner reflectors that are used as reference for zero ΔSWE. Therefore, the corner reflector phase values of the simulated F-SAR high resolution HT products are used as reference. The ΔSWE analysis was performed for snowfall SE1, using the simulated HT products of the flights FL01 – FL05 based on track 10 and track 11 data. The product FL02 and FL08 (spanning 16 days including SE1 and SE2) is not suitable for such an analysis because the signal is almost completely decorrelated and the snowfall amount exceeds the 2π ambiguity more than two-fold. However, such problems can be overcome by means of geosynchronous SAR systems, providing dense time series.

The simulated HT data spanning the snow fall event SE1 show lower coherence than the high-resolution F-SAR product due to the smaller number of looks of the estimation windows. However, suitable phase accuracy can still be achieved. In case of $|\gamma|$ = 0.5 the phase uncertainty is 0.26rad for a 50m x 50m HT window (ENL = 22.5), yielding C-band ΔSWE uncertainty of about 1mm. The computed ΔSWE values of the three RoIs, derived from simulated HT data agree well with the measurement requirements for operational and scientific applications. The mean difference between observed and computed ΔSWE for track 10 is -0.4mm and for track 11 2.6mm. The maximum ΔSWE differences of individual sites are 2.6mm for track 10 and 4.0mm for track 11. These numbers include also uncertainties of the in-situ data that are based on point measurements.

These investigations indicate the suitability of geosynchronous SAR as useful tool for continuous monitoring of changes in SWE as long as the snowpack is dry. For comprehensive assessment of possibilities and constraints of geosynchronous SAR for SWE monitoring, further studies on impacts of snowfall intensity regarding coherence and on effects of observation geometry over complex terrain are needed. For assessing potential applications over specific mountain areas, such as the Alps, it is necessary to check constraints due to the oblique view of geosynchronous SAR using actual topographic data.

7.2   SSM Retrieval from Polarimetric SAR Products

The analysis of the SARSimHT-NG SAR and ground data set presented in Section 5 provides insights into the complementarity of multi-frequency SAR acquisitions and the capability of hyper-temporal SAR data to monitor sub-daily dynamics of irrigation water in soil and crops over a Mediterranean agricultural area. Although the ground data included a variety of crops, the present study focuses on winter wheat, the main crop of the area, and maize due to their different structure and radar response.

The analysis highlights the following findings:

- Due to an increasing contribution from volume scattering, the sensitivity of C-band backscatter to changes in SSM decreases as the angle of incidence increases from 40° to 50°. The interplay of the different scattering mechanisms depends on the crop structure, its stage of development, and the SAR's polarisation and frequency. In comparison, L-band is less affected by the volume contribution at 50° incidence than C-band. In this regard, L-band plays a pivotal role in complementing C-band observations. The integration of multi-frequency/multi-mission SAR observations is essential to enable spatial and temporal continuity in SSM monitoring;

- hyper-temporal SAR observations can resolve rapid soil and vegetation water dynamics in various land processes. For example, a sub-daily revisit can detect transient effects of water interception by vegetation. The data collected during the two campaigns in spring 2022 [A3] support the conclusion that C-band is more sensitive than L-band in detecting the change in water content of wheat;

- high spatial resolution is needed to capture the fine-scale dynamics of irrigation that affect the field or sub-field scale. Conversely, the long integration time of geosynchronous SAR imagery does not preclude the detection of rapid changes in irrigated areas.

The main activities that should be the subject of further work are:

- Extension of the analysis to other irrigated and non-irrigated crops on the trial site;

- systematically retrieve SSM time series from F-SAR C- and L-band data over the entire site and compare patterns with SSM retrieved from Sentinel-1 and SAOCOM or ALOS data. Indeed, in view of the upcoming ROSE-L mission, there is a need to develop and evaluate schemes to optimise the integration of C- and L-band for SSM retrieval;

- a more in-depth analysis of the SARSimHT-NG data set, which can also support the Hydroterra+ candidate mission for ESA's Earth Explorer 12 programme. In particular, it would be beneficial to complement the analysis with data from the Hydrosoil experiment at UPC, which investigated the hyper-temporal radar response of crops at angles of incidence greater than 50°.

7.3   SSM Retrieval from Interferometric SAR Products

As shown in Section 6 the retrieval of surface soil moisture using coherence and phase-triplets obtained from repeat-pass interferometric products remains challenging with the evaluated physical model. Most crops, especially in agricultural areas, introduce a significant decorrelation and require a more complex model. The results over bare surfaces show a better match between the observed interferometric parameters and the model. Still, the model cannot fully explain the observed coherence and triplets based on changes in soil moisture. The simulated Hydroterra data shows a significantly lower coherence than predicted by the model. In addition, the phase-triplets are noisier than expected and do not match the model predictions well. The inverted soil moisture from Hydroterra data over a bare field shows similar spatial patterns to the measured values. However, this is mainly attributed to the first known moisture value and little change in the spatial moisture patterns during the campaign.

In summary, the results of this study indicate that the retrieval of soil moisture under vegetation requires a better interferometric model. Compared to F-SAR, the lower Hydroterra spatial resolution and more noise make the retrieval more challenging. However, the main limitation comes from the low agreement of the model and the observed interferometric parameters.

In the following, some recommendations to different items for future studies are listed.

Model improvements – In order to be effective over agricultural areas at C-band, the physical model needs to be improved and take the vegetation effects into account. Originally, the model was proposed for the L-band where more ground is visible due to the deeper penetration of the longer wavelengths. However, at C-band, the vegetation cannot be ignored and has a strong contribution on the signal. The effects on the interferometric phase and triplets require further intensive investigation.

Longer time series – Future campaigns focusing on repeat-pass interferometry should include a longer time series of observations. In the 22HTERRA campaign, the evaluation is limited by the number of flights and measurements [A3]. For example, only one phase-triplet per mission can be formed for the simulated Hydroterra data. The evaluation of a single phase-triplet is not significant and the interpretation is difficult. In addition, each campaign mission (April and June) covers only two days and the observed change in soil moisture is limited.

Soil moisture variability – A large soil moisture change is preferred for model evaluation. Irrigating the fields during the campaign is an interesting idea and is useful to create such changes. However, acquisitions before <u>and</u> after the irrigation are required to capture the changes, preferably supported by dense ground measurements. For the current campaign, dense ground measurements are only available either before or after the irrigation.

Soil moisture measurements at different depths – The penetration into the ground depends on the soil moisture and the wavelength. If the radar only sees the top layer while the moisture is measured deeper, low agreement between the data and the model is expected. Therefore, it is useful to have data for soil moisture at different depths, preferably on a dense grid.

Longer wavelengths – The evaluated model was originally proposed for L-band and it would be interesting to perform similar analysis at L-band, especially with respect to the planned L-band satellite missions such as NISAR and ROSE-L.

8 Summary

Hydroterra is a concept for a C-band SAR satellite in geosynchronous orbit and was proposed as such in ESA's Earth Explorer 10 mission call in 2018. It would cover Africa and the Mediterranean region to improve the understanding and prediction of rainfall and water availability, floods and landslides.

In 2019, a first airborne SAR experiment with DLR's F-SAR radar system was conducted over the Kaufbeuren calibration test site. The subsequent SARSimHT study [1] used these data to demonstrate the image formation process of Hydroterra by exploiting a zero-baseline repeat-pass multi-temporal airborne SAR image stack.

In the following years, DLR organised two more science-related F-SAR C- and L-band radar campaigns in cooperation with partners in Austria and Italy.

1. The 21HTERRA mission in March 2021 in collaboration with ENVEO IT in Innsbruck (Austria). The objective of the mission was snow water equivalent (SWE). The test site was the Wörgetal in the Tyrolean Alps.
2. The 22HTERRA campaign consisting of two flight missions in April and June 2022 in collaboration with CNR-IREA and CREA-IC in Bari and Foggia (Italy). The test site was part of the 'Apulian Tavoliere', located on the western outskirts of the city of Foggia. The objective of the mission was surface soil moisture (SSM).

The present SARSimHT-NG study, which builds on the results of the previous SARSimHT study, uses these newer data sets to investigate the measurement concept of Hydroterra and geostationary SAR in general to retrieve soil moisture and snow water equivalent [A1].

This Final Report presents the results and conclusions of the analyses carried out with respect to the environmental parameters, SWE and SSM. While the focus was mainly on geostationary SAR, some implications for the upcoming LEO missions, ROSE-L and Sentinel-1 NG, are also provided.

9 Appendix

9.1 Inventory of Input Data

Table 9-1 lists all the geocoded data products generated from conventional (F-SAR) and simulated Hydroterra SAR (GEO and HT) SLC data products that were used as input for the study conducted during WP 240.

The products listed have the size of the full 'Apulian Tavoliere' scene. Cut-outs of individual AoIs, e.g. farms and fields, were generated using their bounding polygons which were provided as part of the SSM database (for details see Section 3.6 of the DAR [A3]).

The files in Table 9-1 with no extension are the geocoded images (visualisation of contrast, magnitude and coherence) used in the study. They can be opened in QGIS, for example, using their ENVI header *.hdr files. All data (288 pairs of image and header files) are archived at DLR.

Table 9-1: List of all the input data products used for the study conducted during WP 240.

Mission	Contrast	Amplitude	Coherence
April	contrastgeo_22hterra_GEO-long_FL01-HH	amplitudegeo_22hterra_GEO-long_FL01-HH	coherencygeo_22hterra_GEO-long_FL01-FL02-HH
April	contrastgeo_22hterra_GEO-long_FL01-HH.hdr	amplitudegeo_22hterra_GEO-long_FL01-HH.hdr	coherencygeo_22hterra_GEO-long_FL01-FL02-HH.hdr
April	contrastgeo_22hterra_GEO-long_FL01-HV	amplitudegeo_22hterra_GEO-long_FL01-HV	coherencygeo_22hterra_GEO-long_FL01-FL02-HV
April	contrastgeo_22hterra_GEO-long_FL01-HV.hdr	amplitudegeo_22hterra_GEO-long_FL01-HV.hdr	coherencygeo_22hterra_GEO-long_FL01-FL02-HV.hdr
April	contrastgeo_22hterra_GEO-long_FL01-VH	amplitudegeo_22hterra_GEO-long_FL01-VH	coherencygeo_22hterra_GEO-long_FL01-FL02-VH
April	contrastgeo_22hterra_GEO-long_FL01-VH.hdr	amplitudegeo_22hterra_GEO-long_FL01-VH.hdr	coherencygeo_22hterra_GEO-long_FL01-FL02-VH.hdr
April	contrastgeo_22hterra_GEO-long_FL01-VV	amplitudegeo_22hterra_GEO-long_FL01-VV	coherencygeo_22hterra_GEO-long_FL01-FL02-VV
April	contrastgeo_22hterra_GEO-long_FL01-VV.hdr	amplitudegeo_22hterra_GEO-long_FL01-VV.hdr	coherencygeo_22hterra_GEO-long_FL01-FL02-VV.hdr
April	contrastgeo_22hterra_GEO-long_FL02-HH	amplitudegeo_22hterra_GEO-long_FL02-HH	coherencygeo_22hterra_GEO-long_FL02-FL03-HH
April	contrastgeo_22hterra_GEO-long_FL02-HH.hdr	amplitudegeo_22hterra_GEO-long_FL02-HH.hdr	coherencygeo_22hterra_GEO-long_FL02-FL03-HH.hdr
April	contrastgeo_22hterra_GEO-long_FL02-HV	amplitudegeo_22hterra_GEO-long_FL02-HV	coherencygeo_22hterra_GEO-long_FL02-FL03-HV
April	contrastgeo_22hterra_GEO-long_FL02-HV.hdr	amplitudegeo_22hterra_GEO-long_FL02-HV.hdr	coherencygeo_22hterra_GEO-long_FL02-FL03-HV.hdr
April	contrastgeo_22hterra_GEO-long_FL02-VH	amplitudegeo_22hterra_GEO-long_FL02-VH	coherencygeo_22hterra_GEO-long_FL02-FL03-VH
April	contrastgeo_22hterra_GEO-long_FL02-VH.hdr	amplitudegeo_22hterra_GEO-long_FL02-VH.hdr	coherencygeo_22hterra_GEO-long_FL02-FL03-VH.hdr
April	contrastgeo_22hterra_GEO-long_FL02-VV	amplitudegeo_22hterra_GEO-long_FL02-VV	coherencygeo_22hterra_GEO-long_FL02-FL03-VV
April	contrastgeo_22hterra_GEO-long_FL02-VV.hdr	amplitudegeo_22hterra_GEO-long_FL02-VV.hdr	coherencygeo_22hterra_GEO-long_FL02-FL03-VV.hdr
April	contrastgeo_22hterra_GEO-long_FL03-HH	amplitudegeo_22hterra_GEO-long_FL03-HH	coherencygeo_22hterra_GEO-long_FL03-FL01-HH
April	contrastgeo_22hterra_GEO-long_FL03-HH.hdr	amplitudegeo_22hterra_GEO-long_FL03-HH.hdr	coherencygeo_22hterra_GEO-long_FL03-FL01-HH.hdr
April	contrastgeo_22hterra_GEO-long_FL03-HV	amplitudegeo_22hterra_GEO-long_FL03-HV	coherencygeo_22hterra_GEO-long_FL03-FL01-HV
April	contrastgeo_22hterra_GEO-long_FL03-HV.hdr	amplitudegeo_22hterra_GEO-long_FL03-HV.hdr	coherencygeo_22hterra_GEO-long_FL03-FL01-HV.hdr
April	contrastgeo_22hterra_GEO-long_FL03-VH	amplitudegeo_22hterra_GEO-long_FL03-VH	coherencygeo_22hterra_GEO-long_FL03-FL01-VH
April	contrastgeo_22hterra_GEO-long_FL03-VH.hdr	amplitudegeo_22hterra_GEO-long_FL03-VH.hdr	coherencygeo_22hterra_GEO-long_FL03-FL01-VH.hdr
April	contrastgeo_22hterra_GEO-long_FL03-VV	amplitudegeo_22hterra_GEO-long_FL03-VV	coherencygeo_22hterra_GEO-long_FL03-FL01-VV
April	contrastgeo_22hterra_GEO-long_FL03-VV.hdr	amplitudegeo_22hterra_GEO-long_FL03-VV.hdr	coherencygeo_22hterra_GEO-long_FL03-FL01-VV.hdr
April	contrastgeo_22hterra_GEO-short_FL01-HH	amplitudegeo_22hterra_GEO-short_FL01-HH	coherencygeo_22hterra_GEO-short_FL01-FL02-HH
April	contrastgeo_22hterra_GEO-short_FL01-HH.hdr	amplitudegeo_22hterra_GEO-short_FL01-HH.hdr	coherencygeo_22hterra_GEO-short_FL01-FL02-HH.hdr
April	contrastgeo_22hterra_GEO-short_FL01-HV	amplitudegeo_22hterra_GEO-short_FL01-HV	coherencygeo_22hterra_GEO-short_FL01-FL02-HV
April	contrastgeo_22hterra_GEO-short_FL01-HV.hdr	amplitudegeo_22hterra_GEO-short_FL01-HV.hdr	coherencygeo_22hterra_GEO-short_FL01-FL02-HV.hdr

April	contrastgeo_22hterra_GEO-short_FL01-VH	amplitudegeo_22hterra_GEO-short_FL01-VH	coherencygeo_22hterra_GEO-short_FL01-FL02-VH
April	contrastgeo_22hterra_GEO-short_FL01-VH.hdr	amplitudegeo_22hterra_GEO-short_FL01-VH.hdr	coherencygeo_22hterra_GEO-short_FL01-FL02-VH.hdr
April	contrastgeo_22hterra_GEO-short_FL01-VV	amplitudegeo_22hterra_GEO-short_FL01-VV	coherencygeo_22hterra_GEO-short_FL01-FL02-VV
April	contrastgeo_22hterra_GEO-short_FL01-VV.hdr	amplitudegeo_22hterra_GEO-short_FL01-VV.hdr	coherencygeo_22hterra_GEO-short_FL01-FL02-VV.hdr
April	contrastgeo_22hterra_GEO-short_FL02-HH	amplitudegeo_22hterra_GEO-short_FL02-HH	coherencygeo_22hterra_GEO-short_FL02-FL03-HH
April	contrastgeo_22hterra_GEO-short_FL02-HH.hdr	amplitudegeo_22hterra_GEO-short_FL02-HH.hdr	coherencygeo_22hterra_GEO-short_FL02-FL03-HH.hdr
April	contrastgeo_22hterra_GEO-short_FL02-HV	amplitudegeo_22hterra_GEO-short_FL02-HV	coherencygeo_22hterra_GEO-short_FL02-FL03-HV
April	contrastgeo_22hterra_GEO-short_FL02-HV.hdr	amplitudegeo_22hterra_GEO-short_FL02-HV.hdr	coherencygeo_22hterra_GEO-short_FL02-FL03-HV.hdr
April	contrastgeo_22hterra_GEO-short_FL02-VH	amplitudegeo_22hterra_GEO-short_FL02-VH	coherencygeo_22hterra_GEO-short_FL02-FL03-VH
April	contrastgeo_22hterra_GEO-short_FL02-VH.hdr	amplitudegeo_22hterra_GEO-short_FL02-VH.hdr	coherencygeo_22hterra_GEO-short_FL02-FL03-VH.hdr
April	contrastgeo_22hterra_GEO-short_FL02-VV	amplitudegeo_22hterra_GEO-short_FL02-VV	coherencygeo_22hterra_GEO-short_FL02-FL03-VV
April	contrastgeo_22hterra_GEO-short_FL02-VV.hdr	amplitudegeo_22hterra_GEO-short_FL02-VV.hdr	coherencygeo_22hterra_GEO-short_FL02-FL03-VV.hdr
April	contrastgeo_22hterra_GEO-short_FL03-HH	amplitudegeo_22hterra_GEO-short_FL03-HH	coherencygeo_22hterra_GEO-short_FL03-FL01-HH
April	contrastgeo_22hterra_GEO-short_FL03-HH.hdr	amplitudegeo_22hterra_GEO-short_FL03-HH.hdr	coherencygeo_22hterra_GEO-short_FL03-FL01-HH.hdr
April	contrastgeo_22hterra_GEO-short_FL03-HV	amplitudegeo_22hterra_GEO-short_FL03-HV	coherencygeo_22hterra_GEO-short_FL03-FL01-HV
April	contrastgeo_22hterra_GEO-short_FL03-HV.hdr	amplitudegeo_22hterra_GEO-short_FL03-HV.hdr	coherencygeo_22hterra_GEO-short_FL03-FL01-HV.hdr
April	contrastgeo_22hterra_GEO-short_FL03-VH	amplitudegeo_22hterra_GEO-short_FL03-VH	coherencygeo_22hterra_GEO-short_FL03-FL01-VH
April	contrastgeo_22hterra_GEO-short_FL03-VH.hdr	amplitudegeo_22hterra_GEO-short_FL03-VH.hdr	coherencygeo_22hterra_GEO-short_FL03-FL01-VH.hdr
April	contrastgeo_22hterra_GEO-short_FL03-VV	amplitudegeo_22hterra_GEO-short_FL03-VV	coherencygeo_22hterra_GEO-short_FL03-FL01-VV
April	contrastgeo_22hterra_GEO-short_FL03-VV.hdr	amplitudegeo_22hterra_GEO-short_FL03-VV.hdr	coherencygeo_22hterra_GEO-short_FL03-FL01-VV.hdr
April	contrastgeo_22hterra_HT-long_FL01-HH	amplitudegeo_22hterra_HT-long_FL01-HH	coherencygeo_22hterra_HT-long_FL01-FL02-HH
April	contrastgeo_22hterra_HT-long_FL01-HH.hdr	amplitudegeo_22hterra_HT-long_FL01-HH.hdr	coherencygeo_22hterra_HT-long_FL01-FL02-HH.hdr
April	contrastgeo_22hterra_HT-long_FL01-HV	amplitudegeo_22hterra_HT-long_FL01-HV	coherencygeo_22hterra_HT-long_FL01-FL02-HV
April	contrastgeo_22hterra_HT-long_FL01-HV.hdr	amplitudegeo_22hterra_HT-long_FL01-HV.hdr	coherencygeo_22hterra_HT-long_FL01-FL02-HV.hdr
April	contrastgeo_22hterra_HT-long_FL01-VH	amplitudegeo_22hterra_HT-long_FL01-VH	coherencygeo_22hterra_HT-long_FL01-FL02-VH
April	contrastgeo_22hterra_HT-long_FL01-VH.hdr	amplitudegeo_22hterra_HT-long_FL01-VH.hdr	coherencygeo_22hterra_HT-long_FL01-FL02-VH.hdr
April	contrastgeo_22hterra_HT-long_FL01-VV	amplitudegeo_22hterra_HT-long_FL01-VV	coherencygeo_22hterra_HT-long_FL01-FL02-VV
April	contrastgeo_22hterra_HT-long_FL01-VV.hdr	amplitudegeo_22hterra_HT-long_FL01-VV.hdr	coherencygeo_22hterra_HT-long_FL01-FL02-VV.hdr
April	contrastgeo_22hterra_HT-long_FL02-HH	amplitudegeo_22hterra_HT-long_FL02-HH	coherencygeo_22hterra_HT-long_FL02-FL03-HH
April	contrastgeo_22hterra_HT-long_FL02-HH.hdr	amplitudegeo_22hterra_HT-long_FL02-HH.hdr	coherencygeo_22hterra_HT-long_FL02-FL03-HH.hdr
April	contrastgeo_22hterra_HT-long_FL02-HV	amplitudegeo_22hterra_HT-long_FL02-HV	coherencygeo_22hterra_HT-long_FL02-FL03-HV
April	contrastgeo_22hterra_HT-long_FL02-HV.hdr	amplitudegeo_22hterra_HT-long_FL02-HV.hdr	coherencygeo_22hterra_HT-long_FL02-FL03-HV.hdr
April	contrastgeo_22hterra_HT-long_FL02-VH	amplitudegeo_22hterra_HT-long_FL02-VH	coherencygeo_22hterra_HT-long_FL02-FL03-VH
April	contrastgeo_22hterra_HT-long_FL02-VH.hdr	amplitudegeo_22hterra_HT-long_FL02-VH.hdr	coherencygeo_22hterra_HT-long_FL02-FL03-VH.hdr
April	contrastgeo_22hterra_HT-long_FL02-VV	amplitudegeo_22hterra_HT-long_FL02-VV	coherencygeo_22hterra_HT-long_FL02-FL03-VV
April	contrastgeo_22hterra_HT-long_FL02-VV.hdr	amplitudegeo_22hterra_HT-long_FL02-VV.hdr	coherencygeo_22hterra_HT-long_FL02-FL03-VV.hdr
April	contrastgeo_22hterra_HT-long_FL03-HH	amplitudegeo_22hterra_HT-long_FL03-HH	coherencygeo_22hterra_HT-long_FL03-FL01-HH
April	contrastgeo_22hterra_HT-long_FL03-HH.hdr	amplitudegeo_22hterra_HT-long_FL03-HH.hdr	coherencygeo_22hterra_HT-long_FL03-FL01-HH.hdr
April	contrastgeo_22hterra_HT-long_FL03-HV	amplitudegeo_22hterra_HT-long_FL03-HV	coherencygeo_22hterra_HT-long_FL03-FL01-HV
April	contrastgeo_22hterra_HT-long_FL03-HV.hdr	amplitudegeo_22hterra_HT-long_FL03-HV.hdr	coherencygeo_22hterra_HT-long_FL03-FL01-HV.hdr
April	contrastgeo_22hterra_HT-long_FL03-VH	amplitudegeo_22hterra_HT-long_FL03-VH	coherencygeo_22hterra_HT-long_FL03-FL01-VH
April	contrastgeo_22hterra_HT-long_FL03-VH.hdr	amplitudegeo_22hterra_HT-long_FL03-VH.hdr	coherencygeo_22hterra_HT-long_FL03-FL01-VH.hdr

April	contrastgeo_22hterra_HT-long_FL03-VV	amplitudegeo_22hterra_HT-long_FL03-VV	coherencygeo_22hterra_HT-long_FL03-FL01-VV
April	contrastgeo_22hterra_HT-long_FL03-VV.hdr	amplitudegeo_22hterra_HT-long_FL03-VV.hdr	coherencygeo_22hterra_HT-long_FL03-FL01-VV.hdr
April	contrastgeo_22hterra_HT-short_FL01-HH	amplitudegeo_22hterra_HT-short_FL01-HH	coherencygeo_22hterra_HT-short_FL01-FL02-HH
April	contrastgeo_22hterra_HT-short_FL01-HH.hdr	amplitudegeo_22hterra_HT-short_FL01-HH.hdr	coherencygeo_22hterra_HT-short_FL01-FL02-HH.hdr
April	contrastgeo_22hterra_HT-short_FL01-HV	amplitudegeo_22hterra_HT-short_FL01-HV	coherencygeo_22hterra_HT-short_FL01-FL02-HV
April	contrastgeo_22hterra_HT-short_FL01-HV.hdr	amplitudegeo_22hterra_HT-short_FL01-HV.hdr	coherencygeo_22hterra_HT-short_FL01-FL02-HV.hdr
April	contrastgeo_22hterra_HT-short_FL01-VH	amplitudegeo_22hterra_HT-short_FL01-VH	coherencygeo_22hterra_HT-short_FL01-FL02-VH
April	contrastgeo_22hterra_HT-short_FL01-VH.hdr	amplitudegeo_22hterra_HT-short_FL01-VH.hdr	coherencygeo_22hterra_HT-short_FL01-FL02-VH.hdr
April	contrastgeo_22hterra_HT-short_FL01-VV	amplitudegeo_22hterra_HT-short_FL01-VV	coherencygeo_22hterra_HT-short_FL01-FL02-VV
April	contrastgeo_22hterra_HT-short_FL01-VV.hdr	amplitudegeo_22hterra_HT-short_FL01-VV.hdr	coherencygeo_22hterra_HT-short_FL01-FL02-VV.hdr
April	contrastgeo_22hterra_HT-short_FL02-HH	amplitudegeo_22hterra_HT-short_FL02-HH	coherencygeo_22hterra_HT-short_FL02-FL03-HH
April	contrastgeo_22hterra_HT-short_FL02-HH.hdr	amplitudegeo_22hterra_HT-short_FL02-HH.hdr	coherencygeo_22hterra_HT-short_FL02-FL03-HH.hdr
April	contrastgeo_22hterra_HT-short_FL02-HV	amplitudegeo_22hterra_HT-short_FL02-HV	coherencygeo_22hterra_HT-short_FL02-FL03-HV
April	contrastgeo_22hterra_HT-short_FL02-HV.hdr	amplitudegeo_22hterra_HT-short_FL02-HV.hdr	coherencygeo_22hterra_HT-short_FL02-FL03-HV.hdr
April	contrastgeo_22hterra_HT-short_FL02-VH	amplitudegeo_22hterra_HT-short_FL02-VH	coherencygeo_22hterra_HT-short_FL02-FL03-VH
April	contrastgeo_22hterra_HT-short_FL02-VH.hdr	amplitudegeo_22hterra_HT-short_FL02-VH.hdr	coherencygeo_22hterra_HT-short_FL02-FL03-VH.hdr
April	contrastgeo_22hterra_HT-short_FL02-VV	amplitudegeo_22hterra_HT-short_FL02-VV	coherencygeo_22hterra_HT-short_FL02-FL03-VV
April	contrastgeo_22hterra_HT-short_FL02-VV.hdr	amplitudegeo_22hterra_HT-short_FL02-VV.hdr	coherencygeo_22hterra_HT-short_FL02-FL03-VV.hdr
April	contrastgeo_22hterra_HT-short_FL03-HH	amplitudegeo_22hterra_HT-short_FL03-HH	coherencygeo_22hterra_HT-short_FL03-FL01-HH
April	contrastgeo_22hterra_HT-short_FL03-HH.hdr	amplitudegeo_22hterra_HT-short_FL03-HH.hdr	coherencygeo_22hterra_HT-short_FL03-FL01-HH.hdr
April	contrastgeo_22hterra_HT-short_FL03-HV	amplitudegeo_22hterra_HT-short_FL03-HV	coherencygeo_22hterra_HT-short_FL03-FL01-HV
April	contrastgeo_22hterra_HT-short_FL03-HV.hdr	amplitudegeo_22hterra_HT-short_FL03-HV.hdr	coherencygeo_22hterra_HT-short_FL03-FL01-HV.hdr
April	contrastgeo_22hterra_HT-short_FL03-VH	amplitudegeo_22hterra_HT-short_FL03-VH	coherencygeo_22hterra_HT-short_FL03-FL01-VH
April	contrastgeo_22hterra_HT-short_FL03-VH.hdr	amplitudegeo_22hterra_HT-short_FL03-VH.hdr	coherencygeo_22hterra_HT-short_FL03-FL01-VH.hdr
April	contrastgeo_22hterra_HT-short_FL03-VV	amplitudegeo_22hterra_HT-short_FL03-VV	coherencygeo_22hterra_HT-short_FL03-FL01-VV
April	contrastgeo_22hterra_HT-short_FL03-VV.hdr	amplitudegeo_22hterra_HT-short_FL03-VV.hdr	coherencygeo_22hterra_HT-short_FL03-FL01-VV.hdr
June	contrastgeo_22hterra_GEO-long_FL05-HH	amplitudegeo_22hterra_GEO-long_FL05-HH	coherencygeo_22hterra_GEO-long_FL05-FL06-HH
June	contrastgeo_22hterra_GEO-long_FL05-HH.hdr	amplitudegeo_22hterra_GEO-long_FL05-HH.hdr	coherencygeo_22hterra_GEO-long_FL05-FL06-HH.hdr
June	contrastgeo_22hterra_GEO-long_FL05-HV	amplitudegeo_22hterra_GEO-long_FL05-HV	coherencygeo_22hterra_GEO-long_FL05-FL06-HV
June	contrastgeo_22hterra_GEO-long_FL05-HV.hdr	amplitudegeo_22hterra_GEO-long_FL05-HV.hdr	coherencygeo_22hterra_GEO-long_FL05-FL06-HV.hdr
June	contrastgeo_22hterra_GEO-long_FL05-VH	amplitudegeo_22hterra_GEO-long_FL05-VH	coherencygeo_22hterra_GEO-long_FL05-FL06-VH
June	contrastgeo_22hterra_GEO-long_FL05-VH.hdr	amplitudegeo_22hterra_GEO-long_FL05-VH.hdr	coherencygeo_22hterra_GEO-long_FL05-FL06-VH.hdr
June	contrastgeo_22hterra_GEO-long_FL05-VV	amplitudegeo_22hterra_GEO-long_FL05-VV	coherencygeo_22hterra_GEO-long_FL05-FL06-VV
June	contrastgeo_22hterra_GEO-long_FL05-VV.hdr	amplitudegeo_22hterra_GEO-long_FL05-VV.hdr	coherencygeo_22hterra_GEO-long_FL05-FL06-VV.hdr
June	contrastgeo_22hterra_GEO-long_FL06-HH	amplitudegeo_22hterra_GEO-long_FL06-HH	coherencygeo_22hterra_GEO-long_FL06-FL07-HH
June	contrastgeo_22hterra_GEO-long_FL06-HH.hdr	amplitudegeo_22hterra_GEO-long_FL06-HH.hdr	coherencygeo_22hterra_GEO-long_FL06-FL07-HH.hdr
June	contrastgeo_22hterra_GEO-long_FL06-HV	amplitudegeo_22hterra_GEO-long_FL06-HV	coherencygeo_22hterra_GEO-long_FL06-FL07-HV
June	contrastgeo_22hterra_GEO-long_FL06-HV.hdr	amplitudegeo_22hterra_GEO-long_FL06-HV.hdr	coherencygeo_22hterra_GEO-long_FL06-FL07-HV.hdr
June	contrastgeo_22hterra_GEO-long_FL06-VH	amplitudegeo_22hterra_GEO-long_FL06-VH	coherencygeo_22hterra_GEO-long_FL06-FL07-VH
June	contrastgeo_22hterra_GEO-long_FL06-VH.hdr	amplitudegeo_22hterra_GEO-long_FL06-VH.hdr	coherencygeo_22hterra_GEO-long_FL06-FL07-VH.hdr
June	contrastgeo_22hterra_GEO-long_FL06-VV	amplitudegeo_22hterra_GEO-long_FL06-VV	coherencygeo_22hterra_GEO-long_FL06-FL07-VV
June	contrastgeo_22hterra_GEO-long_FL06-VV.hdr	amplitudegeo_22hterra_GEO-long_FL06-VV.hdr	coherencygeo_22hterra_GEO-long_FL06-FL07-VV.hdr

June	contrastgeo_22hterra_GEO-long_FL07-HH	amplitudegeo_22hterra_GEO-long_FL07-HH	coherencygeo_22hterra_GEO-long_FL07-FL05-HH
June	contrastgeo_22hterra_GEO-long_FL07-HH.hdr	amplitudegeo_22hterra_GEO-long_FL07-HH.hdr	coherencygeo_22hterra_GEO-long_FL07-FL05-HH.hdr
June	contrastgeo_22hterra_GEO-long_FL07-HV	amplitudegeo_22hterra_GEO-long_FL07-HV	coherencygeo_22hterra_GEO-long_FL07-FL05-HV
June	contrastgeo_22hterra_GEO-long_FL07-HV.hdr	amplitudegeo_22hterra_GEO-long_FL07-HV.hdr	coherencygeo_22hterra_GEO-long_FL07-FL05-HV.hdr
June	contrastgeo_22hterra_GEO-long_FL07-VH	amplitudegeo_22hterra_GEO-long_FL07-VH	coherencygeo_22hterra_GEO-long_FL07-FL05-VH
June	contrastgeo_22hterra_GEO-long_FL07-VH.hdr	amplitudegeo_22hterra_GEO-long_FL07-VH.hdr	coherencygeo_22hterra_GEO-long_FL07-FL05-VH.hdr
June	contrastgeo_22hterra_GEO-long_FL07-VV	amplitudegeo_22hterra_GEO-long_FL07-VV	coherencygeo_22hterra_GEO-long_FL07-FL05-VV
June	contrastgeo_22hterra_GEO-long_FL07-VV.hdr	amplitudegeo_22hterra_GEO-long_FL07-VV.hdr	coherencygeo_22hterra_GEO-long_FL07-FL05-VV.hdr
June	contrastgeo_22hterra_GEO-short_FL05-HH	amplitudegeo_22hterra_GEO-short_FL05-HH	coherencygeo_22hterra_GEO-short_FL05-FL06-HH
June	contrastgeo_22hterra_GEO-short_FL05-HH.hdr	amplitudegeo_22hterra_GEO-short_FL05-HH.hdr	coherencygeo_22hterra_GEO-short_FL05-FL06-HH.hdr
June	contrastgeo_22hterra_GEO-short_FL05-HV	amplitudegeo_22hterra_GEO-short_FL05-HV	coherencygeo_22hterra_GEO-short_FL05-FL06-HV
June	contrastgeo_22hterra_GEO-short_FL05-HV.hdr	amplitudegeo_22hterra_GEO-short_FL05-HV.hdr	coherencygeo_22hterra_GEO-short_FL05-FL06-HV.hdr
June	contrastgeo_22hterra_GEO-short_FL05-VH	amplitudegeo_22hterra_GEO-short_FL05-VH	coherencygeo_22hterra_GEO-short_FL05-FL06-VH
June	contrastgeo_22hterra_GEO-short_FL05-VH.hdr	amplitudegeo_22hterra_GEO-short_FL05-VH.hdr	coherencygeo_22hterra_GEO-short_FL05-FL06-VH.hdr
June	contrastgeo_22hterra_GEO-short_FL05-VV	amplitudegeo_22hterra_GEO-short_FL05-VV	coherencygeo_22hterra_GEO-short_FL05-FL06-VV
June	contrastgeo_22hterra_GEO-short_FL05-VV.hdr	amplitudegeo_22hterra_GEO-short_FL05-VV.hdr	coherencygeo_22hterra_GEO-short_FL05-FL06-VV.hdr
June	contrastgeo_22hterra_GEO-short_FL06-HH	amplitudegeo_22hterra_GEO-short_FL06-HH	coherencygeo_22hterra_GEO-short_FL06-FL07-HH
June	contrastgeo_22hterra_GEO-short_FL06-HH.hdr	amplitudegeo_22hterra_GEO-short_FL06-HH.hdr	coherencygeo_22hterra_GEO-short_FL06-FL07-HH.hdr
June	contrastgeo_22hterra_GEO-short_FL06-HV	amplitudegeo_22hterra_GEO-short_FL06-HV	coherencygeo_22hterra_GEO-short_FL06-FL07-HV
June	contrastgeo_22hterra_GEO-short_FL06-HV.hdr	amplitudegeo_22hterra_GEO-short_FL06-HV.hdr	coherencygeo_22hterra_GEO-short_FL06-FL07-HV.hdr
June	contrastgeo_22hterra_GEO-short_FL06-VH	amplitudegeo_22hterra_GEO-short_FL06-VH	coherencygeo_22hterra_GEO-short_FL06-FL07-VH
June	contrastgeo_22hterra_GEO-short_FL06-VH.hdr	amplitudegeo_22hterra_GEO-short_FL06-VH.hdr	coherencygeo_22hterra_GEO-short_FL06-FL07-VH.hdr
June	contrastgeo_22hterra_GEO-short_FL06-VV	amplitudegeo_22hterra_GEO-short_FL06-VV	coherencygeo_22hterra_GEO-short_FL06-FL07-VV
June	contrastgeo_22hterra_GEO-short_FL06-VV.hdr	amplitudegeo_22hterra_GEO-short_FL06-VV.hdr	coherencygeo_22hterra_GEO-short_FL06-FL07-VV.hdr
June	contrastgeo_22hterra_GEO-short_FL07-HH	amplitudegeo_22hterra_GEO-short_FL07-HH	coherencygeo_22hterra_GEO-short_FL07-FL05-HH
June	contrastgeo_22hterra_GEO-short_FL07-HH.hdr	amplitudegeo_22hterra_GEO-short_FL07-HH.hdr	coherencygeo_22hterra_GEO-short_FL07-FL05-HH.hdr
June	contrastgeo_22hterra_GEO-short_FL07-HV	amplitudegeo_22hterra_GEO-short_FL07-HV	coherencygeo_22hterra_GEO-short_FL07-FL05-HV
June	contrastgeo_22hterra_GEO-short_FL07-HV.hdr	amplitudegeo_22hterra_GEO-short_FL07-HV.hdr	coherencygeo_22hterra_GEO-short_FL07-FL05-HV.hdr
June	contrastgeo_22hterra_GEO-short_FL07-VH	amplitudegeo_22hterra_GEO-short_FL07-VH	coherencygeo_22hterra_GEO-short_FL07-FL05-VH
June	contrastgeo_22hterra_GEO-short_FL07-VH.hdr	amplitudegeo_22hterra_GEO-short_FL07-VH.hdr	coherencygeo_22hterra_GEO-short_FL07-FL05-VH.hdr
June	contrastgeo_22hterra_GEO-short_FL07-VV	amplitudegeo_22hterra_GEO-short_FL07-VV	coherencygeo_22hterra_GEO-short_FL07-FL05-VV
June	contrastgeo_22hterra_GEO-short_FL07-VV.hdr	amplitudegeo_22hterra_GEO-short_FL07-VV.hdr	coherencygeo_22hterra_GEO-short_FL07-FL05-VV.hdr
June	contrastgeo_22hterra_HT-long_FL05-HH	amplitudegeo_22hterra_HT-long_FL05-HH	coherencygeo_22hterra_HT-long_FL05-FL06-HH
June	contrastgeo_22hterra_HT-long_FL05-HH.hdr	amplitudegeo_22hterra_HT-long_FL05-HH.hdr	coherencygeo_22hterra_HT-long_FL05-FL06-HH.hdr
June	contrastgeo_22hterra_HT-long_FL05-HV	amplitudegeo_22hterra_HT-long_FL05-HV	coherencygeo_22hterra_HT-long_FL05-FL06-HV
June	contrastgeo_22hterra_HT-long_FL05-HV.hdr	amplitudegeo_22hterra_HT-long_FL05-HV.hdr	coherencygeo_22hterra_HT-long_FL05-FL06-HV.hdr
June	contrastgeo_22hterra_HT-long_FL05-VH	amplitudegeo_22hterra_HT-long_FL05-VH	coherencygeo_22hterra_HT-long_FL05-FL06-VH
June	contrastgeo_22hterra_HT-long_FL05-VH.hdr	amplitudegeo_22hterra_HT-long_FL05-VH.hdr	coherencygeo_22hterra_HT-long_FL05-FL06-VH.hdr
June	contrastgeo_22hterra_HT-long_FL05-VV	amplitudegeo_22hterra_HT-long_FL05-VV	coherencygeo_22hterra_HT-long_FL05-FL06-VV
June	contrastgeo_22hterra_HT-long_FL05-VV.hdr	amplitudegeo_22hterra_HT-long_FL05-VV.hdr	coherencygeo_22hterra_HT-long_FL05-FL06-VV.hdr
June	contrastgeo_22hterra_HT-long_FL06-HH	amplitudegeo_22hterra_HT-long_FL06-HH	coherencygeo_22hterra_HT-long_FL06-FL07-HH
June	contrastgeo_22hterra_HT-long_FL06-HH.hdr	amplitudegeo_22hterra_HT-long_FL06-HH.hdr	coherencygeo_22hterra_HT-long_FL06-FL07-HH.hdr

June	contrastgeo_22hterra_HT-long_FL06-HV	amplitudegeo_22hterra_HT-long_FL06-HV	coherencygeo_22hterra_HT-long_FL06-FL07-HV
June	contrastgeo_22hterra_HT-long_FL06-HV.hdr	amplitudegeo_22hterra_HT-long_FL06-HV.hdr	coherencygeo_22hterra_HT-long_FL06-FL07-HV.hdr
June	contrastgeo_22hterra_HT-long_FL06-VH	amplitudegeo_22hterra_HT-long_FL06-VH	coherencygeo_22hterra_HT-long_FL06-FL07-VH
June	contrastgeo_22hterra_HT-long_FL06-VH.hdr	amplitudegeo_22hterra_HT-long_FL06-VH.hdr	coherencygeo_22hterra_HT-long_FL06-FL07-VH.hdr
June	contrastgeo_22hterra_HT-long_FL06-VV	amplitudegeo_22hterra_HT-long_FL06-VV	coherencygeo_22hterra_HT-long_FL06-FL07-VV
June	contrastgeo_22hterra_HT-long_FL06-VV.hdr	amplitudegeo_22hterra_HT-long_FL06-VV.hdr	coherencygeo_22hterra_HT-long_FL06-FL07-VV.hdr
June	contrastgeo_22hterra_HT-long_FL07-HH	amplitudegeo_22hterra_HT-long_FL07-HH	coherencygeo_22hterra_HT-long_FL07-FL05-HH
June	contrastgeo_22hterra_HT-long_FL07-HH.hdr	amplitudegeo_22hterra_HT-long_FL07-HH.hdr	coherencygeo_22hterra_HT-long_FL07-FL05-HH.hdr
June	contrastgeo_22hterra_HT-long_FL07-HV	amplitudegeo_22hterra_HT-long_FL07-HV	coherencygeo_22hterra_HT-long_FL07-FL05-HV
June	contrastgeo_22hterra_HT-long_FL07-HV.hdr	amplitudegeo_22hterra_HT-long_FL07-HV.hdr	coherencygeo_22hterra_HT-long_FL07-FL05-HV.hdr
June	contrastgeo_22hterra_HT-long_FL07-VH	amplitudegeo_22hterra_HT-long_FL07-VH	coherencygeo_22hterra_HT-long_FL07-FL05-VH
June	contrastgeo_22hterra_HT-long_FL07-VH.hdr	amplitudegeo_22hterra_HT-long_FL07-VH.hdr	coherencygeo_22hterra_HT-long_FL07-FL05-VH.hdr
June	contrastgeo_22hterra_HT-long_FL07-VV	amplitudegeo_22hterra_HT-long_FL07-VV	coherencygeo_22hterra_HT-long_FL07-FL05-VV
June	contrastgeo_22hterra_HT-long_FL07-VV.hdr	amplitudegeo_22hterra_HT-long_FL07-VV.hdr	coherencygeo_22hterra_HT-long_FL07-FL05-VV.hdr
June	contrastgeo_22hterra_HT-short_FL05-HH	amplitudegeo_22hterra_HT-short_FL05-HH	coherencygeo_22hterra_HT-short_FL05-FL06-HH
June	contrastgeo_22hterra_HT-short_FL05-HH.hdr	amplitudegeo_22hterra_HT-short_FL05-HH.hdr	coherencygeo_22hterra_HT-short_FL05-FL06-HH.hdr
June	contrastgeo_22hterra_HT-short_FL05-HV	amplitudegeo_22hterra_HT-short_FL05-HV	coherencygeo_22hterra_HT-short_FL05-FL06-HV
June	contrastgeo_22hterra_HT-short_FL05-HV.hdr	amplitudegeo_22hterra_HT-short_FL05-HV.hdr	coherencygeo_22hterra_HT-short_FL05-FL06-HV.hdr
June	contrastgeo_22hterra_HT-short_FL05-VH	amplitudegeo_22hterra_HT-short_FL05-VH	coherencygeo_22hterra_HT-short_FL05-FL06-VH
June	contrastgeo_22hterra_HT-short_FL05-VH.hdr	amplitudegeo_22hterra_HT-short_FL05-VH.hdr	coherencygeo_22hterra_HT-short_FL05-FL06-VH.hdr
June	contrastgeo_22hterra_HT-short_FL05-VV	amplitudegeo_22hterra_HT-short_FL05-VV	coherencygeo_22hterra_HT-short_FL05-FL06-VV
June	contrastgeo_22hterra_HT-short_FL05-VV.hdr	amplitudegeo_22hterra_HT-short_FL05-VV.hdr	coherencygeo_22hterra_HT-short_FL05-FL06-VV.hdr
June	contrastgeo_22hterra_HT-short_FL06-HH	amplitudegeo_22hterra_HT-short_FL06-HH	coherencygeo_22hterra_HT-short_FL06-FL07-HH
June	contrastgeo_22hterra_HT-short_FL06-HH.hdr	amplitudegeo_22hterra_HT-short_FL06-HH.hdr	coherencygeo_22hterra_HT-short_FL06-FL07-HH.hdr
June	contrastgeo_22hterra_HT-short_FL06-HV	amplitudegeo_22hterra_HT-short_FL06-HV	coherencygeo_22hterra_HT-short_FL06-FL07-HV
June	contrastgeo_22hterra_HT-short_FL06-HV.hdr	amplitudegeo_22hterra_HT-short_FL06-HV.hdr	coherencygeo_22hterra_HT-short_FL06-FL07-HV.hdr
June	contrastgeo_22hterra_HT-short_FL06-VH	amplitudegeo_22hterra_HT-short_FL06-VH	coherencygeo_22hterra_HT-short_FL06-FL07-VH
June	contrastgeo_22hterra_HT-short_FL06-VH.hdr	amplitudegeo_22hterra_HT-short_FL06-VH.hdr	coherencygeo_22hterra_HT-short_FL06-FL07-VH.hdr
June	contrastgeo_22hterra_HT-short_FL06-VV	amplitudegeo_22hterra_HT-short_FL06-VV	coherencygeo_22hterra_HT-short_FL06-FL07-VV
June	contrastgeo_22hterra_HT-short_FL06-VV.hdr	amplitudegeo_22hterra_HT-short_FL06-VV.hdr	coherencygeo_22hterra_HT-short_FL06-FL07-VV.hdr
June	contrastgeo_22hterra_HT-short_FL07-HH	amplitudegeo_22hterra_HT-short_FL07-HH	coherencygeo_22hterra_HT-short_FL07-FL05-HH
June	contrastgeo_22hterra_HT-short_FL07-HH.hdr	amplitudegeo_22hterra_HT-short_FL07-HH.hdr	coherencygeo_22hterra_HT-short_FL07-FL05-HH.hdr
June	contrastgeo_22hterra_HT-short_FL07-HV	amplitudegeo_22hterra_HT-short_FL07-HV	coherencygeo_22hterra_HT-short_FL07-FL05-HV
June	contrastgeo_22hterra_HT-short_FL07-HV.hdr	amplitudegeo_22hterra_HT-short_FL07-HV.hdr	coherencygeo_22hterra_HT-short_FL07-FL05-HV.hdr
June	contrastgeo_22hterra_HT-short_FL07-VH	amplitudegeo_22hterra_HT-short_FL07-VH	coherencygeo_22hterra_HT-short_FL07-FL05-VH
June	contrastgeo_22hterra_HT-short_FL07-VH.hdr	amplitudegeo_22hterra_HT-short_FL07-VH.hdr	coherencygeo_22hterra_HT-short_FL07-FL05-VH.hdr
June	contrastgeo_22hterra_HT-short_FL07-VV	amplitudegeo_22hterra_HT-short_FL07-VV	coherencygeo_22hterra_HT-short_FL07-FL05-VV
June	contrastgeo_22hterra_HT-short_FL07-VV.hdr	amplitudegeo_22hterra_HT-short_FL07-VV.hdr	coherencygeo_22hterra_HT-short_FL07-FL05-VV.hdr

9.2   List of Areas of Interest (AoI)

Table 9-2 lists the 50 AoIs selected for the study during WP 240. Among them 47 fields or field stripes, both the Caione and CREA farms and the whole 'Apulian Tavoliere' test site.

The meaning of the abbreviations is: CA = Caione farm, CREA = CREA farm, DW = Durum wheat, AA = Alfalfa, MA = Maize, SF = Sunflower, BS = Bare soil, QU = Quinoa.

Fields, that were irrigated, are indicated in Table 9-2 by coloured frames, April (red) and June (green).

Table 9-2: Areas of interest, monitored fields, their crops and known irrigation procedures.

No.	Field	Field ID April	Crop April	Irrigation April	Field ID June	Crop June	Irrigation June	Area
1	CA01_DW	24	wheat		486	wheat		10.57 ha
2	CA01_DW_stripe24		wheat	23.-24.04.2022				
3	CA01_DW_stripe27		wheat	26.-27.04.2022				
4	CA01_DW_stripe28		wheat	27.-28.04.2022				
5	CA01_DW_stripe29		wheat	28.-29.04.2022				
6	CA02_DW	25	wheat		485	wheat		7.43 ha
7	CA02_DW_stripe24		wheat	23.-24.04.2022				
8	CA02_DW_stripe27		wheat	26.-27.04.2022				
9	CA02_DW_stripe28		wheat	27.-28.04.2022				
10	CA02_DW_stripe29		wheat	28.-29.04.2022				
11	CA_AA					alfalfa		
12	CA_AA_1					alfalfa		
13	CA_AA_2					alfalfa		
14	CA_AA_3					alfalfa		
15	CA_MA					maize		
16	CA_MA_stripe13					maize	13.06.2023	
17	CA_MA_stripe14					maize	14.06.2023	
18	CA_MA_4					maize		
19	FIELD_376	75	wheat		376			18.57 ha
20	FIELD_378	70	wheat		378			23.86 ha
21	FIELD_379	68			379	tomato		20.50 ha
22	FIELD_381	60	wheat		381			18.62 ha
23	FIELD_395	71	wheat		395			27.58 ha
24	FIELD_090	90	wheat		404			34.72 ha
25	FIELD_401	91	chickpea		401	chickpea		8.70 ha
26	FIELD_484	26	wheat		484			26.46 ha
27	CREA_043	43	bare		493	tomato		7.01 ha
28	CREA_003	3	wheat		459	bare		2.16 ha
29	CREA_DW		wheat					
30	CREA_DW_stripe26		wheat	26.04.2022				
31	CREA_DW_stripe27		wheat	27.04.2022				
32	CREA_DW_stripe28		wheat	28.04.2022				
33	CREA_DW_stripe29		wheat	29.04.2022				
34	CREA_MA	42	bare soil		506	maize		0.79 ha
35	CREA_MA_1					maize		
36	CREA_MA_2					maize		
37	CREA_SF	42	bare soil		505	sunflower		0.51 ha
38	CREA_SF_stripe14					sunflower	14.06.2023	
39	CREA_BS_SUB		bare soil					
40	CREA_BS		bare soil					
41	CREA_BS_stripe26_27		bare soil	26.-27.04.2022				
42	CREA_QU					quinoa		

43	CREA_QU_stripe14					quinoa	14.06.2023	
44	FIELD_509	100	horse bean		509	bare		10.10 ha
45	FIELD_508	99	bare soil		508	tomato		6.69 ha
46	FIELD_437	116	asparagus		437	asparagus		10.99 ha
47	FIELD_456-500	130	wheat		456 + 500	bare		11.95 ha
48	Caione_farm		miscellaneous			miscellaneous		
49	CREA_farm		miscellaneous			miscellaneous		
50	AOI_ApulianTavoliere		miscellaneous			miscellaneous		

9.3   Inventory of Results

The results of the study are compiled as geocoded images and plots in PDF files (see Table 9-3). There are six PDFs per AoI studied, a total of 300 files for the 50 AoIs selected. Two per quality measure (mean value, contrast and coherence) and one each per simulated SAR system implementation, e.g. GEO and HT. All data (300 PDF files) are archived at DLR.

Table 9-3: List of PDF files (containing images and plots) resulting from the study carried out in WP 240.

No.	Analysis Result (PDF)
1	22hterra_AOI_ApulianTavoliere_amplitudegeo_GEO.pdf
2	22hterra_AOI_ApulianTavoliere_amplitudegeo_HT.pdf
3	22hterra_AOI_ApulianTavoliere_coherencygeo_GEO.pdf
4	22hterra_AOI_ApulianTavoliere_coherencygeo_HT.pdf
5	22hterra_AOI_ApulianTavoliere_contrastgeo_GEO.pdf
6	22hterra_AOI_ApulianTavoliere_contrastgeo_HT.pdf
7	22hterra_CA01_DW_amplitudegeo_GEO.pdf
8	22hterra_CA01_DW_amplitudegeo_HT.pdf
9	22hterra_CA01_DW_coherencygeo_GEO.pdf
10	22hterra_CA01_DW_coherencygeo_HT.pdf
11	22hterra_CA01_DW_contrastgeo_GEO.pdf
12	22hterra_CA01_DW_contrastgeo_HT.pdf
…	…
289	22hterra_FIELD_508_amplitudegeo_GEO.pdf
290	22hterra_FIELD_508_amplitudegeo_HT.pdf
291	22hterra_FIELD_508_coherencygeo_GEO.pdf
292	22hterra_FIELD_508_coherencygeo_HT.pdf
293	22hterra_FIELD_508_contrastgeo_GEO.pdf
294	22hterra_FIELD_508_contrastgeo_HT.pdf
295	22hterra_FIELD_509_amplitudegeo_GEO.pdf
296	22hterra_FIELD_509_amplitudegeo_HT.pdf
297	22hterra_FIELD_509_coherencygeo_GEO.pdf
298	22hterra_FIELD_509_coherencygeo_HT.pdf
299	22hterra_FIELD_509_contrastgeo_GEO.pdf
300	22hterra_FIELD_509_contrastgeo_HT.pdf